Multiple-Quantum MAS NMR of Half-Integer Quadrupolar Nuclei

Submitted in partial fulfilment of the requirements

for the degree of Doctor of Philosophy

Steven Paul Brown

Merton College, Oxford

Trinity 1997

Multiple-Quantum MAS NMR of Half-Integer Quadrupolar Nuclei

Steven Paul Brown, Merton College.

Abstract of D. Phil. Thesis, Trinity 1997.

The only NMR-accessible nuclides of many chemically important elements, *e.g.*, ^{17}O, ^{23}Na, and ^{27}Al, are quadrupolar with half-integer spin (*i.e.*, I = 3/2, 5/2). The ability of NMR to provide information about the local environment of such nuclei in the solid state has been severely limited as a consequence of second-order quadrupolar broadening, which is not completely removed by conventional magic-angle spinning (MAS). This broadening is typically of the order of kilohertz and usually obscures any chemical shift information. In early 1995, Frydman and Harwood demonstrated that high resolution can be achieved in NMR spectra of half-integer quadrupolar nuclei in the solid state by performing a two-dimensional experiment, referred to as the multiple-quantum MAS, or MQMAS, experiment, in which multiple- and single-quantum coherences are correlated in the presence of MAS. This new NMR experiment is investigated in detail in this thesis.

To date, most MQMAS experiments have been performed in such a way that, to obtain an NMR spectrum displaying only isotropic shifts (both chemical and second-order quadrupolar), it is necessary to apply a shearing transformation to the two-dimensional data set. It is shown that shearing can result in an unwelcome distortion of the two-dimensional lineshape, and alternative MQMAS experiments are presented in which both multiple- and single-quantum evolution occurs during the t_1 interval of the two-dimensional NMR experiment. As well as avoiding the requirement for a shearing transformation, the amount of data processing necessary to achieve the optimum sensitivity is considerably reduced for these "split-t_1" experiments. Furthermore, in certain important cases, the sensitivity is expected theoretically and demonstrated experimentally to be better for the split-t_1 approach.

The MQMAS experiment is applied to two problems of current chemical interest. Firstly, high-resolution ^{27}Al MQMAS spectra are obtained for two molecular sieves which undergo a topotactic phase transformation at elevated temperature. Secondly, an ^{17}O MQMAS spectrum of the synthesised geologically-interesting mineral forsterite is presented, and the potential for providing information about water incorporation in the earth's mantle is discussed.

Acknowledgements

Firstly, I would like to thank my supervisor, Dr. Steve Wimperis, for the considerable help and guidance he has given me during my D. Phil. and Part II. I also thank past and present members of the SCW group for their help and input, in particular Sharon Ashbrook for helping with the acquisition and interpretation of some of the MQMAS spectra presented in this thesis. Special thanks to Colan Hughes, Dr. David Tunstall, Sharon Ashbrook, and Dr. Steve Heyes for finding the time to read this weighty tome, and for making helpful suggestions for improvements. Further thanks to: Courtaulds Research (in particular, my industrial supervisors Dr. Roger Ibbett and Dr. Ian Herbert) and EPSRC for funding my D. Phil.; Mark Simpson and Dr. Steve Heyes for their technical advice concerning MAS; Dr. Paul Hodgkinson for writing the processing software to my very demanding specifications; Monica Price for happily grinding up specimens from the Oxford University minerals collection in the name of research; Vinton Carter and others at St. Andrew's University for introducing me to topotactic phase transformations; and Dr. Andrew Berry for synthesising the ^{17}O-enriched forsterite sample.

Outside science, I think of all the many friends I have made during my seven years in Oxford. In particular, I want to say thank you to Dave, Jamie and Suzanne, Jon, and Patrick. I remember the many residents of Commonwealth House, from near and far, whom I met during an interesting and challenging three years there. Thanks also to the OURHC for allowing me to escape from Oxford to the mountains of Britain and beyond. I am really thankful to all at St. Aldate's church, and special thanks to the two and three year-olds in the Tumblers for helping me take my mind off NMR for an hour on a Sunday morning. To close, I especially thank my family, in particular Mum and Dad, for all their love and support, and most importantly, I acknowledge my Lord and Saviour, Jesus Christ.

"In him we have redemption through his blood, the forgiveness of sins,
in accordance with the riches of God's grace that he lavished on us
with all wisdom and understanding."

Ephesians 1: 7-8 (NIV)

Contents

Chapter 1

Introduction

Since the first reported demonstration in the bulk phase in 1946 [1, 2], nuclear magnetic resonance (NMR) has developed into one of the most widely used methods for the determination of structure and the study of dynamics. For most liquid samples, NMR lineshapes are inherently narrow as a consequence of rapid molecular motion. However, for powdered solids, where such isotropic motion does not occur, lineshapes are normally at least three orders of magnitude broader. The problem in solid-state NMR spectra is not a lack of information, but rather that there is so much information that the overall result is a broad and often featureless lineshape. The history of solid-state NMR has, therefore, been dominated by the development of experimental methods for removing some or all broadening mechanisms, such that meaningful spectra result.

Line-narrowing methods have sought to mimic how molecular motion in liquids introduces a time-dependence to the anisotropic interactions by either physically rotating the sample or performing rotations in spin space using radiofrequency pulses. The first significant method to be developed was that of magic-angle spinning (MAS) in 1958 [3-5], in which the sample is physically rotated at an angle of 54.74° to the B_0 magnetic field. Successful narrowing was achieved for small dipolar couplings, for example between ^{19}F nuclei in CaF_2 [5], and also where the dominant broadening mechanism was a heteronuclear dipolar coupling or the chemical shift anisotropy (CSA). However, it was found that MAS was not so effective for a homonuclear dipolar broadening larger than the spinning speed. This represented a major limitation since the most problematic broadening is that due to

the homonuclear ^{1}H-^{1}H dipolar coupling, the strength of which is usually greater than even the maximum spinning speeds achievable today (~ 35 kHz).

As a result of the inability of MAS to remove large dipolar couplings, attention turned to methods involving averaging over spin, rather than spatial, parameters. In particular, the aim was to remove homonuclear dipolar broadenings but retain the CSA. In 1965, Lee and Goldberg presented a method [6] in which irradiation took place at the magic angle in the rotating frame, *i.e.*, $\Omega/\omega_1 = \tan(54.74°)$, where Ω is the resonance offset and ω_1 is the nutation frequency of the pulse (see Chapter 4). Such magic angle irradiation averages the homonuclear dipolar coupling, to a first-order approximation, to zero, while the CSA and the heteronuclear dipolar coupling are only scaled by $\sqrt{3}$.

In 1968, Waugh and co-workers presented the first of a series of multiple-pulse train methods, consisting of regularly spaced cycles of on-resonance 90° pulses about the +x, +y, –x, and –y axes of the rotating frame [7, 8]. The initial four-pulse sequence, referred to as the WAHUHA experiment, averages the homonuclear dipolar coupling, up to a second-order approximation, to zero. The understanding of these experiments was aided by the concept of an average Hamiltonian [8], which enabled the development of extended sequences which were designed to remove higher-order dipolar-broadening terms, *e.g.*, the MREV-8 [9-11], BR-24 [12], and BLEW-48 [13] methods.

The demonstration by Pines *et al.* in 1972 that the signal due to a dilute spin, *e.g.* ^{13}C, could be enhanced by cross polarisation (CP) [14-16] from an abundant spin, *e.g.* ^{1}H, led to the development of CP MAS NMR [17-20]. The combination of proton decoupling [21-22] to remove broadening due to the heteronuclear ^{1}H-^{13}C dipolar coupling and MAS to average out the CSA, together with the CP signal enhancement, means that high-resolution ^{13}C spectra can be routinely obtained at natural abundance [23].

In 1977, Gerstein *et al.* showed that high-resolution ^{1}H spectra could be achieved by combined rotation and multiple-pulse spectroscopy (CRAMPS) [24, 25], in which multiple-pulse trains to remove the homonuclear dipolar coupling are synchronised with MAS to remove CSA. Unfortunately, CRAMPS has proved to be very sensitive to the missetting of experimental parameters, although, recently, a technically less-demanding pulse sequence has been proposed which is applicable at the very fast MAS speeds currently attainable [26].

The above discussion has focused on line-narrowing methods for spin I = 1/2 nuclei. However, the only NMR-accessible nuclei of many elements are quadrupolar with half-integer spin. For example, metals such as sodium and aluminium (^{23}Na and ^{27}Al are spin I = 3/2 and I = 5/2, respectively) are constituents of a wide range of industrially important materials, such as glasses and molecular sieves, while the spin I = 5/2 nucleus ^{17}O is the only nuclide with non-zero nuclear spin of the element oxygen, which as well as being ubiquitous in nature is present in an enormous range of inorganic compounds. The success of MAS as a line-narrowing method for spin I = 1/2 nuclei has encouraged its application to half-integer quadrupolar nuclei. The results, however, have been generally disappointing since significant residual second-order quadrupolar broadening of the dominant central transition remains [27, 28]. Although improved narrowing can be achieved by changing the rotor angle in variable-angle spinning (VAS) experiments [29, 30], the attainable resolution is still poor.

In 1988, two methods for the removal of second-order quadrupolar broadening were presented, namely the double rotation (DOR) and dynamic angle spinning (DAS) techniques [31-39]. In both methods, line narrowing is achieved by sample rotation about two axes, either simultaneously (DOR) or sequentially (DAS). Considerable new structural information has been obtained using DOR and DAS, in particular for amorphous materials such as glasses, where the absence of long-range

order means that X-ray diffraction is unsuitable as a method for structure determination. For example, Farnan *et al.* [37] have presented ^{17}O DAS spectra of silicate glasses in which bridging and non-bridging oxygens can be distinguished. By analysing the observed distributions of quadrupolar and chemical shift parameters, valuable information on intermediate-range order within the glasses was obtained.

Although the DOR and DAS techniques are able to remove second-order quadrupolar broadening, the technical complexity and other drawbacks of the experiments has meant that their use has not become widespread. In early 1995, Frydman and Harwood demonstrated that sample rotation about two different axes is not necessary. Instead, second-order quadrupolar broadening can be removed by performing a two-dimensional experiment in which multiple- and single-quantum coherences are correlated in the presence of MAS [40]. This multiple-quantum magic-angle spinning (MQMAS) experiment has generated much interest in the NMR community and beyond [41-78]. By way of example, Fig. 1.1 (overleaf) shows that the narrowing achieved by the MQMAS experiment, as compared to normal MAS, means that the two sodium sites in an approximately equal mixture of sodium oxalate and sodium sulphate are clearly resolved.

This thesis presents a detailed description of all aspects of the MQMAS experiment. Chapter 2 introduces the fundamentals which provide the framework for the discussion in the later chapters. A familiarity with the NMR phenomenon and the general features of the Fourier transform approach (for example, as described in basic texts [79, 80]) is assumed. Firstly, the effect of the quadrupolar coupling on the energy levels of a quadrupolar nucleus is introduced. This is followed by a description of the density operator formalism, by means of which complex multiple-pulse experiments can be understood. The penultimate section of the chapter then discusses the Fourier transformation of one- and two-dimensional data sets and the appearance of the resultant lineshapes. Finally, the NMR

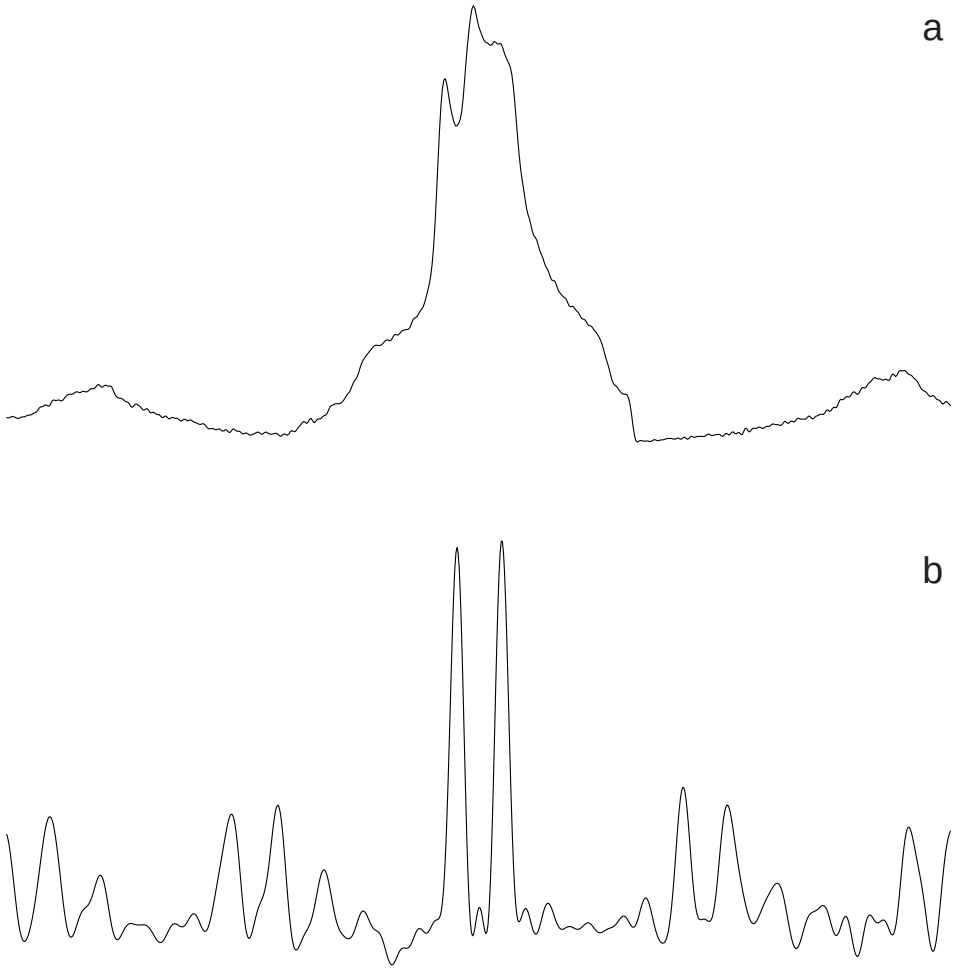

Figure 1.1. ^{23}Na (105.8 MHz) (a) MAS and (b) isotropic MQMAS spectra of an approximately equal mixture of sodium oxalate (BDH) and sodium sulphate (East Anglia Chemicals). In both cases, the displayed spectral width (cut down from 20 kHz) equals 12.5 kHz. In (a), the following experimental conditions were used: 16 transients (consisting of 512 points) were averaged, the relaxation interval was 1 s, a radiofrequency pulse of duration 1.4 μs was used, and the spinning speed was 5.3 kHz. Experimental parameters for (b) are given in Fig. 6.8. It is evident that the two sites, whose second-order quadrupolar-broadened spectra overlap in (a) are clearly resolved in (b). The peaks on either side of the central peaks in both spectra are spinning sidebands.

spectrometers used to acquire the experimental results presented in the thesis are described.

In Chapter 3, the detailed mathematical derivation of the perturbation of the energy levels of a half-integer quadrupolar nucleus by the quadrupolar coupling is presented. The calculated expressions are then used, together with simulated and experimental spectra, to illustrate the effect of sample rotation on the appearance of

quadrupolar-broadened spectra. The final section of this chapter then describes the DAS and DOR experiments, before introducing the MQMAS experiment. The optimisation of coherence transfer is integral to the success of the MQMAS experiment and forms the subject of Chapter 4. In particular, the problem of achieving uniform excitation over the whole powder pattern is considered.

Halfway through the thesis, the position has been reached where the different approaches for the implementation of the MQMAS experiment can be presented. In the original MQMAS experiment of Frydman and Harwood, phase cycling is used to select a coherence transfer pathway which gives rise to two-dimensional "phase-twist" lineshapes. However, Chapter 5 shows that the original experiment can be easily modified to ensure that pure absorption-mode lineshapes are obtained. Two different approaches are described. Firstly, the echo and antiecho pathways are combined with equal amplitude to yield a signal which is amplitude-modulated with respect to t_1; a "hypercomplex" two-dimensional Fourier transform then gives rise to pure absorption-mode lineshapes. Alternatively, if a spin echo is appended onto the original experiment, pure absorption-mode lineshapes can be obtained as a consequence of the properties of whole echoes.

In the experiments described in Chapter 5, the inhomogeneous quadrupolar broadening is spread out along a "ridge" which, for I = 3/2 nuclei, has a slope of –7/9 with respect to the F_2 axis. To obtain a spectrum displaying only isotropic shifts, it is necessary to perform a shearing transformation such that the ridges appear parallel to the F_2 axis. However, Chapter 6 shows that this shearing transformation can cause unwelcome distortions in the two-dimensional lineshape, and alternative experiments in which both multiple- and single-quantum evolution occurs during t_1 are presented. In these experiments, the anisotropic second-order quadrupolar broadening is fully refocused in t_1 and, hence, undistorted inhomogeneously-broadened ridges appear parallel to the F_2 axis without the need for any shearing

transformation. The "split-t_1" experiments are then compared, in terms of relative sensitivity and ease of processing, with the experiments presented in Chapter 5.

In only two and a half years, a number of applications of the MQMAS experiment to novel samples have been published. Chapter 7 summarises the recent developments and describes, as illustrations of the potential of the technique, the application of the MQMAS experiment to two problems of current chemical interest. Firstly, the topotactic phase transformation between two molecular sieves is investigated using ^{27}Al MQMAS NMR. Secondly, an ^{17}O MQMAS spectrum of the synthesised mineral forsterite is presented, and the potential for providing information about water incorporation in the earth's mantle is discussed.

Chapter 2

Fundamentals

2.1 The Quadrupolar Coupling

NMR spectra of nuclei with spin $I \geq 1$ are dominated by the interaction of the nuclear quadrupole moment Q with the electric field gradient at the nucleus. This quadrupolar coupling is very strong, often of the order of megahertz, and causes both large quadrupolar splittings in spectra and efficient quadrupolar relaxation. Quadrupolar relaxation typically gives rise to homogeneous linewidths (*i.e.*, ignoring the broadening associated with the quadrupolar splitting) which are significantly larger than those encountered in high-resolution ^{1}H NMR. However, it is the inhomogeneous broadening associated with the quadrupolar splitting which usually dominates the appearance of solid-state spectra. This section introduces this effect of the quadrupolar coupling on the energy levels of quadrupolar nuclei, with a full mathematical description being given in Chapter 3.

Consider Fig. 2.1 (overleaf) which presents energy level diagrams for spin I = 1 and I = 3/2. As shown in the left-hand side of Figs. 2.1a and 2.1b, the degeneracy of the energy levels is lifted by the Zeeman interaction. This gives rise to, in the absence of a quadrupolar splitting, two (I = 1) or three (I = 3/2) degenerate $\Delta m_I = \pm 1$ transitions having frequency ω_0 rad s^{-1}, where ω_0 is the Larmor frequency. The effect of the quadrupolar coupling on the Zeeman energy levels, can be calculated, to successive degrees of approximation, using perturbation theory (this calculation is presented in detail in Chapter 3 for spin

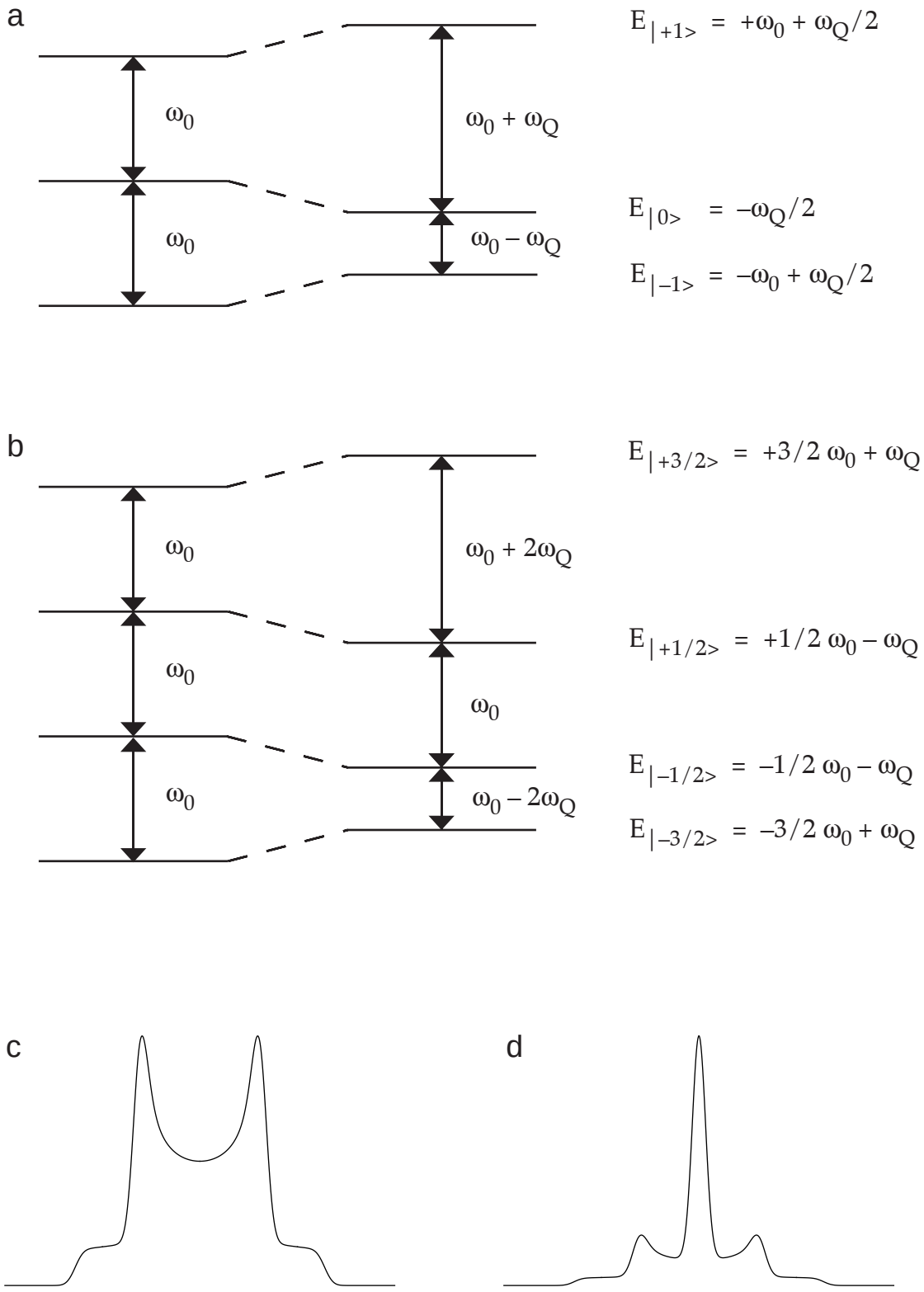

Figure 2.1. (a), (b) The perturbation, to a first-order approximation, of the energy levels of a spin (a) I = 1 and (b) I = 3/2 nucleus by the quadrupolar coupling. The energy levels are labelled according to the m_I quantum number, and energies are given in units of rad s^{-1}. (c), (d) Simulated spin (c) I = 1 and (d) I = 3/2 spectra for a powder distribution of ω_Q, where $\omega_Q^{PAS}/2\pi$ equals 4 and 2 kHz, respectively, and the spectral width is 12.5 kHz. Axial symmetry is assumed.

I = 3/2). When the Zeeman interaction is much greater than the quadrupolar coupling, a first-order approximation suffices. In this case, the $\Delta m_I = \pm 1$ transitions have frequencies $\omega_0 - \omega_Q$ and $\omega_0 + \omega_Q$ (I = 1), and $\omega_0 - 2\omega_Q$, ω_0, and $\omega_0 + 2\omega_Q$ (I = 3/2), where ω_Q is the quadrupolar splitting parameter.

Comparing Figs. 2.1a and 2.1b, a clear difference is observed, namely, for I = 3/2 nuclei, but not for I = 1 nuclei, there is a central transition, whose frequency, to a first-order approximation, does not depend on ω_Q. In a powdered sample, there is a range of ω_Q from zero to ω_Q^{PAS} (see Chapter 3) . This gives rise to characteristic spin I = 1 and I = 3/2 first-order powder patterns, as shown in Figs. 2.1c and 2.1d, respectively. In particular, the presence of a dominant central transition, for the spin I = 3/2 case, is clearly seen in Fig. 2.1d. This difference between integer and half-integer quadrupolar nuclei means that very different strategies are required for handling inhomogeneous broadening in the two cases, and it is solely the latter case which is considered in this thesis.

The simulated spectrum in Fig. 2.1d corresponds to the case where the quadrupolar splitting is very small, as for example where there is significant motional averaging, *e.g.*, in heterogeneous biological systems [81]. However, in a powdered solid, the quadrupolar splitting is normally of the order of megahertz. This has two important consequences on the observed spectra. Firstly, the satellite transitions ($m_I = 3/2 \leftrightarrow m_I = 1/2$ and $m_I = -3/2 \leftrightarrow m_I = -1/2$) are typically inhomogeneously broadened to such an extent that they are lost in the baseline, and only the central transition is observed. Secondly, as shown in, for example, Fig. 1.1a, a broadening of the central transition by the quadrupolar coupling is observed. In terms of perturbation theory, the observed behaviour can be explained by the inclusion of a second-order approximation (see Chapter 3).

Returning to the spin I = 3/2 first-order energy-level diagram of Fig. 2.1b, closer examination reveals that, in addition to the central transition, the triple-

quantum transition ($m_I = 3/2 \leftrightarrow m_I = -3/2$) also does not, to a first-order approximation, depend on ω_Q. Indeed, it is found that, for half-integer quadrupolar nuclei, all symmetric ($m_I = +s \leftrightarrow m_I = -s$) transitions do not, to a first-order approximation, depend on ω_Q. This important fact is exploited in the removal of second-order inhomogeneous quadrupolar broadening by the MQMAS experiment.

2.2 The Density Operator Formalism

This section introduces the density operator formalism [82], which offers a rigorous yet flexible approach for the understanding of complex multiple-pulse NMR experiments. An NMR sample consists of a collection, or ensemble, of independent spin systems, where each spin system is described quantum-mechanically by a wavefunction $\psi(t)$. Consider an expansion of $\psi(t)$ in a complete set of orthonormal basis functions, $|s\rangle$, *i.e.*,

$$\psi(t) = \sum_s c_s(t) \, |s\rangle \, , \tag{2.1}$$

where $c_s(t)$ are time-dependent coefficients. The expectation value of an observable, corresponding to the operator A, is then given by

$$< A > = \sum_{s,\, r} c_s(t) \, c_r(t)^* \, \langle r | A | s \rangle \, . \tag{2.2}$$

The interesting feature of Eq. (2.2) is that the expectation value of any observable always depends on the same products, $c_s(t) \, c_r(t)^*$. This property leads to the definition of the density operator $\sigma(t)$, whose matrix representation, termed the density matrix, has elements, $\sigma_{sr}(t)$, given by

$$\sigma_{sr}(t) = \langle s|\sigma(t)|r\rangle$$

$$= \overline{c_s(t)\, c_r(t)^*}, \qquad (2.3)$$

where the overbar denotes an ensemble average.

It is shown in Appendix A that the expectation value of an observable corresponding to the operator A is given simply by the trace (the sum of the diagonal elements) of the product of the matrix representation of the operator and the density matrix, *i.e.*,

$$< A > = Tr\{ A\, \sigma(t) \} = Tr\{ \sigma(t)\, A \}\,. \qquad (2.4)$$

An example of the application of Eq. (2.4) relates to the calculation of the observable signal in an NMR experiment. The detected x and y components of the magnetisation vector, M_x and M_y, are proportional to the x and y components of the spin angular momentum, I_x and I_y (the matrix representations of I_x and I_y are given in Appendix B). Therefore, the real and imaginary parts of the free induction decay correspond to $< I_x >$ and $< I_y >$, respectively:

$$< I_x > = Tr\{ I_x\, \sigma(t) \} \qquad < I_y > = Tr\{ I_y\, \sigma(t) \}\,. \qquad (2.5)$$

Appendix A further presents the derivation, starting from the time-dependent Schrödinger equation, of an expression describing the time evolution of the density operator. This expression is referred to as the Liouville-von Neumann equation, and is given as:

$$d\sigma(t)/dt = -i\, [\, H(t), \sigma(t)\,]\,, \qquad (2.6)$$

where H(t) is the Hamiltonian of the system. If the Hamiltonian is time-independent or can be made so by a judicious choice of reference frame, Eq. (2.6) can be solved to give

$$\sigma(t) = \exp\{ -i H t \} \sigma(0) \exp\{ +i H t \} , \tag{2.7}$$

where H is now a time-independent Hamiltonian.

The above discussion has introduced density operator theory in terms of a general set of orthonormal basis functions. To follow a specific NMR experiment, a suitable choice of basis set must be made. In this thesis, the set of eigenstates, $|s = m_I\rangle$, of the Zeeman Hamiltonian, $H_Z = \omega_0 I_z$, is used, *i.e.*,

$$H_Z |s = m_I\rangle = m_I \omega_0 |s = m_I\rangle . \tag{2.8}$$

(The matrix representations of the z-component of the spin angular momentum, I_z, are given in Appendix B.) The choice of this basis set lies in the clear physical significance of the individual elements. By way of illustration, the density matrix for a spin I = 3/2 nucleus has the form:

$$\sigma(t) = \begin{pmatrix} \sigma_{11}(t) & \sigma_{12}(t) & \sigma_{13}(t) & \sigma_{14}(t) \\ \sigma_{21}(t) & \sigma_{22}(t) & \sigma_{23}(t) & \sigma_{24}(t) \\ \sigma_{31}(t) & \sigma_{32}(t) & \sigma_{33}(t) & \sigma_{34}(t) \\ \sigma_{41}(t) & \sigma_{42}(t) & \sigma_{43}(t) & \sigma_{44}(t) \end{pmatrix} . \tag{2.9}$$

While the diagonal elements, $\sigma_{11}(t)$, $\sigma_{22}(t)$, $\sigma_{33}(t)$, and $\sigma_{44}(t)$, correspond to the relative populations of the energy levels, the off-diagonal elements correspond to coherent superpositions of eigenstates, or simply coherences. For example, at thermal equilibrium, $\sigma(t)$ is proportional to I_z [82], while the observable central and satellite transition single-quantum coherences are represented by $\sigma_{23}(t)$ and $\sigma_{32}(t)$, and $\sigma_{12}(t)$, $\sigma_{21}(t)$, $\sigma_{34}(t)$, and $\sigma_{43}(t)$, respectively. The other elements then represent

multiple-quantum coherences, for example $\sigma_{14}(t)$ and $\sigma_{41}(t)$ correspond to p = +3 and p = –3 coherences, respectively. It should be noted that the density operator, by definition, is Hermitian, *i.e.*, $\langle r|\sigma(t)|s\rangle = \langle s|\sigma(t)|r\rangle^*$, and therefore coherences of order +p and –p are always present together.

2.3 NMR Lineshapes

In two-dimensional NMR, the design of the experiment affects both the way in which time-domain data sets must be processed, and the appearance of the lineshapes in the resulting spectra [83]. The purpose of this section is to provide an understanding of these considerations, which are very important in the context of the discussion in Chapters 5 and 6 of the different approaches for the implementation of the MQMAS experiment. To begin with, lineshapes resulting from normal one-dimensional NMR experiments are considered.

2.3.1 One-Dimensional Experiments

All modern NMR spectrometers employ quadrature detection to ensure that the sense of precession in the rotating frame can be determined. In the true complex approach, the real and imaginary parts of the free induction decay are simultaneously sampled at intervals of 1/SW, where SW is the spectral width in hertz, using two detectors with orthogonal reference phases. A free induction decay, consisting of a single resonance, can then be described, for $t \geq 0$, as

$$f(t) = \exp\{ i \Omega t \} \exp\{ -R t \} , \qquad (2.10)$$

where Ω is the resonance offset (in rad s^{-1}), and R is a constant describing the transverse relaxation rate.

To obtain the frequency-domain spectrum, F(ω), a complex Fourier transform is then performed:

$$F(\omega) = \int_{-\infty}^{+\infty} f(t) \exp\{ -i \omega t \} dt , \tag{2.11}$$

i.e.,

$$F(\omega) = \int_{0}^{+\infty} \exp\{ - (i (\omega - \Omega) + R) t \} dt . \tag{2.12}$$

Performing the integration in Eq. (2.12) yields

$$F(\omega) = A^L(\omega) - i D^L(\omega) , \tag{2.13}$$

where $A^L(\omega)$ and $D^L(\omega)$ correspond to Lorentzian absorptive and dispersive lineshapes, respectively:

$$A^L(\omega) = \frac{R}{R^2 + (\omega - \Omega)^2} \tag{2.14a}$$

$$D^L(\omega) = \frac{\omega - \Omega}{R^2 + (\omega - \Omega)^2} . \tag{2.14b}$$

These lineshapes are plotted in Fig. 2.2a (overleaf). Considering the absorptive Lorentzian line, it can be shown, using Eq. (2.14a) that the half width at half maximum height, $\Delta\omega_{1/2}$, equals R rad s^{-1}, or, in units of hertz, $\Delta\upsilon_{1/2}$ equals $R/(2\pi)$.

In the context of solid-state NMR, as a consequence of inhomogeneous broadening, it is often found that the observed NMR lineshapes more closely resemble Gaussian, rather than Lorentzian, lines. Such absorptive and dispersive

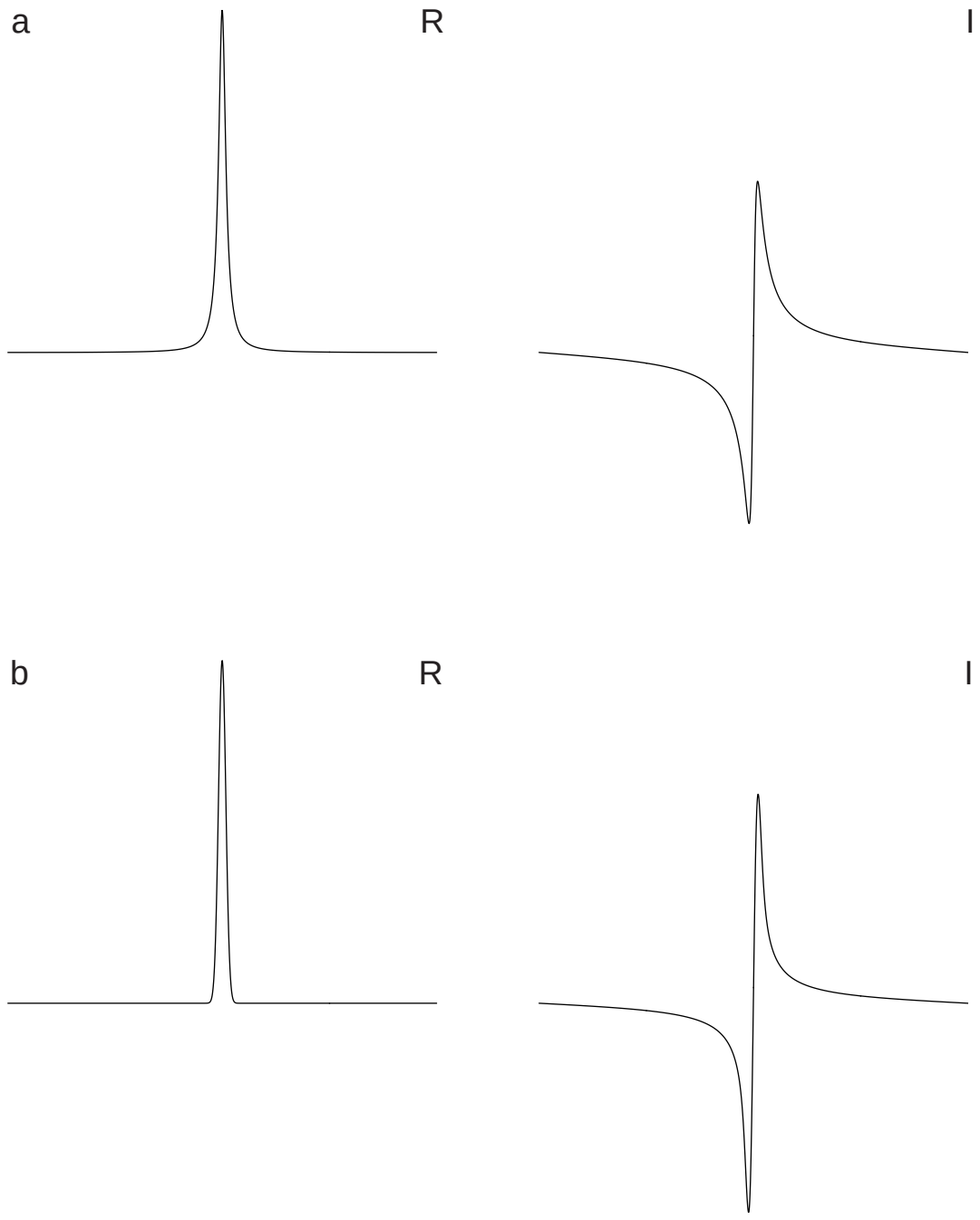

Figure 2.2. The real (R) – absorptive – and imaginary (I) – dispersive – parts of (a) Lorentzian and (b) Gaussian one-dimensional lineshapes. In both cases, $\Delta\upsilon_{1/2}$ equals 125 Hz, while the spectral width equals 12.5 kHz.

Gaussian lineshapes are plotted in Fig. 2.2b. From a comparison of the Lorentzian and Gaussian absorptive lineshapes, it is clear that the Gaussian lineshape is significantly narrower at the base. Mathematically, absorptive and dispersive Gaussian lineshapes are described by

$$A^G(\omega) = \exp\left\{\frac{-(\omega - \Omega)^2}{2\,\Delta^2}\right\} \tag{2.15a}$$

$$D^G(\omega) = \exp\left\{\frac{-(\omega - \Omega)^2}{2\,\Delta^2}\right\} \operatorname{erf}\left\{\frac{(\omega - \Omega)}{\Delta\,2\,\sqrt{2}}\right\}, \tag{2.15b}$$

where Δ^2 is referred to as the second moment (in rad s^{-1}), and erf{z} is the error function:

$$\operatorname{erf}\{z\} = \frac{2}{\sqrt{\pi}} \int_0^z \exp(-X^2)\, dX\,. \tag{2.16}$$

For an absorptive Gaussian line, $\Delta\omega_{1/2}$ equals $\Delta\,\sqrt{(2\,\ln 2)}$ rad s^{-1}.

An alternative approach to obtaining quadrature detection is the so-called Redfield method [84, 85], in which only one detector samples points at an interval of 1/(2 SW), with the phase of detection being incremented by 90° for successive points. (This is the method used by the Bruker spectrometers, on which the experimental results presented in this thesis were recorded.) The resulting free induction decay is then of the form

$$\begin{aligned} f(t) &= \exp\{\, i\,\Omega\, t\,\}\exp\{\, -R\, t\,\}\exp\{\, -i\,(2\pi)\,(SW/2)\, t\,\} \\ &= [\,\cos\{\,\Omega\, t\,\}\cos\{\,(2\pi)\,(SW/2)\, t\,\} + \sin\{\,\Omega\, t\,\}\sin\{\,(2\pi)\,(SW/2)\, t\,\}\,]\exp\{\, -R\, t\,\} \\ &= \cos\{\,(\,\Omega - (2\pi)\,(SW/2)\,)\, t\,\}\exp\{\, -R\, t\,\}\,, \end{aligned} \tag{2.17}$$

where the 2π factor is necessary since SW is in units of hertz. The Fourier transform of a cosine-modulated function gives rise to a spectrum which is symmetric about zero frequency. However, it is apparent from Eq. (2.17) that the net effect of

incrementing the phase of detection is a shift of all resonance frequencies by SW/2. Therefore, although there is no sign discrimination in the spectrum, resonances which lie on either side of the receiver can still be distinguished. Remembering that the spectral width has been doubled, the same spectrum as would result from true complex acquisition is obtained by discarding one of the two symmetric halves of the spectrum.

2.3.2 Two-Dimensional Experiments

The pulse sequence and coherence transfer pathway diagrams [86] for two simple two-dimensional NMR experiments are shown in Fig. 2.3 (overleaf). (The desired coherence transfer pathways can be selected experimentally by the technique of phase cycling [86], the rules for which are given in Appendix H, along with phase cycles for all the MQMAS experiments described in the thesis.) Considering first the experiment in Fig. 2.3a, where only one pathway is selected, the time-domain data set, assuming only evolution under a resonance offset, Ω, is of the form

$$s(t_1, t_2) = \exp\{ -i \Omega t_1 \} \exp\{ -R t_1 \} \exp\{ +i \Omega t_2 \} \exp\{ -R t_2 \} . \qquad (2.18)$$

If a complex Fourier transform is performed in the t_2 dimension, Eq. (2.18) becomes

$$s(t_1, \omega_2) = \exp\{ -i \Omega t_1 \} \exp\{ -R t_1 \} [A_2\{ +\Omega \} - i D_2\{ +\Omega \}] , \qquad (2.19)$$

where $A_2\{\Omega\}$ and $D_2\{\Omega\}$ represent one-dimensional absorptive and dispersive Lorentzian lineshapes centred at a frequency Ω in the ω_2 frequency domain.

Inspection of Eq. (2.19) reveals that the phase of the lineshape in the ω_2 dimension varies as a function of t_1, as shown in Fig. 2.4 (on page 20). Such a data

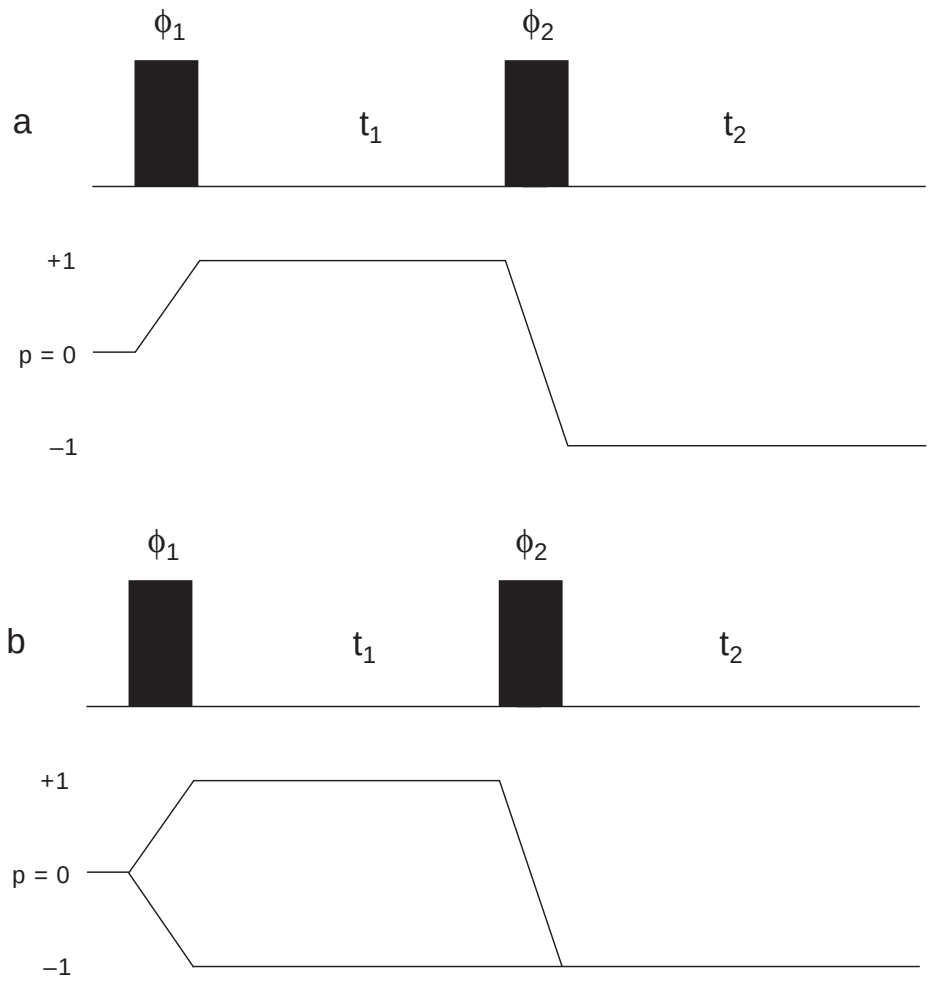

Figure 2.3. Pulse sequences and coherence transfer pathway diagrams for two simple two-dimensional experiments. The resulting signal is phase-modulated and amplitude-modulated with respect to t_1 in (a) and (b), respectively.

set is then described as being *phase-modulated* with respect to t_1. If a complex Fourier transform is subsequently performed in the t_1 dimension, the resulting frequency-domain spectrum is given by

$$s(\omega_1, \omega_2) = [\, A_1\{-\Omega\} - i\, D_1\{-\Omega\} \,] \times [\, A_2\{+\Omega\} - i\, D_2\{+\Omega\} \,]$$

$$= (\, A_1\{-\Omega\}\, A_2\{+\Omega\} - D_1\{-\Omega\}\, D_2\{+\Omega\} \,)$$

$$- i\, (\, A_1\{-\Omega\}\, D_2\{+\Omega\} + D_1\{-\Omega\}\, A_2\{+\Omega\} \,) \,. \qquad (2.20)$$

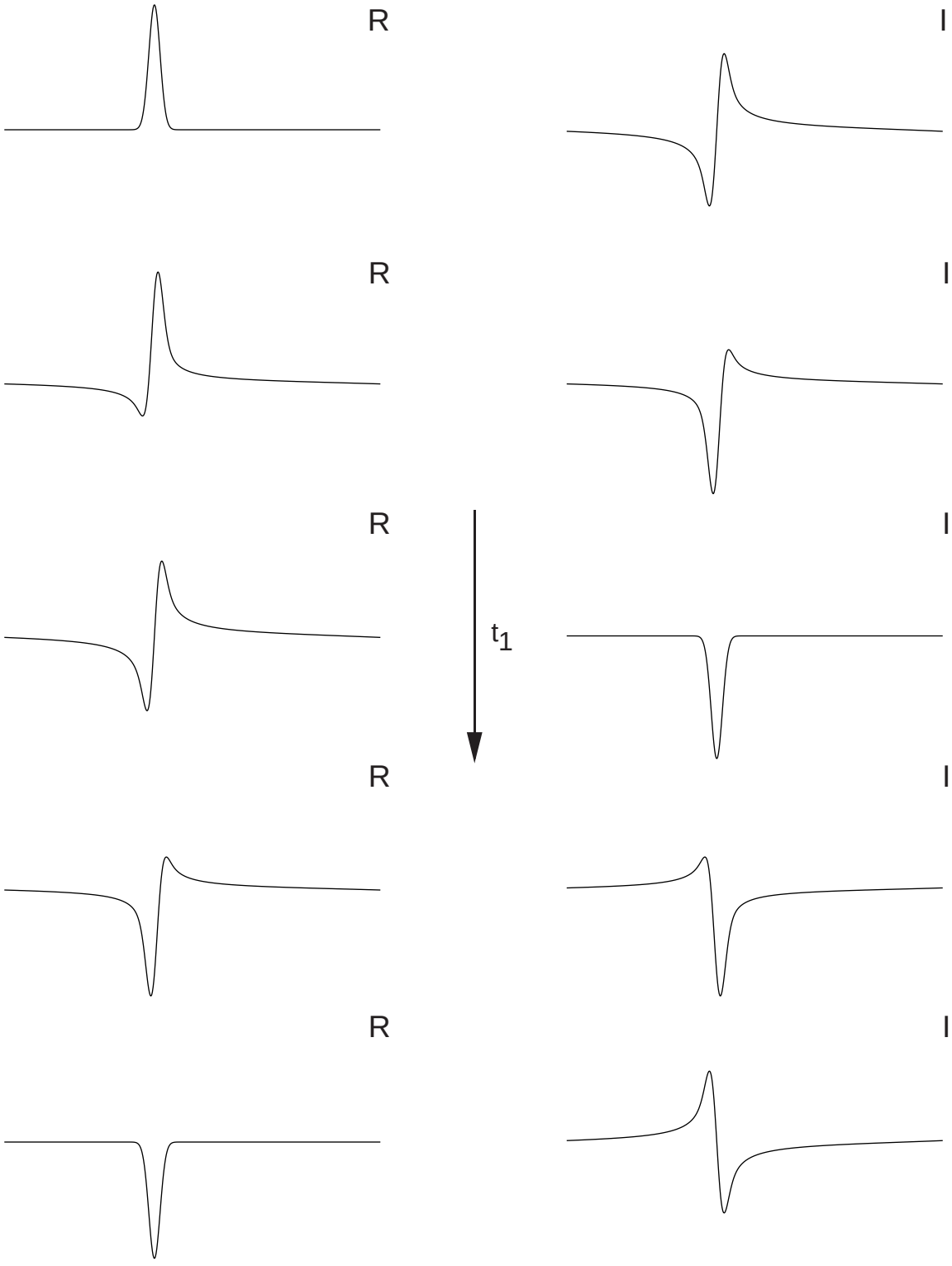

Figure 2.4. The real (R) and imaginary (I) parts of one-dimensional spectra resulting from a complex Fourier transform with respect to t_2 of selected rows, with increasing t_1 as indicated, of a two-dimensional time-domain data set simulated for a single resonance with a small resonance offset, using the experiment of Fig. 2.3a. It can be seen that the spectra are phase-modulated with respect to t_1.

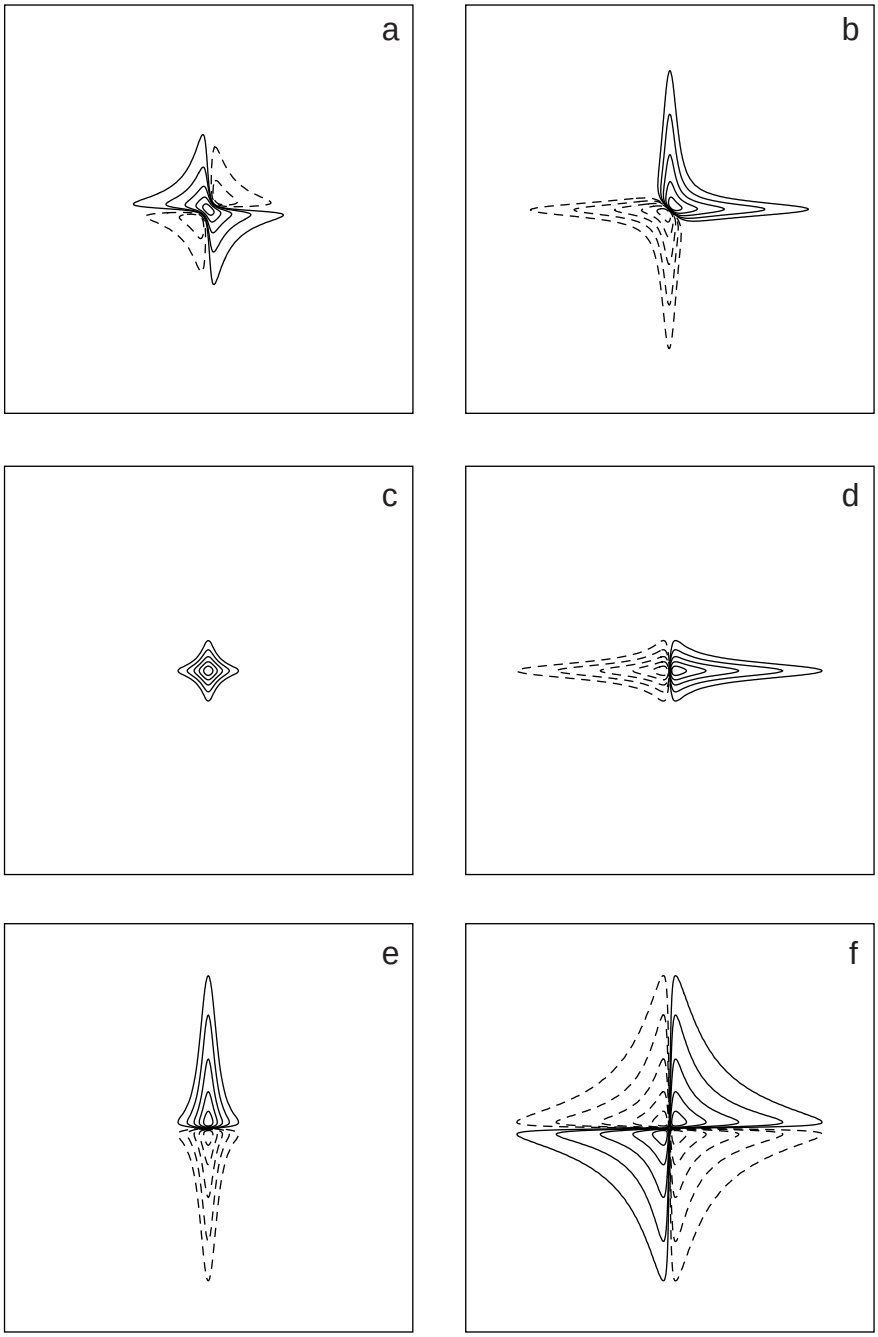

Figure 2.5. (a)-(b) Contour plots of the (a) real and (b) imaginary parts of the two-dimensional spectrum obtained by a complex two-dimensional Fourier transform of a data set, for an on-resonance signal, resulting from the phase-modulated experiment of Fig. 2.3a. The mathematical form of the lineshapes is given by Eq. (2.20). The phase-twisted character of the Lorentzian lineshapes is apparent. (c)-(f) Contour plots of the four components of the two-dimensional spectrum obtained by a hypercomplex two-dimensional Fourier transform of a data set, for an on-resonance signal, resulting from the amplitude-modulated experiment of Fig. 2.3b. The spectra in (c) and (e), and (d) and (f) correspond to the deletion, after Fourier transform with respect to t_2, of the real and imaginary components, respectively. The Lorentzian lineshapes are pure absorption-mode in (c), and dispersion-mode in ω_2, in ω_1, and in both dimensions in (d), (e) and (f), respectively. In all plots, $\Delta\upsilon_{1/2}$ equals 150 Hz, the spectral width in F_1 and F_2 equals 10 kHz, positive and negative contours are shown as solid and dashed lines, and contour levels correspond to 4, 8, 16, 32 and 64% of the maximum height.

The contour plots of the real and imaginary parts of the spectrum described by Eq. (2.20) are presented in Figs. 2.5a and 2.5b (previous page), respectively. It is clear that both components contain a mixture of absorptive and dispersive components. Such phase-twisted two-dimensional lineshapes are very undesirable, since the large "tails" due to the dispersive contribution mean that the resolution of different resonances is greatly reduced.

In the experiment of Fig. 2.3b, both p = +1 and p = –1 coherences are allowed to evolve during t_1. If the pathways are combined equally, the resulting time-domain data set is then described by:

$$s(t_1, t_2) = (\exp\{ -i \Omega t_1 \} + \exp\{ i \Omega t_1 \}) \exp\{ -R t_1 \} \exp\{ +i \Omega t_2 \} \exp\{ -R t_2 \}$$

$$= 2 \cos\{ \Omega t_1 \} \exp\{ -R t_1 \} \exp\{ +i \Omega t_2 \} \exp\{ -R t_2 \} . \qquad (2.21)$$

Complex Fourier transformation in the t_2 dimension then yields

$$s(t_1, \omega_2) = 2 \cos\{ \Omega t_1 \} \exp\{ -R t_1 \} [A_2\{ +\Omega \} - i D_2\{ +\Omega \}] . \qquad (2.22)$$

In contrast to Eq. (2.19), inspection of Eq. (2.22) reveals that varying t_1 changes the amplitude, rather than the phase, of the lineshape in the ω_2 dimension, as shown in Fig. 2.6 (overleaf). Such a data set is, therefore, described as being *amplitude-modulated* with respect to t_1. To obtain pure absorption-mode lineshapes, it is necessary to separate the real and imaginary parts of Eq. (2.22) before performing the complex Fourier transform in the t_1 dimension. This approach is referred to as a hypercomplex two-dimensional Fourier transform to distinguish it from the complex two-dimensional Fourier transform which gave rise to Eq. (2.20). Considering only the real part, Eq. (2.22) becomes

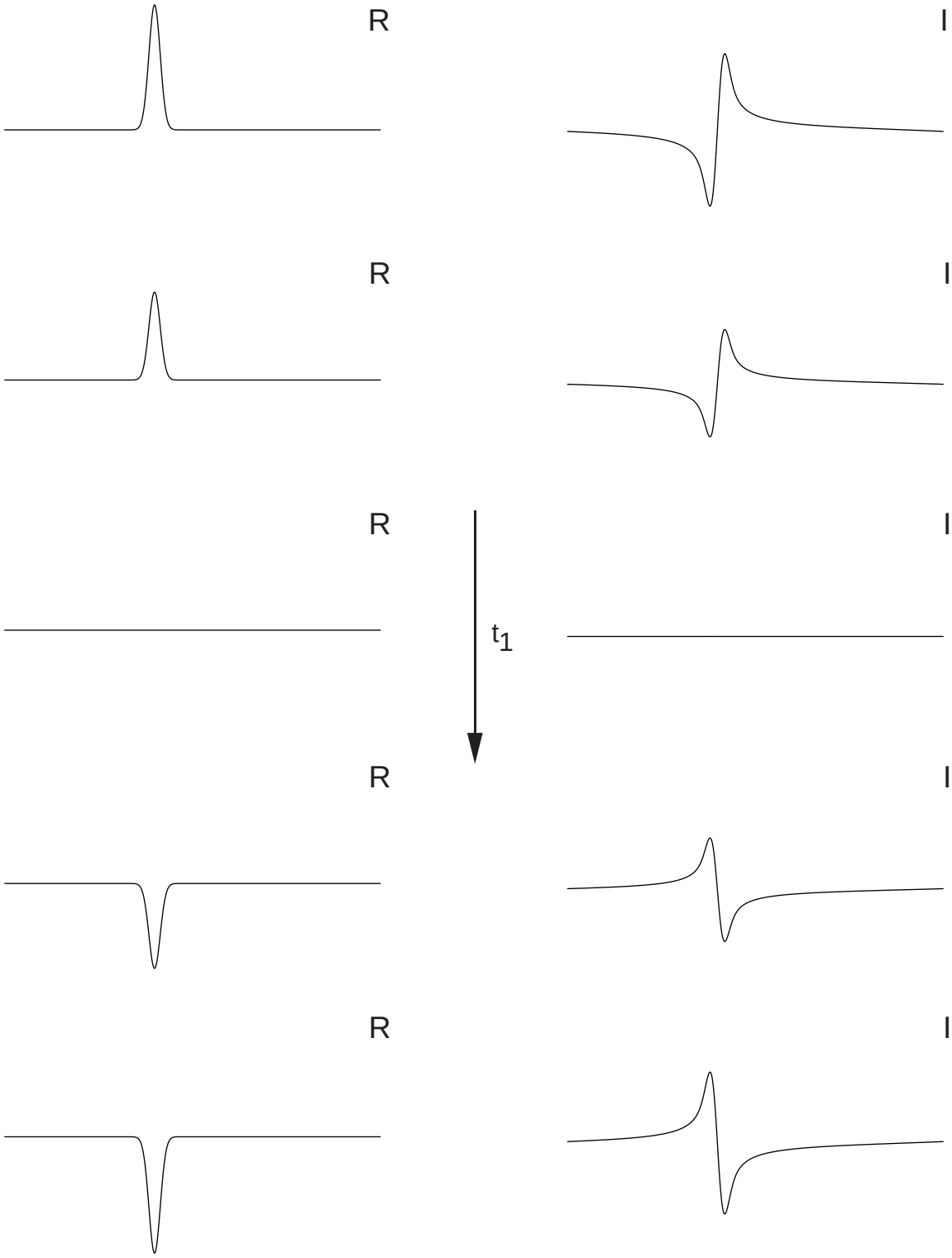

Figure 2.6. The real (R) and imaginary (I) parts of one-dimensional spectra resulting from a complex Fourier transform with respect to t_2 of selected rows, with increasing t_1 as indicated, of a two-dimensional time-domain data set simulated for a single resonance with a small resonance offset, using the experiment of Fig. 2.3b. It can be seen that the spectra are amplitude-modulated with respect to t_1.

$$s(t_1, \omega_2) = 2 \cos\{ \Omega t_1 \} \exp\{ -R t_1 \} A_2\{ +\Omega \}$$

$$= (\exp\{ -i \Omega t_1 \} + \exp\{ i \Omega t_1 \}) \exp\{ -R t_1 \} A_2\{ +\Omega \} . \quad (2.23)$$

Complex Fourier transformation in the t_1 dimension then yields

$$s(\omega_1, \omega_2) = (A_1\{ -\Omega \} A_2\{ -\Omega \} + A_1\{ +\Omega \} A_2\{ +\Omega \})$$

$$- i (D_1\{ -\Omega \} A_2\{+\Omega \} + D_1\{ +\Omega \} A_2\{ +\Omega \}) . \quad (2.24)$$

Figures 2.5c and 2.5e present contour plots of the real and imaginary parts, respectively, of the spectrum described by Eq. (2.24) for an on-resonance signal. Contour plots of the spectra obtained by retaining the imaginary part of Eq. (2.22) are presented in Figs. 2.5d and 2.5f. The two-dimensional Lorentzian lineshapes are pure absorption-mode in Fig. 2.5c, and dispersion-mode in ω_2, in ω_1, and in both dimensions in Figs. 2.5d, 2.5e, and 2.5f, respectively. From a comparison of Figs. 2.5a and 2.5c, it is clear why pure absorption-mode lineshapes are preferred.

For comparison, Fig. 2.7 (overleaf) presents contour plots of the two-dimensional pure absorption-mode Lorentzian and Gaussian lineshapes. It can be seen that while the Lorentzian lineshape is star-shaped with 'tails' parallel to the ω_1 and ω_2 axes, the Gaussian lineshape exhibits circular contours [87].

One apparent disadvantage of the amplitude-modulated experiment is that there is no sign discrimination in ω_1 in the frequency-domain spectrum described by Eq. (2.24). Sign discrimination can, however, be easily restored. One approach, referred to as the States-Haberkorn-Ruben method [88], involves performing a second experiment in which the phase of the first pulse is incremented by 90°, with the result that the two pathways now subtract. The signal is then sine modulated with respect to t_1, *i.e.*,

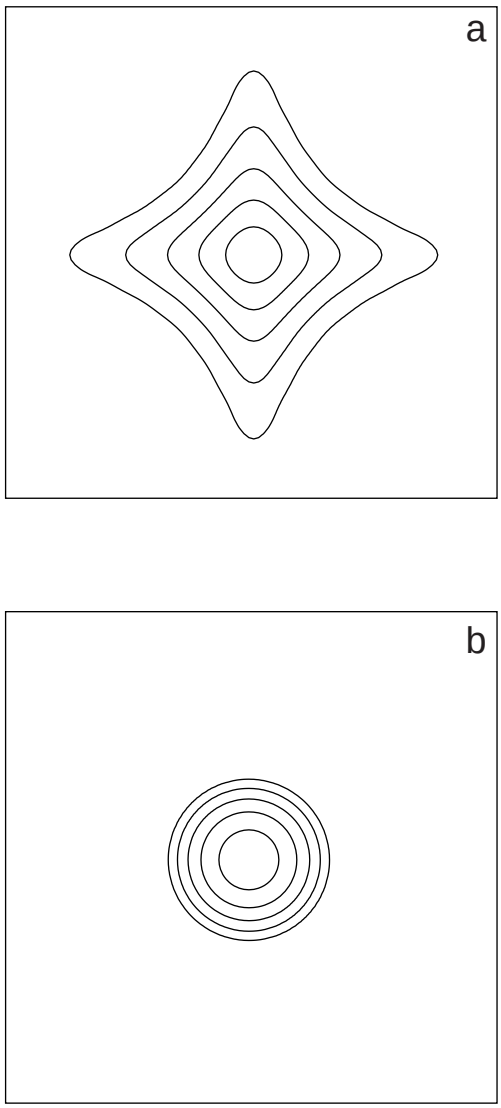

Figure 2.7. Contour plots of two-dimensional pure absorption-mode (a) Lorentzian and (b) Gaussian lineshapes. In both cases, $\Delta\upsilon_{1/2}$ equals 150 Hz, the spectral width in both F_1 and F_2 is 2 kHz, and contour levels correspond to 4, 8, 16, 32 and 64% of the maximum peak height.

$$s(t_1, t_2) = 2 \sin\{ \Omega t_1 \} \exp\{ -R t_1 \} \exp\{ +i \Omega t_2 \} \exp\{ -R t_2 \} . \qquad (2.25)$$

Hypercomplex two-dimensional Fourier transformation of this data set yields, considering only the component containing pure absorption-mode lineshapes,

$$s(\omega_1, \omega_2) = (A_1\{ -\Omega \} A_2\{ +\Omega \} - A_1\{ +\Omega \} A_2\{ +\Omega \}) . \qquad (2.26)$$

It is then clear that sign discrimination in ω_1 is easily restored by combining Eq. (2.26) with the real part of Eq. (2.24).

Alternatively, sign discrimination can be restored by the technique of Time Proportional Phase Increments (TPPI) [89]. This method involves only performing a single experiment, and is analogous to the Redfield method for achieving quadrature detection in F_2. The increment in t_1 is halved to $1/(2\,SW)$, and the phase of the first pulse (or group of pulses) is shifted, for each t_1 increment, by $\pi/(2|p|)$, where p corresponds to the order of coherence which evolves during t_1. TPPI has the effect of modulating a coherence of order p by $\exp\{-i\,p\,\phi\}$, where

$$\phi = \frac{\pi\, t_1}{2\,|p|\,\Delta t_1} = \frac{(2\pi)\,SW\, t_1}{2\,|p|} \quad . \tag{2.27}$$

Noting the dependence of the modulation on the sign of the coherence order, Eq. (2.23) becomes

$$s(t_1, \omega_2) = \left(\exp\{ -i \left(\Omega + (2\pi)\,(SW/2) \right) t_1 \} + \exp\{ i \left(\Omega + (2\pi)\,(SW/2) \right) t_1 \} \right)$$

$$\propto \exp\{ -R\, t_1 \}\, A_2\{ +\Omega \}$$

$$= \cos\{ \left(\Omega + (2\pi)\,(SW/2) \right) t_1 \}\ \exp\{ -R\, t_1 \}\, A_2\{ +\Omega \} \, . \tag{2.28}$$

In an exactly analogous way to the Redfield method, the resultant frequency shift of SW/2 Hz, coupled with the doubling of the spectral width, means that sign discrimination in F_1 is achieved by the TPPI method.

2.4 Instrumentation

Spectra presented in this thesis were recorded on Bruker MSL 500 (St. Andrews), MSL 400 (Oxford), and AC 300 (Coventry) spectrometers, equipped with 11.8 T wide-bore, 9.4 T wide-bore, and 7.1 T standard-bore magnets, respectively. A table of nuclei studied, listing the Larmor frequencies on the different spectrometers, is given in Appendix C. The MSL 500 and MSL 400 spectrometers are both equipped with 1 kW radiofrequency amplifiers, designed for NMR of solid samples, while the AC 300 spectrometer is equipped with a 300 W radiofrequency amplifier, intended for NMR of liquid samples. The typical maximum radiofrequency field strengths obtained are given in Chapter 4.

Each spectrometer uses the same design of MAS apparatus [90], in which, to reduce frictional resistance, the cylindrical rotor is supported by double gas bearings. The rotor is caused to spin about its axis by drive gas which impinges perpendicularly onto flutes in the rotor cap. Probes supporting rotors of 4 mm and 7 mm diameter were used, with typical rotation speeds of approximately 8.5 kHz and 5 kHz, respectively. The rotors and caps are made from zirconium oxide and Kel-F (polymerised $FClC=CF_2$), respectively.

Except where otherwise stated, samples were obtained from commercial suppliers as indicated and used without further purification.

Fourier transformation and other processing were performed offline using software written by Paul Hodgkinson (a former D. Phil student in the Physical Chemistry Laboratory, Oxford). In contour plots, positive and negative contours are shown as solid and dashed lines, and, except where otherwise stated, contour levels correspond to 4, 8, 16, 32 and 64% of the maximum peak height.

Chapter 3

Second-Order Quadrupolar Broadening

3.1 The Perturbation of the Energy Levels

The quadrupolar coupling and its effect on the NMR transitions of a half-integer quadrupolar nucleus were introduced in the previous chapter. The opening two sections of this chapter derive the mathematical expressions for the perturbation of the energy levels by the quadrupolar coupling, which lie behind the general results presented in Section 2.1. These mathematical expressions are then used to explain the effect of sample rotation and other factors on the appearance of second-order quadrupolar-broadened spectra.

Starting from classical electrostatic arguments, the Hamiltonian for the interaction of the nuclear quadrupole moment Q with a second-rank Cartesian tensor, **V**, representing the electric field gradient at the nucleus can be shown [91] to be equal to

$$H_Q^{PAS} = \omega_Q^{PAS} \left[I_z^2 - \frac{1}{3} I(I+1) + \frac{\eta}{3} (I_x^2 - I_y^2) \right], \qquad (3.1)$$

where PAS refers to the principal axis system of the electric field gradient, and the Hamiltonian is in units of rad s^{-1}. The quadrupolar coupling is therefore parameterised by two constants, the quadrupolar frequency, ω_Q^{PAS}, and the

asymmetry parameter, η, where $0 \leq \eta \leq 1$. The quadrupolar frequency is, in turn, equal to

$$\omega_Q^{PAS} = \frac{3 \pi C_Q}{2I (2I - 1)} , \tag{3.2}$$

where C_Q, the quadrupolar coupling constant, is in units of hertz and is given by

$$C_Q = \frac{e^2 q Q}{h} . \tag{3.3}$$

The electric field gradient, eq, and the asymmetry parameter, η, are defined as:

$$eq = V_{zz} \tag{3.4a}$$

$$\eta = \frac{V_{xx} - V_{yy}}{V_{zz}} , \tag{3.4b}$$

where V_{xx}, V_{yy}, and V_{zz} are the principal components of the Cartesian tensor **V**.

The calculation of the perturbation of the energy levels will now be presented for the simplest, spin I = 3/2, case. The final results and an outline of the full derivation presented here have been published previously [32, 92]. The extension of the calculation to include a non-zero asymmetry parameter was carried out by Sharon Ashbrook [93].

The first stage of the calculation involves a rotation from the principal axis system of the electric field gradient to the laboratory frame defined by the Zeeman Hamiltonian. Such a transformation becomes much easier if Eq. (3.1) is re-expressed in terms of irreducible spherical tensor operators [94]. Using the matrix representations of I_x, I_y, and I_z given in Appendix B, the matrix form of the quadrupolar Hamiltonian is

$$H_Q^{PAS} = \omega_Q^{PAS} \begin{pmatrix} 1 & 0 & \frac{\eta}{3} & 0 \\ 0 & -1 & 0 & \frac{\eta}{3} \\ \frac{\eta}{3} & 0 & -1 & 0 \\ 0 & \frac{\eta}{3} & 0 & 1 \end{pmatrix} . \qquad (3.5)$$

It is then clear, from the matrix representations of the relevant tensor operators given in Appendix D, that Eq. (3.1) is equivalent to

$$H_Q^{PAS} = 2\,\omega_Q^{PAS} \left[T_{2,0} + \frac{\eta}{\sqrt{6}} (T_{2,2} + T_{2,-2}) \right] . \qquad (3.6)$$

Tensor operators are particularly suitable for calculations involving axes transformations since their behaviour under rotation is well understood. Formally, in the language of group theory, a tensor operator $T_{l,p}$ transforms according to row p of the irreducible representation $\mathbf{D}^l$ of the full rotation group. This leads to the result that, under a general rotation $R(\alpha, \beta, \gamma)$, where α, β, and γ are the Euler angles [95], the tensor operator $T_{l,p}$ transforms [94] according to:

$$R(\alpha, \beta, \gamma)\, T_{l,p}\, R(\alpha, \beta, \gamma)^{-1} = \sum_{p' = -l}^{l} D^l_{p',p}(\alpha, \beta, \gamma)\, T_{l,p'} , \qquad (3.7)$$

where the Wigner rotation matrix element, $D^l_{p',p}(\alpha, \beta, \gamma)$, is defined [95]:

$$D^l_{p',p}(\alpha, \beta, \gamma) = d^l_{p',p}(\beta) \exp\{ - i (\alpha p' + \gamma p) \} . \qquad (3.8)$$

The reduced rotation matrix elements, $d^l_{p',p}(\beta)$, relevant to this calculation are given in Appendix E.

If the transformation from the principal axis system to the laboratory frame is described by three Euler angles, specified here as ζ, θ, and ϕ, the laboratory-frame Hamiltonian is then, using Eqs. (3.6) and (3.7), given by

$$H_Q = 2\,\omega_Q^{PAS} \sum_{p'=-2}^{2} \left[D^2_{p',0}(\zeta, \theta, \phi) + \frac{\eta}{\sqrt{6}} \left\{ D^2_{p',2}(\zeta, \theta, \phi) + D^2_{p',-2}(\zeta, \theta, \phi) \right\} \right] T_{2,p'} \,. \quad (3.9)$$

Expressing the tensor operators in matrix form, Eq. (3.9) becomes

$$H_Q = \omega_Q^{PAS} \begin{pmatrix} A & -B^+ & C^+ & 0 \\ B^- & -A & 0 & C^+ \\ C^- & 0 & -A & B^+ \\ 0 & C^- & -B^- & A \end{pmatrix}, \quad (3.10)$$

where

$$A = D^2_{0,0}(\zeta, \theta, \phi) + \frac{\eta}{\sqrt{6}} \left\{ D^2_{0,2}(\zeta, \theta, \phi) + D^2_{0,-2}(\zeta, \theta, \phi) \right\} \quad (3.11a)$$

$$B^{\pm} = \sqrt{2} \left[D^2_{\pm1,0}(\zeta, \theta, \phi) + \frac{\eta}{\sqrt{6}} \left\{ D^2_{\pm1,2}(\zeta, \theta, \phi) + D^2_{\pm1,-2}(\zeta, \theta, \phi) \right\} \right] \quad (3.11b)$$

$$C^{\pm} = \sqrt{2} \left[D^2_{\pm2,0}(\zeta, \theta, \phi) + \frac{\eta}{\sqrt{6}} \left\{ D^2_{\pm2,2}(\zeta, \theta, \phi) + D^2_{\pm2,-2}(\zeta, \theta, \phi) \right\} \right] . \quad (3.11c)$$

At first sight, it appears that the quadrupolar Hamiltonian in Eq. (3.10) is not Hermitian. However, if the Wigner rotation matrix elements in Eq. (3.11) are expanded according to Eq. (3.8), it is found that $B^+ = -(B^-)^*$ and $C^+ = (C^-)^*$, where the asterix denotes the complex conjugate. Therefore, the Hermiticity of the quadrupolar Hamiltonian is retained, as required.

The total Hamiltonian of the system, neglecting the contributions of other spin interactions, such as the CSA and homonuclear and heteronuclear dipolar couplings, is a combination of the Zeeman and quadrupolar Hamiltonians:

$$H = H_Z + H_Q \,. \tag{3.12}$$

For nuclei for which the MQMAS experiment is applicable, the quadrupolar Hamiltonian is small compared to the Zeeman Hamiltonian and time-independent perturbation theory [96] can be used to calculate the quadrupolar contribution to the energy levels.

Consider the general case where the total Hamiltonian of the system, H, is a combination of two known time-independent Hamiltonians, H_0 and H_{pert}. If H_0 dominates H_{pert}, and the eigenstates, $|s\rangle$, and energies, $E^{(0)}{}_{|s>}$, of the Hamiltonian H_0 are known, *i.e.*,

$$H_0 \, |s\rangle = E^{(0)}{}_{|s>} \, |s\rangle \,, \tag{3.13}$$

time-independent perturbation theory can be used. The energy of an individual state, $E_{|s>}$, is then given (assuming that third- and higher-order approximations are negligible) as

$$E_{|s>} = E^{(0)}{}_{|s>} + E^{(1)}{}_{|s>} + E^{(2)}{}_{|s>} \,, \tag{3.14}$$

where

$$E^{(1)}{}_{|s>} = (H_{pert})_{ss} \tag{3.15a}$$

$$E^{(2)}{}_{|s>} = \sum_{r \neq s} \left\{ \frac{(H_{pert})_{sr} \, (H_{pert})_{rs}}{E^{(0)}{}_{|s>} - E^{(0)}{}_{|r>}} \right\} \,. \tag{3.15b}$$

The superscripts 1 and 2 refer to first- and second-order approximations, while $(H_{pert})_{rs}$ corresponds to the rs (row r, column s) element of the matrix representation of the Hamiltonian H_{pert}.

Using Eq. (3.15a), the quadrupolar contribution to the energy levels, to a first-order approximation, is given by

$$E^{(1)}_{|3/2>} = E^{(1)}_{|-3/2>} = \omega_Q \tag{3.16a}$$

$$E^{(1)}_{|1/2>} = E^{(1)}_{|-1/2>} = -\omega_Q \,, \tag{3.16b}$$

where the quadrupolar splitting parameter ω_Q is:

$$\omega_Q = \omega_Q^{PAS} \left[D^2_{0,0}(\zeta, \theta, \phi) + \frac{\eta}{\sqrt{6}} \{ D^2_{0,2}(\zeta, \theta, \phi) + D^2_{0,-2}(\zeta, \theta, \phi) \} \right]$$

$$= \frac{\omega_Q^{PAS}}{2} (3\cos^2\theta - 1 + \eta \sin^2\theta \cos 2\phi) \,. \tag{3.17}$$

The result derived here is therefore clearly in agreement with the energy-level diagram of Fig. 2.1b.

The quadrupolar coupling is frequently of such magnitude that a second-order approximation must be considered. To calculate this second-order contribution to the energy levels, it is clear from Eqs. (3.10) and (3.15b) that it is necessary to take the product of two Wigner rotation matrix elements. From angular momentum theory [95], such a product is given by

$$D^l_{p',p}(\alpha, \beta, \gamma)\, D^m_{q',q}(\alpha, \beta, \gamma) = \sum_n \langle lp, mq | nr \rangle \langle lp', mq' | nr' \rangle\, D^n_{r',r}(\alpha, \beta, \gamma) \,, \tag{3.18}$$

TABLE 3.1

Coefficients of the zero-, second-, and fourth-rank terms in Eq. (3.19)

I	s	A_s^I	B_s^I	C_s^I
3/2	1/2	–2/5	–8/7	54/35
3/2	3/2	6/5	0	–6/5
5/2	1/2	–16/15	–64/21	144/35
5/2	3/2	–4/5	–40/7	228/35
5/2	5/2	20/3	40/21	–60/7

where r = p + q, r' = p' + q', and n takes all values $|l - m|, |l - m + 1|, ..., |l + m|$. The first two terms in the summation are constants referred to as Clebsch-Gordan coefficients, the values of which are given in standard reference texts [97].

Using the expansion in Eq. (3.18), the following general expression for the second-order quadrupolar contribution to the energy levels can then be derived:

$$E^{(2)}_{|s>} = -E^{(2)}_{|-s>} = \frac{(\omega_Q^{PAS})^2}{2\omega_0} \{ A_s^I \Gamma^0(\eta) + B_s^I \Gamma^2(\zeta, \theta, \phi, \eta) + C_s^I \Gamma^4(\zeta, \theta, \phi, \eta) \} , \quad (3.19)$$

where s is positive. The expression in Eq. (3.19) is valid for any half-integer quadrupolar spin, and Table 3.1 gives the coefficients A_s^I, B_s^I, and C_s^I for spins I = 3/2 and 5/2.

The other functions in Eq. (3.19) are given by

$$\Gamma^0(\eta) = (1 + \frac{\eta^2}{3}) \quad (3.20a)$$

$$\Gamma^2(\zeta, \theta, \phi, \eta) = \left(1 - \frac{\eta^2}{3}\right) D^2_{0,0}(\zeta, \theta, \phi) - \frac{\sqrt{2}}{\sqrt{3}} \eta \{ D^2_{0,2}(\zeta, \theta, \phi) + D^2_{0,-2}(\zeta, \theta, \phi) \} \quad (3.20b)$$

$$\Gamma^4(\zeta, \theta, \phi, \eta) = \left(1 + \frac{\eta^2}{18}\right) D^4_{0,0}(\zeta, \theta, \phi) + \frac{\sqrt{10}}{6} \eta \{ D^4_{0,2}(\zeta, \theta, \phi) + D^2_{0,-2}(\zeta, \theta, \phi) \}$$

$$+ \frac{35}{18\sqrt{70}} \eta^2 \{ D^4_{0,4}(\zeta, \theta, \phi) + D^4_{0,-4}(\zeta, \theta, \phi) \} . \quad (3.20c)$$

It is interesting to note that the symmetry of the Wigner rotation matrix elements means that there are only even-rank Wigner rotation matrix elements in Eq. (3.20).

3.2 Sample Rotation

The previous section derived expressions for the quadrupolar contributions to the energy levels in terms of three Euler angles, specified as ζ, θ, and ϕ, defining the rotation from the principal axis system to the laboratory frame. When an experiment is performed under conditions of sample rotation, this transformation is best broken down into two parts: (i) the rotation of the principal axis system onto the sample frame, described by angles β and γ; (ii) the rotation of the sample frame onto the laboratory frame, described by angles χ and $(-\omega_r t + \xi)$, where χ is the angle between the spinning axis and the z axis of the laboratory frame, ω_r is the spinning frequency, and ξ is the initial phase of the crystallite relative to the rotor. The Wigner rotation matrix elements in Eq. (3.20) can then be expanded:

$$D^l_{0,p}(\zeta, \theta, \phi) = \sum_m D^l_{0,m}(0, \chi, -\omega_r t + \xi) D^l_{m,p}(0, \beta, \gamma) , \quad (3.21)$$

where m = $-l$, ($-l$ + 1), ..., l. The above equation means that the second-order quadrupolar contribution to a given energy level changes with time as a function of the spinning frequency.

If an average over an integer number of rotor periods is assumed, Eq. (3.21) becomes time-independent. Consider the following integral, where the upper limit corresponds to an integer number of rotor periods:

$$I = \int_0^{(2n\pi/\omega_r)} \exp\{ i\, m\, \omega_r\, t \}\, dt\,. \tag{3.22}$$

This integral is only non-zero when m equals zero, and, therefore, Eq. (3.21) becomes:

$$< D^{l}_{0,p}(\zeta, \theta, \phi) > \; = \; d^{l}_{0,0}(\chi)\, D^{l}_{0,p}(0, \beta, \gamma)\,. \tag{3.23}$$

On substituting Eq. (3.23) into Eq. (3.19), the second-order quadrupolar contribution to the energy levels over an integer number of rotor periods becomes

$$< E^{(2)}{}_{|s>} > \; = \; - < E^{(2)}{}_{|-s>} > \; = \; \frac{(\omega_Q^{PAS})^2}{2\,\omega_0} \{ A_s^I\; Q^0(\eta) + B_s^I\; d^2_{0,0}(\chi)\, Q^2(\beta, \gamma, \eta)$$

$$+ C_s^I\; d^4_{0,0}(\chi)\, Q^4(\beta, \gamma, \eta) \}\,, \tag{3.24}$$

where

$$Q^0(\eta) \; = \; \left(1 + \frac{\eta^2}{3} \right) \tag{3.25a}$$

$$Q^2(\beta, \gamma, \eta) \; = \; \left(1 - \frac{\eta^2}{3} \right) d^2_{0,0}(\beta) - \frac{\sqrt{8}}{\sqrt{3}}\, \eta\, d^2_{2,0}(\beta) \cos 2\gamma \tag{3.25b}$$

$$Q^4(\beta, \gamma, \eta) = \left(1 + \frac{\eta^2}{18} \right) d^4_{0,0}(\beta) + \frac{\sqrt{10}}{3} \eta \, d^4_{2,0}(\beta) \cos 2\gamma$$

$$+ \frac{35}{9\sqrt{70}} \eta^2 \, d^4_{4,0}(\beta) \cos 4\gamma \, . \qquad (3.25c)$$

Using Eq. (3.24), the second-order quadrupolar contribution to the central transition frequency of a half-integer quadrupolar nucleus, assuming an integer number of rotor periods, is then given by

$$\langle E^{(2)}|_{1/2} - E^{(2)}|_{-1/2} \rangle = \frac{(\omega_Q^{PAS})^2}{\omega_0} \{ A^I_{1/2} \, Q^0(\eta) + B^I_{1/2} \, d^2_{0,0}(\chi) \, Q^2(\beta, \gamma, \eta)$$

$$+ C^I_{1/2} \, d^4_{0,0}(\chi) \, Q^4(\beta, \gamma, \eta) \} \, . \qquad (3.26)$$

Thus, for a single crystallite spinning about an axis χ, there is an isotropic frequency shift of the central transition of $A^I_{1/2} \, Q^0(\eta) \, (\omega_Q^{PAS})^2/\omega_0$, as well as second- and fourth-rank anisotropic shifts with amplitudes that depend on the angles χ, β, and γ. In a powdered sample, a spherical average over all orientations of the angles β and γ gives rise to second- and fourth-rank inhomogeneous broadening.

The dependence of the reduced rotation matrix elements in Eq. (3.26) on the rotor angle is given by

$$d^2_{0,0}(\chi) = \frac{1}{2} (3 \cos^2\chi - 1) \qquad (3.27a)$$

$$d^4_{0,0}(\chi) = \frac{1}{8} (35 \cos^4\chi - 30 \cos^2\chi + 3) \, . \qquad (3.27b)$$

The solutions of the equation

$$d^l_{0,0}(\chi) = 0 \qquad (3.28)$$

are

$$\chi = 54.74° \qquad \text{when } l = 2 \tag{3.29a}$$

$$\chi = 30.56° \text{ or } 70.12° \quad \text{when } l = 4 . \tag{3.29b}$$

Therefore, since the two $d^{l}_{0,0}(\chi)$ terms do not have a common root, spinning around a unique angle χ cannot remove both second- and fourth-rank anisotropic broadenings. For example, spinning at the magic angle will completely remove second-rank broadening, since $d^{2}_{0,0}(54.7°) = 0$, but only partially average fourth-rank broadening.

3.3 Magic-Angle Spinning

The previous section showed that, over an integral number of rotor periods, second-rank quadrupolar broadening is removed by MAS. Experimentally, this assumption is equivalent to sampling the free induction decay at the start of every rotor period. However, the free induction decay is not normally acquired in a rotor-synchronised fashion. To understand the effect of MAS in this case it is necessary to examine the explicit time-dependence of the Wigner rotation matrix elements described by Eq. (3.21). Consider first a spin interaction which gives rise to solely second-rank inhomogeneous broadening, *e.g.*, the CSA. Using Eq. (3.21), the contribution to the central transition frequency (neglecting any isotropic shifts and assuming axial symmetry) is of the form

$$E_{|1/2\rangle} - E_{|-1/2\rangle} = K \sum_{m=-2}^{2} \{ D^{2}_{0,m}(0, \chi, -\omega_r t + \xi)\, d^{2}_{m,0}(\beta) \} , \tag{3.30}$$

where K is a constant describing the magnitude of the spin interaction. If the Wigner rotation matrix elements are expanded using Eq. (3.8), Eq. (3.30) becomes

$$E_{|1/2>} - E_{|-1/2>} = K \{ d^2_{0,0}(\chi)\, d^2_{0,0}(\beta)$$

$$- 2\, d^2_{0,1}(\chi)\, d^2_{0,1}(\beta) [\cos \omega_r t \cos \xi - \sin \omega_r t \sin \xi]$$

$$+ 2\, d^2_{0,2}(\chi)\, d^2_{0,2}(\beta) [\cos 2\omega_r t \cos 2\xi - \sin 2\omega_r t \sin 2\xi] \} . \quad (3.31)$$

The presence of trigonometric terms with an explicit time dependence in Eq. (3.31) means that the derivation and understanding of analytical solutions for the frequency-domain spectrum is rather complex, requiring the use of Bessel functions [98, 99]. An alternative approach, which is adopted in this section, is the computer simulation of spectra using a brute-force numerical method.

Figure 3.1a (overleaf) shows the static second-rank powder pattern. Figure 3.1b then considers the effect of MAS at a frequency which is relatively small compared to the width of the powder pattern. It can be seen that the static pattern breaks up into narrow lines, separated by the spinning frequency, with the envelope of the lines approximately corresponding to the static lineshape. For a powder pattern, all lines in the spinning sideband manifold have the same phase [100]. As the spinning frequency increases in Fig. 3.1c, the resemblance to the static pattern is lost, and eventually, when the spinning frequency is significantly greater than the width of the powder pattern, a solitary centreband at the isotropic frequency is observed, as shown in Fig. 3.1d. It should be noted that the spectra in Figs. 3.1b to 3.1d are normalised relative to each other, such that it is clear that the integrated signal intensity is independent of the spinning frequency.

Referring back to Eq. (3.31), the contribution of the different terms is now apparent. While the time-dependent terms give rise to spinning sidebands, the first, time-independent, term represents the narrowing of the inhomogeneously-broadened powder pattern achieved by spinning. In this case, since $d^2_{0,0}(54.7°) = 0$,

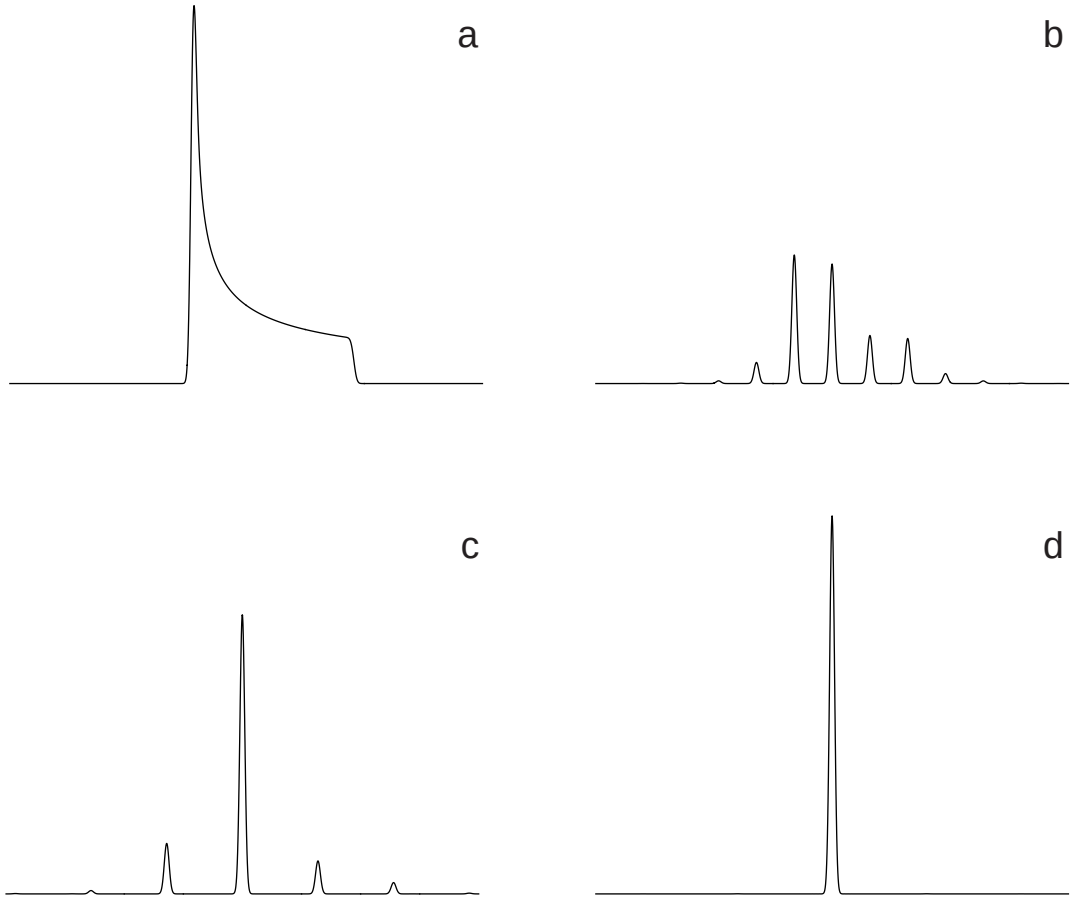

Figure 3.1. Simulated spectra showing the effect of MAS on an axially-symmetric second-rank powder pattern. In (a) the sample is static, while the MAS spinning frequency equals 1, 2 and 40 kHz in (b), (c) and (d), respectively. In all spectra, the spectral width equals 12.5 kHz. Time-domain data sets were simulated using an explicit density-matrix calculation (summing over 200 equally-spaced values of the angle θ in (a), and 90 equally-spaced values of the angles β and ξ in (b), (c) and (d)). A Gaussian line-broadening equivalent to a $\Delta\upsilon_{1/2}$ of 75 Hz was applied. Uniform excitation of single-quantum coherence over all values of the anisotropic frequency shift was assumed. In the MAS simulations, the rotor periods were broken into 50 equally-spaced intervals. The same vertical scale is used in (b), (c) and (d).

there is no inhomogeneous contribution to the linewidth of the centreband and sidebands.

An analogous expression to Eq. (3.31) can be calculated for the second-order quadrupolar broadening of the central transition, where there are both second- and fourth-rank contributions. In this case, since $d^4_{0,0}(54.7°) \neq 0$, the fourth-rank inhomogeneous contribution to the linewidth of the centreband and sidebands is only reduced, not removed, by MAS. This is illustrated in Fig 3.2. Figure 3.2a shows

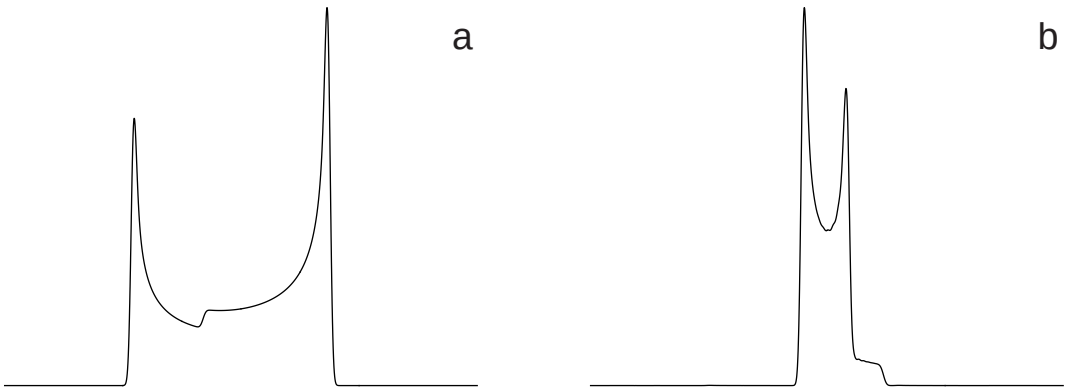

Figure 3.2. Simulated spectra showing the effect of MAS on a spin I = 3/2 second-order quadrupolar-broadened central transition powder pattern. In (a) the sample is static, while the MAS spinning frequency equals 40 kHz in (b). The parameters describing the second-order quadrupolar broadening were: C_Q = 2 MHz, $\eta = 0$, $\omega_0/2\pi$ = 100 MHz. Otherwise, the same simulation parameters as described in Fig. 3.1 were used.

a static second-order quadrupolar-broadened powder pattern. It can be seen, in Fig. 3.2b, where the spinning frequency is significantly greater than the width of the inhomogeneously-broadened powder pattern, that a residual fourth-rank second-order quadrupolar broadening remains. Comparing Figs 3.2a and 3.2b, it is apparent that MAS has narrowed the static powder pattern to approximately a third of its initial width.

Figure 3.3 (overleaf) presents experimental ^{87}Rb NMR spectra obtained using a sample of rubidium nitrate, $RbNO_3$, which is known to have a unit cell containing three crystallographically distinct Rb sites. In the static spectrum of Fig. 3.3a, the expected sharp features due to the second-order quadrupolar broadening are lost under additional broadening due to the CSA and dipolar interactions. These latter two broadenings are removed along with the second-rank second-order quadrupolar broadening by MAS. However, the residual fourth-rank second-order quadrupolar broadening means that the three sites are not resolved, as shown in Fig. 3.3b. For comparison, Fig. 3.3c presents the

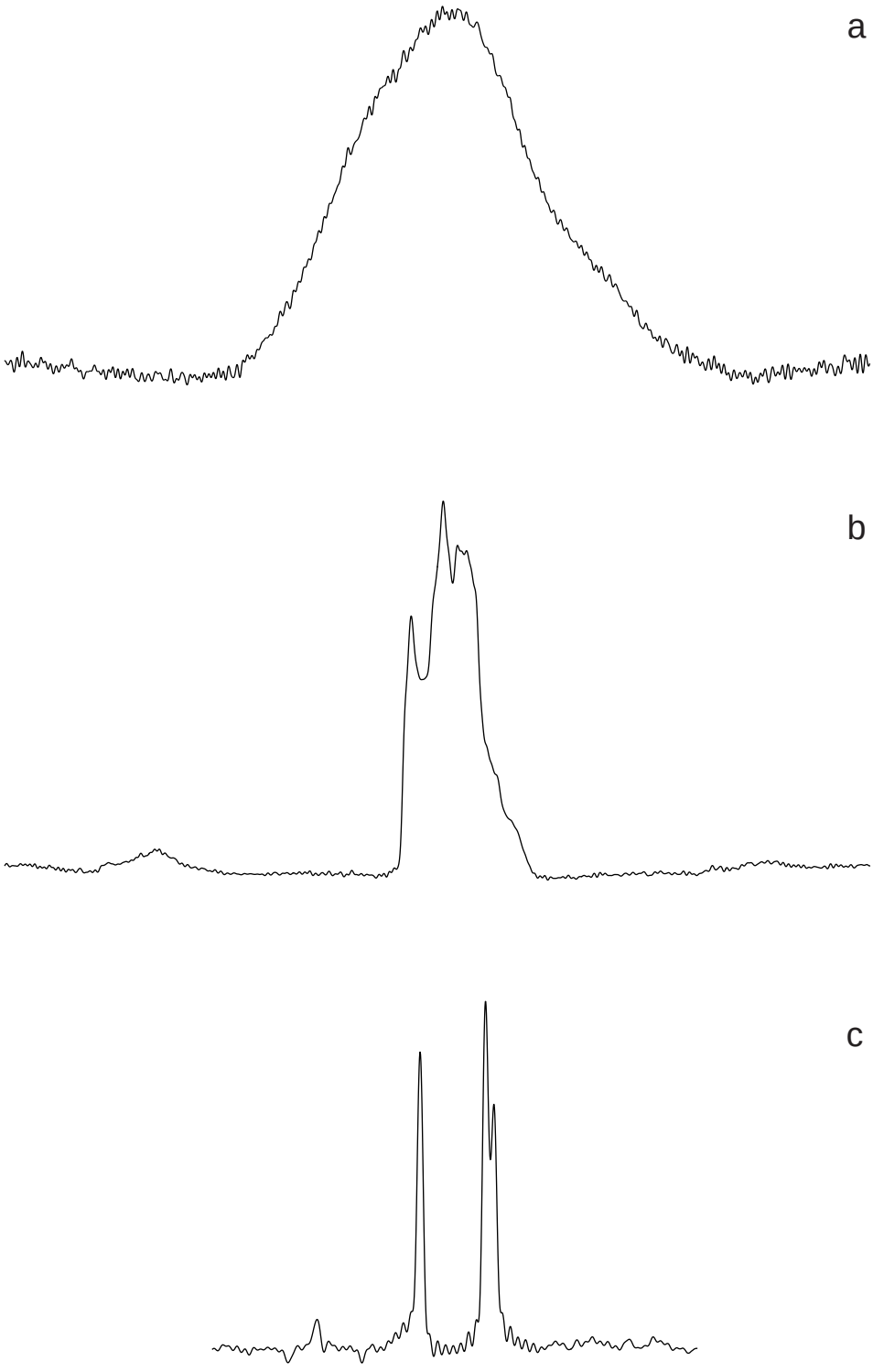

Figure 3.3. Experimental ^{87}Rb (130.9 MHz) (a) static and (b) MAS spectra of $RbNO_3$ (Aldrich). The displayed spectral width (cut down from 20 kHz) equals 15 kHz. The following experimental conditions were used: 4 transients (consisting of 512 points) were averaged, the relaxation interval was 100 ms, and a radiofrequency pulse of duration 1.3 μs was used. The spinning speed was 5.3 kHz in (b). (c) Isotropic MQMAS spectrum. Experimental parameters are given in Fig. 6.9c. The displayed spectral width equals 8.4 kHz. Peaks either side of the central spectral features in (b) and (c) are spinning sidebands.

isotropic MQMAS spectrum, where all inhomogeneous broadening is removed, such that the three separate sites are now revealed.

Returning to Eq. (3.31), it is interesting to note that the time-independent term is equal to the second-rank term in Eq. (3.26), which was calculated assuming an integer number of rotor periods. Since it is the time-dependent terms in Eq. (3.31) which correspond to spinning sidebands, it is then clear that Eq. (3.26) corresponds to a spectrum containing solely the centreband. Therefore, if a knowledge of the spinning sideband manifold is unnecessary, Eq. (3.26) is a perfectly acceptable approximation. This approximation is used in the simulation of spectra in the following section, and in Chapters 5 and 6 to explain how the MQMAS experiment works.

3.4 The Appearance of Second-Order Quadrupolar-Broadened MAS Spectra

The inability of MAS to remove the fourth-rank second-order quadrupolar broadening, such that crystallographically distinct sites are often unresolved, has been clearly demonstrated in Figs. 1.1a and 3.3b. Although, initially, it may be thought that it is simply desirable to totally remove the inhomogeneous broadening, there is potentially valuable information in the quadrupolar parameters, C_Q and η, which describe this broadening. Therefore, the spectroscopist ideally wants a technique which, as well as resolving the individual sites, allows their individual quadrupolar parameters to be determined. As is demonstrated in later chapters, this is exactly what the MQMAS experiment achieves. The two-dimensional nature of the experiment means that, as well as obtaining high-resolution isotropic spectra of the type shown in Figs. 1.1b and 3.3c, rows corresponding to the individual MAS spectra can be extracted. These MAS spectra can then be fitted to obtain the quadrupolar parameters. The purpose of this section is to illustrate the effect of the

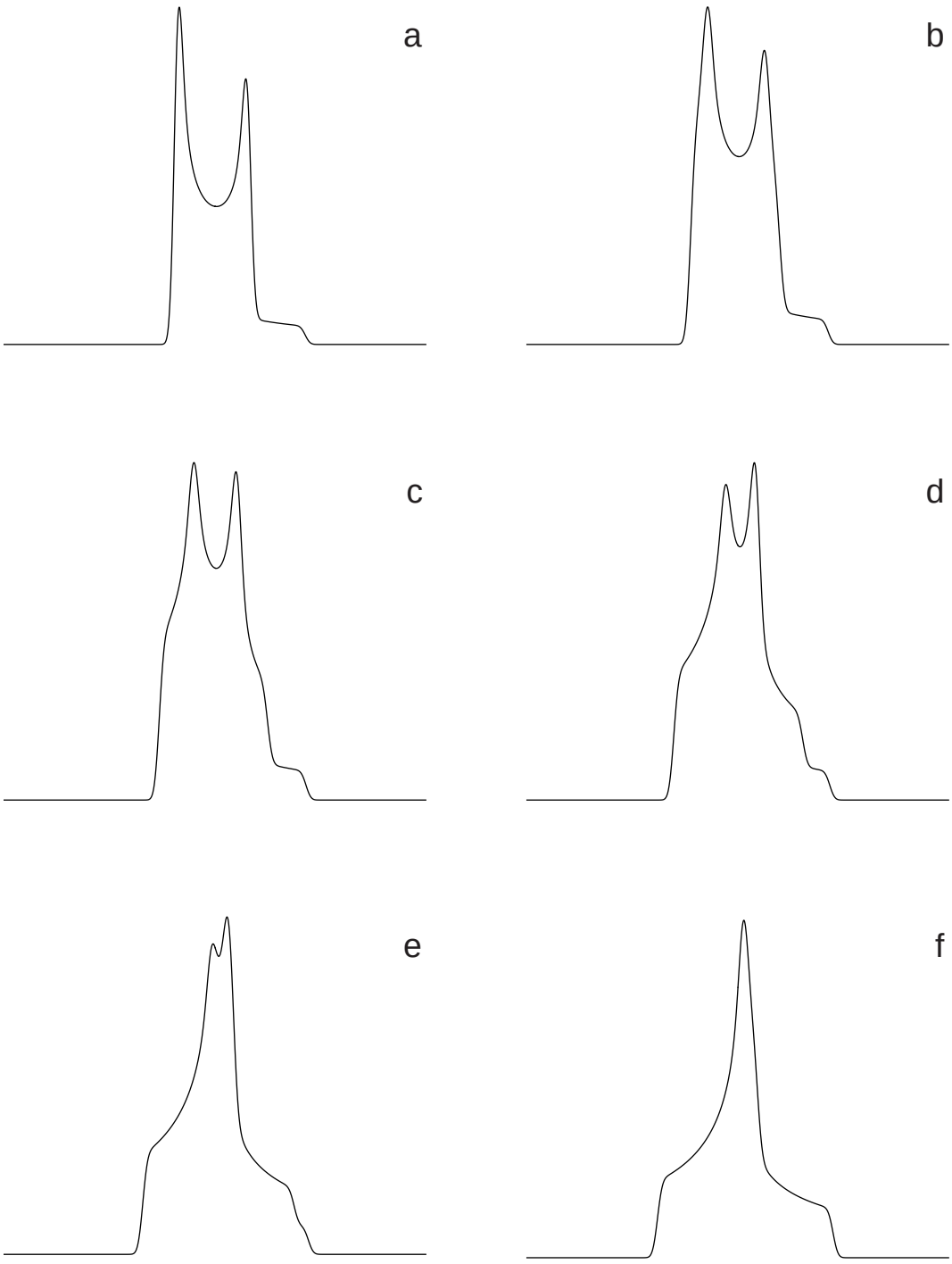

Figure 3.4. Simulated spin I = 3/2 second-order quadrupolar-broadened central transition MAS spectra, where the asymmetry parameter, η, equals 0.0 in (a), 0.2 in (b), 0.4 in (c), 0.6 in (d), 0.8 in (e) and 1.0 in (f). Spectra were simulated in the frequency-domain (summing over 200 equally-spaced values of the two angles β and γ, with a Gaussian linewidth of $\Delta\upsilon_{1/2}$ = 75 Hz) using a modified version of a program written by Sharon Ashbrook [93]. The following parameters were used: C_Q = 2 MHz, $\omega_0/2\pi$ = 100 MHz, and the spectral width equals 7 kHz. The centre of each spectrum corresponds to the isotropic frequency shift.

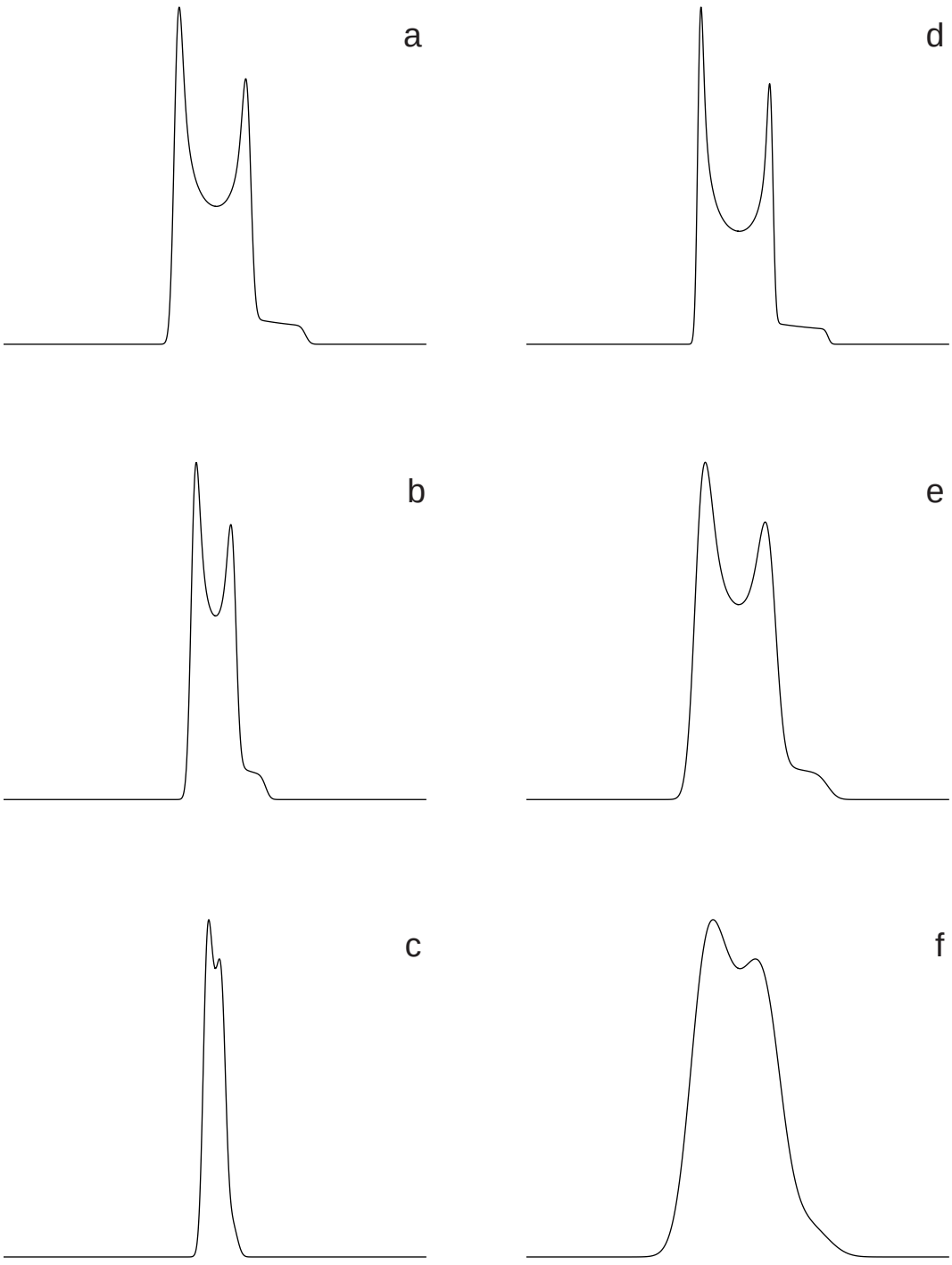

Figure 3.5. Simulated spin I = 3/2 second-order quadrupolar-broadened central transition MAS spectra. For (a) to (c), the quadrupolar coupling constant equals 2.0 MHz in (a), 1.5 MHz in (b), and 1.0 MHz in (c), and a Gaussian linewidth of $\Delta\upsilon_{1/2}$ = 75 Hz was used. For (d) to (f), the $\Delta\upsilon_{1/2}$ of the individual Gaussian lineshapes equals 50 Hz in (d), 150 Hz in (e), and 300 Hz in (f), and the quadrupolar coupling constant equals 2.0 MHz. In each case, the asymmetry parameter was set equal to zero. Otherwise, the same simulation parameters as described in Fig. 3.4 were used.

quadrupolar parameters and other factors on the appearance of these second-order quadrupolar-broadened MAS spectra.

Figure 3.4 (on page 44) demonstrates how the appearance of the spin I = 3/2 spectrum is progressively altered as the asymmetry parameter changes from 0 to 1, while Fig. 3.5 (previous page) shows the effect of changing the size of the quadrupolar coupling constant, C_Q, and the homogeneous linewidth. It is interesting to note from Fig. 3.5 that the characteristic features of the second-order quadrupolar-broadened lineshape can be obscured by either a reduction in C_Q (Fig. 3.5c) or an increase in the homogeneous linewidth (Fig. 3.5f). A closer examination of Figs. 3.5a and 3.5c further reveals that, as expected from the $(\omega_Q^{PAS})^2$ dependence in Eq. (3.26), doubling C_Q causes a four-fold increase in the width of the second-order quadrupolar-broadened spectrum. Additionally, Eq. (3.26) further shows that the degree of second-order quadrupolar broadening is inversely proportional to the Larmor frequency, ω_0. This is clearly demonstrated in Fig. 3.6 (overleaf), which presents ^{87}Rb MAS spectra of $RbNO_3$ obtained at 98.2, 130.9, and 163.8 MHz. In addition to the reduction in the total linewidth, it is apparent that the nature of the observed lineshape changes with increasing frequency. This latter change is explained in Section 7.5.

From Eq. (3.2), it can be seen that the quadrupolar frequency, ω_Q^{PAS}, depends on the spin quantum number, I. This has the consequence that for a given C_Q, the quadrupolar frequency for a spin I = 5/2 nucleus is 3/10 the size of that for a spin I = 3/2 nucleus. This is demonstrated in Fig. 3.7 (on page 48), which show ^{23}Na and ^{27}Al MAS spectra of sodium sulphate, Na_2SO_4, and the mineral albite (Oxford University Museum, OUM 9408), $NaSi_3AlO_8$, respectively. It is known that both samples only contain one crystallographic site for the observed nucleus. The quadrupolar parameters, as determined by a fitting performed by Sharon Ashbrook [93], are $C_Q = 2.42 \pm 0.05$ MHz and $\eta = 0.65 \pm 0.05$, and $C_Q = 3.21 \pm 0.05$ MHz and $\eta = 0.65 \pm 0.1$ for Na_2SO_4 and albite, respectively. Even though the

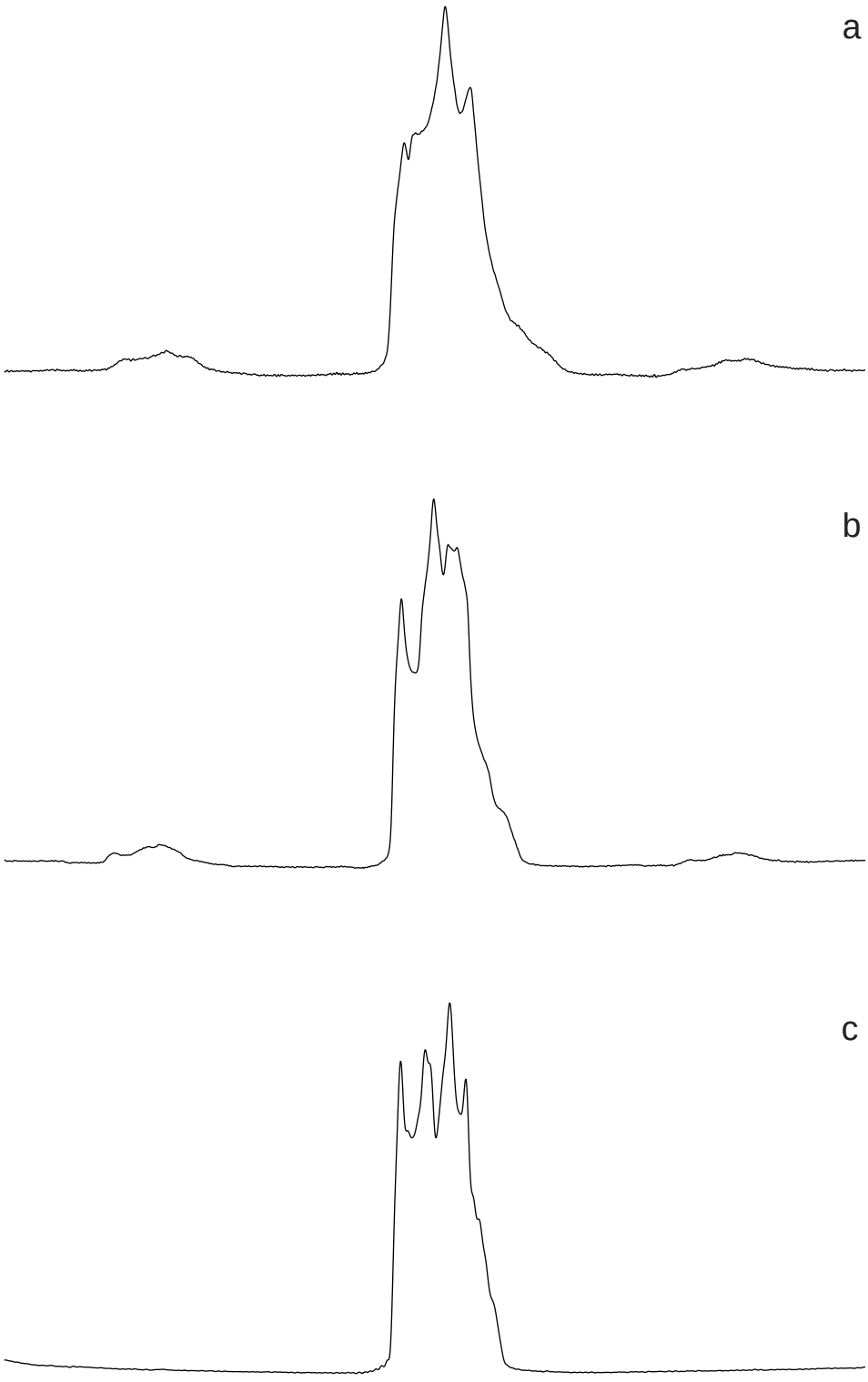

Figure 3.6. Experimental ^{87}Rb MAS NMR spectra of $RbNO_3$, recorded at Larmor frequencies of (a) 98.2 MHz, (b) 130.9 MHz, and (c) 163.6 MHz. In all spectra, the displayed spectral width (cut down from 25 kHz) equals 15 kHz. The following experimental conditions were used: 128 transients (consisting of 1024 points) were averaged and the relaxation interval was 100 ms. In (a), (b), and (c) respectively, a radiofrequency pulse of duration 2 μs, 1 μs, and 1.3 μs was used, and the spinning speed was 5.0 kHz, 5.0 kHz, and 8.5 kHz. Peaks either side of the central spectral features are spinning sidebands.

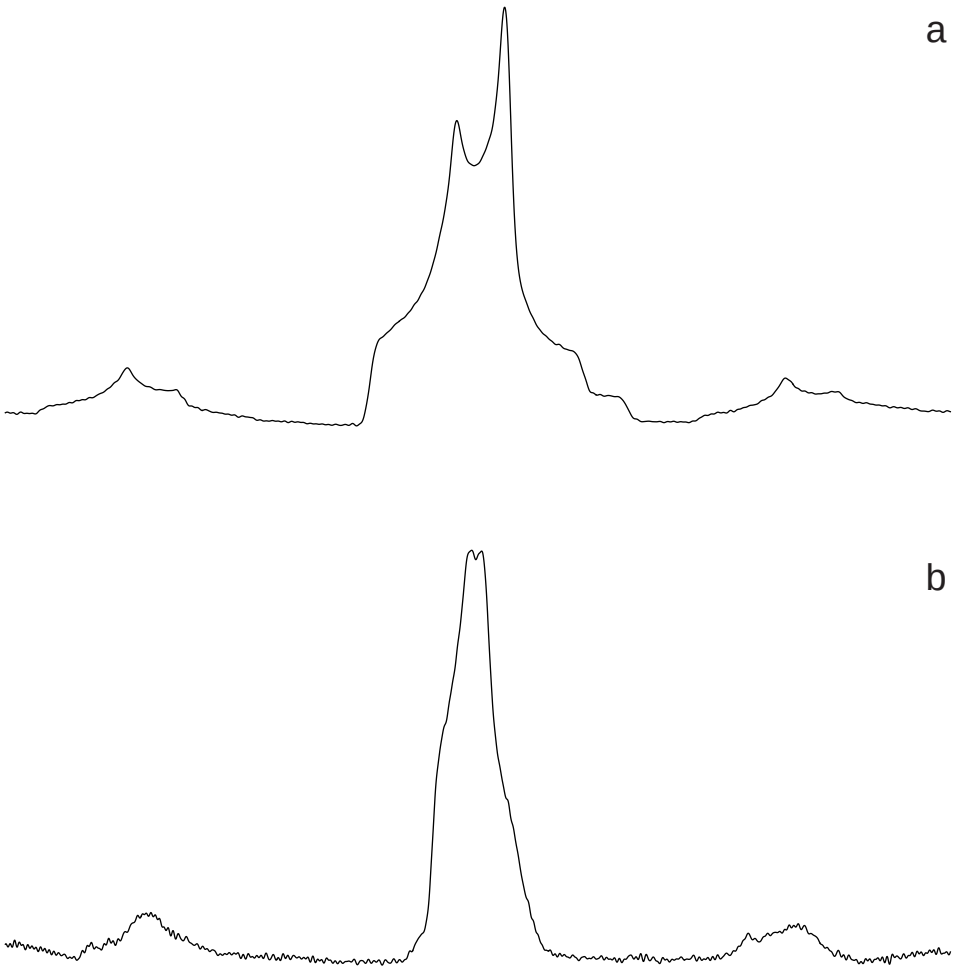

Figure 3.7. (a) Experimental ^{23}Na (105.8 MHz) MAS spectrum of Na_2SO_4. The following experimental conditions were used: 16 transients (consisting of 512 points) were averaged, the relaxation interval was 1 s, a radiofrequency pulse of duration 1.0 μs was used, and the spinning speed was 5.2 kHz. (b) Experimental ^{27}Al (104.3 MHz) MAS spectrum of a sample of albite. The following experimental conditions were used: 64 transients (consisting of 512 points) were averaged, the relaxation interval was 1 s, a radiofrequency pulse of duration 1.2 μs was used, and the spinning speed was 5.2 kHz. In both cases, the displayed spectral width (cut down from 25 and 17.2 kHz in (a) and (b), respectively) equals 15 kHz. Peaks either side of the central spectral features are spinning sidebands.

quadrupolar coupling constant is larger for the spin I = 5/2 nucleus, ^{27}Al, it is evident that there is significantly more second-order quadrupolar broadening for the spin I = 3/2 nucleus, ^{23}Na.

In a similar way to the use of chemical shifts, the quadrupolar parameters, C_Q and η, have the potential to offer much chemically relevant information. For

example, it has been shown that C_Q values for ^{17}O increase as the ionic character of the neighbouring bonds decrease. In this way, it is possible to distinguish Al-O-Al, Si-O-Al, and Si-O-Si bonds in aluminosilicate glasses [73]. Moreover, Farnan *et al.* have stated that an observed ^{17}O asymmetry parameter can be interpreted in terms of the M-O-M bond angle [37]. To date, however, there have been few published examples of correlations between the quadrupolar parameters and chemical structure. It is hoped that, as the library of these parameters builds up as a consequence of the MQMAS experiment, the understanding of their correlation to chemical structure will improve.

3.5 The Quest for High Resolution

To obtain an informative high-resolution spectrum, it is necessary to remove the anisotropic shifts, while retaining the isotropic shifts. From Eq. (3.29), it is clear that sample rotation around a single axis cannot achieve this for second-order quadrupolar broadening. In 1988, two ingenious approaches to this problem were proposed, namely dynamic angle spinning (DAS) and double rotation (DOR) [31-39]. Both these methods involve sample rotation around two axes, either sequentially with DAS or simultaneously with DOR. This section first describes these two experiments, noting their significant drawbacks, and then introduces the MQMAS experiment.

3.5.1 Dynamic Angle Spinning

The pulse sequence and coherence transfer pathway diagram for the simplest DAS experiment [35] is shown in Fig. 3.8a (overleaf). It can be seen that DAS involves a switch of the rotor angle between the two evolution periods, t_1 and t_2, during which the magnetisation is stored as a population distribution. Considering the coherence pathway represented by the solid line, the separate

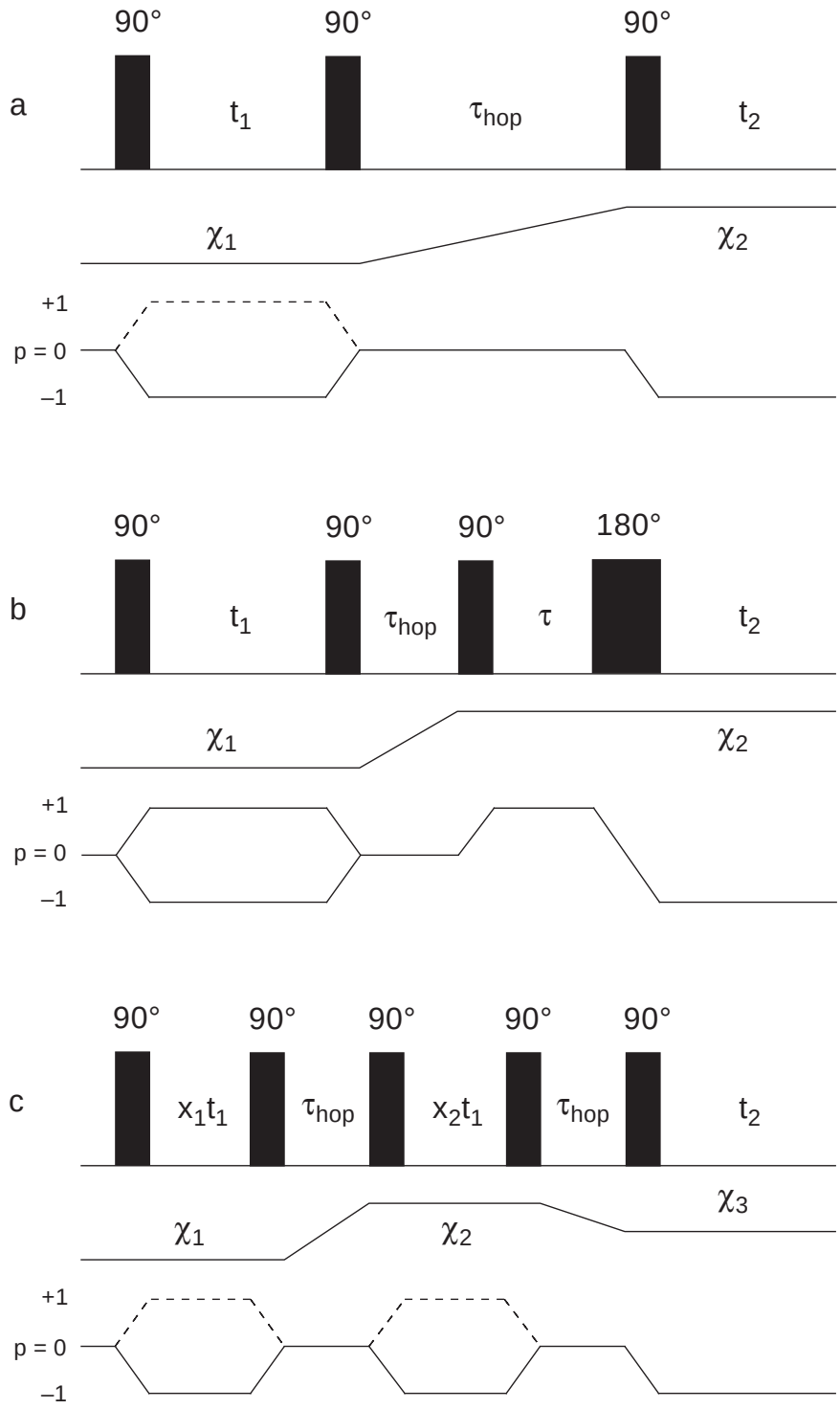

Figure 3.8. Pulse sequences and coherence transfer pathway diagrams for three DAS experiments. The rotor angles χ_1 and χ_2 form a DAS pair as discussed in the text, while χ_3 in (c) equals 54.7°. All flip angles refer to the nutation of the central transition. In (a) and (c), the selection of both the solid and dotted pathways gives rise to an amplitude-modulated signal with respect to t_1. In (b), whole echoes are acquired in t_2 as a consequence of the added spin-echo sequence. The experiments in (a), (b), and (c) are analogous to the *z*-filtered amplitude-modulated MQMAS experiment of Fig. 5.11, the amplitude-modulated whole-echo MQMAS experiment of Fig. 5.1b, and the *z*-filtered amplitude-modulated split-t_1 MQMAS experiment of Fig. 6.3a, respectively.

second- and fourth-rank contributions to the resulting signal, using Eq. (3.26), are given by

$$s_{l=2}(t_1, t_2) = \exp\left[\frac{(\omega_Q^{PAS})^2}{\omega_0} \{ B^I_{1/2} \; d^2_{0,0}(\chi_1) \, Q^2(\beta, \gamma, \eta) \} t_1 \right]$$

$$\propto \exp\left[\frac{(\omega_Q^{PAS})^2}{\omega_0} \{ B^I_{1/2} \; d^2_{0,0}(\chi_2) \, Q^2(\beta, \gamma, \eta) \} t_2 \right] \quad (3.32a)$$

$$s_{l=4}(t_1, t_2) = \exp\left[\frac{(\omega_Q^{PAS})^2}{\omega_0} \{ C^I_{1/2} \; d^4_{0,0}(\chi_1) \, Q^4(\beta, \gamma, \eta) \} t_1 \right]$$

$$\propto \exp\left[\frac{(\omega_Q^{PAS})^2}{\omega_0} \{ C^I_{1/2} \; d^4_{0,0}(\chi_2) \, Q^4(\beta, \gamma, \eta) \} t_2 \right] . \quad (3.32b)$$

The two rotor angles are chosen such that at a time $(x_2/x_1)\, t_1$ during t_2, both second- and fourth-rank inhomogeneous broadening is refocused. From Eq. (3.32), suitable pairs of angles satisfy the following conditions:

$$x_1 \, d^2_{0,0}(\chi_1) + x_2 \, d^2_{0,0}(\chi_2) = 0 \quad (3.33a)$$

$$x_1 \, d^4_{0,0}(\chi_1) + x_2 \, d^4_{0,0}(\chi_2) = 0 \quad (3.33b)$$

$$x_1 + x_2 = 1 . \quad (3.33c)$$

Although there is a continuous set of solutions to Eqs. (3.33a) to (3.33c), the most commonly-used angle pairs are (37.38°, 79.19°) and (0°, 63.43°), where x_1 and x_2 are (1/2, 1/2) and (1/6, 5/6), respectively. The latter case has two advantages [39]: first, cross polarisation is most efficient when the rotor angle equals 0°; and second, this pair of angles corresponds to the most effective narrowing of any homonuclear dipolar broadening. It should be noted that the CSA, which gives rise to a second-rank anisotropic contribution analogous to that in Eq. (3.32a), is also refocused in the DAS experiment.

The refocusing of the inhomogeneous broadening at a time $(x_2/x_1)\ t_1$ during t_2 gives rise to the appearance of inhomogeneously-broadened ridges, with gradient (x_2/x_1), in the frequency-domain two-dimensional spectrum. The isotropic DAS spectrum then corresponds to a projection onto an axis perpendicular to the ridges. Such a projection is, however, normally obtained by performing a shearing projection such that the ridges are parallel to the F_2 axis. Two approaches have been proposed to ensure that pure absorption-mode lineshapes are obtained: firstly, the two pathways are combined with equal amplitude using a *z* filter [36], as in Fig. 3.8a; alternatively, a spin echo is appended such that a whole echo is acquired in t_2 [38], as in Fig. 3.8b. In the experiment of Fig. 3.8c, a second rotor hop to the magic angle is incorporated to ensure that the CSA and dipolar broadenings are removed from the anisotropic lineshapes [36]. In this case, the inhomogeneous broadening is refocused at $t_2 = 0$ such that the ridges appear parallel to the F_2 axis without the need for a shearing transformation. All these experimental features have MQMAS analogues which are discussed at length in Chapters 5 and 6.

There are three significant drawbacks to the DAS experiment. Firstly, the technique cannot be applied to samples where the longitudinal relaxation time, T_1, is less than the time required for the switch in rotor angle (typically 50 ms). Secondly, homonuclear dipolar broadenings are not removed from isotropic DAS spectra. As a consequence, residual linewidths of the order of 1 kHz are often observed in, for example, ^{11}B and ^{27}Al DAS spectra [64]. In comparison, such small homogeneous broadenings are easily removed by MAS. The final disadvantage relates to the considerable cost and mechanical unreliability of DAS hardware.

3.5.2 Double Rotation

In the DOR experiment, the sample spins inside an inner rotor which is itself embedded inside a second outer rotor. It can be shown that both second- and fourth-rank quadrupolar broadening is removed if the inner rotor axis is inclined at an angle of 30.56° to the outer rotor axis, which is itself inclined at an angle of 54.74° to the B_0 field [34]. These angles are, respectively, the roots of the fourth- and second-rank reduced rotation matrix elements given in Eq. (3.29). Although rotor-synchronisation methods [34] have been devised which partially alleviate the problem, a significant complication is the large number of spinning sidebands which result from the necessarily slow spinning frequency of the outer rotor (typically 1 kHz). Additionally, the experiment is intrinsically one-dimensional and, to obtain the quadrupolar parameters, it is necessary to perform an often complicated fitting of the spinning sideband manifold. Finally, like DAS, the DOR hardware is very expensive and prone to mechanical breakdown.

3.5.3 Multiple-Quantum Magic-Angle Spinning

In 1995, Frydman and Harwood demonstrated that sample rotation about two different angles is not necessary to remove the second-order quadrupolar broadening. In particular, they recognised that the coefficients of the isotropic and anisotropic shifts differ between single- and multiple-quantum transitions, as shown in Table 3.1. The fourth-rank anisotropic broadening can hence be refocused, whilst still retaining the isotropic information, by performing a two-dimensional experiment in which (odd-order) multiple- and single-quantum coherences are correlated, while spinning at the magic angle to remove second-rank anisotropic broadening. Spinning at the magic angle has the advantages that (i) conventional MAS hardware can be used and (ii) MAS will also average any additional first-order broadening due to dipolar couplings or the CSA.

Chapter 4

Coherence Transfer

4.1 "Hard" and "Soft" Pulses

In Fourier transform NMR, an important parameter is the inherent nutation frequency of a radiofrequency pulse, $\omega_1 = -\gamma B_1$, where γ is the gyromagnetic ratio, and B_1 is the radiofrequency field strength. When recording an NMR spectrum, it is normally desirable that ω_1 exceeds the range of resonance frequencies to be studied; a radiofrequency pulse is then said to be "hard". This, however, is not normally possible for half-integer quadrupolar nuclei in the solid state. In a powdered sample, the quadrupolar splitting parameter, ω_Q, ranges from zero to ω_Q^{PAS}. There is then a distribution of crystallites with values of the ratio ω_Q/ω_1 from zero upwards. (Strictly speaking, the ratio referred to is $|\omega_Q/\omega_1|$ since both ω_Q and ω_1 can be either positive or negative. However, to avoid unnecessarily complicated notation, the magnitude signs are not included here or elsewhere in the thesis.) Therefore, while for some crystallites $\omega_Q < \omega_1$ and the pulse is hard, there are many crystallites for which, even using the highest radiofrequency power amplification currently available, the ratio ω_Q/ω_1 is significantly greater than unity. In the latter case, the radiofrequency pulse is considered to be "soft", and only the central transition is excited. This first section investigates the effect of such a distribution for a simple single-pulse experiment, before the latter sections move on to consider the individual coherence transfer processes relevant to the MQMAS experiment.

The different nutation properties of hard and soft pulses can be understood by considering a pulse applied along the rotating frame *x* axis to a system at thermal equilibrium. Section 2.2 stated that the evolution of the density operator is described by the Liouville-von Neumann equation, Eq. (2.6). For a hard pulse, the Hamiltonian equals $\omega_1 I_x$, and, therefore,

$$\frac{d\sigma(t)}{dt} = -i [\omega_1 I_x, I_z]$$

$$= -\omega_1 I_y . \qquad (4.1)$$

Equation (4.1) describes the nutation of the magnetisation towards the $-y$ axis at a rate ω_1 .

For a soft pulse, only the central transition is excited, and the system is effectively simplified to one involving only two levels. The understanding of such a system is simplified by the introduction of the "fictitious spin I = 1/2 operators" [101-103]. Using spin I = 3/2 as an example, the matrix representations of $I_x^{(1/2,-1/2)}$ and $I_y^{(1/2,-1/2)}$ are:

$$I_x^{(1/2,-1/2)} = \frac{1}{2} \begin{pmatrix} 0 & 0 & 0 & 0 \\ 0 & 0 & 1 & 0 \\ 0 & 1 & 0 & 0 \\ 0 & 0 & 0 & 0 \end{pmatrix} \qquad (4.2a)$$

$$I_y^{(1/2,-1/2)} = \frac{i}{2} \begin{pmatrix} 0 & 0 & 0 & 0 \\ 0 & 0 & -1 & 0 \\ 0 & 1 & 0 & 0 \\ 0 & 0 & 0 & 0 \end{pmatrix} . \qquad (4.2b)$$

Closer examination reveals that the central 2×2 fragments of the matrices correspond to the spin I = 1/2 matrix representations of I_x and I_y (given in Appendix

B). Using these operators, the evolution of the density operator, for general half-integer quadrupolar spin I, is then described by

$$\frac{d\sigma(t)}{dt} = -i\left[\left(I+\frac{1}{2}\right)\omega_1 I_x^{(1/2,-1/2)}, I_z\right]$$

$$= -\left(I+\frac{1}{2}\right)\omega_1 I_y^{(1/2,-1/2)} . \qquad (4.3)$$

Comparing Eqs. (4.1) and (4.3), it is apparent that the nutation frequency, when the pulse is selective for the central transition, is (I + 1/2) times faster than in the hard pulse case.

This difference in nutation frequency is demonstrated in Fig. 4.1 (overleaf), which plots, for a spin I = 3/2 nucleus, the dependence of the central transition amplitude on the flip angle for different values of ω_Q/ω_1. The two limiting cases, namely ω_Q/ω_1 equals zero and infinity are plotted as solid and dotted lines, respectively. The factor of two difference in nutation frequency then means that the same pulse duration corresponds to the maximum signal (a flip angle of 90°) and a null (a flip angle of 180°) for a hard and soft pulse, respectively. To avoid confusion, this thesis adopts the convention, as demonstrated in the labelling of the *x* axis in Fig. 4.1, that quoted flip angles refer to the hard pulse case, unless explicitly stated otherwise. (The flip angle of a pulse equals $\omega_1 \tau_p$ rad or $(180\ \omega_1 \tau_p)/\pi$ degrees, where τ_p is the duration of the pulse.) In addition to the increase in nutation frequency, it is evident that, if only the central transition is excited, the maximum signal amplitude is also reduced by (I + 1/2) relative to the hard pulse amplitude.

In a powdered sample, there is a range of ω_Q/ω_1 values, and, therefore, there is a gradation in nutation frequency between the hard and soft limits. For example, the dashed line in Fig. 4.1 represents an intermediate case where ω_Q/ω_1 equals 0.5. A distribution of nutation frequency across a powder pattern would be expected to lead to significant distortions in the observed spectrum. To investigate this, consider

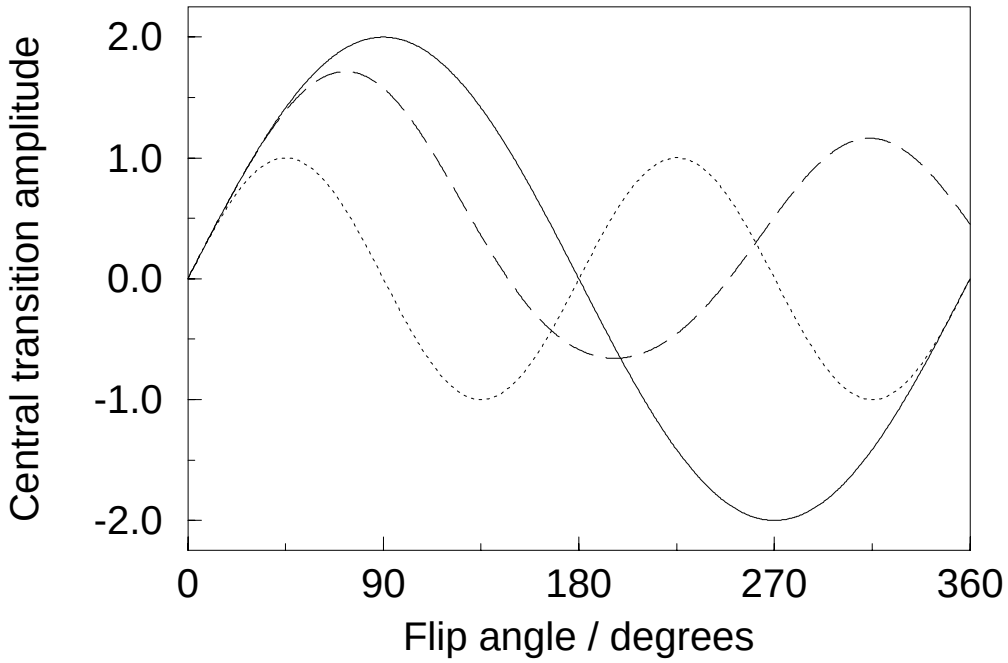

Figure 4.1. The dependence of the spin I = 3/2 central transition amplitude on the flip angle of an on-resonance excitation pulse, for ω_Q/ω_1 equal to zero (solid line), 0.5 (dashed line), and (effectively) infinity (dotted line). The data sets were simulated using an explicit density matrix calculation, in which the sample was assumed to be static and only first-order quadrupolar contributions (assuming axial symmetry) to the energy levels were considered. The vertical scale is normalised relative to the maximum single-quantum coherence generated by a pulse which is selective for the central transition. The labelling of the *x* axis corresponds to the hard pulse case, *i.e.*, where ω_Q/ω_1 equals zero, such that the flip angle of a pulse equals $(180\ \omega_1\ \tau_p)/\pi$ degrees, where τ_p is the duration of the pulse.

Fig. 4.2 (overleaf), which presents simulated static and MAS spin I = 3/2 second-order quadrupolar-broadened central-transition spectra for a range of flip angles. For a 45° pulse (i) there are no observable distortions in both the static and MAS lineshapes. However, in the static case, it is very clear that a clean null is not obtained for a 90° pulse and there is significant lineshape distortion for a 135° pulse (iv). In contrast, in the MAS case, there is a fairly clean null and only small distortions in the spectra corresponding to larger flip angles. Referring back to Eq. (3.21), this difference can be related to the additional averaging over the initial phase of a crystallite relative to the rotor in the MAS case. (This is discussed further in Section 4.2.2.)

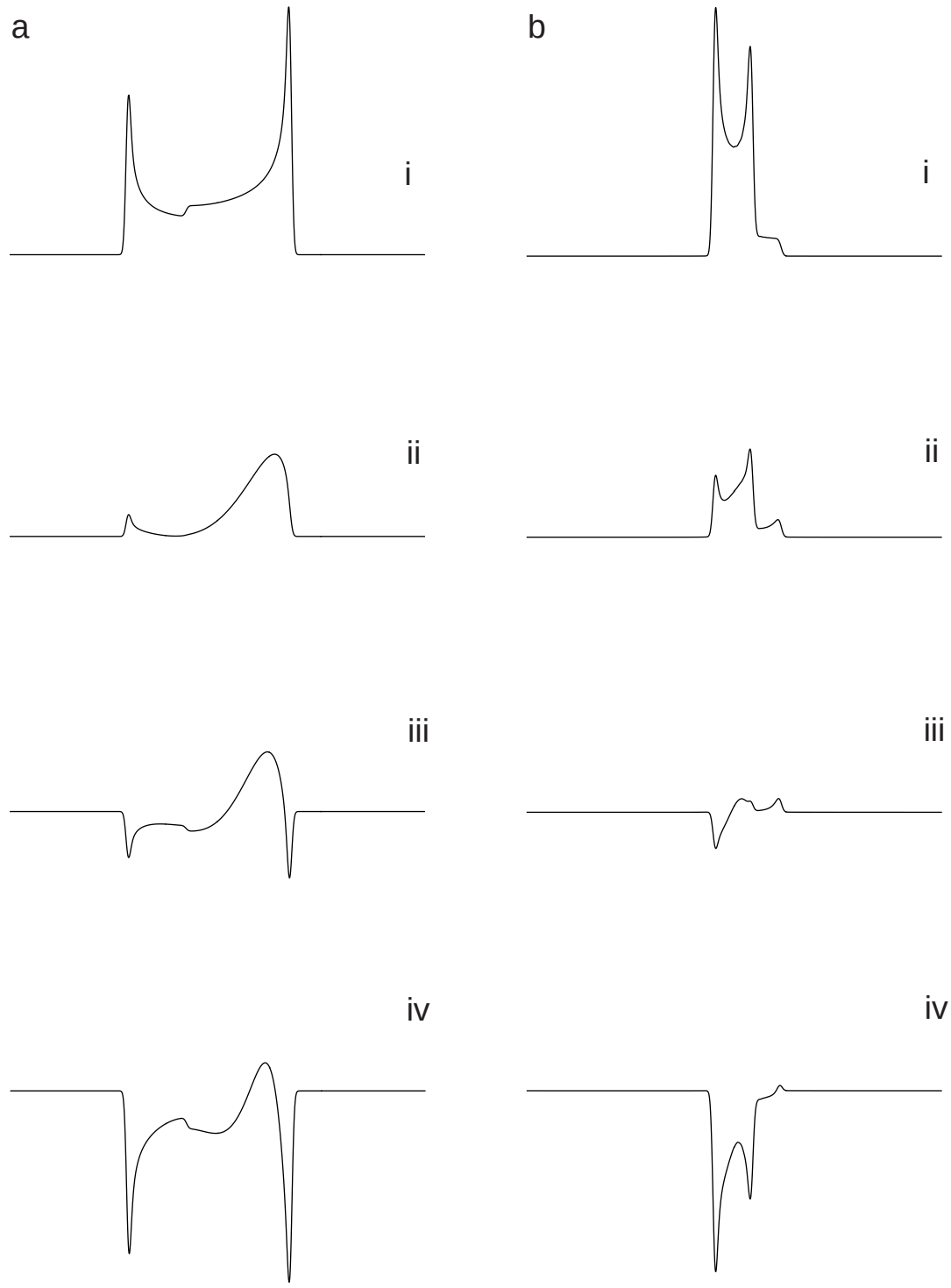

Figure 4.2. Simulated (a) static and (b) MAS spin I = 3/2 second-order quadrupolar-broadened central transition spectra, where the flip angle of the excitation pulse equals (i) 45°, (ii) 90°, (iii) 105°, and (iv) 135°. Time-domain data sets were simulated using an explicit density matrix calculation (summing over 200 equally-spaced values of the angle θ in (a), and 90 equally-spaced values of the angles β and ξ in (b)). The following parameters were used: C_Q = 2 MHz, η = 0, and $\omega_0/2\pi$ = 100 MHz, and a Gaussian line-broadening equivalent to a $\Delta\upsilon_{1/2}$ equal to 75 Hz was applied. In all spectra, the spectral width equals 12.5 kHz. The centre of each spectrum corresponds to the isotropic frequency shift.

4.2 The Excitation and Reconversion of Multiple-Quantum Coherence

Although only single-quantum coherence can be detected directly in an NMR experiment, many important NMR experiments incorporate the excitation of multiple-quantum coherence [104-106]. In liquid-state NMR of spin I = 1/2 nuclei, examples include the double-quantum filtered correlation spectroscopy (DQF-COSY) experiment [107, 108], heteronuclear multiple-quantum coherence (HMQC) experiments [109], the INADEQUATE experiment [110], spin topology filters [111], and heteronuclear editing techniques, *e.g.* DEPT [112]. Moreover, in spin I = 3/2 NMR, double- and triple-quantum filtered techniques enable both the reliable measurement of relaxation rates in liquids [113] and the differentiation of nuclear environments in heterogeneous systems [81]. Furthermore, the excitation of multiple-quantum coherence also has advantages in the context of NMR imaging [114].

In the solid state, the extensive dipolar couplings of abundant spins, *e.g.* ^{1}H, means that very high multiple-quantum coherence orders can be excited ($p > 100$ has been observed). In such systems, useful structural information can be obtained using spin-counting experiments [115, 116]. Alternatively, Spiess and co-workers have recently shown that the combination of fast MAS and dipolar recoupling schemes, *e.g.*, DRAMA [117], allows the resolution of ^{1}H-^{1}H dipolar couplings [118, 119]. Multiple-quantum spectroscopy has also been applied to quadrupolar nuclei in the solid state. For example, a double-quantum spectrum of a spin I = 1 nucleus, *e.g.* ^{2}H, reveals chemical shift information, which is obscured by the quadrupolar broadening in the single-quantum spectrum [120, 121]. (As can be seen from Fig. 2.1a, the double-quantum transition does not, to a first-order approximation, depend on ω_Q.) Moreover, it was demonstrated as early as 1980 that triple-quantum coherence can be excited in the solid-state for spin I = 3/2 nuclei [122].

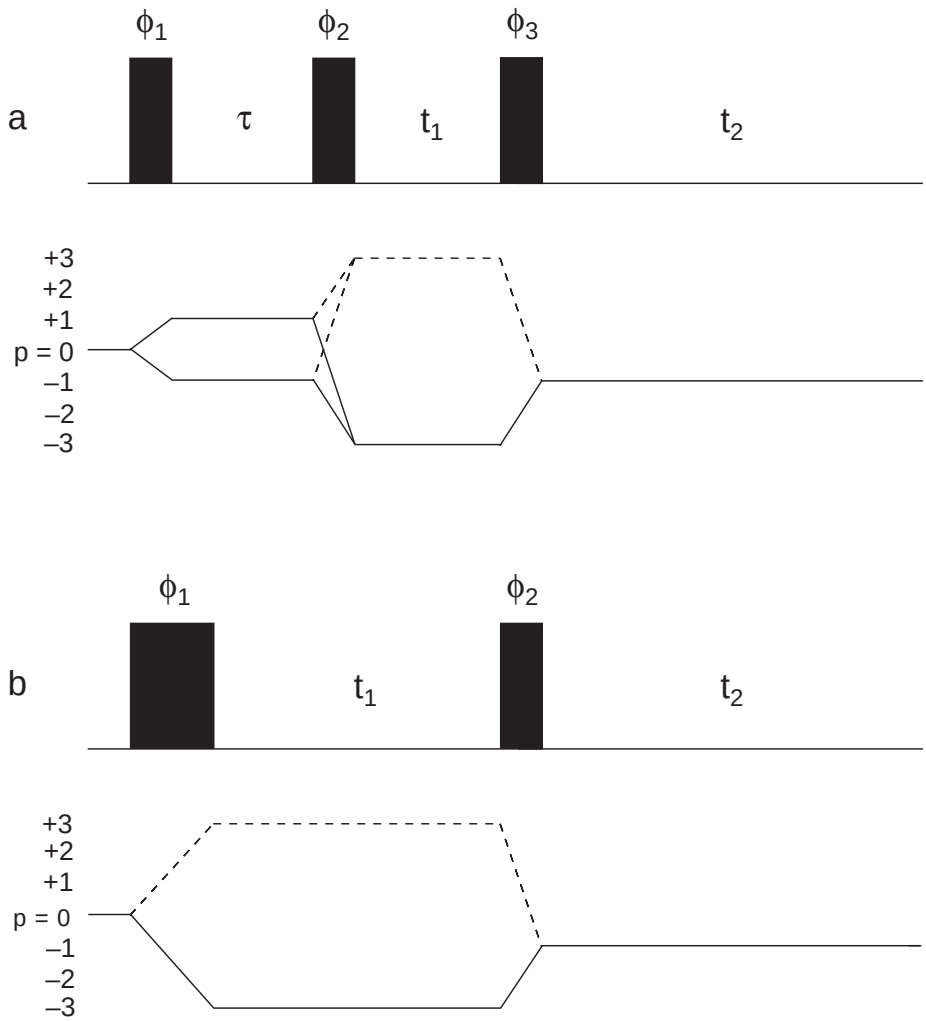

Figure 4.3. Pulse sequences and coherence transfer pathway diagrams for (a) two-pulse and (b) single-pulse excitation of triple-quantum coherence. The optimisation of the flip angles in (b) is discussed in the text. Factors affecting the choice of pathway are discussed in Section 5.1.

When working with liquid samples, multiple-quantum coherence is usually excited using a two-pulse excitation method [123], such as that shown in Fig. 4.3a for the excitation of triple-quantum coherence (an additional 180° pulse is usually inserted in the centre of the τ evolution period to refocus any B_0 inhomogeneity). Although this method was used in the first demonstration of the MQMAS experiment by Frydman and Harwood [40], several researchers have subsequently shown that the single-pulse excitation method shown in Fig. 4.3b is more efficient for powder samples where $\omega_1 < \omega_Q^{PAS}$ [41-45]. The theoretical description of how multiple-quantum coherence can be excited by a single pulse for a spin I = 3/2

nucleus was first presented by Wokaun and Ernst [102], and the calculation presented here is based on their work.

4.2.1 Excitation of Triple-Quantum Coherence by a Single Pulse

Considering a static sample, the Hamiltonian for an on-resonance pulse along the $+x$ axis of the rotating frame, including the effect of evolution under a quadrupolar splitting, is given by

$$H = \omega_1 I_x + \omega_Q \left(I_z^2 - \frac{1}{3} I (I + 1) \right) . \tag{4.4}$$

In matrix form, the spin I = 3/2 Hamiltonian is then:

$$H = \omega_Q \begin{pmatrix} 1 & \frac{\sqrt{3}\, z}{2} & 0 & 0 \\ \frac{\sqrt{3}\, z}{2} & -1 & z & 0 \\ 0 & z & -1 & \frac{\sqrt{3}\, z}{2} \\ 0 & 0 & \frac{\sqrt{3}\, z}{2} & 1 \end{pmatrix} , \tag{4.5}$$

where $z = \omega_1 / \omega_Q$.

To calculate the evolution of the density operator using the Liouville-von Neumann equation (Eq. 2.7), it is first necessary to diagonalise the Hamiltonian. This diagonalisation can be performed analytically by a two step process. Firstly, the transformation

$$H' = X H X^{-1} , \tag{4.6}$$

where the matrix X equals

$$X = \frac{1}{\sqrt{2}} \begin{pmatrix} 1 & 0 & 0 & 1 \\ 0 & 1 & 1 & 0 \\ 1 & 0 & 0 & -1 \\ 0 & 1 & -1 & 0 \end{pmatrix}, \tag{4.7}$$

gives

$$H' = \omega_Q \begin{pmatrix} 1 & \frac{\sqrt{3}\,z}{2} & 0 & 0 \\ \frac{\sqrt{3}\,z}{2} & z-1 & 0 & 0 \\ 0 & 0 & 1 & \frac{\sqrt{3}\,z}{2} \\ 0 & 0 & \frac{\sqrt{3}\,z}{2} & -z-1 \end{pmatrix}. \tag{4.8}$$

The matrix H' consists of two 2×2 submatrices, and can be diagonalised by the transformation

$$H_D = W\,H'\,W^{-1}, \tag{4.9}$$

where the matrix W is:

$$W = \begin{pmatrix} \cos\theta_- & \sin\theta_- & 0 & 0 \\ -\sin\theta_- & \cos\theta_- & 0 & 0 \\ 0 & 0 & \cos\theta_+ & \sin\theta_+ \\ 0 & 0 & -\sin\theta_+ & \cos\theta_+ \end{pmatrix}, \tag{4.10}$$

with

$$\tan 2\theta_\pm = \frac{z\sqrt{3}}{2 \pm z}. \tag{4.11}$$

The diagonalised Hamiltonian, H_D, is then:

$$H_D = \begin{pmatrix} E_{11} & 0 & 0 & 0 \\ 0 & E_{22} & 0 & 0 \\ 0 & 0 & E_{33} & 0 \\ 0 & 0 & 0 & E_{44} \end{pmatrix}, \tag{4.12}$$

where

$$E_{11} = \omega_Q \{ \frac{z}{2} - \sqrt{(1 - z + z^2)} \} \tag{4.13a}$$

$$E_{22} = \omega_Q \{ \frac{z}{2} + \sqrt{(1 - z + z^2)} \} \tag{4.13b}$$

$$E_{33} = \omega_Q \{ \frac{-z}{2} + \sqrt{(1 + z + z^2)} \} \tag{4.13c}$$

$$E_{44} = \omega_Q \{ \frac{-z}{2} - \sqrt{(1 + z + z^2)} \} . \tag{4.13d}$$

Applying the Liouville-von Neumann equation, the density operator at time t is then given by

$$\sigma(t) = X^{-1} W^{-1} \exp \{ -i H_D t \} W X \sigma(0) X^{-1} W^{-1} \exp \{ +i H_D t \} W X . \tag{4.14}$$

Although, as demonstrated in Ref. [122], a general analytical solution can be obtained using the full form of Eq. (4.14), the calculation is considerably simplified if $\omega_1 \ll \omega_Q$. In this limit, z is assumed to be sufficiently close to zero that $\theta_+ = \theta_- = 0$, and, therefore, W is the unit matrix. If this approximation is made, it can be shown, by expanding the square roots in Eq. (4.13) as power series, that

$$\sigma(t) = X^{-1} \exp \{ -i H_D t \} \sigma'(0) \exp \{ +i H_D t \} X , \tag{4.15}$$

where

$$\sigma'(0) = X\,\sigma(0)\,X^{-1}$$

$$= \begin{pmatrix} 0 & 0 & \frac{3}{2} & 0 \\ 0 & 0 & 0 & \frac{1}{2} \\ \frac{3}{2} & 0 & 0 & 0 \\ 0 & \frac{1}{2} & 0 & 0 \end{pmatrix} . \qquad (4.16)$$

Performing the matrix multiplication then yields

$$\sigma(t) = \frac{1}{2}\begin{pmatrix} 3\cos(\lambda_3 t) & 0 & 0 & 3i\sin(\lambda_3 t) \\ 0 & \cos(\lambda_1 t) & i\sin(\lambda_1 t) & 0 \\ 0 & -i\sin(\lambda_1 t) & -\cos(\lambda_1 t) & 0 \\ -3i\sin(\lambda_3 t) & 0 & 0 & -3\cos(\lambda_3 t) \end{pmatrix} , \qquad (4.17)$$

where

$$\lambda_1 = 2\,\omega_1 \qquad (4.18a)$$

$$\lambda_3 = \frac{3\,\omega_1^3}{8\,\omega_Q^2} . \qquad (4.18b)$$

Examining the off-diagonal elements, it is clear that triple-quantum coherence ($\sigma_{14}(t)$ and $\sigma_{41}(t)$) as well as single-quantum coherence ($\sigma_{23}(t)$ and $\sigma_{32}(t)$) is generated by the pulse:

$$\sigma_{23}(t) = -\sigma_{32}(t) = i\sin(2\,\omega_1 t) \qquad (4.19a)$$

$$\sigma_{14}(t) = -\sigma_{41}(t) = 3i\sin\left(\frac{3\,\omega_1^3 t}{8\,\omega_Q^2}\right) . \qquad (4.19b)$$

Using Eq. (4.19), and the fact that the duration of a 90° pulse, $\tau_p^{90°}$, equals $\pi/2\omega_1$, the pulse duration, τ_p^{max}, corresponding to the first maxima for the build-up of single- and triple-quantum coherence are given as

$$\tau_p{}^{max}{}_{p=-1} = \frac{\tau_p^{90°}}{2} \tag{4.20a}$$

$$\tau_p{}^{max}{}_{p=-3} = \frac{8}{3}\left(\frac{\omega_Q}{\omega_1}\right)^2 \tau_p^{90°}. \tag{4.20b}$$

For single-quantum coherence, the first maximum corresponds to a 45° flip angle, as demonstrated earlier in Fig. 4.1. In comparison, for triple-quantum coherence, Eq. (4.20b) predicts that the optimum flip angle depends on the ratio ω_Q/ω_1.

When ω_Q/ω_1 equals 5, Eq. (4.20b) predicts that maximum triple-quantum coherence is obtained using a flip angle of 6000°. This is demonstrated by the solid line in Fig. 4.4 (overleaf), where the amount (calculated by an exact numerical method) of triple-quantum coherence generated by a single pulse is plotted as a function of flip angle for different values of ω_Q/ω_1. The vertical scale is normalised relative to the amount of single-quantum coherence generated by a single pulse acting on the central transition.

A closer examination of Fig. 4.4 reveals that there are small oscillations in the sine curve for the case where ω_Q/ω_1 equals 5. These oscillations are a consequence of terms which would be present in Eq. (4.19b) if the simplifying approximation that ω_1/ω_Q tends to zero had not been made. It is expected that the build up curves would deviate further from the ideal sinusoidal behaviour, as the ratio ω_Q/ω_1 decreases. This is indeed observed in Fig. 4.4 where the dashed and dotted lines correspond to ω_Q/ω_1 values equal to 2 and 1, respectively. Nevertheless it is interesting to note that, even though the approximation that ω_Q/ω_1 tends to zero is clearly not appropriate in these cases, the theoretical flip angles corresponding to

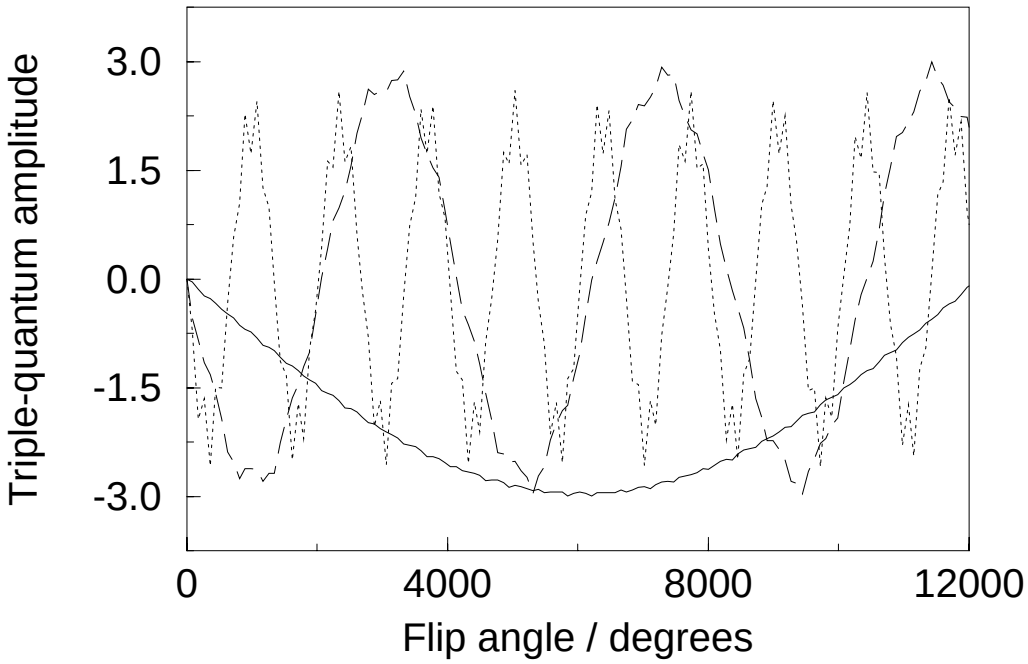

Figure 4.4. The dependence of the triple-quantum coherence amplitude on the flip angle of an on-resonance excitation pulse, for ω_Q/ω_1 equal to 5 (solid line), 2 (dashed line), and 1 (dotted line). Otherwise, the same simulation parameters as described in Fig. 4.1 were used. The vertical scale is normalised as in Fig. 4.1.

maximum triple-quantum coherence are in reasonable agreement with the observed values in Fig. 4.4. (Eq. (4.20b) predicts values of 1440° and 240°, respectively.)

4.2.2 Excitation and Reconversion of Multiple-Quantum Coherence in the MQMAS Experiment

In the context of the MQMAS experiment, Medek *et al.* [44] and Amoureux *et al.* [51] have carried out detailed studies of the conditions necessary to optimise multiple-quantum excitation and reconversion, and the discussion presented here is based on their work.

On the basis of Fig. 4.4, it might be expected that it would be necessary to use a very large flip angle to excite triple-quantum coherence. However, if a powder distribution of ω_Q is considered, it is found, for a range of ω_Q^{PAS}/ω_1 values, that the optimum flip angle for a spin I = 3/2 nucleus is

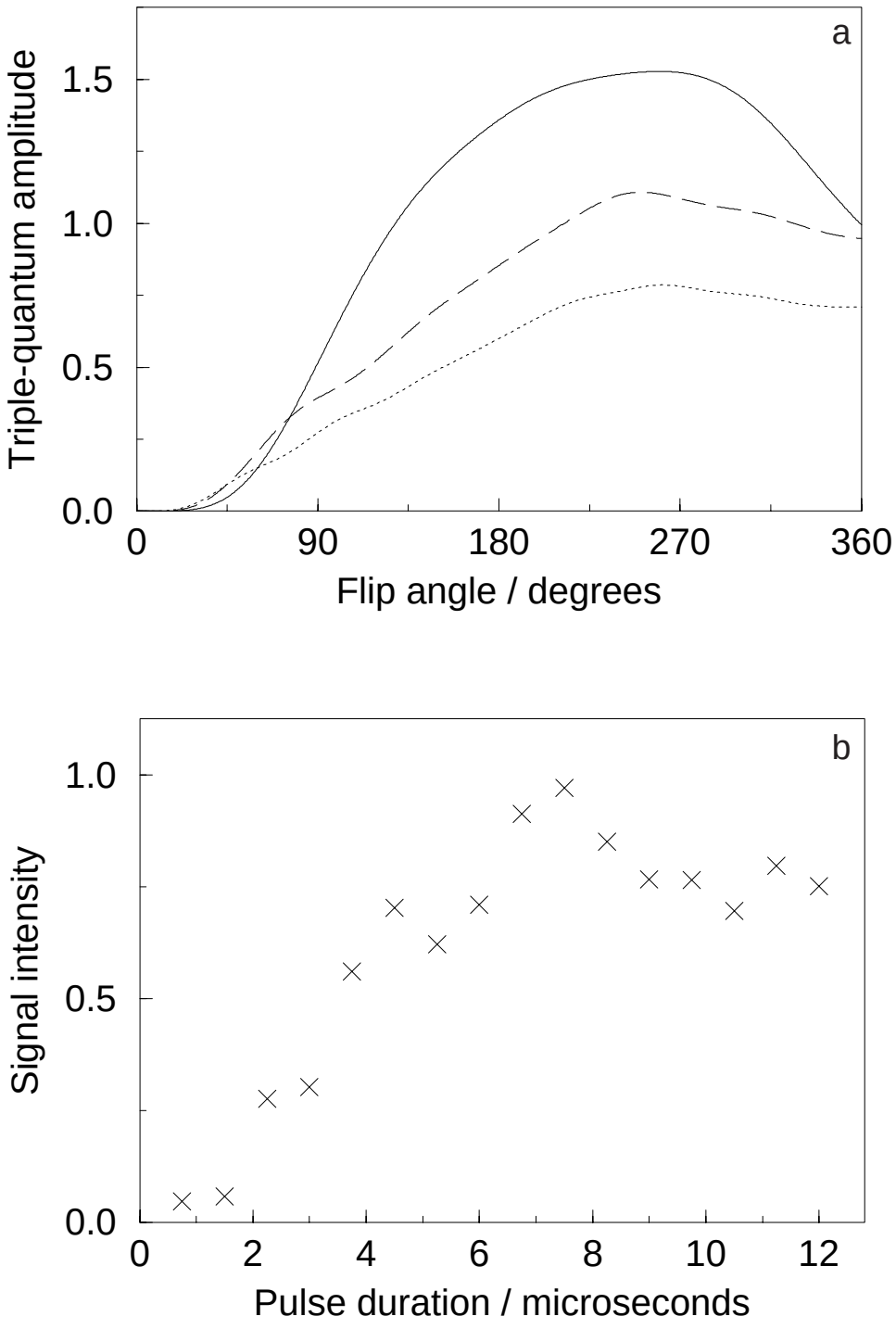

Figure 4.5. (a) The dependence of the spin I = 3/2 triple-quantum coherence amplitude on the flip angle of an on-resonance excitation pulse for a powder distribution (summing over 90 equally-spaced values of the angle θ), where ω_Q^{PAS}/ω_1 equals 2.5 (solid line), 5 (dashed line), and 7.5 (dotted line). Otherwise, the same simulation parameters as described in Fig. 4.1 were used. The vertical scale is normalised as in Fig. 4.1. (b) Experimental ^{23}Na (105.8 MHz) results for Na_2SO_4 showing how the height of the triple-quantum filtered MAS spectrum varies as a function of the flip angle of the excitation pulse. The vertical scale is in arbitrary units. The following experimental conditions were used: 24 transients (consisting of 512 points) were averaged, the relaxation interval was 1 s, a reconversion pulse of duration 1.5 μs was used, the spectral width was 25 kHz, and the spinning speed was 5.2 kHz. The ratio ω_Q^{PAS}/ω_1 equals 7.7 and the 90° pulse length is 3.2 μs.

approximately 240°. This is shown in Fig. 4.5a (previous page). The vertical scale in Fig. 4.5a is normalised relative to the amount of single-quantum coherence generated by a single pulse. It is therefore evident that triple-quantum excitation is a relatively efficient process, although it becomes less efficient as ω_Q^{PAS}/ω_1 increases. For comparison, Fig. 4.5b presents experimental ^{23}Na NMR results obtained for a sample of Na_2SO_4, showing how the height of the triple-quantum filtered spectrum varies as a function of the flip angle of the excitation pulse. There is good agreement between experimental and simulated results. (In Fig. 4.5b, ω_Q^{PAS}/ω_1 equals 7.7 and the 90° pulse length is 3.2 μs.)

Since only single-quantum coherences are directly observable in an NMR experiment, it is necessary to reconvert the multiple-quantum coherence into observable signal. As shown in the following chapter, the flip angle dependence of the efficiency of the separate $p = +3 \rightarrow p = -1$, and $p = -3 \rightarrow p = -1$ coherence transfer steps in Fig. 4.3b is different. Moreover, Chapter 5 further demonstrates that the choice of flip angle can depend on factors other than the simple maximisation of signal. Keeping these considerations in mind, Fig. 4.6a (overleaf) presents plots showing the effect of varying the flip angle of the reconversion pulse for a spin I = 3/2 nucleus for the experiment in Fig. 4.3b where only the $p = -3$ to $p = -1$ pathway is selected (the choice of this pathway is discussed in Section 5.1). For comparison, Fig. 4.6b presents experimental results again obtained for a sample of sodium sulphate. The optimum flip angle can be seen to correspond to approximately 60°.

An obvious feature of Fig. 4.6a is the significant loss of signal compared to a single-pulse experiment. Since Fig. 4.5a showed that triple-quantum coherence can be excited with a sensitivity comparable to the excitation of single-quantum coherence in a single-pulse experiment, the loss of sensitivity must be a consequence of the reconversion pulse. This is because a weak pulse cannot convert triple-quantum coherence into central transition single-quantum

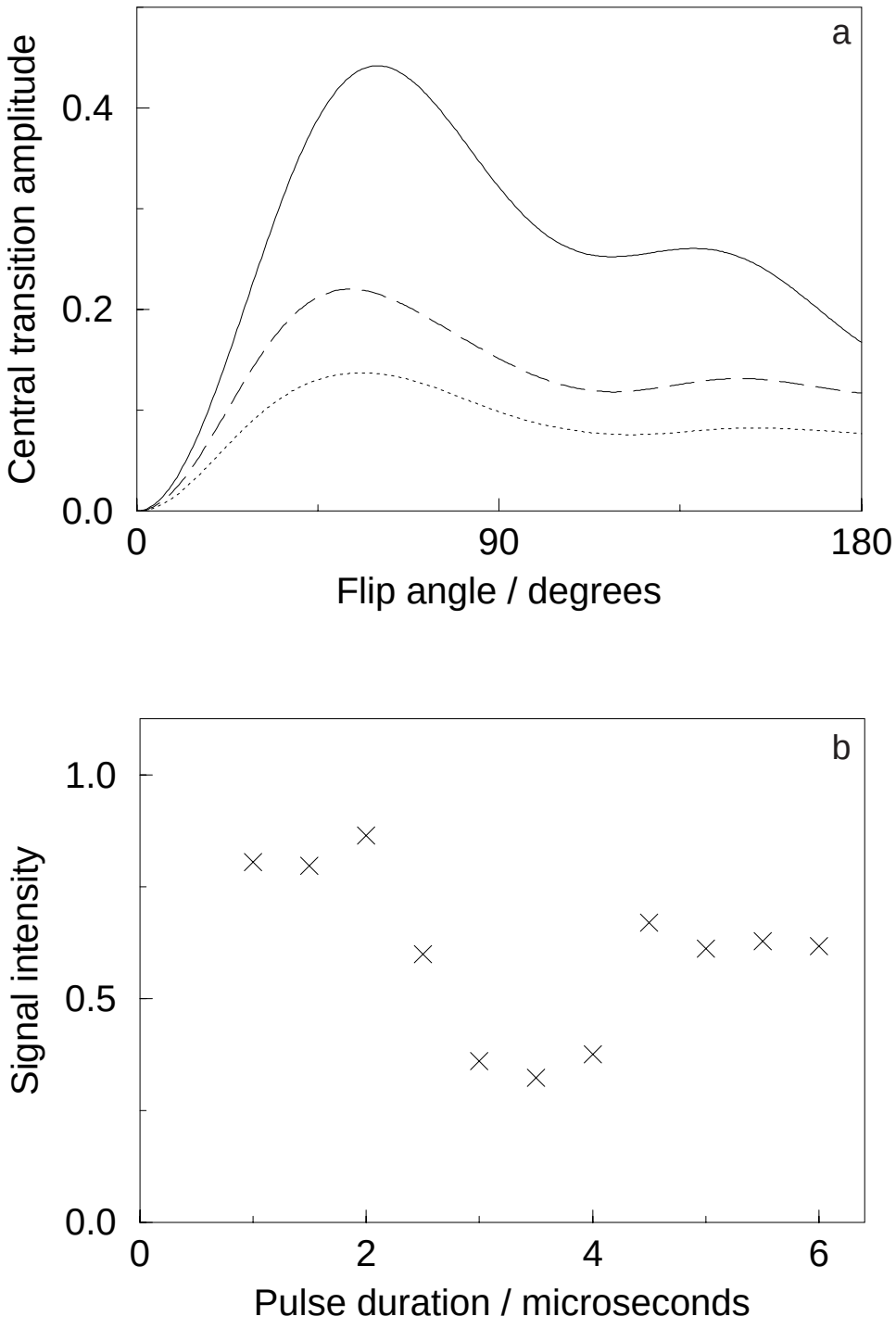

Figure 4.6. (a) The dependence, for the triple-quantum excitation experiment in Fig. 4.3b (selecting the p = –3 to p = –1 pathway), of the spin I = 3/2 central transition amplitude on the flip angle of an on-resonance reconversion pulse for a powder distribution, where ω_Q^{PAS}/ω_1 equals 2.5 (solid line), 5 (dashed line), and 7.5 (dotted line). In each case, the flip angle of the on-resonance excitation pulse was 240°. Otherwise, the same simulation parameters as described in Fig. 4.5a were used. The vertical scale is normalised as in Fig. 4.1. (b) Experimental ^{23}Na (105.8 MHz) results for Na_2SO_4 showing how the height of the triple-quantum filtered MAS spectrum varies as a function of the flip angle of the reconversion pulse. The vertical scale is in arbitrary units. An excitation pulse of duration 7.5 μs was used. Otherwise, the same experimental parameters as described in Fig. 4.5b were used.

coherence. Instead, it can be shown, using Eq. (4.15), that an initial state of triple-quantum coherence ($\sigma_{41}(t) = -\sigma_{14}(t) = i$) is converted by a weak pulse ($\omega_1 << \omega_Q$) into

$$\sigma(t) = \begin{pmatrix} \sin(\lambda_3 t) & 0 & 0 & -i\cos(\lambda_3 t) \\ 0 & 0 & 0 & 0 \\ 0 & 0 & 0 & 0 \\ i\cos(\lambda_3 t) & 0 & 0 & -\sin(\lambda_3 t) \end{pmatrix} . \qquad (4.21)$$

Therefore, the resulting state is solely a population difference across the outer two energy levels. To obtain central transition single-quantum coherence, a hard pulse is required; this is apparent from Fig. 4.6a, where the maximum signal increases with decreasing ω_Q^{PAS}/ω_1.

Figure 4.7 (overleaf) presents plots of the dependence, for a spin I = 3/2 nucleus, of the final central transition amplitude on the quadrupolar coupling constant, C_Q, for different values of ω_1. (Optimum flip angles are used for the excitation and reconversion of triple-quantum coherence.) While the dotted and dashed lines correspond to $\omega_1/2\pi$ equal to 75 kHz and 100 kHz, respectively (the nutation frequencies typically obtained experimentally for the 7 mm and 4 mm probes, respectively), the solid line represents an $\omega_1/2\pi$ of 300 kHz (the nutation frequency claimed by the instrument manufacturer, Bruker, for its newly-released dedicated MQMAS probe). In each case, the signal intensity rises from zero (triple-quantum coherence cannot be excited if the quadrupolar splitting equals zero) reaches a maximum and then falls away, as C_Q increases. It is important to note that as ω_1 is increased the C_Q value corresponding to the maximum signal increases.

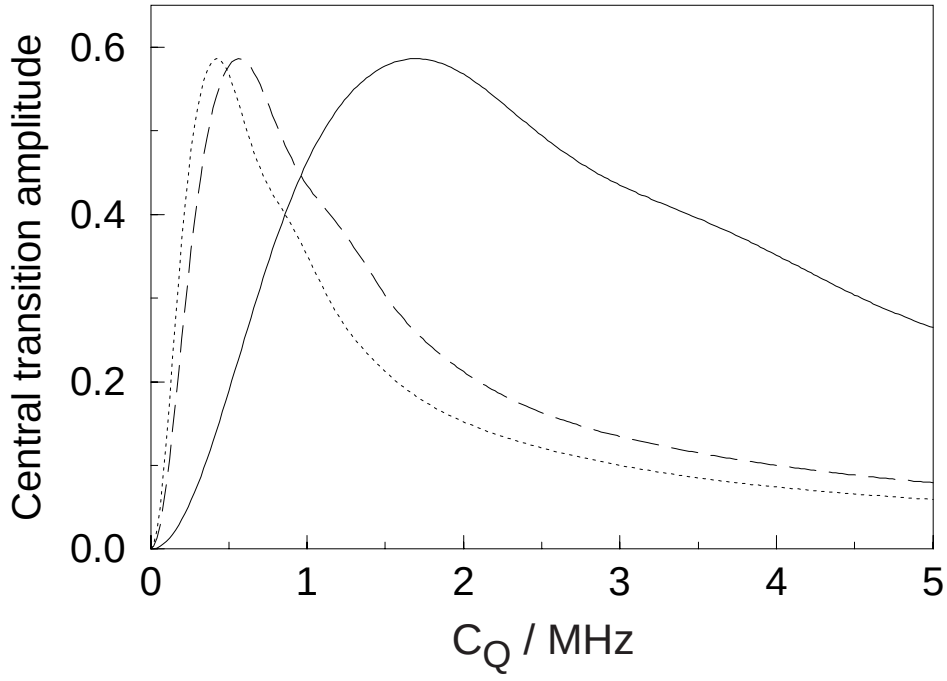

Figure 4.7. The dependence, for the triple-quantum excitation experiment in Fig. 4.3b (selecting the p = –3 to p = –1 pathway), of the spin I = 3/2 central transition amplitude on the quadrupolar coupling constant, C_Q, for $\omega_1/2\pi$ equal to 300 kHz (solid line), 100 kHz (dashed line), and 75 kHz (dotted line). In each case, the flip angles of the on-resonance excitation and reconversion pulses were 240° and 60°, respectively. Otherwise, the same simulation parameters as described in Fig. 4.5a were used. The vertical scale is normalised as in Fig. 4.1.

The main current drawback of the MQMAS experiment is clearly illustrated by Fig. 4.7. Namely, nuclear sites with different C_Q values are not excited with equal amplitude. The experiment is therefore not quantitative, and in the worst case some nuclear sites are excited with such low amplitude that they are lost in the noise. For example, on the MSL 400 spectrometer, it was only possible to observe the third ^{23}Na site, where C_Q equals 3.7 MHz, in an MQMAS experiment recorded on a sample of dibasic sodium phosphate, Na_2HPO_4, if the 4 mm probe, where ω_1 is larger, was used. There is obviously major interest in the development of solutions to this problem. In addition to the development of amplifiers and probes which give rise to larger radiofrequency field strengths, alternative methods of excitation and reconversion, for example the use of adiabatic or shaped pulses [55, 74], are being considered.

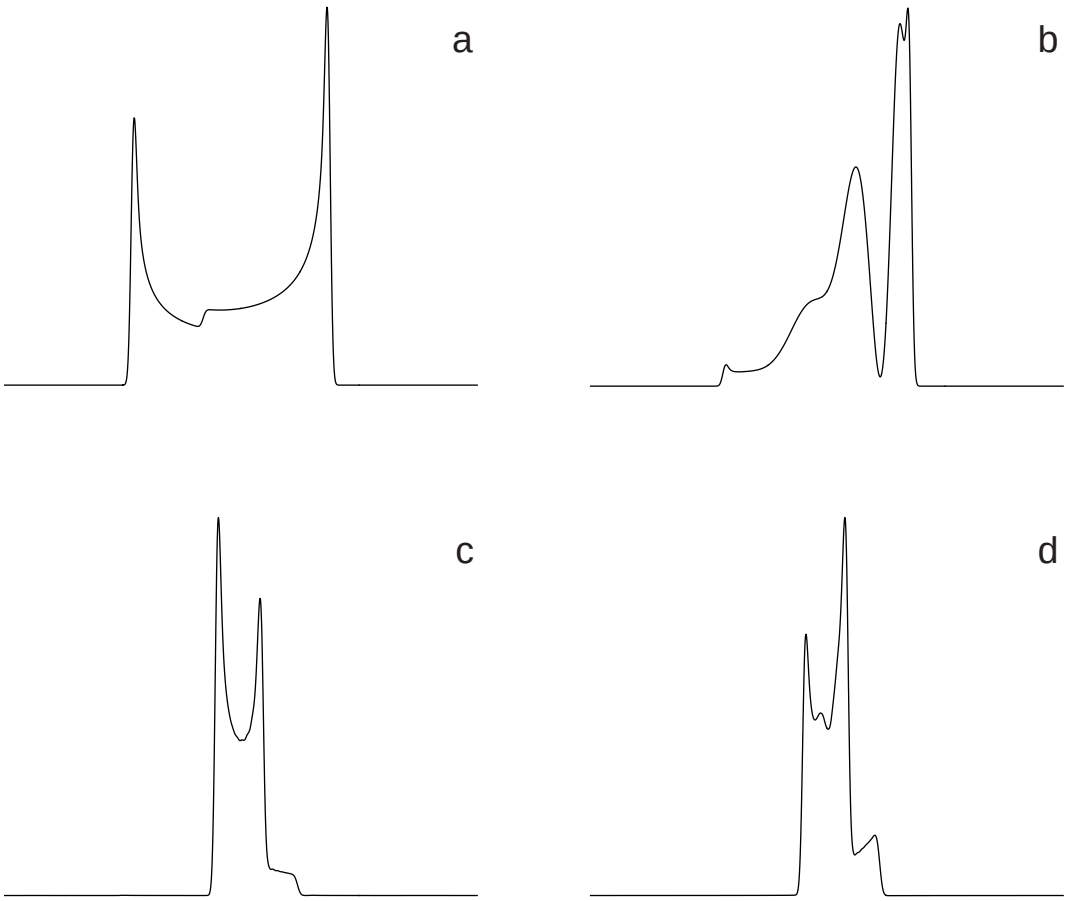

Figure 4.8. Simulated (a and b) static and (c and d) MAS second-order quadrupolar-broadened central transition spectra for, (a and c), a simple single-pulse experiment and, (b and d), the triple-quantum excitation experiment in Fig. 4.3b (selecting the p = –3 to p = –1 pathway). In (a) and (c), uniform excitation of single-quantum coherence over all values ω_Q was assumed, while in (b) and (d), the flip angles of the on-resonance excitation and reconversion pulses were 240° and 60°, respectively. Otherwise, the same simulation parameters as described in Fig. 4.2 were used.

An important question which arises is, does the dependence of the efficiency of multiple-quantum excitation on the quadrupolar splitting give rise to distorted second-order quadrupolar-broadened spectra? Figure 4.8 shows that, although the static triple-quantum filtered spectrum is severely distorted, the corresponding MAS spectrum is relatively undistorted. This difference can be understood in the following way. Consider, for a static sample, the crystallites lying on a cone subtending an angle of 54.7° with respect to the B_0 field. The quadrupolar splitting, ω_Q, for all these crystallites (assuming axial symmetry) equals zero ($\theta = 54.7°$ in Eq. (3.17)), and thus multiple-quantum coherence cannot be excited. This gives rise to a

"hole" in the multiple-quantum filtered spectrum (Fig. 4.8b). In an MAS experiment, in contrast, during a rotor period each crystallite experiences a range of ω_Q characteristic (again assuming axial symmetry) of the angles β and $(\xi - \omega_r t)$. As described in Section 3.2, β describes the rotation of the principal axis system onto the sample frame, while ξ is the initial phase of the crystallite relative to the rotor. It is important to note that the set of crystallites with the same β, but different ξ, have associated with them the same rotor-averaged ω_Q, which determines the second-order quadrupolar shift. However, at the instant when a pulse is applied, these crystallites have a range of instantaneous values of ω_Q. Therefore, for the particular set of crystallites with a rotor-averaged ω_Q equal to zero, multiple-quantum coherence can still be excited, since the instantaneous ω_Q is non-zero for virtually all crystallites.

For comparison, Fig. 4.9 (overleaf) presents ^{87}Rb MAS and triple-quantum filtered MAS spectra obtained for $RbNO_3$. The spectra are presented on different vertical scales indicating the loss of signal associated with excitation and reconversion of triple-quantum coherence. It should be further noted that there are only very small differences between the two lineshapes.

The discussion so far in this section has focused on spin I = 3/2 nuclei. The MQMAS experiment is equally applicable to spin I = 5/2 (and indeed I = 7/2, 9/2 nuclei), and it is therefore necessary to investigate the optimum conditions for the excitation and reconversion of multiple-quantum coherence for such nuclei. For spin I = 5/2 nuclei, quintuple- as well as triple-quantum coherence evolution can be used in an MQMAS experiment. Analogous simulations (not shown) to those presented for spin I = 3/2 show that a flip angle of approximately 180° corresponds to the optimum excitation of both triple- and quintuple-quantum coherence, while flip angles of 65° and 75° give rise to the most efficient $p = +3 \rightarrow p = -1$ and $p = -5 \rightarrow p = -1$ reconversion steps, respectively (the choice of these pathways is discussed in Section 5.1). Using these optimum flip angles, Figs. 4.10a and 4.10b (overleaf) show

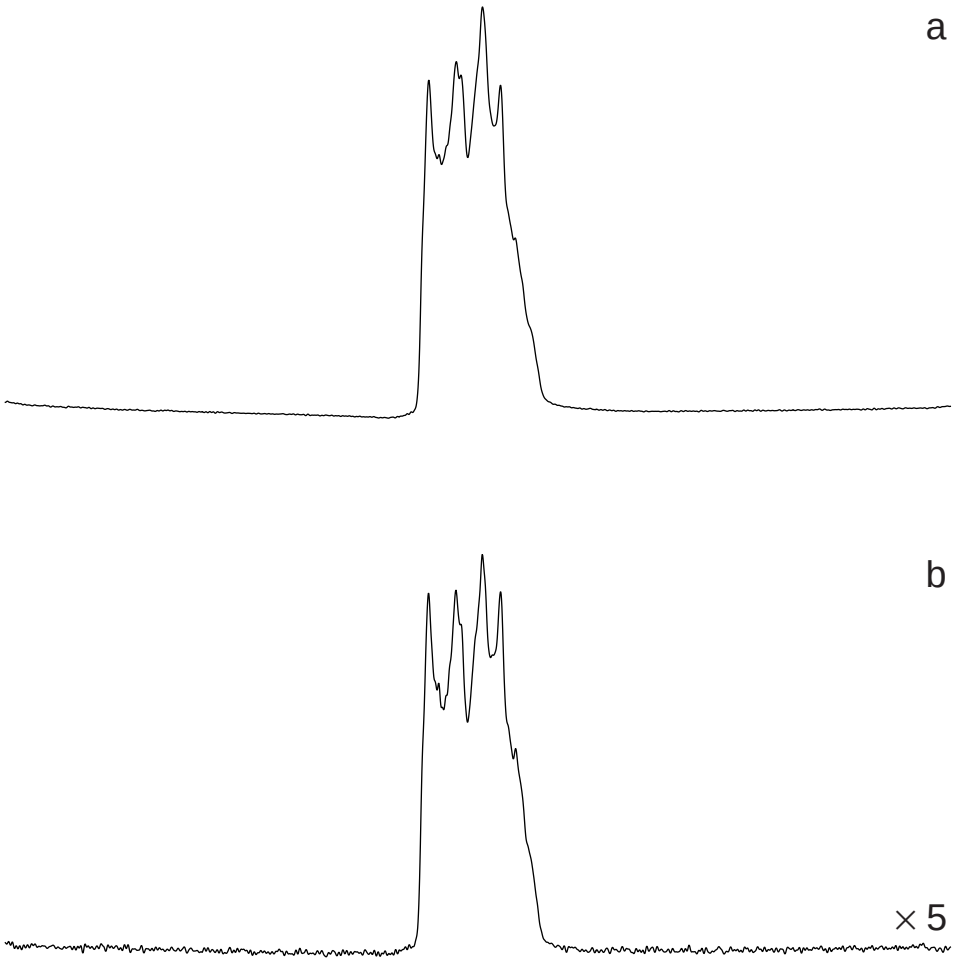

Figure 4.9. Experimental ^{87}Rb (163.6 MHz) MAS spectra of $RbNO_3$ obtained using (a) a simple single-pulse experiment, and (b) the triple-quantum excitation experiment in Fig. 4.3b (selecting the p = –3 to p = –1 pathway). In both cases, 128 transients (consisting of 1024 points) were averaged, with a relaxation interval of 100 ms, and the spinning speed was 8.5 kHz. In (a), a radiofrequency pulse of duration 1.3 μs was used, while in (b), the excitation and reconversion pulses were of duration 4.1 and 1.1 μs, respectively. In both spectra, the displayed spectral width (cut down from 25 kHz) equals 15 kHz.

plots of the resulting central transition amplitude as a function of C_Q for the triple- and quintuple-quantum experiments. It is clear that both the overall signal intensity is less and the fall off occurs at lower C_Q for the quintuple-quantum experiment. However, as demonstrated in Chapter 7, there are some important advantages associated with performing a quintuple-quantum MQMAS experiment.

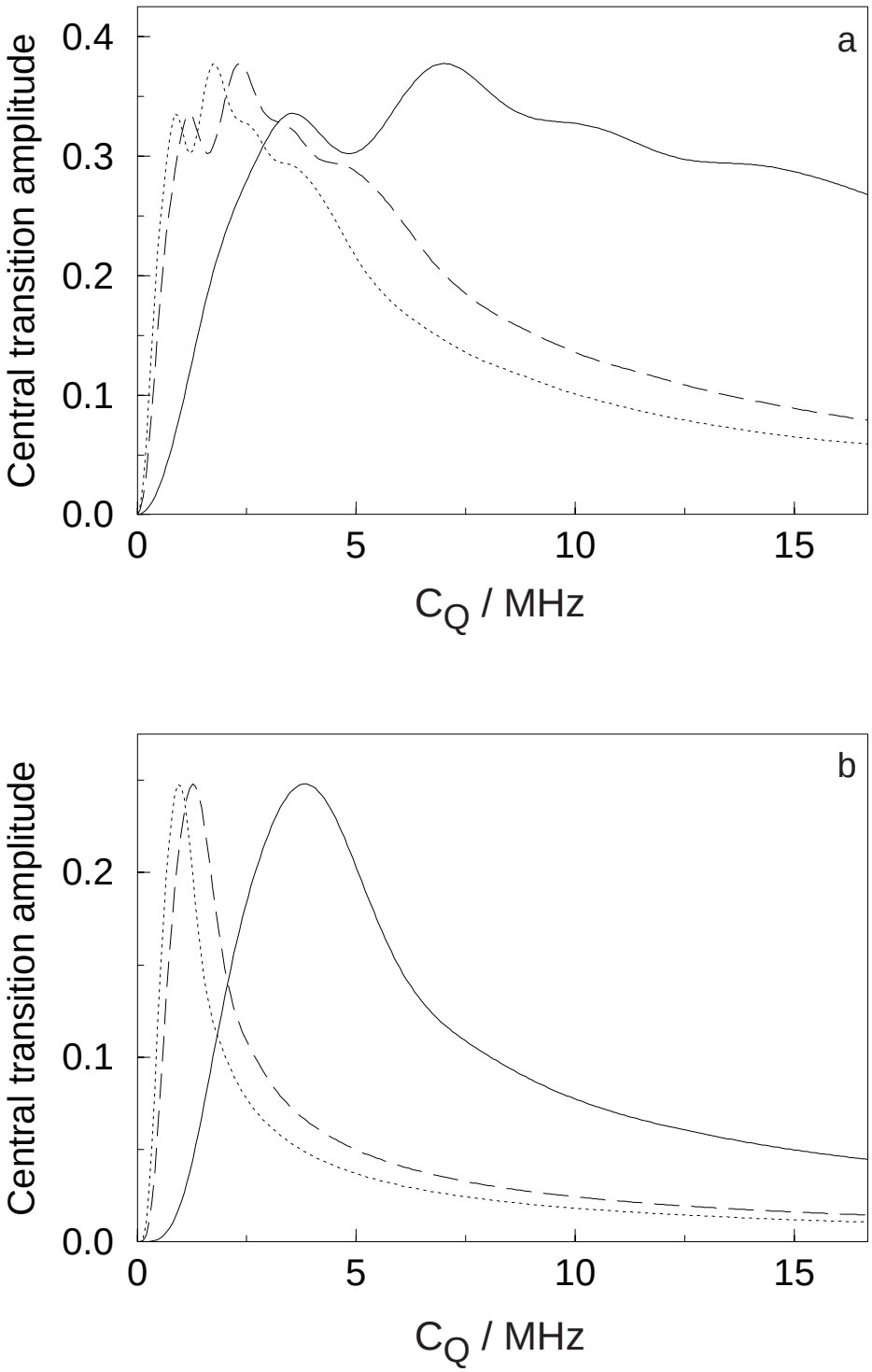

Figure 4.10. The dependence, for (a) the triple-quantum excitation experiment in Fig. 4.3b (selecting the p = +3 to p = –1 pathway) and (b) a quintuple-quantum excitation experiment (selecting the p = –5 to p = –1 pathway), of the spin I = 5/2 central transition amplitude on the quadrupolar coupling constant, C_Q, for $\omega_1/2\pi$ equal to 300 kHz (solid line), 100 kHz (dashed line), and 75 kHz (dotted line). The flip angles of the on-resonance excitation and reconversion pulses were 180° and 65°, respectively in (a), and 180° and 75°, respectively in (b). Otherwise, the same simulation parameters as described in Fig. 4.5a were used. The vertical scale is normalised as in Fig. 4.1.

4.3 Central Transition Coherence Transfer Processes

The previous section showed that the reconversion of multiple-quantum into single-quantum coherence, rather than multiple-quantum excitation, is the inefficient step of a multiple-quantum experiment. A hard pulse is required to convert multiple-quantum coherence (for spin I = 3/2 between the outer two energy levels) into central transition single-quantum coherence. However, in some cases, for example the inversion of central transition single-quantum coherence ($p = +1 \rightarrow$

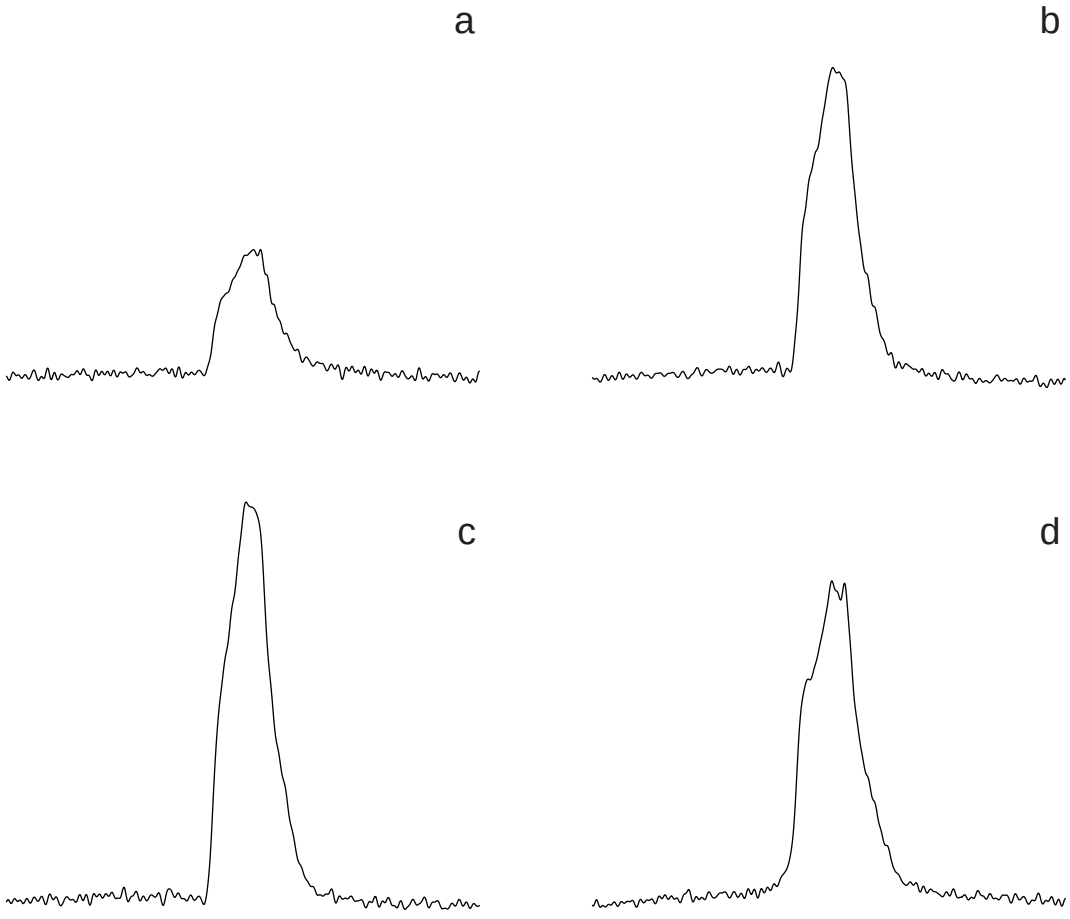

Figure 4.11. Experimental ^{27}Al (104.3 MHz) MAS spectra of a sample of albite obtained using a spin-echo experiment. The nutation frequency, $\omega_1/2\pi$, of the central transition 180° inversion pulse was 75 kHz (full power) in (a), 42 kHz in (b), 17 kHz in (c), and 6 kHz in (d). The following experimental conditions were used: 32 transients (consisting of 512 points) were averaged, the relaxation interval was 1 s, a full-power pulse of duration 1 μs was used to excite single-quantum coherence, and the spinning speed was 5.3 kHz. In all spectra, the displayed spectral width (cut down from 25 kHz) equals 8 kHz.

p = –1) in a spin-echo experiment, it is desirable to avoid the loss of signal that would result from unwanted coherence transfer processes. In this case, it is found that the signal intensity increases as ω_1 is reduced, *i.e.*, as the pulse becomes selective for the central transition. This is demonstrated in Fig. 4.11, which presents ^{27}Al spectra of albite obtained using a spin-echo experiment. As the nutation frequency, $\omega_1/2\pi$, of the inversion pulse is reduced, the signal intensity is observed to rise to a maximum in Fig. 4.11c. Beyond the optimum value of ω_1 in Fig. 4.11c, the observed signal decreases since the pulse is no longer able to excite the full extent of the second-order quadrupolar-broadened central transition. As shown in the following chapters, for many MQMAS experiments, the requirement to reduce ω_1 for pulses which are selective for the central transition is often essential to achieve an acceptable sensitivity.

Chapter 5

The MQMAS Experiment

5.1 Echoes, Antiechoes, and Shifted Echoes

The principle of the MQMAS experiment was introduced at the end of Chapter 3. It was stated that the fourth-rank anisotropic broadening can be refocused, whilst still retaining the isotropic information, by performing a two-dimensional experiment in which multiple- and single-quantum coherences are correlated. The second-rank anisotropic broadening is removed by spinning at the magic angle. For spin I = 3/2, the simplest implementation of the MQMAS experiment is represented by the solid coherence transfer pathway in Fig. 5.1a (overleaf). (This corresponds to the original experiment of Frydman and Harwood [40], except that, as discussed in Section 4.2, Frydman and Harwood initially used a two-pulse sequence for the excitation of multiple-quantum coherence.) Using Eq. (3.24), the time-domain signal for this experiment, in the presence of MAS and neglecting homogeneous broadening and chemical shift terms, is given by

$$s(t_1, t_2) = \exp\{ i \frac{(\omega_Q^{PAS})^2}{\omega_0} [\frac{6}{5} Q^0(\eta) - \frac{6}{5} d^4_{0,0}(\chi) Q^4(\alpha, \beta, \eta)] t_1 \}$$

$$\times \exp\{ i \frac{(\omega_Q^{PAS})^2}{\omega_0} [-\frac{2}{5} Q^0(\eta) + \frac{54}{35} d^4_{0,0}(\chi) Q^4(\alpha, \beta, \eta)] t_2 \} . \quad (5.1)$$

Examination of Eq. (5.1) reveals that an echo corresponding to the refocusing of the fourth-rank inhomogeneous broadening forms at

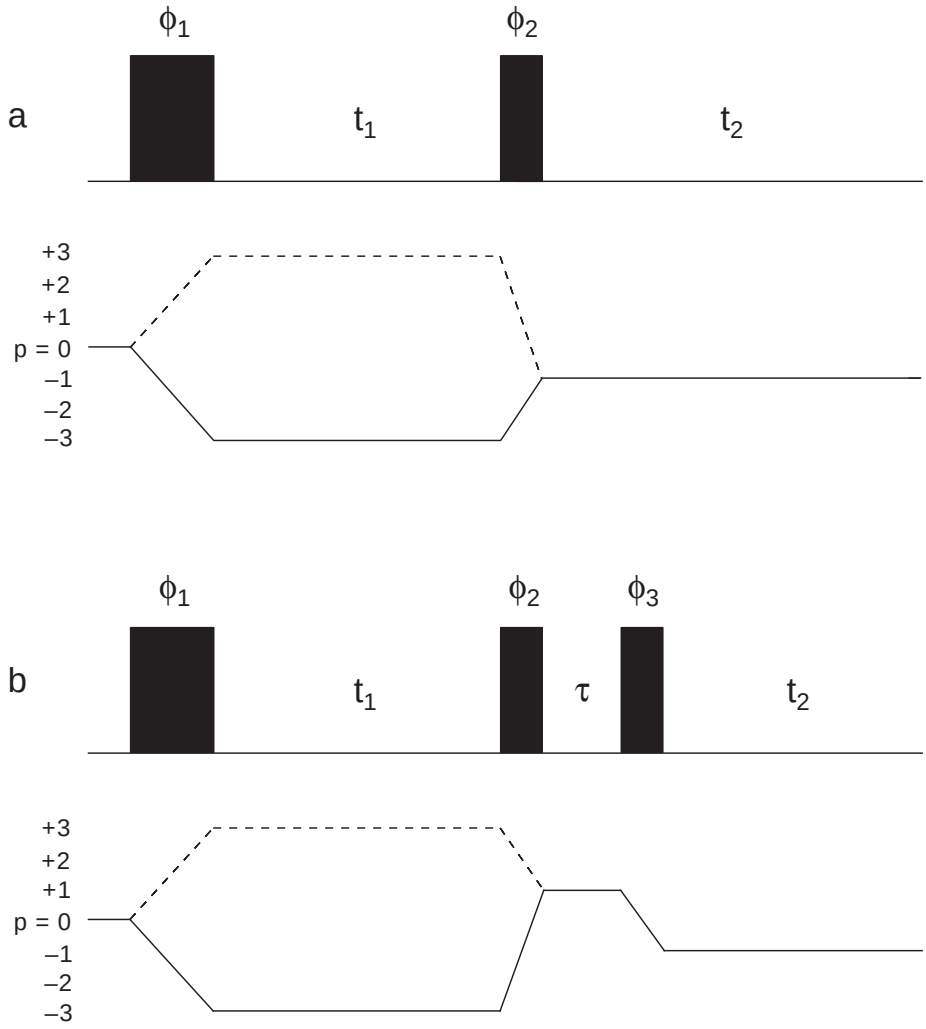

Figure 5.1. Pulse sequences and coherence transfer pathway diagrams for the (a) simple echo (solid line) and simple antiecho (dashed line) and (b) shifted-echo (solid line) and shifted-antiecho (dashed line) MQMAS experiments (for spin I = 3/2 nuclei). Amplitude-modulated experiments result if both the echo and antiecho pathways are retained and have equal amplitudes. The optimum flip angles for the individual pulses are described in the text. The spin-echo interval, τ, in (b) should be chosen to ensure that a whole echo is obtained in t_2 for all values of t_1. Phase cycling schemes for the pulse phases ϕ_1, ϕ_2 and ϕ_3 and for the receiver R_X are given in Tables H1 and H2 of Appendix H.

$$t_2 = \frac{6}{5}\left(\frac{35}{54}\right) t_1 = \frac{7}{9}\, t_1 \,. \qquad (5.2)$$

This is shown in Fig. 5.2a (overleaf), which presents a schematic representation of the time-domain data set. When $t_1 = 0$, it is seen that a half echo (*i.e.*, the signal falls from its maximum value to zero) forms at $t_2 = 0$. As t_1 increases, the echo tracks forwards through t_2, until eventually a point is reached where a whole echo (*i.e.*, the signal

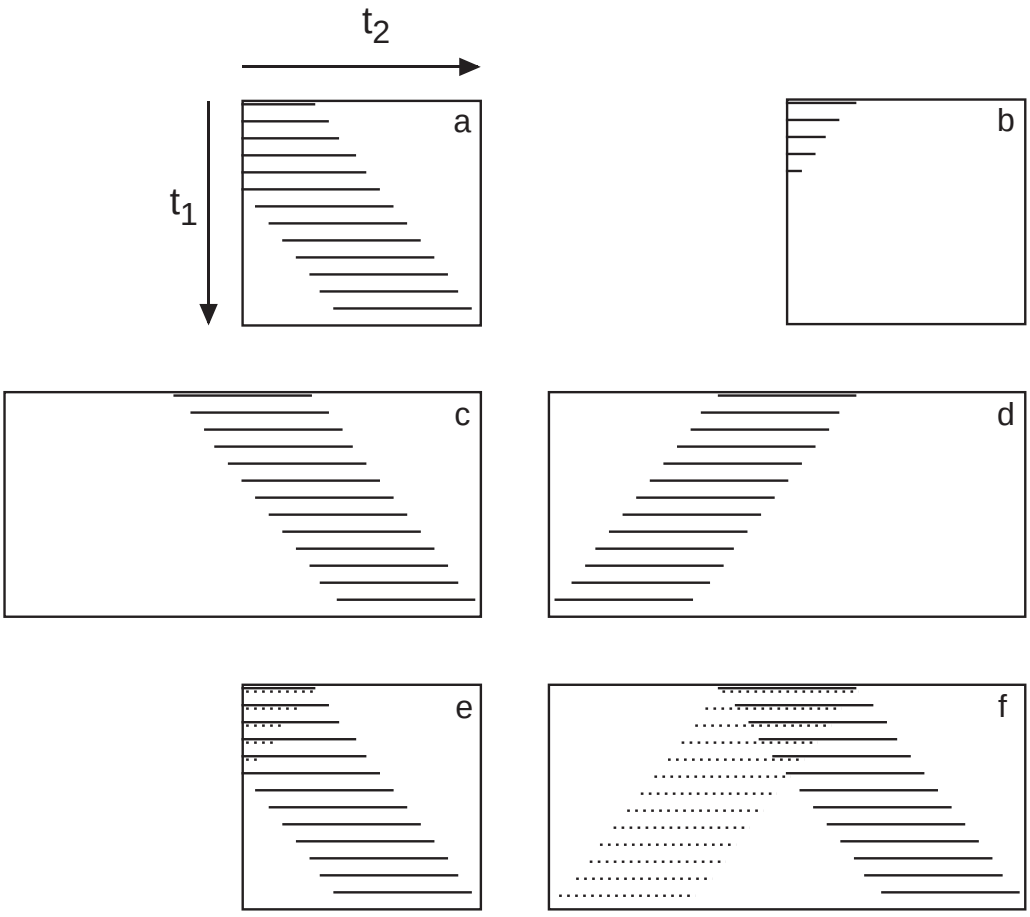

Figure 5.2. Schematic representations of the spin I = 3/2 time-domain signal obtained with the (a) simple echo, (b) simple antiecho, (c) shifted-echo, (d) shifted-antiecho, (e) simple amplitude-modulated, and (f) amplitude-modulated whole-echo experiments. In (e) and (f), the contributions of the echo and antiecho pathways are shown as solid and dotted lines, respectively.

starts from zero, rises to its maximum value, then returns to zero) is observed. Fourier transformation of the one-dimensional data set $s(t_1, t_2 = (7/9)t_1)$ gives rise to an isotropic spectrum of the type presented in Figs. 1.1b and 3.3c.

From Eq. (5.2b), it is clear that the position in t_2 at which the echo forms depends on the ratio of the fourth-rank anisotropic broadening between multiple- and single-quantum coherences. This ratio is of such significance in these experiments that it will hence be referred to as the MQMAS ratio. For spin I = 3/2 and 5/2, the (triple-quantum) MQMAS ratio equals –7/9 and 19/12, respectively (refer to Table 3.1). The key feature of all MQMAS experiments is that the fourth-

rank anisotropic broadening is refocused when the ratio of the durations of the single- and triple-quantum coherence evolution periods equals the magnitude of the MQMAS ratio. It is important to note the difference in sign in the MQMAS ratio between I = 3/2 and 5/2 nuclei; as will become clearer in the following discussion, this has significant consequences with respect to coherence transfer pathway selection. For clarity, the discussion in the opening sections of this chapter will be restricted to spin I = 3/2, with the spin I = 5/2 case being considered in Section 5.4.

The sign of the MQMAS ratio is very important since it determines the relative sign of triple- and single-quantum coherences necessary to refocus the second-order broadening and form an echo. Thus, for spin I = 3/2 nuclei, since the MQMAS ratio is negative, the *echo pathway* corresponds to the correlation of p = –3 and p = –1 coherences, as shown above. In describing MQMAS experiments, it is also useful to introduce the concept of an *antiecho pathway* (represented by the dashed line in Fig. 5.1a), where the fourth-rank anisotropic broadening appears to be refocused at negative values of the acquisition time, t_2. The difference between experiments that select the echo and antiecho pathways is illustrated in Figs. 5.2a and 5.2b. When $t_1 = 0$, there is no difference between the two experiments, with a half echo forming at $t_2 = 0$ for both pulse sequences. However, as t_1 increases, the echo can be seen to track forwards and backwards through t_2 for the echo and antiecho sequences, respectively. Eventually a point is reached where, while there is a whole echo in Fig. 5.2a, the signal has disappeared outside the acquisition window in Fig. 5.2b.

Extending methods developed for the DAS technique (refer to Fig. 3.8b of Section 3.5.1), Massiot *et al.* have recently presented MQMAS experiments in which the signals from the echo and antiecho experiments are *shifted* in t_2 by forming a spin echo using a selective inversion pulse on the central transition [43]. The shifted-echo (solid line) and shifted-antiecho (dashed line) coherence transfer pathways are shown in Fig. 5.1b, while Figs. 5.2c and 5.2d show schematic representations of the

time-domain data sets obtained for the two experiments. As in Figs. 5.2a and 5.2b, the echo still moves forwards and backwards, respectively, in t_2 as t_1 increases but there are now two important differences. Provided the spin-echo interval, τ, is of sufficient length, firstly, at $t_1 = 0$, a whole, rather than half, echo is formed and, secondly, the antiecho signal does not disappear from the acquisition window as t_1 increases. Since whole echoes are obtained for all values of t_1, experiments based on shifted-echo and shifted-antiecho sequences are referred to as *whole-echo* experiments.

5.2 Pure Absorption-Mode Two-Dimensional Lineshapes

In the original experiment of Frydman and Harwood (Fig. 5.1a), phase cycling is used to select a pathway which, as is evident from Eq. (5.1), is phase-modulated with respect to t_1. As discussed in Section 2.3.2, the complex two-dimensional Fourier transform of a time-domain data set of the type $\exp\{iAt_1\}\exp\{iBt_2\}$ gives rise to undesirable two-dimensional phase-twist lineshapes, and therefore such lineshapes result from this experiment. This is demonstrated by Figs. 5.3a and 5.3b (overleaf), which show simulated spectra for the simple echo and simple antiecho experiments, respectively. In both cases, the presence of the fourth-rank anisotropic broadening means that the phase-twist lineshapes add up to form a ridge. However, while, for the echo sequence, the phase-twist lineshapes add up constructively with the gradient of the ridge (with respect to the F_2 axis) equalling the MQMAS ratio, for the antiecho sequence the gradient has the opposite sign to the MQMAS ratio and the phase-twist lineshapes add up destructively. The consequences of the constructive and destructive summation of lineshapes is evident in Figs. 5.3a and 5.3b; in particular, the dispersive character is less apparent in the echo pathway lineshape, especially at the centre of the ridge. In addition, it should be noted that the signal maximum in Fig. 5.3a

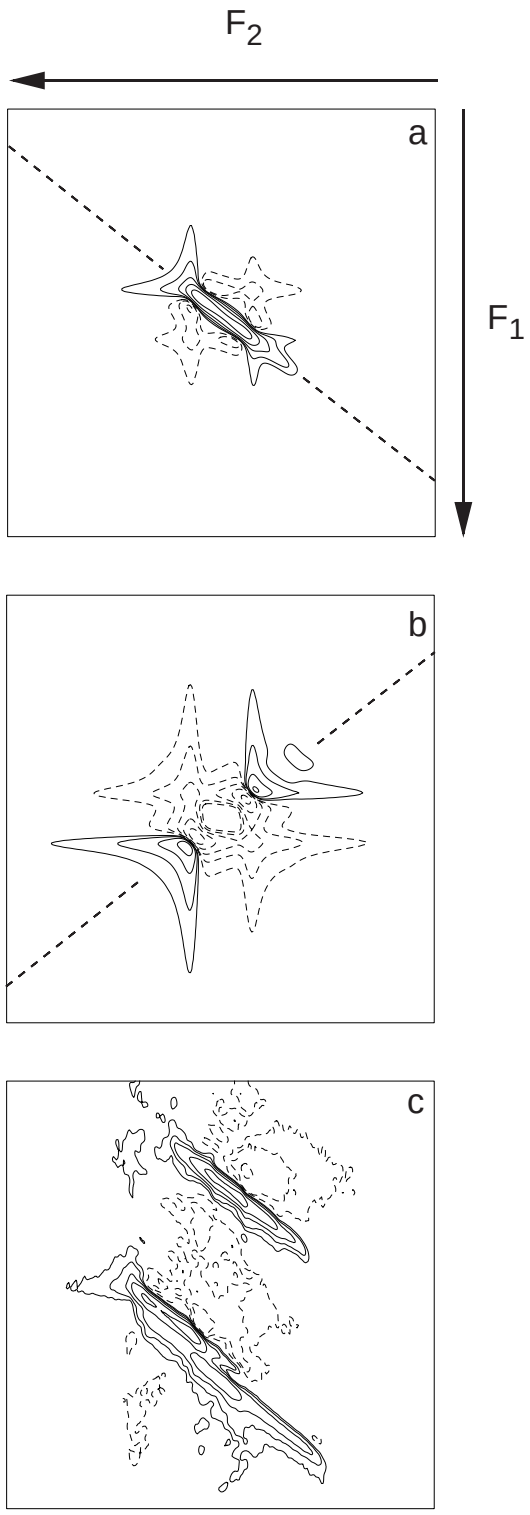

Figure 5.3. Contour plots of spin I = 3/2 spectra obtained with the, (a) and (c), simple echo and, (b), simple antiecho experiments in Fig. 5.1a. The spectra in (a) and (b) were simulated in the time domain and it can be seen that phase-twist lineshapes add up to form a ridge, as indicated by the dashed line. The contour plot in (c) corresponds to a 5×5 kHz region of a ^{87}Rb (130.9 MHz) MQMAS spectrum of $RbNO_3$. The full F_1 and F_2 spectral widths were 25 and 17.2 kHz, respectively, 96 transients (consisting of 512 points each) were averaged for each of 128 increments of t_1, and the relaxation interval was 100 ms. The durations of the triple-quantum excitation and the p = –3 to p = –1 reconversion pulses were 6.8 and 2.4 μs, respectively.

is twice that in Fig. 5.3b, which is unsurprising if the time-domain representations shown in Figs. 5.2a and 5.2b are compared.

Figure 5.3c shows a ^{87}Rb MQMAS spectrum of $RbNO_3$ obtained with the simple echo sequence in Fig. 5.1a. The spectrum contains three ridges corresponding to the three Rb sites in the unit cell (the lower two ridges are only partially separated). The obvious dispersive character of the "mixed-phase" lineshapes reduces the degree to which different sites are resolved, and it is, therefore, much better to obtain pure absorption-mode two-dimensional lineshapes. The next three subsections discuss methods for obtaining such lineshapes.

5.2.1 The Simple Amplitude-Modulated Experiment

If the echo and antiecho pathways in Fig. 5.1a are combined with the same amplitude, an amplitude-modulated signal is obtained as a function of t_1 [41-43]. In the case where the two pathways add, the signal is cosine-modulated:

$$s(t_1, t_2) = 2\cos\{\frac{(\omega_Q^{PAS})^2}{\omega_0}\,[\,\frac{6}{5}\,Q^0(\eta) - \frac{6}{5}\,d^4_{0,0}(\chi)\,Q^4(\alpha, \beta, \eta)\,]\,t_1\,\}$$

$$\times\,\exp\{\,i\,\frac{(\omega_Q^{PAS})^2}{\omega_0}\,[\,-\frac{2}{5}\,Q^0(\eta) + \frac{54}{35}\,d^4_{0,0}(\chi)\,Q^4(\alpha, \beta, \eta)\,]\,t_2\,\}\,. \qquad (5.3)$$

The processing of amplitude-modulated data sets was discussed in Section 2.3, where it was shown that firstly, pure absorption-mode lineshapes are obtained in the frequency-domain spectrum if a hypercomplex two-dimensional Fourier transform is performed. Secondly, sign discrimination can be restored using the States-Haberkorn-Ruben or TPPI methods, which in this case, since p = +3 and –3 coherences evolve during t_1, involves incrementing the phase of the first pulse by 30°. For comparison, a schematic representation of the time-domain data set for the simple amplitude-modulated experiment is given in Fig. 5.2e, with the contributions

of the echo and antiecho pathways being shown as solid and dashed lines, respectively.

5.2.2 Phase-Modulated Whole-Echo Experiments

The pulse sequence and coherence transfer pathway diagram for the shifted-echo experiment was shown in Fig. 5.1b. This experiment differs from the simple echo experiment only in the presence of a spin echo, and the time-domain signal is now given as

$$s(t_1, t_2) = \exp\{ i \frac{(\omega_Q^{PAS})^2}{\omega_0} [\frac{6}{5} Q^0(\eta) - \frac{6}{5} d^4_{0,0}(\chi) Q^4(\alpha, \beta, \eta)] t_1 \}$$

$$\times \exp\{ i \frac{(\omega_Q^{PAS})^2}{\omega_0} [-\frac{2}{5} Q^0(\eta) + \frac{54}{35} d^4_{0,0}(\chi) Q^4(\alpha, \beta, \eta)] (t_2 - \tau) \} , \quad (5.4)$$

where τ is the length of the spin-echo interval. From Eq. (5.4), it can be seen that the fourth-rank anisotropic frequency shifts are refocused when

$$t_2 = \tau + \frac{6}{5}\left(\frac{35}{54}\right) t_1 = \tau + \frac{7}{9} t_1 . \quad (5.5)$$

An analogous expression to Eq. (5.5) can easily be obtained for the shifted-antiecho experiment, and it is found that refocusing now occurs when

$$t_2 = \tau - \frac{7}{9} t_1 . \quad (5.6)$$

Thus, as demonstrated in Figs. 5.2c and 5.2d, as t_1 increases, the echo moves forwards and backwards in t_2 for the shifted-echo and shifted-antiecho experiments, respectively. In practice, this has the obvious consequence that the τ interval must be significantly longer in the shifted-antiecho experiment, hence there is more signal loss through relaxation than in the shifted-echo experiment. For the shifted-echo

experiment, the τ period can be kept to a minimum, since it only needs to be of sufficient length to ensure that the echo is not truncated.

The difference in the direction in which the echo moves as t_1 is incremented might also be expected to have an effect on the resolution of the isotropic projection. The expressions given so far for the time-domain signal have neglected the effect of relaxation. To include the effect of transverse relaxation in the expression for the shifted-echo experiment, given in Eq. (5.4), it is necessary to multiply by an additional factor of

$$\exp\{ - R^{TQ} t_1 \} \exp\{ - R^{SQ} (\tau + t_2) \} , \qquad (5.7)$$

where R^{TQ} and R^{SQ} correspond to the relaxation rates of triple- and (central-transition) single-quantum coherence. The effect of relaxation on the shifted-antiecho experiment is also given by Eq. (5.7), except that, as discussed above, the τ interval will be much longer. Considering only the point at which refocusing occurs, substituting the expressions for t_2 in Eqs. (5.5) and (5.6) into Eq. (5.7) yields

$$\exp\{ - (R^{TQ} \pm \frac{7}{9} R^{SQ}) t_1 \} \exp\{ - 2 R^{SQ} \tau \} , \qquad (5.8)$$

where the + or – sign refers to the shifted-echo and shifted-antiecho experiments, respectively. Equation (5.8) describes the decay due to transverse relaxation of the time-domain counterpart of the projection of the two-dimensional spectrum onto an axis orthogonal to the ridges. Unless R^{SQ} is significantly less than R^{TQ}, it would, therefore, be expected that relaxation is slower, and, hence, the resolution in the isotropic projection is better for the shifted-antiecho experiment. However, to date, no convincing experimental evidence for a difference in resolution between the shifted-echo and shifted-antiecho experiments has been observed.

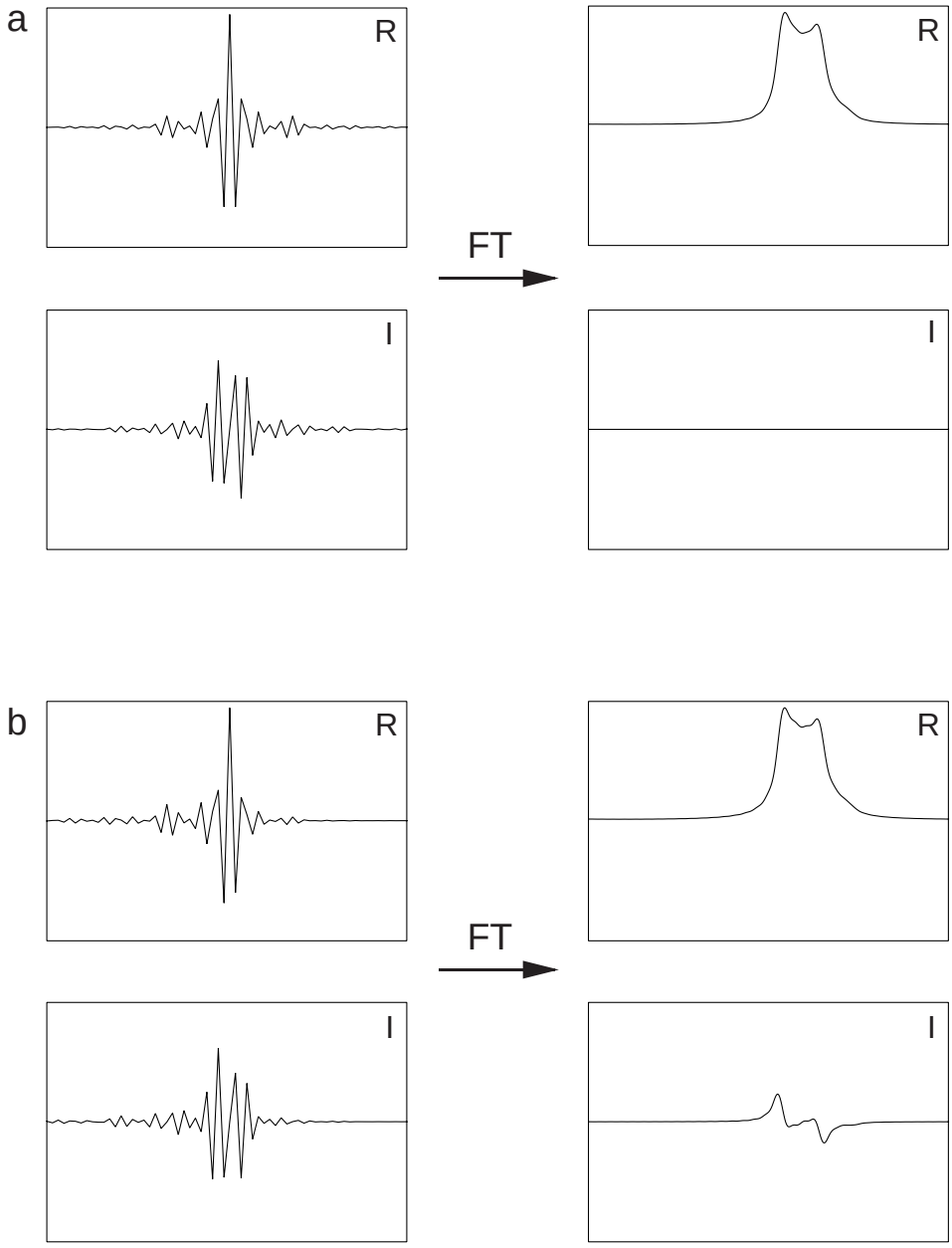

Figure 5.4. (a) The complex Fourier transform of a simulated time-domain signal whose real (R) and imaginary (I) parts are symmetric and anti-symmetric about t = 0, respectively, gives rise to a frequency-domain signal whose real part is purely absorptive and whose imaginary part is zero. (b) When the symmetry of the echo is lost (in this case, due to the application of an exponential damping function to mimic the effects of relaxation), the imaginary part is no longer zero, but now contains a dispersive contribution.

The success of these experiments, with regards to obtaining pure absorption-mode two-dimensional lineshapes, depends on the properties of whole echoes. A principle much used in magnetic resonance imaging [124] is that the complex one-dimensional Fourier transform of a function whose real and imaginary parts are respectively symmetric and anti-symmetric around t = 0 yields a spectrum whose real part is purely absorptive and whose imaginary part is zero. This is illustrated in Fig. 5.4a (previous page). In the shifted-echo and shifted-antiecho MQMAS experiments, to obtain such a symmetric function, it is essential that the inhomogeneous second-order quadrupolar broadening dominates the homogeneous broadening [43]. When the homogeneous broadening becomes significant, the symmetry of the echo is lost. In such a situation, as shown in Fig. 5.4b, the imaginary part of the spectrum now contains a dispersive contribution.

Experimentally, since the echo forms at $t_2 = \tau$, rather than $t_2 = 0$, when $t_1 = 0$, it is necessary to apply a τ-dependent first-order phase correction equal to $\exp\{i\,\omega_2\,\tau\}$ [43]. If the echo forms at the centre of t_2, the application of this phase correction becomes considerably easier. As shown in Fig. 5.5 (next page), such a phase correction then corresponds to simply either shifting the time origin of the Fourier transform to the centre of the echo, or, in frequency domain, negating alternate data points [125].

The properties of whole echoes, therefore, mean that, even though the time-domain signal in Eq. (5.4) is phase-modulated with respect to t_1, as in the original experiment of Frydman and Harwood, a complex two-dimensional Fourier transform gives rise to pure absorption-mode lineshapes, provided the inhomogeneous broadening dominates the homogeneous broadening. Furthermore, the selection of phase modulation intrinsically yields sign discrimination in F_1. As an experimental example, Fig. 5.6 (on page 90) presents the real and imaginary parts of a ^{87}Rb free induction decay obtained for $RbNO_3$

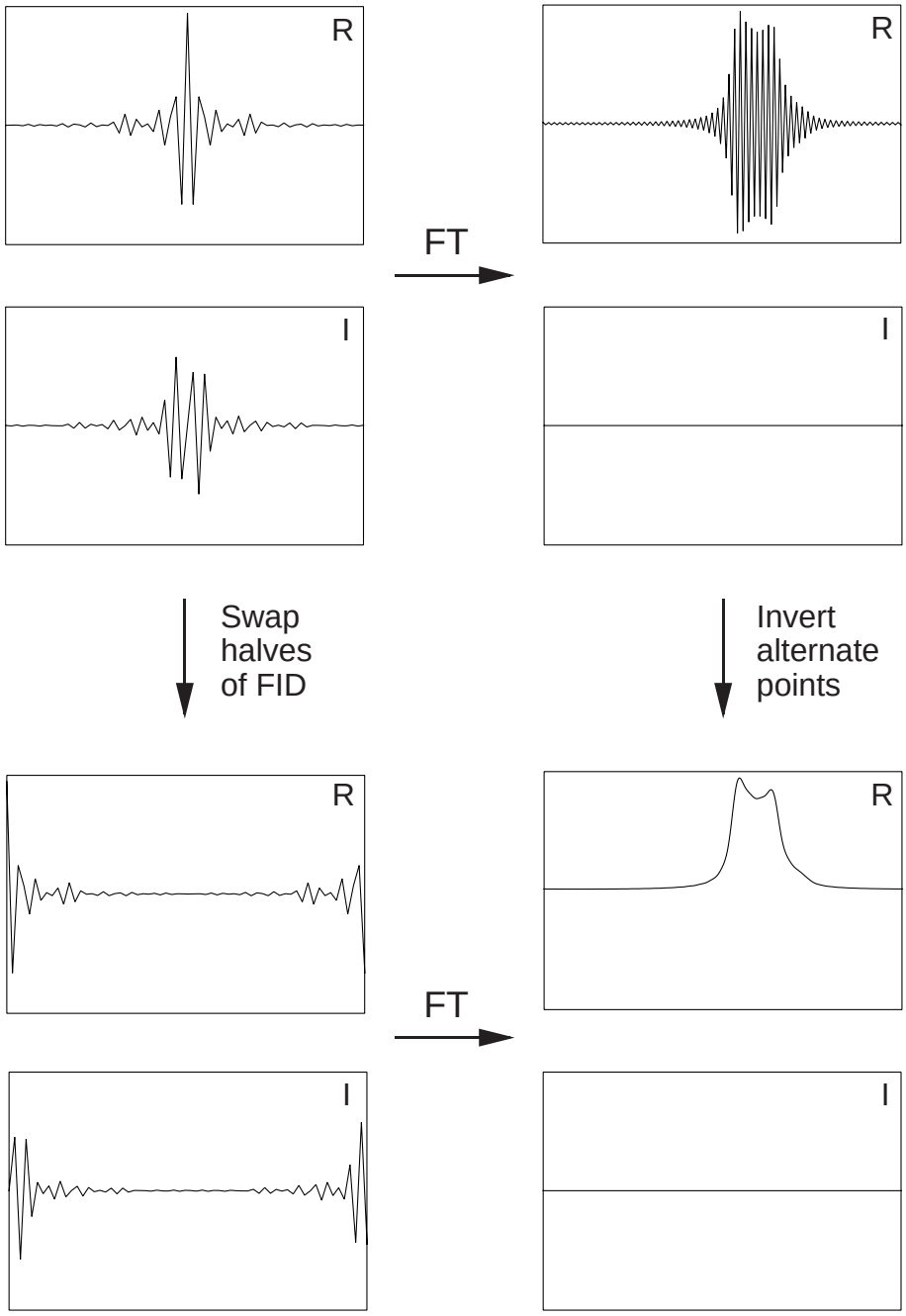

Figure 5.5. The Fourier transformation and processing of a simulated time-domain signal whose real (R) and imaginary (I) parts are, respectively, symmetric and anti-symmetric about the centre of t_2. The required τ-dependent first-order phase correction, $\exp\{i\omega_2\tau\}$, here simply corresponds to inverting the sign of alternate data points. The same result can be achieved by redefining the time origin of the Fourier transform to be the top of the echo.

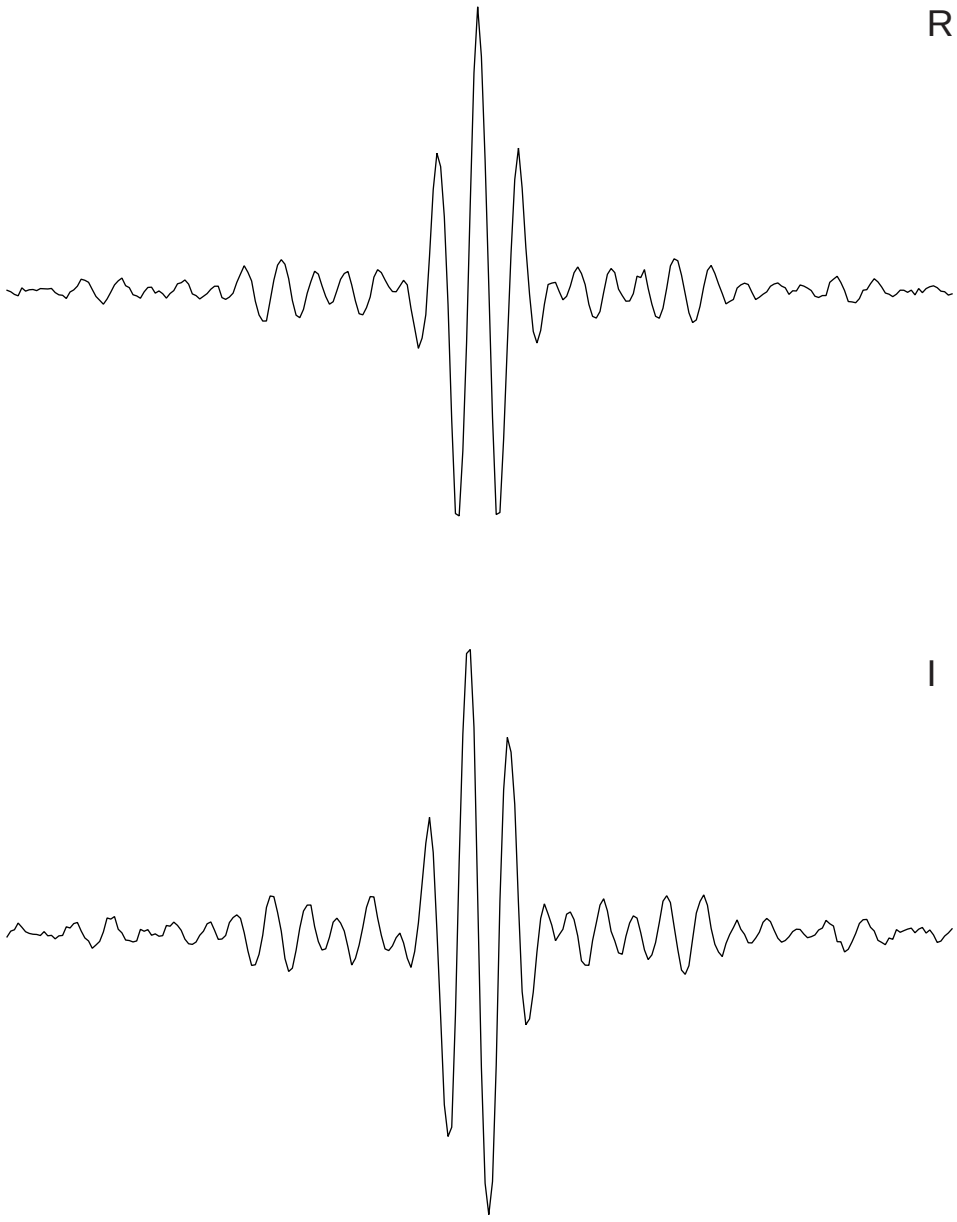

Figure 5.6. The real (R) and imaginary (I) parts of a ^{87}Rb free induction decay obtained for $RbNO_3$ using the shifted-antiecho experiment in Fig. 5.1b (dashed line) with $t_1 = 0$. A spin-echo interval, τ, of duration 4.4 ms was used and the total acquisition time displayed equals 8.7 ms. The displayed free induction decay corresponds to the first row of a two-dimensional data set, the frequency-domain spectrum of which is presented, along with all the experimental parameters, in Fig. 6.9c.

using the shifted-antiecho experiment in Fig. 5.1b (dashed line) with $t_1 = 0$. The spin-echo interval, τ, was chosen such that the fourth-rank inhomogeneous broadening was refocused at the centre of the acquisition period.

5.2.3 The Amplitude-Modulated Whole-Echo Experiment

Massiot *et al.* have also presented an amplitude-modulated whole-echo experiment [43], which is simply a combination of the shifted-echo and shifted-antiecho sequences of Fig. 5.1b. A schematic time-domain data set for the experiment is shown in Fig. 5.2f, with the contributions of the shifted-echo and shifted-antiecho pathways again being shown as solid and dashed lines respectively. As with the phase-modulated whole-echo experiment, pure absorption-mode lineshapes are only obtained when the inhomogeneous broadening dominates the homogeneous broadening. It should be noted that a genuinely amplitude-modulated signal only arises when the contributions of the shifted-echo and shifted-antiecho pathways are equal. However, as a consequence of the properties of whole echoes, a hypercomplex two-dimensional Fourier transform still gives rise to pure absorption-mode lineshapes even when the contributions of the two pathways are unequal. Sign discrimination must again be restored using the States-Haberkorn-Ruben or TPPI methods. An important further point to note is that it is necessary to use the much longer spin-echo interval required by the shifted-antiecho sequence.

5.3 Conversion of Triple- to Single-Quantum Coherence

An important part of all MQMAS experiments is the conversion of triple-quantum coherences into single-quantum coherences of the central transition. Consideration of the coherence transfer pathway diagrams in Fig. 5.1 shows that there are two different changes in coherence order, $|\Delta p|$, associated with this pulse, namely $|\Delta p| = 2$ and $|\Delta p| = 4$. It is, therefore, instructive to examine the flip angle dependence of the efficiency of the two different conversions. Figures 5.7a-c (overleaf) show such plots for different ratios of the quadrupolar frequency, ω_Q^{PAS}, to the nutation frequency of the pulse, ω_1.

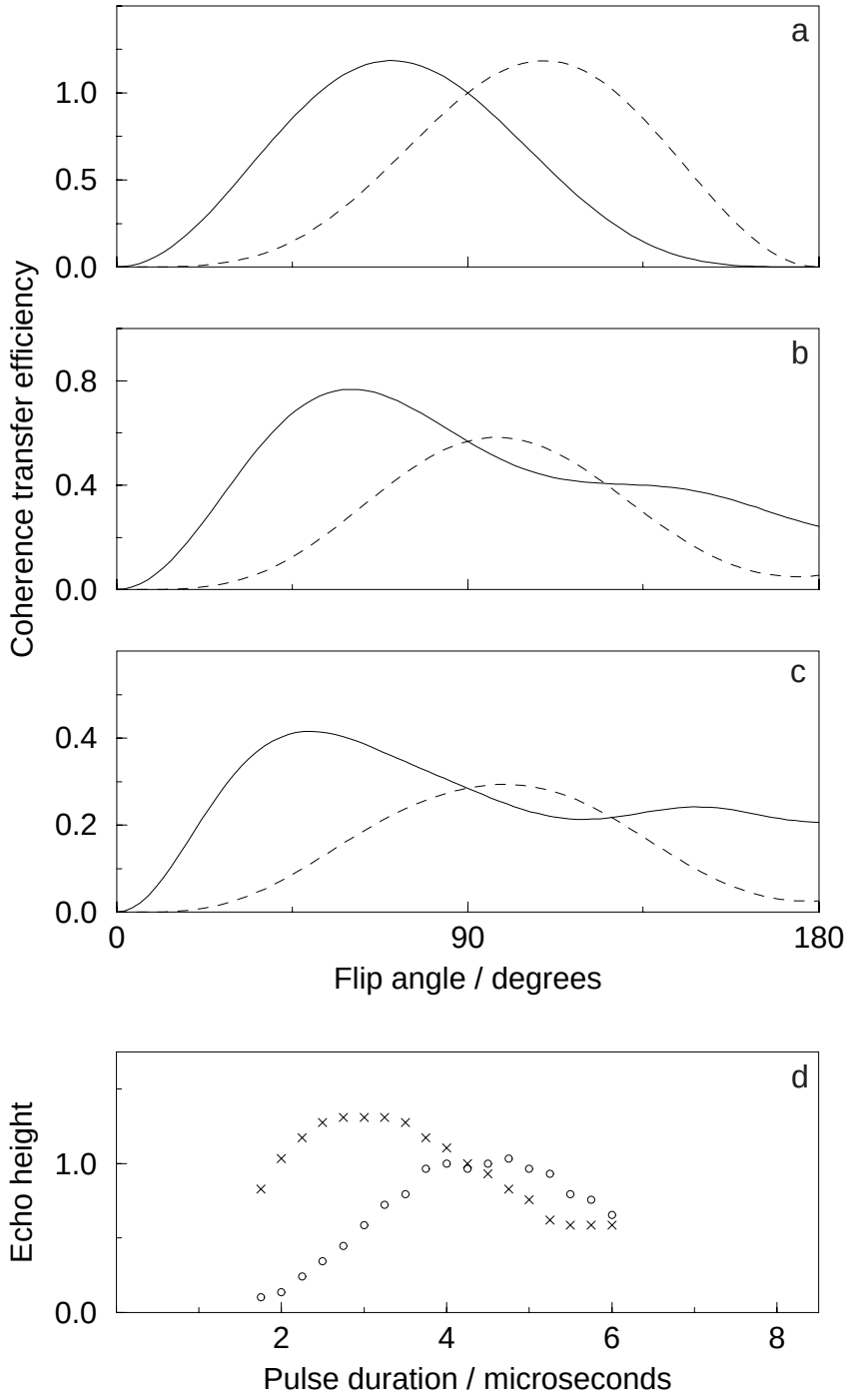

Figure 5.7. (a-c) Calculated efficiency of coherence transfer between coherence orders p = +3 and p = +1 (solid line) and p = –3 and p = +1 (dashed line) for a spin I = 3/2 nucleus over a range of values of the flip angle. The single-quantum coherences (p = ±1) are those of the central transition only. The ratio ω_Q^{PAS}/ω_1 is 0.0 in (a), 2.5 in (b), and 5.0 in (c). The efficiency of coherence transfer has been normalised such that it is equal to 1.0 for the intense ($\omega_1 >> \omega_Q^{PAS}$) 90° pulse in (a). The calculation assumes a powder distribution of crystallite orientations. (d) Experimental efficiency of coherence transfer between coherence orders p = +3 and p = +1 (crosses) and p = –3 and p = +1 (circles) over a range of pulse durations for ^{87}Rb NMR (98.2 MHz) of $RbNO_3$. The results were obtained by measuring the height of the echo for the shifted-antiecho and shifted-echo experiments in Fig. 5.1b, respectively. The vertical scale in (d) has been normalised such that it is equal to 1.0 where the two efficiencies are equal, corresponding to a 90° pulse.

From Fig. 5.7a, it is seen that, for a hard pulse, where $\omega_Q^{PAS}/\omega_1 \approx 0$, the two amplitudes are equal when the flip angle equals 90°; this is a familiar result from NMR of liquids [126]. Furthermore, in this limit, the maximum transfer intensities for the $|\Delta p| = 2$ and $|\Delta p| = 4$ pathways are the same, although that for $|\Delta p| = 2$ occurs at a lower flip angle (70.5°) than that for $|\Delta p| = 4$ (109.5°). An obvious, though significant, point is that the maximum coherence transfer intensities for the individual pathways are greater than the transfer intensity corresponding to the flip angle where the two conversions are equal.

As stated in Chapter 4, it is usually the case that ω_1, is significantly less than ω_Q^{PAS}; this is the situation shown in Figs. 5.7b and 5.7c, where ω_Q^{PAS}/ω_1 equals 2.5 and 5, respectively. The following important features are evident from these plots. Firstly, the two pathways are again equal when the flip angle equals 90° [41, 51]. Secondly, the maximum transfer intensity is now greater for the smaller coherence transfer change, $|\Delta p| = 2$, with this maximum occurring at a lower flip angle as before. It is should be noted, as discussed in Chapter 4, that the magnitude of the transfer intensity decreases as ω_Q^{PAS}/ω_1 increases.

For comparison, Fig. 5.7d presents ^{87}Rb experimental transfer intensities obtained, by measuring the signal in the shifted-echo and shifted-antiecho experiments, for a sample of $RbNO_3$. It is clear that the same features, as seen in the simulations, are observed. In particular, the $|\Delta p| = 2$ change is more efficient than the $|\Delta p| = 4$ change. (It should be noted that this plot is in fact a superposition of three curves, associated with the three cystallographically inequivalent Rb sites in the unit cell. There is, however, not much difference between the shapes of the individual curves, since the difference in ω_Q between the sites is small.) The results in Fig. 5.7d were obtained on the Bruker AC 300 spectrometer, equipped with only a 300 W radiofrequency amplifier, such that ω_Q^{PAS}/ω_1 ranged between 7.1 and 8.2 for the three sites (using the C_Q values given in Ref. [43]). Similar results have been obtained on the Bruker MSL 400 spectrometer, equipped with a 1 kW amplifier,

while analogous ^{23}Na NMR results for Na_2SO_4 have recently been presented in Ref. [51].

It was stated earlier that pure absorption-mode lineshapes are obtained in the simple amplitude-modulated experiment when the two pathways are combined with equal amplitude. An important question to ask is, what happens when the flip angle of the triple- to single-quantum coherence conversion pulse is such that the two pathways are not combined with equal amplitude? The effect of a complex two-dimensional Fourier transform on simulated data sets resulting from the separate echo and antiecho pathways of Fig. 5.1a was demonstrated in Figs. 5.3a and 5.3b. In the case where the two pathways add up with equal intensity in the simple amplitude-modulated experiment, the dispersive parts of the lineshapes cancel leaving a pure absorption-mode lineshape. This is demonstrated in Fig. 5.8a (overleaf).

Figures 5.8b and 5.8c show what happens when the spectra from the two pathways are not combined with equal amplitude. The ratios of the echo to antiecho pathways equal 0.7 and 2.5, respectively, and were chosen to correspond to those in the experimental spectra of Figs. 5.8e and 5.8f. From these contour plots, it is evident that the degree of dispersive character only becomes significant in Fig. 5.8c, where the ratio of the two pathways differs considerably from unity. Figures 5.8d-f show experimental ^{87}Rb MQMAS spectra of $RbNO_3$ obtained with the simple amplitude-modulated experiment in Fig. 5.1a, where the flip angle of the $p = \pm 3$ to $p = -1$ conversion pulse is varied. The spectra were recorded at the same time as the results in Fig. 5.7d, and the ratio of the two pathways, $|\Delta p| = 2$ to $|\Delta p| = 4$, can be read off from Fig. 5.7d, namely (d) 1 at 4.25 μs, (e) 0.7 at 5.25 μs, and (f) 2.5 at 2.75 μs. As in the simulations, there is only evidence of significant dispersive character in (f), where the ratio differs most from unity.

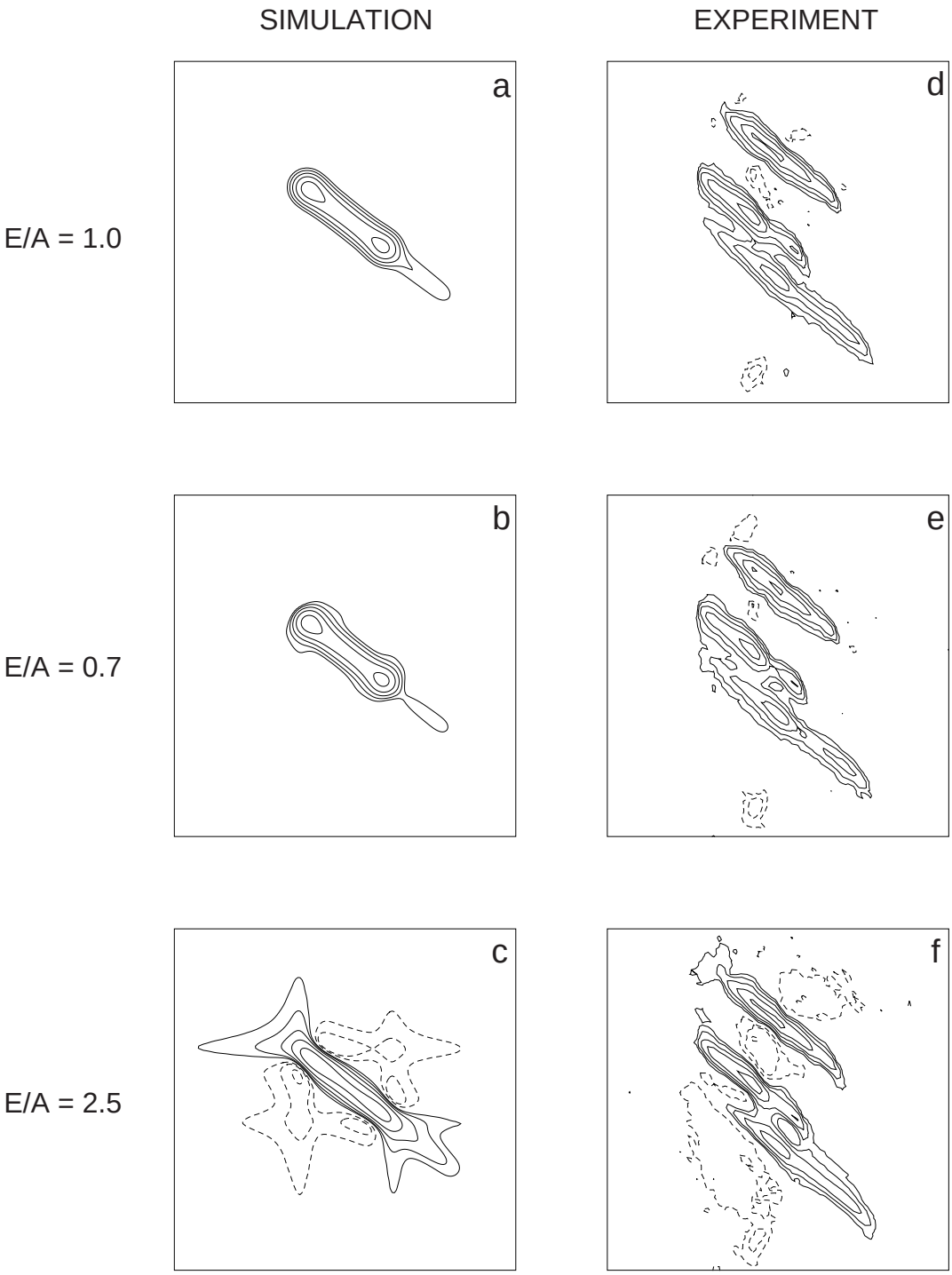

Fig. 5.8. Contour plots of simulated (a-c) and experimental (d-f) spectra obtained with the simple amplitude-modulated experiment in Fig. 5.1a, where the echo and antiecho pathways are combined with different amplitudes. The ratio of the two pathways is denoted E/A and is indicated in the figure. The contour plots in (d-f) show 6 ∞ 6 kHz regions of ^{87}Rb (98.2 MHz) MQMAS spectra of $RbNO_3$. The full F_1 and F_2 spectral widths were 40 and 25 kHz, respectively, 192 transients (consisting of 512 points each) were averaged for each of 192 increments of t_1, and the relaxation interval was 100 ms. The duration of the triple-quantum excitation pulse was 8.5 μs. The duration of the p = ±3 to p = –1 reconversion pulse was 4.3, 5.3, and 2.8 μs in (d), (e) and (f), respectively.

5.4 Spin I = 5/2 Nuclei

For spin I = 5/2 nuclei, quintuple-quantum as well as triple-quantum coherence can be correlated with single-quantum coherence in an MQMAS experiment. However, for clarity, the discussion in this and the next chapter is restricted to the triple-quantum case, with the quintuple-quantum experiment not being considered until Chapter 7. Considering the triple-quantum case, it was stated earlier that the MQMAS ratio for spin I = 5/2 equals 19/12. The difference in sign to that for spin I = 3/2 (MQMAS ratio equals –7/9) means that the echo pathway now corresponds to the correlation of triple- and single-quantum coherences of opposite sign. The solid and dashed lines in Fig. 5.1 therefore now correspond to the antiecho and echo pathways, respectively. Furthermore, the echo now forms at $t_2 = (19/12)\, t_1$, and the inhomogeneously-broadened ridges have a gradient equal to 19/12.

For spin I = 3/2, as illustrated in Fig. 5.9a (overleaf), the coherence transfer amplitudes for the p = +3 to p = –1 and the p = –3 to p = –1 steps are the same, for all values of ω_Q/ω_1, if a pulse with a flip angle of 90° is used. However, for spin I = 5/2, there is no flip angle where the p = ±3 to p = –1 amplitudes are the same for all values of ω_Q/ω_1. The difference between the two transitions is minimised for a 60° pulse. This case is illustrated in Fig. 5.9b. When this flip angle is used in the simple amplitude-modulated experiment, apparently pure absorption-mode lineshapes are often observed.

However, in some of the first published MQMAS spectra obtained using the simple amplitude-modulated experiment in Fig. 5.1a [52, 59], the mixed-phase character of the lineshapes is evident. As an example, Fig. 5.10a (on page 98) presents a ^{27}Al MQMAS spectrum of γ-alumina, obtained using the simple amplitude-modulated experiment. While the narrow ridge (bottom left-hand corner), corresponding to the tetrahedral site, is apparently pure absorption-mode, the lineshapes (both the central peak and the spinning sidebands in F_1)

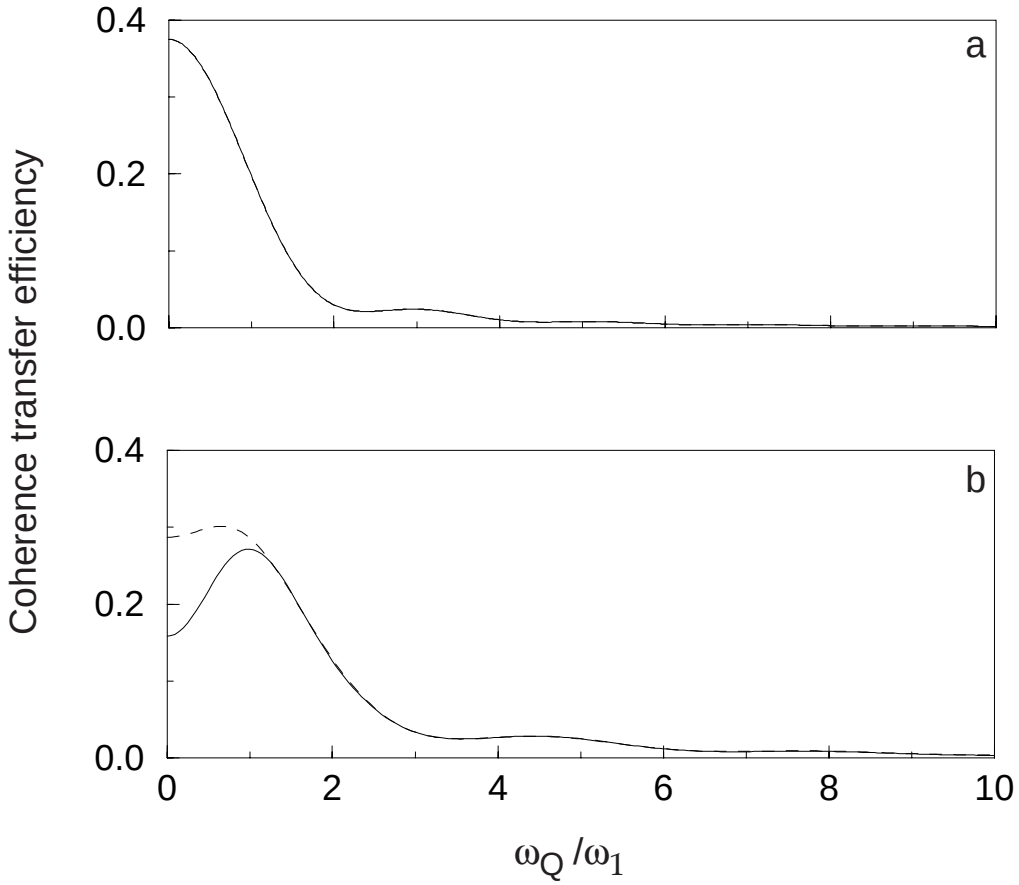

Figure 5.9. Plots comparing the efficiency of coherence transfer as a function of ω_Q/ω_1 between coherence orders p = –3 and p = –1 (solid line) and p = +3 and p = –1 (dashed line) for (a) spin I = 3/2 nuclei and (b) spin I = 5/2 nuclei. The single-quantum coherences (p = ±1) are those of the central transition only. It should be noted that the two curves are superimposed in (a). In each case, the optimised flip angle is used such that the difference between the two transitions is minimised, namely 90° in (a) and 60° in (b). The vertical scale gives the normalised coherence transfer amplitudes calculated for the relevant states expressed in a single-element operator basis.

corresponding to the octahedral site, where the homogeneous broadening is significant compared to the inhomogeneous broadening, are clearly mixed-phase.

In response to this problem, Amoureux *et al.* have recently presented an experiment in which, as shown in Fig. 5.11 (on page 99), the p = ±3 coherences are converted to p = –1 coherences via a population state, p = 0 [49, 61]. The symmetry of such a *z*-filtered [127] experiment means that the two pathways always combine with equal amplitude. The success of this *z*-filtered simple

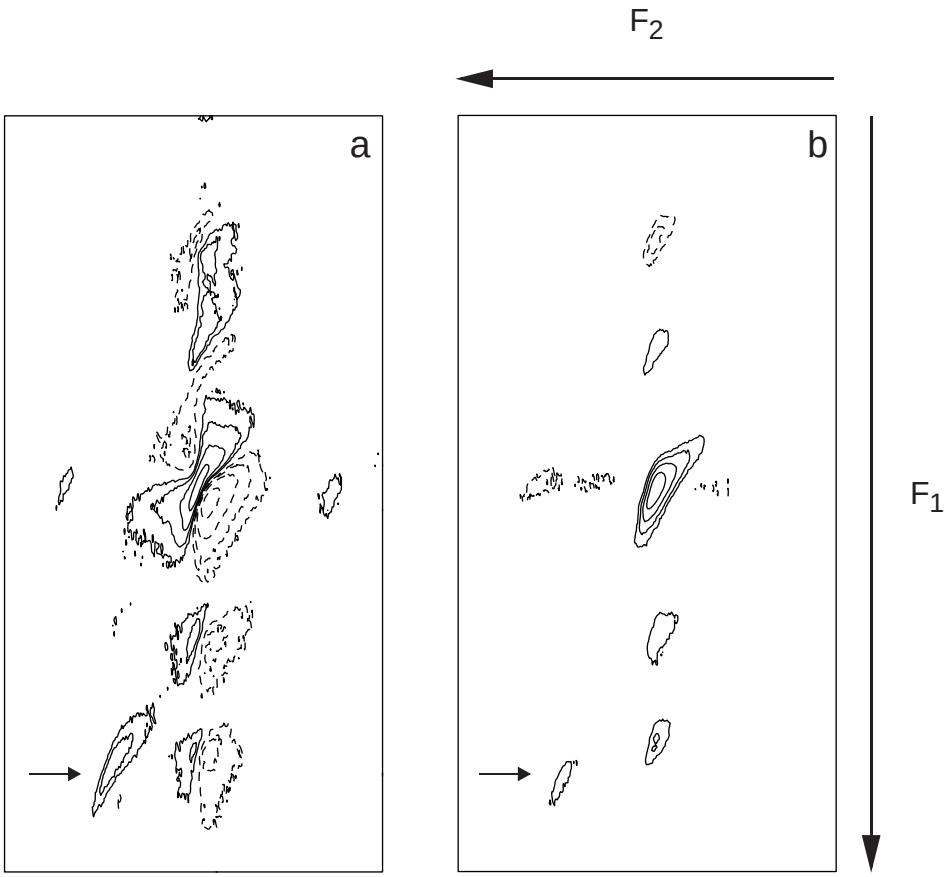

Figure 5.10. Contour plots of experimental ^{27}Al (104.3 MHz) MQMAS spectra of a sample of γ-alumina (BDH), obtained with (a) the simple amplitude-modulated experiment in Fig. 5.1a and (b) the *z*-filtered simple amplitude-modulated experiment in Fig. 5.10. (These spectra were recorded in collaboration with Sharon Ashbrook [93].) Two Al environments can be distinguished, namely an octahedral site (the centre of the spectrum, with spinning sidebands either side in both F_1 and F_2) and a tetrahedral site (indicated by an arrow). It is clear that pure absorption-mode lineshapes are only obtained for both sites in (b). In both cases, the displayed F_1 and F_2 spectral widths are 50 kHz (cut down from 100 kHz) and 25 kHz, respectively. The following experimental parameters were used: 168 transients (consisting of 512 points each) were averaged for each of 256 increments of t_1, the relaxation interval was 1 s, and the spinning speed was 8.9 kHz. The duration of the triple-quantum excitation pulse was 3 μs. The duration of the $p = \pm 3$ to $p = -1$ reconversion pulse in (a), and the $p = \pm 3$ to $p = 0$ pulse in (b) were of duration 1.5 μs and 1 μs, respectively. The duration of the $p = 0$ to $p = -1$ pulse in (b), selective for the central transition, was 45 μs, with the nutation frequency, $\omega_1/2\pi$, being reduced to 3 kHz. In both experiments, sign discrimination was restored using the TPPI method of incrementing the phase of the first pulse by 30° for each increment of t_1. The bottom contour in both spectra corresponds to 8% of the maximum height. The observed spinning sideband patterns in F_1 are discussed in Appendix I.

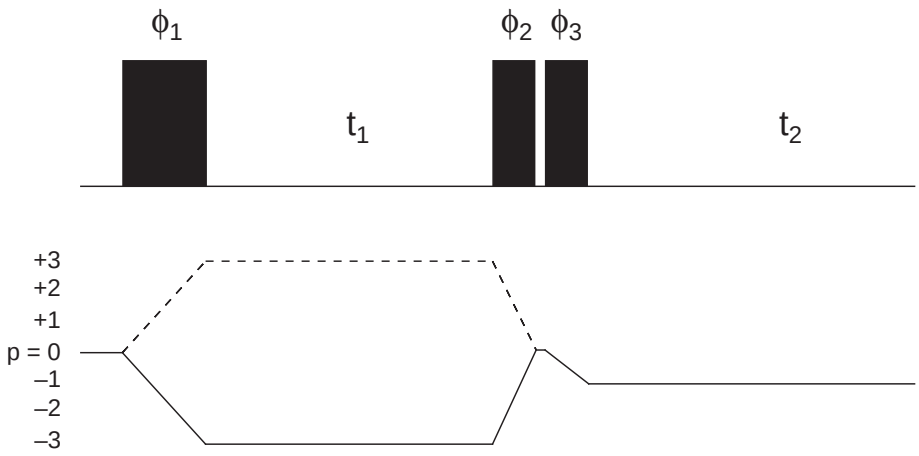

Figure 5.11. Pulse sequence and coherence transfer pathway diagram for the *z*-filtered simple amplitude-modulated experiment. The symmetry of the experiment ensures that the echo and antiecho pathways are combined with equal amplitude. The optimum flip angles for the individual pulses are described in the text. The interval between the second and third pulses is of negligible duration (~ 3 μs). A phase cycling scheme for the pulse phases ϕ_1, ϕ_2 and ϕ_3 and for the receiver R_X is given in Table H1 of Appendix H.

amplitude-modulated experiment with regards to obtaining pure absorption-mode lineshapes is clearly demonstrated in Fig. 5.10b. Furthermore, it should be noted that the experiment is equally applicable in the spin I = 3/2 case, where it avoids the necessity for the careful calibration of the flip angle of the conversion pulse.

At first sight, it would be thought that the optimum flip angles for the p = 0 to p = ±3 and p = ±3 to p = 0 conversions in Fig. 5.11 would be the same. However, Eq. (4.21) showed that, for spin I = 3/2, a weak pulse only converts triple-quantum coherence into a population difference across the outer energy levels, rather than across the central transition as required. Therefore, a strong pulse is required. An analogous result is obtained for spin I = 5/2, and, in both cases, it is found that the optimum flip angle for the p = ±3 to p = 0 conversion is 60°. Additionally, the sensitivity of the experiment is improved if ω_1 is reduced for the final pulse (p = 0 to p = –1), such that it is selective for the central transition.

5.5 Signal-to-Noise Considerations

When choosing which experiment to perform, a vital question to ask is, which experiment yields the best signal-to-noise ratio (henceforth denoted S/N)? The final section of this chapter, therefore, examines the relative S/N of the three basic experiments presented in Section 5.2. The discussion here is restricted to a qualitative comparison, with quantitative results being given in the next chapter. Schematic representations of time-domain data sets for the simple amplitude-modulated experiment, the shifted-echo experiment, and the amplitude-modulated whole-echo experiment are given in Figs. 5.2e, 5.2c and 5.2f, respectively. Initially, an idealised situation will be considered where, firstly, there is no signal loss associated with the spin echo, and, secondly, the contributions of the echo and antiecho pathways are equal and the same in each of the experiments. When these simplifications are made, comparing the S/N of the three different experiments is relatively straightforward.

Examining first the amplitude-modulated whole-echo data set in Fig. 5.2f, it is evident that the time-domain signal is symmetric about the centre of t_2, with each mirror image being identical to that of the simple amplitude-modulated data set in Fig. 5.2e. Therefore, the signal in Fig. 5.2f is double that in Fig. 5.2e. However, the noise is $\sqrt{2}$ greater, since the acquisition time in Fig. 5.2f is double that in Fig. 5.2e, and, hence, there is only a $\sqrt{2}$ improvement in S/N between the two experiments.

Furthermore, when the contribution of the two pathways in the amplitude-modulated whole-echo experiment is equal, the imaginary part, after performing the Fourier transform in the t_2 dimension, only contains noise, and can therefore be deleted and zero-filled. In contrast, in the phase-modulated whole-echo experiment, the imaginary part contains signal and cannot be deleted. There is, therefore, $\sqrt{2}$ less noise in the frequency-domain for the amplitude-modulated whole-echo experiment. There is no difference in the height of the individual peaks, and, thus, the amplitude-

modulated whole-echo experiment offers a √2 improvement in S/N over the phase-modulated whole-echo experiment. Thus, for these idealised data sets, the relative S/N of the three experiments is in the ratio of 1:1:√2 for the simple amplitude-modulated, the phase-modulated whole-echo, and the amplitude-modulated whole-echo experiments, respectively.

Unsurprisingly, in practice, the situation is significantly more complicated than that discussed above for an idealised case. Firstly, there will, of course, be signal loss associated with the spin echo as a consequence of transverse relaxation. Furthermore, if the pulse which inverts the central transition is not perfectly selective, additional signal will be lost. Clearly, these features will tend to degrade the S/N of the two whole-echo experiments in Fig. 5.1b relative to the simple amplitude-modulated experiment in Fig. 5.1a. In addition, to record the shifted-antiecho signal in the amplitude-modulated whole-echo experiment, it is necessary to use a much longer spin-echo interval than in the phase-modulated experiment. More signal is, hence, lost through relaxation, and the √2 difference in S/N between the two experiments is significantly reduced.

A second important consideration is the relative contribution of the echo and antiecho pathways. For the idealised data sets discussed above, the contribution of the two pathways was assumed to be equal and the same in all data sets. However, Fig. 5.7 showed that the maximum coherence transfer amplitudes for the individual $|\Delta p| = 2$ or $|\Delta p| = 4$ steps are greater than the transfer amplitude when the two steps are equal. This has the consequence that the optimum flip angle for the triple- to single-quantum coherence conversion pulse differs between the three experiments and, hence, the S/N of the single-pathway, phase-modulated whole-echo experiments improve relative to the other two.

From the representations of the time-domain data sets in Fig. 5.2, it is evident that significant amounts of the acquisition time are spent recording only noise. In

order to achieve the optimum sensitivity, the application of time-domain filters, whose position changes as a function of t_1, has been proposed [38, 43]. In both the simple amplitude-modulated and amplitude-modulated whole-echo experiments, the proportion of the acquisition time occupied by signal increases as t_1 increases. For example, in Fig. 5.2e, at $t_1 = 0$, a half echo forms in t_2, while at larger t_1, a whole echo forms. In contrast, in the phase-modulated whole-echo experiments, a whole echo of the same length is formed for all values of t_1. The consequence of this is that a greater amount of noise can be filtered out in the phase-modulated whole-echo experiments, hence increasing their S/N relative to that of the other two experiments.

Chapter 6

The Split-t_1 Approach

6.1 Shearing

In Chapter 5, it was simply stated and shown that the inhomogeneous quadrupolar broadening is spread out along a ridge, the gradient of which depends on the MQMAS ratio. Usually, the purpose of performing an MQMAS experiment is to obtain, firstly, a spectrum displaying only isotropic shifts (both chemical and second-order quadrupolar in origin), and secondly, the second-order quadrupolar-broadened one-dimensional spectra corresponding to the resolved sites. To achieve this, it is necessary to perform a shearing transformation such that the ridges appear parallel to the F_2 axis. To avoid interpolation problems, it is preferable to perform the shearing transformation in the mixed frequency-time domain, $S(t_1, \omega_2)$. Grandinetti *et al.* [38] have shown that this shearing transformation corresponds to the application of the following t_1-dependent first-order phase correction [83]:

$$S'(t_1', \omega_2') = \exp\{ - i G \omega_2 t_1 \} S(t_1, \omega_2) , \qquad (6.1)$$

where G denotes the gradient of the ridge in the frequency domain, which equals plus or minus the MQMAS ratio, depending on the sign of the multiple-quantum coherence which evolves during t_1. As discussed in Refs. [43, 53], shearing the data set reduces the spectral width in F_1 by a factor, using the notation of Table 3.1, of $|C^I_{1/2}|/(|C^I_{1/2}| + |C^I_{3/2}|)$, *i.e.*, 9/16 and 12/31 for spin I = 3/2 and I = 5/2 (triple-quantum), respectively.

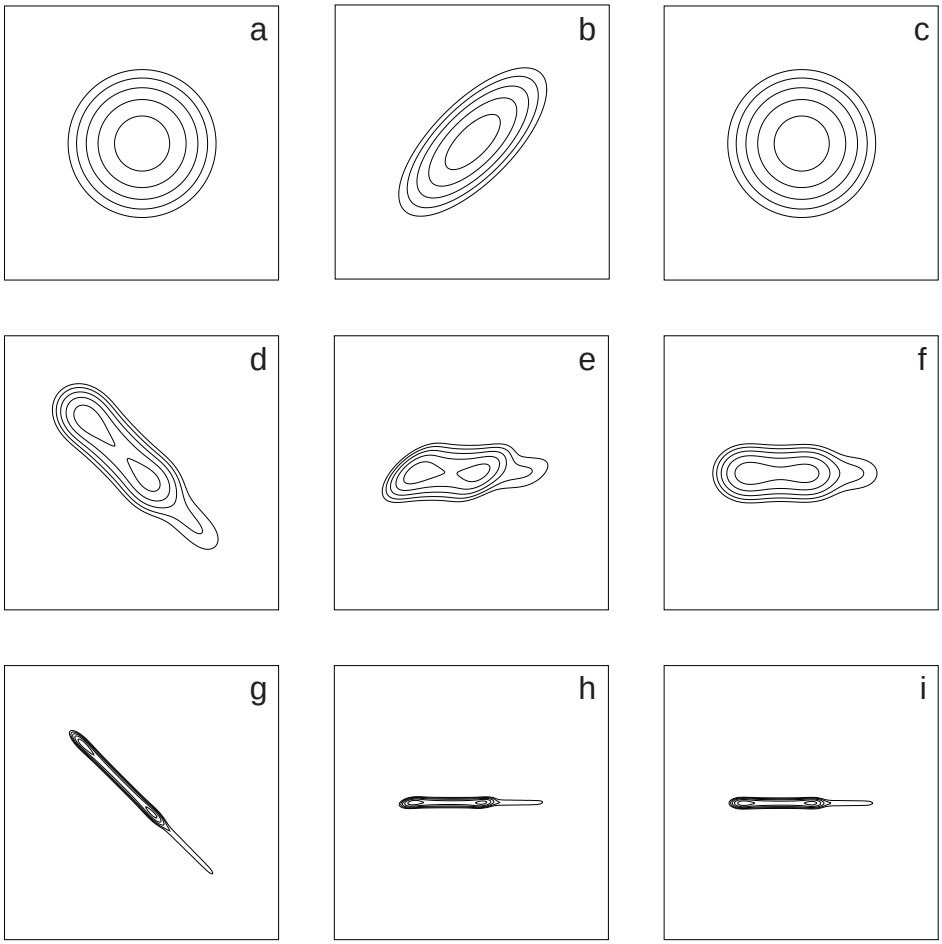

Figure 6.1. Contour plots showing how the ratio of the inhomogeneous to homogeneous broadening affects the degree of distortion associated with shearing. In (a-c), there is no inhomogeneous broadening, while in (d-f) and (g-i) significant inhomogeneous broadening is present, with the ratio taking its largest value in (g-i). In (d) and (g), two-dimensional Gaussian lineshapes are summed along the diagonal $F_1 = -F_2$, such that the projection onto an axis parallel to the ridge is a typical second-order quadrupolar-broadened spectrum. The middle column, (b, e, h), shows the effect of performing a shearing transformation on the lineshapes in (a, d, g). For comparison, the right-hand column, (c, f, i), illustrates the case where the same Gaussian lineshapes are summed parallel to the F_2 axis.

Shearing, however, is not a perfect solution, even if carried out in the $S(t_1, \omega_2)$ domain. Although it must be stressed that shearing does not affect the isotropic projection, it can cause distortions in the two-dimensional lineshapes. Figure 6.1 shows how the ratio of the inhomogeneous to homogeneous broadening affects the degree of distortion associated with shearing. The top row of Fig. 6.1 illustrates the case where there is no inhomogeneous broadening, and Fig. 6.1a is simply a plot of a two-dimensional pure absorption-mode Gaussian lineshape. Figures 6.1d and 6.1g

correspond to a summation of Gaussian lineshapes along the diagonal $F_1 = -F_2$, such that the projection onto an axis parallel to the ridge is a typical second-order quadrupolar-broadened spectrum. The ratio of the inhomogeneous to homogeneous broadening is greater in Fig. 6.1g, and the ridge is seen to be considerably narrower.

Figures 6.1b, 6.1e and 6.1h show the effect of performing a shearing transformation on the frequency-domain data sets of Figs. 6.1a, 6.1d and 6.1g, respectively. For comparison, Figs. 6.1c, 6.1f and 6.1i illustrate the case where the same Gaussian lineshapes add up parallel to the F_2 axis. It is clear that the degree of distortion associated with shearing decreases as the ratio of the inhomogeneous to homogeneous broadening increases. A frequency-domain shearing transformation was used in Figs. 6.1b, 6.1e and 6.1h but, for the special case of a 1:1 ridge (*i.e.*, one along $F_1 = \pm F_2$), there are no interpolation problems associated with this method. Exactly the same result would have been obtained if the shearing had been performed in the mixed frequency-time domain using Eq. (6.1). Analytical expressions supporting the above conclusions have been derived, and are presented in Appendix F.

The undesirable effects associated with shearing are further demonstrated by the experimental ^{23}Na MQMAS spectra in Fig. 6.2 (overleaf). Figure 6.2a shows an unsheared spectrum, displaying two of the three crystallographically inequivalent sites in Na_2HPO_4, obtained with the simple amplitude-modulated experiment in Fig. 5.1a. Two ridges are seen in the centre of the spectrum with spinning sidebands either side, the ratio of the inhomogeneous to homogeneous broadening being greater for the lower ridge. The spectrum in Fig. 6.2b corresponds to the same experimental data set as in Fig. 6.2a, except that, as described above, a shearing transformation has been performed in the $S(t_1, \omega_2)$ domain, such that the ridges now lie parallel to the F_2 axis. It is clear that the broader ridge, in particular, has been distorted by the shearing transformation (although this would not affect the isotropic

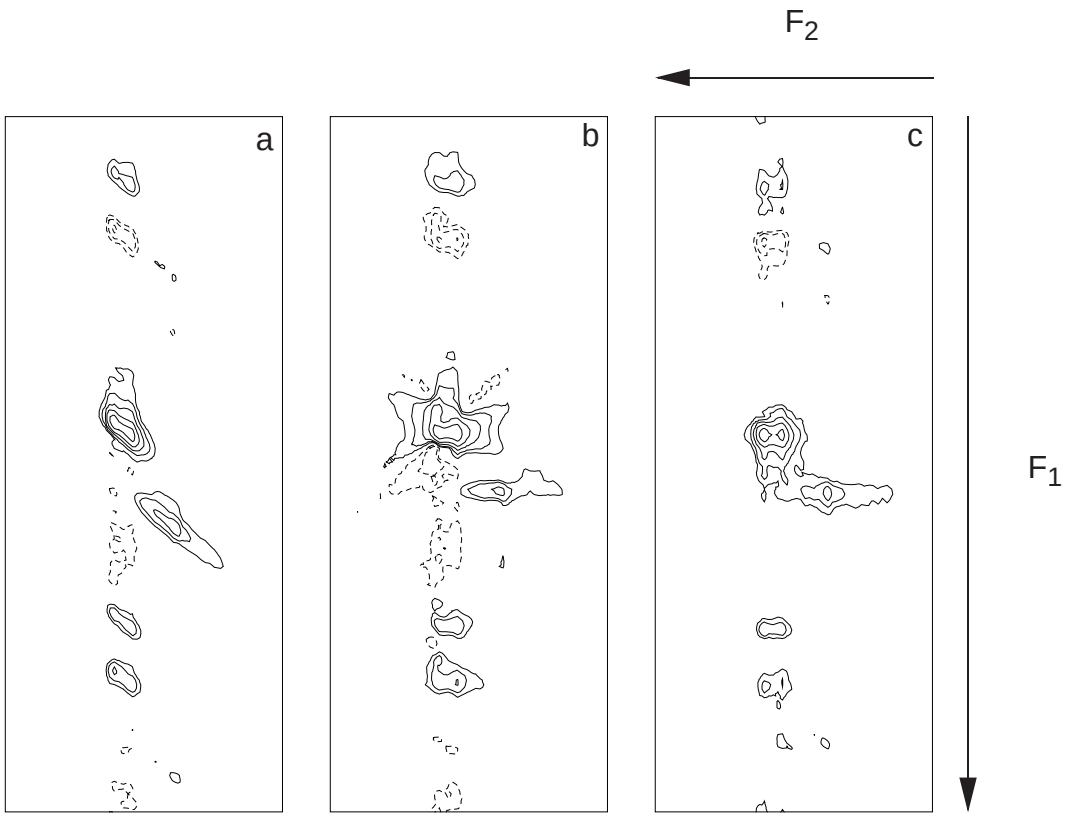

Figure 6.2. Contour plots taken from ^{23}Na (105.8 MHz) MQMAS spectra of Na_2HPO_4 (Aldrich) obtained with, (a) and (b), the simple amplitude-modulated experiment in Fig. 5.1a and, (c), the amplitude-modulated split-t_1 experiment in Fig. 6.3a. In (a), the displayed F_1 and F_2 spectral widths are 15 and 6 kHz, respectively. The spectrum in (b) is the result of applying a shearing transformation in the $S(t_1, \omega_2)$ domain, as described in the text, to the data set in (a). The shearing transformation reduces the F_1 spectral width by 9/16, such that the displayed F_1 spectral width is 8.4 kHz in (b). For comparison, the displayed F_1 and F_2 spectral widths in (c) are 8.4 and 6 kHz, respectively. It was not necessary to apply a shearing transformation in (c). Experimental conditions as similar as possible were used for the two experiments: the full F_2 spectral width was 25 kHz, 192 transients (consisting of 512 points each) were averaged for each of 128 increments of t_1, the relaxation interval was 1 s, and the spinning speed was 5.3 kHz. The duration of the triple-quantum excitation pulse was 8.0 μs. Sign discrimination was restored using the TPPI method of incrementing the phase of the first pulse by 30° for each increment of t_1. The full F_1 spectral width equalled 25 and 14.1 kHz in (a) and (c), respectively. The duration of the $p = \pm 3$ to $p = -1$ reconversion pulse in (a) was 3 μs, while that of the $p = +3$ to $p = +1$ and $p = -3$ to $p = -1$ conversion pulse in (c) was 1.5 μs. The first and second pulses in the *z* filter in (c) had duration 1 μs and 20 μs respectively, with the nutation frequency, $\omega_1/2\pi$, being reduced to 6 kHz for the latter pulse. The observed spinning sideband patterns in F_1 are discussed in Appendix I.

projection). The spectrum in Fig. 6.2c corresponds to an experiment described in the following section, where undistorted ridge lineshapes appear parallel to the F_2 axis.

6.2 Refocusing the Anisotropic Quadrupolar Broadening in t_1

The previous section showed that shearing can cause unwanted distortions in two-dimensional lineshapes. Although an undistorted spectrum showing isotropic shifts (the projection onto the F_1 axis after shearing) can still be obtained, problems occur when F_2 cross sections through the two-dimensional spectrum are used to extract the parameters C_Q and η, especially when lineshapes overlap. This section therefore describes modified amplitude- and phase-modulated experiments where the ridges appear parallel to the F_2 axis without the need for a shearing transformation. As shown in Figs. 6.1c, 6.1f and 6.1i, this yields two-dimensional lineshapes that are completely free of distortion. Again, for clarity, the discussion is first restricted to spin I = 3/2 nuclei, with spin I = 5/2 nuclei being considered in Section 6.4.

The key feature of all MQMAS experiments is the refocusing of the fourth-rank anisotropic broadening when the ratio of the durations of the single- and multiple-quantum evolution periods equals the magnitude of the MQMAS ratio. In all of the experiments introduced so far, this refocusing has occurred within the t_2 period. If, however, the t_1 period is split into single- and multiple-quantum evolution periods in the ratio of the MQMAS ratio, the fourth-rank anisotropic broadening is refocused at the end of the t_1 period, for all values of t_1. This refocusing of the quadrupolar broadening at $t_2 = 0$ means that undistorted inhomogeneously-broadened ridges appear parallel to the F_2 axis without the need for a shearing transformation. Furthermore, as discussed later, the fact that the signal always appears at the same position in t_2 has important advantages, in particular with regards to achieving the optimum sensitivity. The partition of t_1 into two separate evolution periods means that experiments based on this approach are collectively referred to as split-t_1 experiments.

6.2.1 Amplitude-Modulated Split-t_1 Experiments

Figure 6.3 shows the pulse sequences and coherence transfer pathway diagrams for two amplitude-modulated experiments where the t_1 period can be seen to be split into single- and triple-quantum evolution periods in the ratio of the MQMAS ratio. A schematic representation of a time-domain data set resulting from such amplitude-modulated split-t_1 experiments is presented in Fig. 6.4a, from which

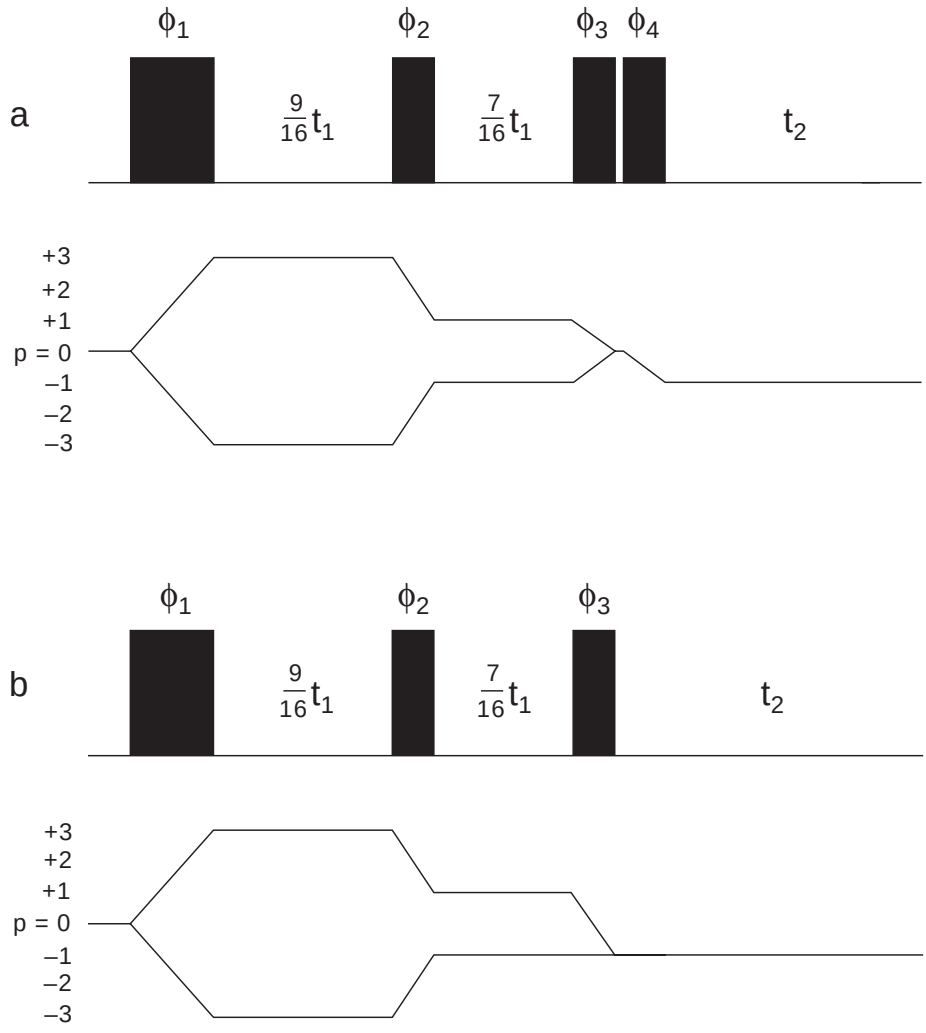

Figure 6.3. Pulse sequences and coherence transfer pathway diagrams for two amplitude-modulated split-t_1 experiments (for spin I = 3/2 nuclei). The experiment in (a) uses a *z* filter at the end of the evolution period, t_1, while that in (b) uses a single pulse to transfer the two mirror image pathways into observable coherence. The evolution period is split between single- and triple-quantum evolution according to the MQMAS ratio as indicated. The optimum flip angles for the individual pulses are described in the text. The interval between the third and fourth pulses in (a) is of negligible duration (~ 3 μs). Phase cycling schemes for the pulse phases ϕ_1, ϕ_2, ϕ_3 and ϕ_4 and for the receiver R_x are given in Table H3 of Appendix H.

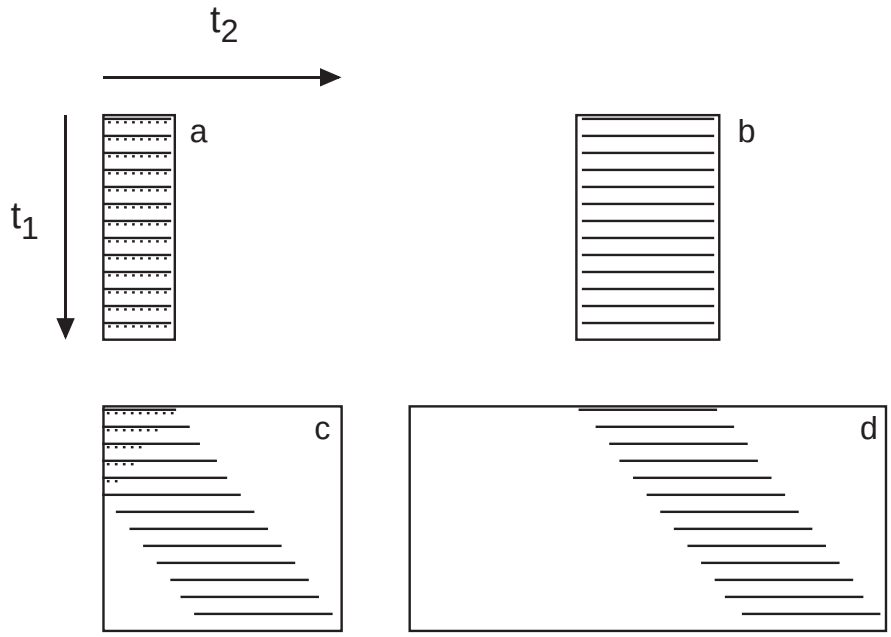

Figure 6.4. Schematic representations of the spin I = 3/2 time-domain signal obtained with the (a) amplitude-modulated split-t_1, (b) phase-modulated split-t_1, (c) simple amplitude-modulated, and (d) shifted-echo experiments. In (a) and (c), the contributions of the echo and antiecho pathways are shown as solid and dotted lines, respectively.

it is clear, as stated above, that the signal appears at the same position in t_2, for all values of t_1. For comparison, Fig. 6.4c presents the time-domain representation for the simple amplitude-modulated experiment (repeated from Fig. 5.2e). As with the simple amplitude-modulated experiment, sign discrimination in F_1 can again be restored in the amplitude-modulated split-t_1 experiments by using the States-Haberkorn-Ruben or TPPI methods.

To obtain genuinely pure absorption-mode lineshapes, it is necessary that the two mirror-image coherence transfer pathways combine with equal amplitude. This can be achieved most reliably, for all pulse powers, using a *z* filter, as shown in Fig. 6.3a. The flip angles of the two pulses of the *z* filter should be set equal to 45° pulses (*i.e.*, for optimum sensitivity, they should be fully selective ($\omega_1 << \omega_Q$) 90° pulses on the central transition). Figure 6.2c presents an experimental ^{23}Na spectrum of Na_2HPO_4 for this experiment. It can be seen that, unlike in Fig. 6.2b, undistorted ridges, lying parallel to the F_2 axis, are obtained. It should be noted that the data sets

leading to the spectra in Fig. 6.2 were recorded using experimental conditions that were as similar as possible. In particular, although the full spectral width in F_1 equals 25 and 14.0625 kHz, respectively, for Figs. 6.2a and 6.2c, shearing reduces the spectral width by 9/16 and, therefore, the F_1 spectral widths are the same in Figs. 6.2b and 6.2c. This is unsurprising since the triple-quantum evolution period is incremented by the same amount and the echo forms at the same time in both experiments.

The *z*-filtered split-t_1 experiment in Fig. 6.3a requires two pulses more than the simple amplitude-modulated experiment in Fig. 5.1a and, if these pulses cannot be fully optimised, this will result in reduced sensitivity. An alternative is to use a single pulse to convert between p = ±1 and p = –1 coherences, as shown in Fig. 6.3b. It was shown in Fig. 5.9a, for the simple amplitude-modulated experiment, that the coefficients of the p = +3 to p = –1 and p = –3 to p = –1 coherence transfer steps are the same, for all values of ω_Q/ω_1, if a 90° pulse is used. Unfortunately, for the split-t_1 experiment in Fig. 6.3b, as with the spin I = 5/2 p = ±3 to p = –1 case, there is no single flip angle where the coefficients of the p = +1 to p = –1 and p = –1 to p = –1 coherence transfer steps are the same for all values of ω_Q/ω_1. However, as shown in Fig. 6.5 (overleaf), when the flip angle is 45° the difference between the two transfer coefficients is small. It should be noted that, as the magnitude of ω_Q/ω_1 increases, the two curves converge and that the efficiency of coherence transfer increases. Clearly, the optimum pulse for this coherence transfer step, therefore, is a 45° pulse with $\omega_1 << \omega_Q$, *i.e.*, a fully selective 90° pulse on the central transition.

Figure 6.6 (on page 112) presents ^{23}Na MQMAS spectra of a mixture of Na_2SO_4 and $Na_2C_2O_4$ obtained with the simple amplitude-modulated experiment in Fig. 5.1a and the amplitude-modulated split-t_1 experiment in Fig. 6.3b. Experimental conditions as similar as possible were again used, although, as discussed above, the duration of the pulse which combines the two pathways equalled 3.7 and 1.9 μs (equivalent to 90° and 45° flip angles) in Fig. 6.6a and Fig. 6.6c, respectively. As

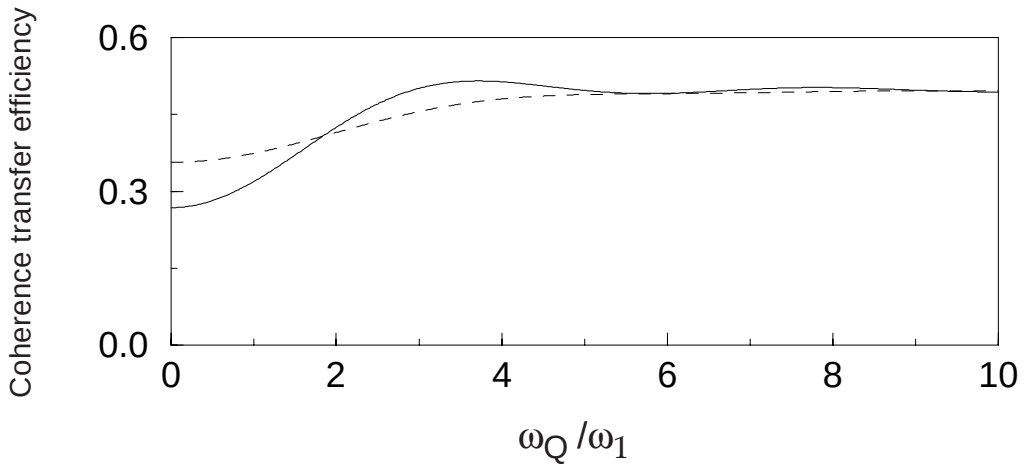

Figure 6.5. A comparison (for spin I = 3/2 nuclei) of the efficiency of coherence transfer as a function of ω_Q/ω_1 between coherence orders p = –1 and p = –1 (solid line) and p = +1 and p = –1 (dashed line) of the central transition. The optimised flip angle, 45°, is used such that the difference between the two conversions is minimised. The vertical scale is normalised as in Fig. 5.9.

predicted in Fig. 6.1, it is clear from Fig. 6.6b that, with long narrow ridges, shearing does not produce any distortion of the lineshape. Using the pulse sequence in Fig. 6.3b, pure absorption-mode lineshapes are apparently obtained in Fig. 6.6c although, in order to achieve this, full radiofrequency power had to be used for the final pulse. This is a good example of a general feature of amplitude-modulated MQMAS experiments that was frequently encountered experimentally: namely, it is straightforward to achieve pure absorption-mode lineshapes in *z*-filtered experiments, but much more difficult to achieve them in single-pulse conversion experiments.

6.2.2 Phase-Modulated Split-t_1 Experiments

The split-t_1 approach is equally applicable to the phase-modulated whole-echo experiments presented in Section 5.2.2, and Fig. 6.7 (on page 113) shows the pulse sequences and coherence transfer pathway diagrams for two possible experiments. The two experiments shown select coherence transfer pathways

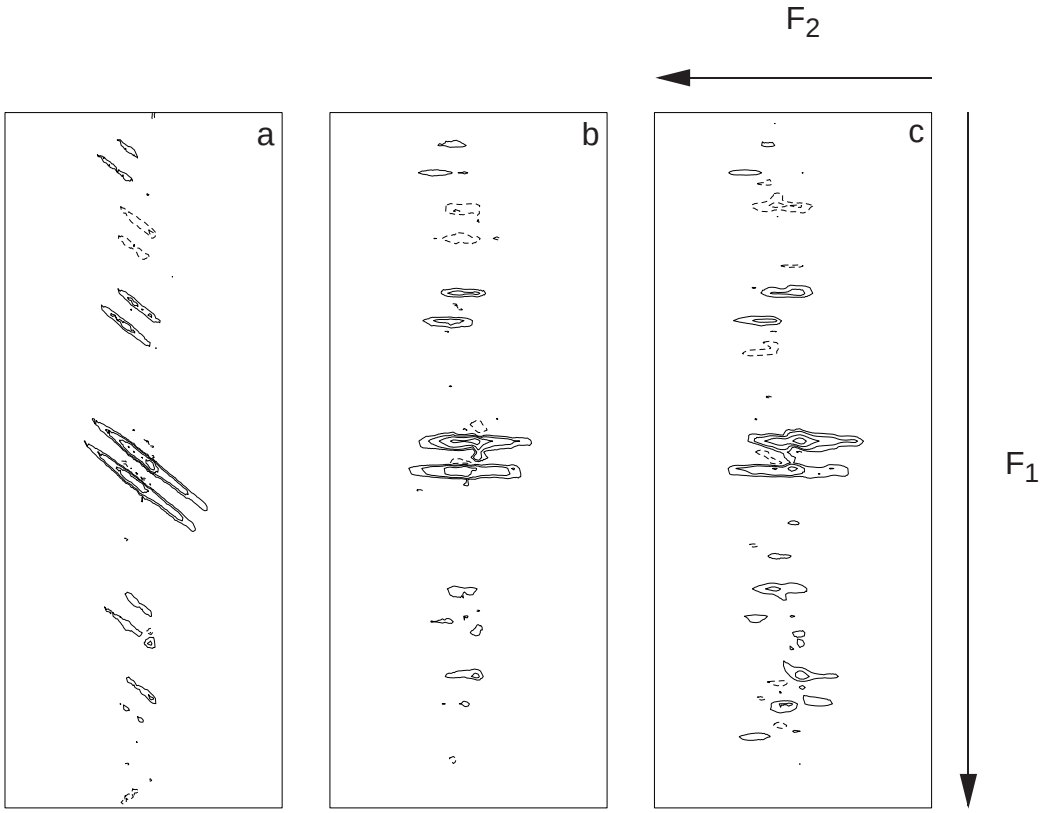

Figure 6.6. Contour plots taken from ^{23}Na (105.8 MHz) MQMAS spectra of a mixture of $Na_2C_2O_4$ and Na_2SO_4 obtained with, (a) and (b), the simple amplitude-modulated experiment in Fig. 5.1a and, (c), the amplitude-modulated split-t_1 experiment in Fig. 6.3b. In (a), the displayed F_1 and F_2 spectral widths are 25 and 10 kHz, respectively. The spectrum in (b) is the result of applying a shearing transformation in the $S(t_1, \omega_2)$ domain, as described in the text, to the data set in (a). The shearing transformation reduces the F_1 spectral width by 9/16, such that the displayed F_1 spectral width is 14.1 kHz in (b). For comparison, the displayed F_1 and F_2 spectral widths in (c) are 14.1 and 10 kHz, respectively. It was not necessary to apply a shearing transformation in (c). Experimental conditions as similar as possible were used for the two experiments: the full F_2 spectral width was 25 kHz, 96 transients (consisting of 256 points each) were averaged for each of 256 increments of t_1, the relaxation interval was 1 s, and the spinning speed was 5.4 kHz. The duration of the triple-quantum excitation pulse was 7.4 μs. Sign discrimination was restored using the TPPI method of incrementing the phase of the first pulse by 30° for each increment of t_1. The full F_1 spectral width equalled 50 and 28.1 kHz in (a) and (c), respectively. The duration of the p = ±3 to p = –1 reconversion pulse in (a) was 3.7 μs, while that of the p = +3 to p = +1 and p = –3 to p = –1 conversion pulse in (c) was 2.0 μs. The p = ±1 to p = –1 conversion pulse in (c) had duration 1.9 μs. The bottom contour in each spectrum corresponds to 8% of the maximum height. The observed spinning sideband patterns in F_1 are discussed in Appendix I.

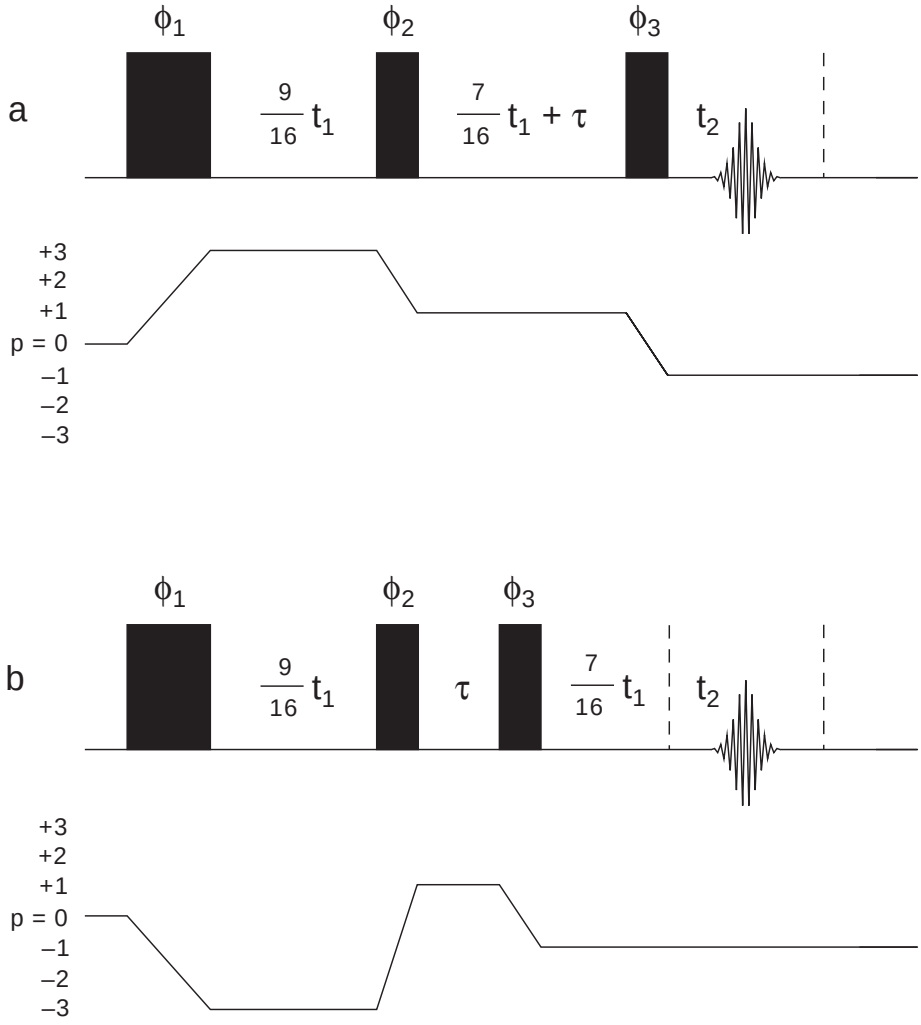

Figure 6.7. Pulse sequences and coherence transfer pathway diagrams for two phase-modulated split-t_1 experiments (for spin I = 3/2 nuclei). The evolution period, t_1, is split between single- and triple-quantum evolution according to the MQMAS ratio as indicated. The second pulse changes the coherence order by Δp = –2 in (a) and by Δp = +4 in (b). As a result, if $\omega_1 < \omega_Q$, the sensitivity of the experiment in (a) is higher than that in (b) and makes it the phase-modulated experiment of choice for spin I = 3/2 nuclei. A whole echo always forms at the centre of the acquisition period, t_2, for all values of t_1. The optimum flip angles for the individual pulses are described in the text. The spin-echo interval, τ, should be of sufficient length to ensure that the whole echo is not truncated. The phase cycling schemes for the pulse phases ϕ_1, ϕ_2 and ϕ_3 and for the receiver R_x are the same as those for the shifted-antiecho and shifted-echo experiments in Fig. 5.1b and are given in Table H2 of Appendix H.

which differ in the change of coherence order induced by the second pulse. It was shown in Section 5.3 that the maximum coherence transfer efficiency for $|\Delta p| = 2$ is greater than that for $|\Delta p| = 4$, and hence the sequence in Fig. 6.7a is to be preferred. The experiments in Fig. 6.7 involve the correlation of triple- and single-quantum coherences of the same sign, and are, therefore, modified versions of the shifted-echo

sequence. (Similarly modified versions of the shifted-antiecho sequence also exist; however, as discussed earlier, a much longer spin-echo interval is necessary in this case.) A schematic representation of the time-domain data set resulting from a phase-modulated split-t_1 experiment is shown in Fig. 6.4b, along with, for comparison, in Fig. 6.4d, the time-domain representation for the shifted-echo experiment (repeated from Fig. 5.2c).

Comparison of the shifted-echo experiment in Fig. 5.1b and the split-t_1 experiment in Fig. 6.7b reveals that they only differ in how t_1 is defined, and hence there is no inherent difference in resolution or sensitivity between the two approaches. Furthermore, it was shown in Section 6.1 that phase-modulated whole-echo experiments only give rise to pure absorption-mode lineshapes when the inhomogeneous broadening dominates the homogeneous broadening. In this limit, shearing does not distort the two-dimensional lineshape. However, it is shown in the next section that there are still important advantages associated with using the split-t_1 experiments.

As an experimental example, Fig. 6.8 (overleaf) presents a ^{23}Na MQMAS spectrum of a mixture of Na_2SO_4 and $Na_2C_2O_4$ obtained with the phase-modulated split-t_1 experiment in Fig. 6.7a. (The isotropic spectrum obtained by projecting the two-dimensional spectrum onto the F_1 axis was shown in Fig. 1.1b.) It should be noted that this experiment involves the evolution of $p = +3$ coherence, as compared to $p = -3$ coherence in the shifted-echo experiment. This has the consequence that the F_1 frequency of a ridge in a spectrum obtained using the split-t_1 experiment of Fig. 6.7a will be of opposite sign to that observed in a sheared spectrum obtained using the shifted-echo (or simple amplitude-modulated) experiment. To avoid confusion, the F_1 axis in Fig. 6.8 has been flipped, such that the displayed spectrum is equivalent to that shown in Fig. 6.6.

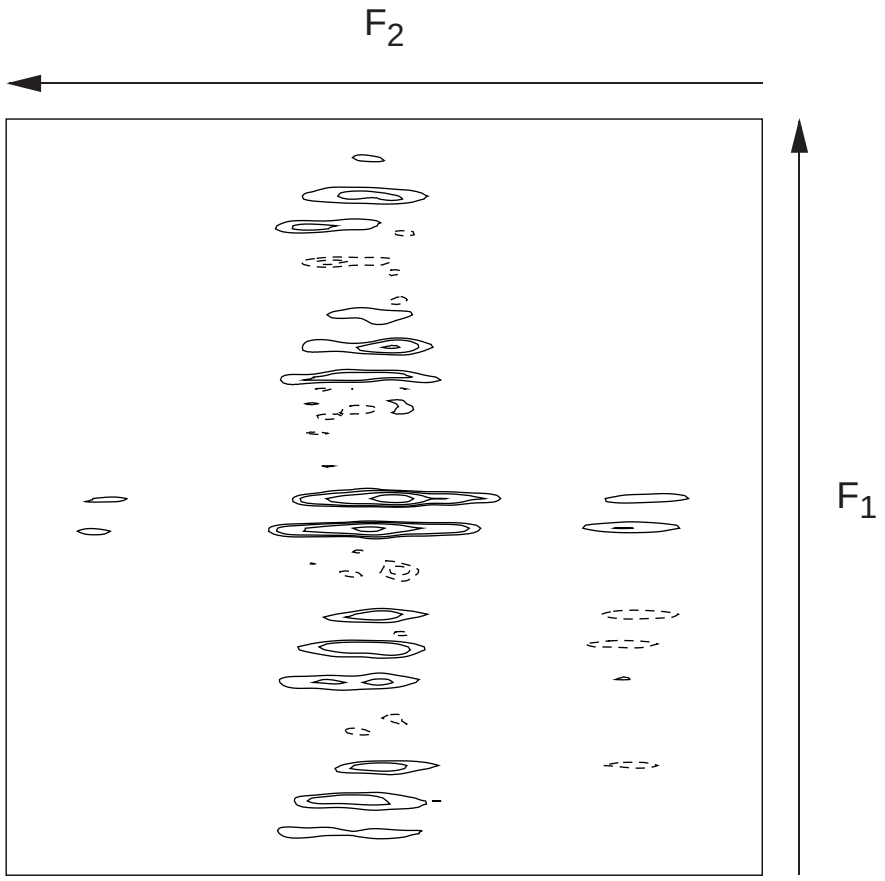

Figure 6.8. Contour plot taken from a ^{23}Na (105.8 MHz) MQMAS spectrum of a mixture of $Na_2C_2O_4$ and Na_2SO_4, recorded using the phase-modulated split-t_1 experiment in Fig. 6.7a. The displayed spectral width is 15 kHz in both the F_1 and F_2 dimensions. The full F_1 and F_2 spectral widths were 15 kHz and 50 kHz, 192 transients (consisting of 256 points each) were averaged for each of 64 increments of t_1, the relaxation interval was 1 s, and the spinning speed was 5.3 kHz. The triple-quantum excitation pulse, the p = +3 to +1 conversion pulse, and the selective central transition inversion pulse were of duration 6.1 μs, 2.1 μs, and 4.0 μs, respectively. The spin-echo interval, τ, was 1.33 ms. It was not necessary to apply a shearing transformation. The bottom contour in each spectrum corresponds to 8% of the maximum height. The observed spinning sideband pattern in F_1 is discussed in Appendix I.

6.3 Signal-to-Noise Considerations

A qualitative comparison of the sensitivity of the simple amplitude-modulated, the shifted-echo, and the amplitude-modulated whole-echo experiments was presented in Section 5.5. This purpose of this section is then twofold: firstly, to compare, both qualitatively and quantitatively, the sensitivity of the split-t_1 experiments to that of their direct Chapter 5 analogues; and secondly, to determine,

using ^{87}Rb NMR of $RbNO_3$ as a model example, which experiment overall has the best S/N.

Considering first the phase-modulated split-t_1 experiment in Fig. 6.7b, it was stated in the previous section that there is no inherent difference in resolution or sensitivity between this experiment and the phase-modulated shifted-echo experiment in Fig. 5.1b. However, the processing required to obtain the optimum S/N is considerably simpler in the split-t_1 experiments. In addition to not needing to apply a shearing transformation, the key advantage, as illustrated in Fig. 6.4b, is the fact that the echo always forms at the same position in t_2. This has the following favourable consequences. Firstly, since the echo does not move through t_2, the length of the acquisition period, and hence the introduction of noise, can be kept to a minimum. There is, thus, no requirement to use t_1-dependent weighting functions to optimise the S/N. Secondly, to record an echo which is symmetric about its centre, it is obvious that the centre of the echo should correspond to the centre of t_2. As discussed earlier, this means that it is very easy to apply the necessary phase correction to ensure that the centre of the echo corresponds to $t_2 = 0$, when $t_1 = 0$.

Furthermore, there is an additional advantage of the phase-modulated split-t_1 experiment in Fig. 6.7a as a consequence of the $|\Delta p| = 2$ change being more efficient than the $|\Delta p| = 4$ change. For the experiments in Fig. 5.1b, where there is only triple-quantum coherence evolution during t_1, it is the shifted-antiecho sequence that has the favourable coherence order change. However, it was stated earlier that there will be greater signal loss due to relaxation in the shifted-antiecho sequence as a consequence of the longer spin-echo interval. In contrast, the split-t_1 experiment in Fig. 6.7a has both the optimum coherence order change and the optimum spin-echo interval.

To confirm these predictions, ^{87}Rb MQMAS spectra of $RbNO_3$ were obtained using the shifted-echo and shifted-antiecho experiments in Fig. 5.1b, and the phase-modulated split-t_1 experiment in Fig. 6.7a. As similar as possible experimental conditions were used, except, as noted above, it was necessary to use a longer spin-echo interval in the shifted-antiecho experiment, and the unfavourable $|\Delta p| = 4$ coherence transfer step for the shifted-echo experiment. The spectra obtained using the shifted-antiecho and split-t_1 experiments are presented in Fig. 6.9 (overleaf). In this case, since the inhomogeneous broadening must dominate the homogeneous broadening for the whole-echo approach to be applicable, it is unsurprising that there is no evidence of any distortion of the two-dimensional lineshapes in the sheared spectrum (Fig. 6.9b).

Comparing the S/N for the three experiments, the S/N of the shifted-antiecho experiment was 1.6 times higher than that of the shifted-echo experiment, while that of the phase-modulated split-t_1 experiment in Fig. 6.7a was 2.0 times higher. Hence, the predicted sensitivity advantage for spin I = 3/2 nuclei of the split-t_1 experiment in Fig. 6.7a is confirmed. (It should be noted that the measured S/N in spectra obtained using the shifted-echo and shifted-antiecho experiments were optimised by the application of t_1-dependent time-domain filters to remove unwanted noise.)

Turning to the amplitude-modulated split-t_1 experiments in Fig. 6.3, it is clear that at least one additional pulse is required relative to the simple amplitude-modulated experiment in Fig. 5.1a (as also for the *z*-filtered simple amplitude-modulated experiment in Fig. 5.11). Although the favourable $|\Delta p| = 2$ coherence transfer step is carried out by the triple- to single-quantum conversion pulse, it would still be expected that the amplitude-modulated split-t_1 experiments have poorer S/N. This was indeed found to be the case in the experimental ^{23}Na NMR spectra in Fig. 6.2, where, recorded under as similar conditions as possible, the S/N of the simple amplitude-modulated spectrum in

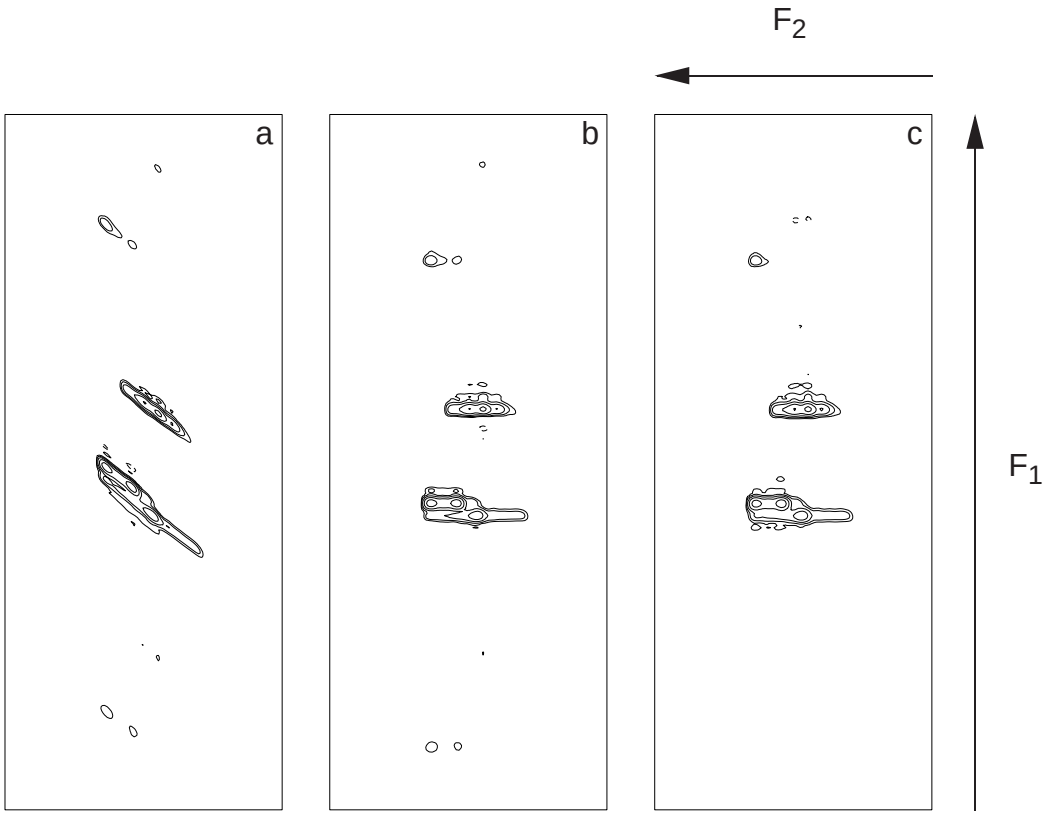

Figure 6.9. Contour plots taken from ^{87}Rb (130.9 MHz) MQMAS spectra of $RbNO_3$ obtained with, (a) and (b), the shifted-antiecho experiment in Fig. 5.1b (dashed line) and, (c), the phase-modulated split-t_1 experiment in Fig. 6.7a. (These spectra were recorded in collaboration with Sharon Ashbrook [93].) In (a), the displayed F_1 and F_2 spectral widths are 15 and 6 kHz, respectively. The spectrum in (b) is the result of applying a shearing transformation in the $S(t_1, \omega_2)$ domain, as described in the text, to the data set in (a). The shearing transformation reduces the F_1 spectral width by 9/16, such that the displayed F_1 spectral width is 8.4 kHz in (b). For comparison, the displayed F_1 and F_2 spectral widths in (c) are 8.4 and 6 kHz, respectively. It was not necessary to apply a shearing transformation in (c). Experimental conditions as similar as possible were used for the two experiments: the full F_2 spectral width was 29.4 kHz, 96 transients (consisting of 1024 and 512 points each in (a) and (c), respectively) were averaged for each of 192 increments of t_1, the relaxation interval was 100 ms, and the spinning speed was 5.2 kHz. The full F_1 spectral width equalled 44.4 and 25 kHz in (a) and (c), respectively. The durations of the triple-quantum excitation and the p = +3 to p = +1 conversion pulses were 6.8 and 1.0 μs, respectively. The duration of the central transition inversion pulse was 70 μs, with the nutation frequency, $\omega_1/2\pi$, being reduced to 4 kHz. The spin-echo interval, τ, was 7.8 ms in (a) and 4.4 ms in (c).

Fig. 6.2a was 1.5 times higher than that of the *z*-filtered split-t_1 spectrum in Fig. 6.2c. Nevertheless, depending on the particular experimental application, this modest reduction in sensitivity may be a price worth paying to ensure that undistorted lineshapes are obtained. It should be noted that the *z*-filtered simple amplitude-modulated experiment yielded an even smaller sensitivity advantage over the *z*-filtered split-t_1 experiment: a ^{23}Na NMR spectrum of Na_2HPO_4 (not shown) recorded under comparable conditions to the split-t_1 spectrum in Fig. 6.2c had a S/N that was only 1.1 times better.

It should be noted that, as with the phase-modulated split-t_1 experiments, the amplitude-modulated split-t_1 experiments in Fig. 6.3 have the practical advantage that the time-domain signal does not move within the acquisition period t_2, meaning that this can be kept short and that normal (*i.e.*, t_1-independent) weighting functions can be used to optimise the S/N. It is also interesting to note that the S/N of the experiments in Fig. 6.3 can, in principle, be increased by a factor of $\sqrt{2}$ by appending a spin echo to the pulse sequence and acquiring a whole, rather than half, echo.

In a separate experimental study to that described above for the phase-modulated split-t_1 experiments, ^{87}Rb MQMAS spectra of $RbNO_3$ were obtained using the phase-modulated split-t_1 experiment in Fig. 6.7a, the simple amplitude-modulated, the amplitude-modulated whole-echo experiment, and the *z*-filtered simple amplitude-modulated experiment. The S/N of the four experiments were then in the ratio 1.0: 0.7: 0.6: 0.5, indicating that the phase-modulated split-t_1 experiment has the best sensitivity.

6.4 Spin I = 5/2 Nuclei

The split-t_1 experiments introduced in Section 6.2 are equally applicable to spin I = 5/2 nuclei, and the optimum (triple-quantum) amplitude- and phase-

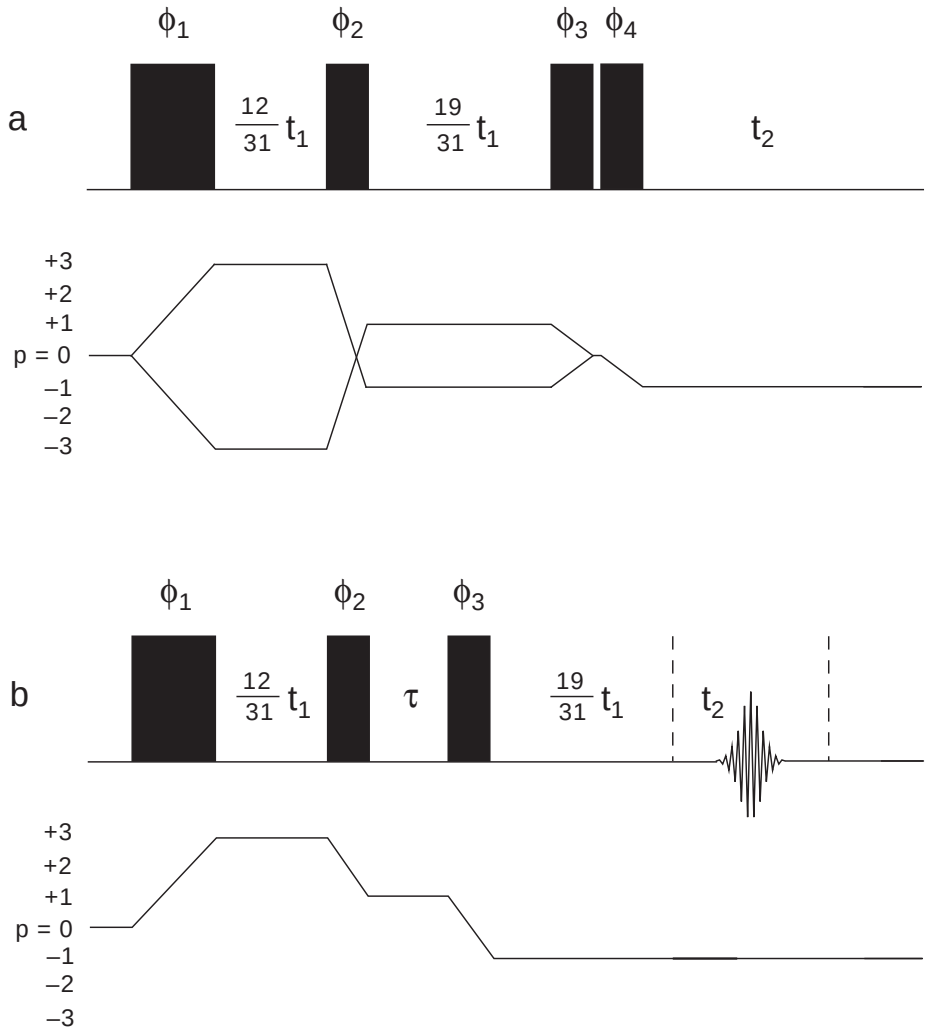

Figure 6.10. Pulse sequences and coherence transfer pathway diagrams for the optimum (a) amplitude-modulated split-t_1 experiment and (b) phase-modulated split-t_1 experiment for spin I = 5/2 nuclei. The evolution period, t_1, is split between single- and triple-quantum evolution according to the MQMAS ratio as indicated. A whole echo always forms at the centre of the acquisition period, t_2, for all values of t_1 in (b). Phase cycling schemes for the pulse phases ϕ_1, ϕ_2 and ϕ_3 and for the receiver R_x in (a) is given in Table H3 of Appendix H, while that in (b) is the same as that for the shifted-antiecho experiment in Fig. 5.1b and is given in Table H2 of Appendix H.

modulated experiments are presented in Fig. 6.10. In this case, the evolution time is now partitioned between single- and triple-quantum evolution in the ratio of 19/12.

For spin I = 5/2 nuclei, it was observed, experimentally, that the maximum transfer amplitude, for a range of samples, was much lower for the $|\Delta p| = 4$ triple- to single-quantum conversion step than that for the $|\Delta p| = 2$ case, typically between 3 and 6 times smaller. This has a significant consequence on the sensitivity of the

amplitude-modulated split-t_1 experiment, which, since the MQMAS ratio is positive, utilises this unfavourable change. As an example, Fig. 6.11 (overleaf) presents ^{27}Al MQMAS spectra of aluminium hydroxide, $Al(OH)_3$, recorded using the *z*-filtered simple amplitude-modulated in Fig. 5.11 and the amplitude-modulated split-t_1 experiment in Fig. 6.10a. The ratio of the inhomogeneous to homogeneous broadening for the two resolvable ridges is small, and, to avoid the distortion of the two-dimensional lineshapes caused by shearing in Fig. 6.11b, it is necessary to perform an amplitude-modulated split-t_1 experiment. However, as shown by the poor quality of the lineshapes in Fig. 6.11c, there is an unacceptable loss of sensitivity (ten times, in this case) associated with this experiment. (It should be noted that, although the correlation of triple-quantum with single-quantum evolution has given rise to two-dimensional spectra in Fig. 6.11 offering more information than that observed in a one-dimensional spectrum, in this case, the MQMAS experiment has not achieved any observable line narrowing in F_1. This suggests that second-order quadrupolar broadening is not the dominant line-broadening mechanism.)

For the phase-modulated split-t_1 experiment, the more efficient $|\Delta p| = 2$ triple- to single-quantum conversion can be used, with, as shown in Fig. 6.10b, the second part of the t_1 period now following the final pulse. As an example, Fig. 6.12 (on page 123) presents a ^{27}Al spectrum of the mineral kyanite (Oxford University Museum, OUM 29205), Al_2SiO_5, obtained with the experiment in Fig. 6.10b. Three long narrow ridges can be identified (the isotropic shifts are marked with arrows in the F_1 dimension) and, as two of the C_Q values for kyanite are very similar [53], these correspond to the four crystallographically inequivalent sites.

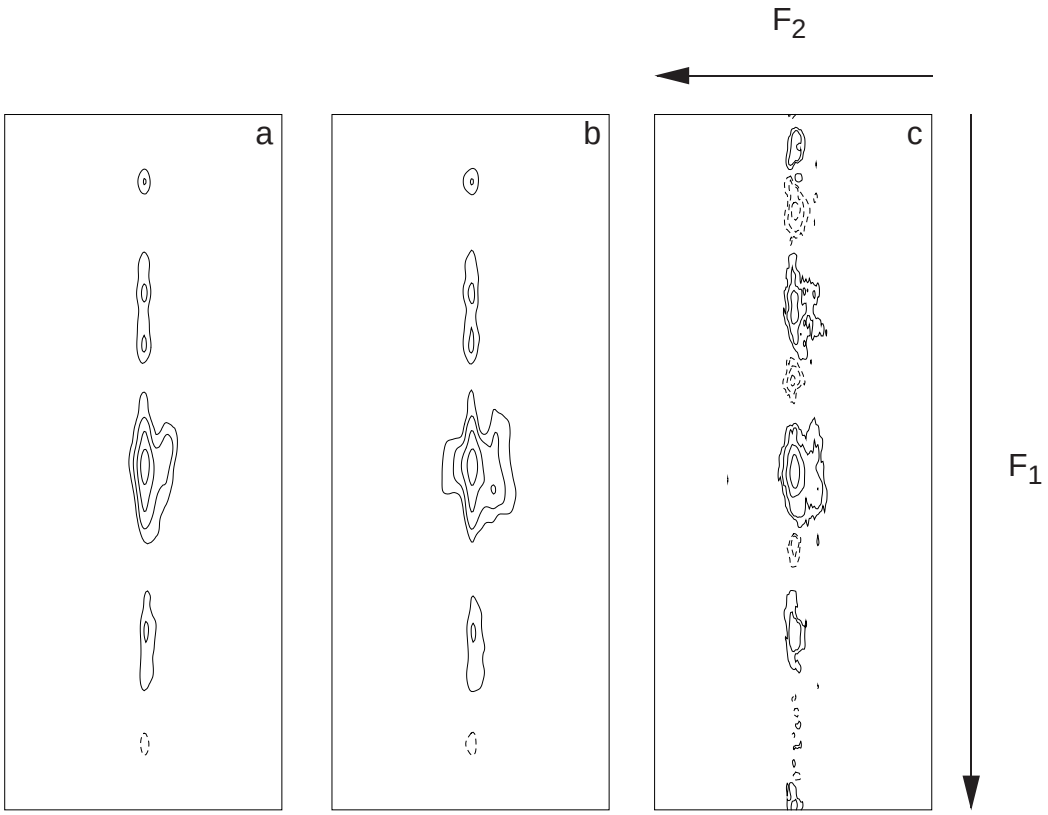

Figure 6.11. Contour plots taken from ^{27}Al (104.3 MHz) MQMAS spectra of $Al(OH)_3$ (BDH) obtained with, (a) and (b), the *z*-filtered simple amplitude-modulated experiment in Fig. 5.11 and, (c), the amplitude-modulated split-t_1 experiment in Fig. 6.10a. In (a), the displayed F_1 and F_2 spectral widths are 40 and 16 kHz, respectively. The spectrum in (b) is the result of applying a shearing transformation in the $S(t_1, \omega_2)$ domain, as described in the text, to the data set in (a). The shearing transformation reduces the F_1 spectral width by 12/31, such that the displayed F_1 spectral width is 15.5 kHz in (b). For comparison, the displayed F_1 and F_2 spectral widths in (c) are 15.5 and 16 kHz, respectively. It was not necessary to apply a shearing transformation in (c). The following experimental conditions were used for the two experiments: the full F_2 spectral width was 50 kHz, 768 transients (consisting of 512 points) were averaged for each of 128 increments of t_1, the relaxation interval was 500 ms, and the spinning speed was 9.5 kHz. Sign discrimination was restored using the TPPI method of incrementing the phase of the first pulse by 30° for each increment of t_1. The full F_1 spectral width equalled 100 and 27.6 kHz in (a) and (c), respectively. The duration of the $p = \pm 3$ to $p = 0$ pulse in (a) was 1.2 μs, while that of the $p = +3$ to $p = -1$ and $p = -3$ to $p = +1$ conversion pulse in (c) was 2.0 μs. The duration of the triple-quantum excitation pulse was 3.5 μs. The duration of all pulses acting on the central transition inversion pulse was 25 μs, with the nutation frequency, $\omega_1/2\pi$, being reduced to 5 kHz. The bottom contour in each spectrum corresponds to 8% of the maximum height. The observed spinning sideband patterns in F_1 are discussed in Appendix I.

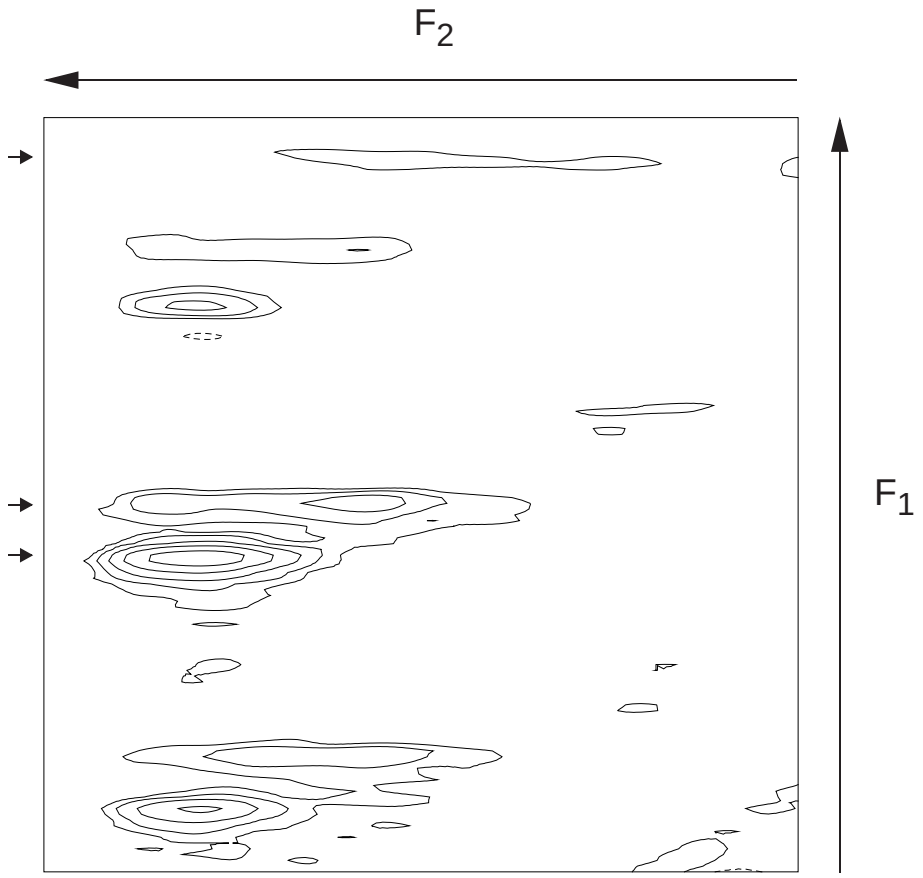

Figure 6.12. A contour plot taken from an ^{27}Al (104.2 MHz) MQMAS spectrum of kyanite recorded using the phase-modulated split-t_1 experiment in Fig. 6.10b. (This spectrum was recorded in collaboration with Sharon Ashbrook [93].) The displayed spectral width is 10 kHz (cut down from 38.7 and 50 kHz, respectively) in both the F_1 and F_2 dimensions. The following experimental conditions were used: 672 transients (consisting of 256 points each) were averaged for each of 192 increments of t_1, the relaxation interval was 500 ms, and the spinning speed was 8.5 kHz. The durations of the triple-quantum excitation and the p = +3 to p = +1 conversion pulses were 3.6 and 0.8 μs, respectively. The duration of the central transition inversion pulse was 30 μs, with the nutation frequency, $\omega_1/2\pi$, being reduced to 8 kHz. The spin-echo interval, τ, was 1.4 ms. It was not necessary to apply a shearing transformation. The observed spinning sideband pattern in F_1 is discussed in Appendix I.

6.5 Discussion and Conclusions

This and the previous chapter have presented the different methods by which the MQMAS technique can be implemented; before moving on, in the final chapter, to describe some novel experimental applications, the final section of this chapter will summarise the discussion of these different MQMAS experiments.

It has been shown that the various methods proposed for obtaining pure absorption-mode lineshapes in MQMAS experiments of half-integer quadrupolar nuclei can be classified according to whether the data is amplitude- or phase-modulated as a function of t_1. To date, both classes of experiment have most often been performed in such a way that the inhomogeneous quadrupolar broadening is spread out along a ridge which has a slope of –7/9 or 19/12 with respect to the F_2 axis for spin I = 3/2 and 5/2, respectively. In this chapter, it has been shown that there are disadvantages associated with recording the data in this fashion. Firstly, this approach means that the echo that is formed moves through the acquisition period, t_2, as the evolution period, t_1, is incremented, which, in turn, means that the t_2 period is much longer than necessary and that complicated t_1-dependent weighting functions must be used to optimise the sensitivity. Secondly, to obtain both the isotropic projection and the individual second-order broadened spectra, the spectroscopist has to apply a shearing transformation to the final spectrum. This transformation can result in a significant distortion of the two-dimensional lineshapes and, in particular, of the F_2 cross sections containing the individual second-order broadened spectra.

Phase-modulated whole-echo MQMAS experiments yield pure absorption-mode lineshapes when the inhomogeneous quadrupolar broadening is much greater than the homogeneous broadening. In this limit, compared to the amplitude-modulated experiments in Figs. 5.1a and 6.3, they have the advantage that only a single coherence transfer pathway need be selected, thereby avoiding the need to use *z* filters or carefully calibrated single pulses to combine two mirror-image pathways with equal amplitudes. Phase-modulated split-t_1 experiments were introduced, where the whole echo is stationary within the acquisition period, t_2 (meaning that the t_2 period is short and that simple weighting functions can be used), and where the inhomogeneously-broadened ridges are parallel to F_2, thereby avoiding the need for shearing.

In addition to these practical advantages, for spin I = 3/2, the inherent sensitivity of the optimum phase-modulated split-t_1 experiment (Fig. 6.7a) is expected (and was indeed experimentally demonstrated) to be better than that of either the shifted-echo or shifted antiecho experiment in Fig. 5.1b since it features both a short spin-echo interval, τ, and an optimum coherence transfer step of $|\Delta p| = 2$. Moreover, it is further expected that the sensitivity of the optimum versions of the phase-modulated split-t_1 experiment (Figs. 6.7a and 6.10b for spin I = 3/2 and 5/2, respectively) will often be better than that of the amplitude-modulated whole-echo experiment, since the latter, despite its theoretical $\sqrt{2}$ sensitivity advantage, requires a longer spin-echo interval, τ, and makes use of a coherence transfer step with $|\Delta p| = 4$. This result was again experimentally demonstrated for ^{87}Rb NMR of $RbNO_3$.

Amplitude-modulated MQMAS experiments can be used to yield pure absorption-mode lineshapes whatever the ratio of the inhomogeneous to homogeneous broadening. Amplitude-modulated split-t_1 experiments were introduced, where the time-domain signal is stationary within the acquisition period, t_2, and where the inhomogeneously-broadened ridges are parallel to F_2. In spite of these practical advantages, the sensitivities of the two amplitude-modulated split-t_1 experiments are expected (and, for spin I = 3/2, observed) to be slightly worse than that of the simple amplitude-modulated experiment in Fig. 5.1a. This is because at least one additional pulse is always required. It should be noted, however, that the amplitude-modulated experiments are most clearly preferable to the phase-modulated MQMAS experiments when the inhomogeneous broadening is small and that it is in this limit that shearing is least desirable. For spin I = 5/2, the requirement that the coherence transfer pathways utilise the unfavourable $|\Delta p| = 4$ triple- to single-quantum conversion step means that the sensitivity of the amplitude-modulated split-t_1 experiment is found to be very poor.

In summary, therefore, it has been shown that MQMAS experiments which refocus the anisotropic second-order quadrupolar broadening in the evolution

period, t_1, have many advantages over those experiments that require the application of a shearing transformation to the final spectrum. The sensitivities of split-t_1 MQMAS experiments are comparable to those of the other methods and, in the case of phase-modulated MQMAS experiments for spin $I = 3/2$, are even expected to be slightly superior.

Chapter 7

Novel Experimental Applications

7.1 Overview

In the previous chapters, the general and specific features of the MQMAS experiment have been demonstrated experimentally using model compounds, which were chosen on account of their favourable sensitivity and short T_1 relaxation times. However, for the MQMAS experiment to be of interest beyond the NMR community, the technique must be applicable to samples of current chemical and physical interest. The purpose of this chapter is to show that structural information can be obtained, for a wide range of novel samples, using the MQMAS experiment.

The industrially-important samples studied to date by ^{27}Al, ^{11}B, ^{23}Na, and ^{17}O MQMAS NMR are detailed in Table 7.1. From this table, it is evident that interest has mainly focused on two areas of materials science, namely microporous solids and glasses. In the latter, solid-state NMR can provide structural information which is inaccessible by X-ray diffraction as a consequence of a lack of long-range order [37, 53, 60, 128, 129], while in the context of microporous solids, ^{27}Al MQMAS NMR has enabled the unambiguous resolution of the predicted ^{27}Al nuclear sites [42, 47, 52, 56, 62, 67], which was not possible by MAS alone due to the presence of second-order quadrupolar broadening. In addition, the MQMAS technique has provided valuable information with regards to understanding temperature-dependent phase transformations in, for example, Na_2HfO_3 [50] and VPI-5 [56].

TABLE 7.1 Applications of the MQMAS Experiment

Nucleus	Sample	Ref(s)
^{27}Al	$AlPO_4$-11 (microporous)	42
^{27}Al	VPI-5 (microporous)	42, 56
^{27}Al	triclinic CHA-like precursor of $AlPO_4$-34 (microporous)	47
^{27}Al	$AlPO_4$-14 (microporous)	52, 61
^{27}Al	$CaAl_2Si_2O_8$ (glass)	53
^{27}Al	magnesium aluminoborate glass	53
^{27}Al	Mo, P impregnated γ-alumina (hydrodenitrogenation catalysts)	59
^{27}Al	AlMePO-β (microporous)	62
^{27}Al	ZSM-5 (microporous)	63
^{27}Al	fluorinated-triclinic CHA-like precursor of $AlPO_4$-34	67
^{27}Al	κ-alumina	75
^{11}B	Na_2O-B_2O_3-SiO_2 (glass)	46
^{11}B	vitreous B_2O_3 (glass)	48, 66
^{11}B	potassium borate glass	48
^{11}B	vitreous B_2S_3 (glass)	66
^{11}B	borane-triphenylphosphite complex	68
^{23}Na	Na_2HfO_3	50
^{23}Na	$Na_3AlP_3O_9N$ and $Na_2Mg_2P_3O_9N$ nitridophosphates	57
^{23}Na	Na_2O-B_2O_3-SiO_2 (glass)	60
^{17}O	stilbite	64
^{17}O	aluminosilicate glass	73

In the following sections, two specific applications of the MQMAS experiment are presented. The main part of the discussion focuses on molecular sieves, a general introduction to which is given is Section 7.2. One area of current interest are the aluminium methylphosphonates (AlMePOs) [62, 130-133]; ^{27}Al MQMAS spectra of these microporous inorganic-organic materials are presented in Sections 7.3 and 7.4, and the inferences which can be drawn with regards to the understanding of the phase transformation between the α and β forms are discussed. In addition, these MQMAS spectra are used to demonstrate, firstly in Section 7.4, the enhanced resolution which can be achieved by the quintuple-quantum MQMAS experiment, and, secondly in Section 7.5, how the separate isotropic chemical and second-order quadrupolar shifts can be extracted from a single MQMAS spectrum.

At first sight, the spin I = 5/2 nucleus ^{17}O, with its very low natural abundance of 0.037% and its relatively small Larmor frequency (see Appendix C), looks a distinctly unpromising nucleus for NMR studies. However, it is shown, in Section 7.6, that, with the help of isotopic enrichment, an ^{17}O MQMAS spectrum of the synthesised mineral forsterite can still be obtained. The potential of the ^{17}O MQMAS experiment for providing insight into geological processes is then discussed.

7.2 Molecular Sieves

The term molecular sieve encompasses zeolites and other analogous structures with different elemental compositions. These crystalline microporous materials have a very narrow pore-size distribution, such that they allow the highly selective discrimination of molecules on the basis of their dimensions. The purpose of this section is to provide a general introduction to these industrially important materials [134, 135].

Molecular sieves are classified, irrespective of their chemical composition, according to their topology (in simple terms, the three-dimensional shape). The observed pore diameters, which can be arranged in a one-, two-, or three-dimensional system, are typically in the range 4 - 13 Å. For example, while VPI-5 contains unidimensional channels of diameter 12 Å, ZSM-5 has a three-dimensional pore system with pore diameters of 5 Å. The range of available topologies means that a wide variety of molecules can be adsorbed selectively. Moreover, by changing the elemental composition of the framework, molecules can be discriminated further on the basis of their chemical properties.

In zeolites themselves, the framework consists of corner sharing TO_4 tetrahedra, where T is Si or Al with the ratio Si:Al between 1 and infinity. Since the replacement of tetravalent Si by trivalent Al results in a charge-deficient framework, alkali metal or alkaline earth cations are also present to maintain charge balance. Such a structure means that zeolites are hydrophilic and possess ion exchange sites. Furthermore, zeolites containing hydrated alkaline earth cations act as strong Brønsted acids of comparable strength to sulphuric acid. Another important class of microporous material are the aluminophosphates, or AlPOs, in which the framework contains trivalent Al and pentavalent P in equal proportion and is therefore neutral overall. As a result, AlPOs, in contrast to zeolites, do not possess acidic sites.

As well as finding applications as ion exchange materials and adsorbents, molecular sieves act as catalysts in many industrial processes. For example, zeolites are widely used as environmentally friendly alternatives to conventional mineral acids in oil refining and petrochemical manufacture. Moreover, there is growing interest in the use of microporous materials in the manufacture of fine chemicals, whereby the introduction of a redox metal centre into a molecular sieve enables its use as a heterogeneous catalyst for the liquid-phase oxidation of organic compounds. Such a catalysed process removes the necessity to use stoichiometric amounts of an inorganic oxidant, along with all the associated problems of the disposal of large

quantities of waste material. There is, therefore, much interest in the understanding of existing and the development of new molecular sieves, and MQMAS NMR of, in particular, ^{27}Al has considerable potential to provide valuable structural information, complementary to that achievable by other techniques, *e.g.*, X-ray diffraction.

7.3 Triple-Quantum MQMAS NMR of AlMePOs

In microporous AlPOs, the chemical character of the pores is dominated by the oxygen anions; this, for example, explains the observed hydrophilic character. Recently, the synthesis and characterisation of two members of a new family of microporous aluminium methylphosphonates, or AlMePOs, have been presented [130-132], in which the channel walls are modified by the introduction of hydrophobic methyl groups attached to phosphorous atoms. The two forms, AlMePO-α and AlMePO-β, are structurally very similar, containing unidimensional channels, with the three oxygen atoms in each CH_3PO_3 unit being bound to one six-coordinate (octahedral) and two four-coordinate (tetrahedral) aluminium atoms. There are, therefore, three tetrahedral Al sites to every one octahedral site, although the symmetry of AlMePO-α means that there is only one crystallographically-distinct octahedral and tetrahedral site, compared to one octahedral and three tetrahedral crystallographically-distinct sites in AlMePO-β.

Carter *et al.* [133] have recently reported that the β polymorph undergoes a topotactic (*i.e.*, the crystal axes remain in the same orientation) transformation into the α polymorph when heated up to 500°C under water vapour partial pressures of 30 Torr. Such a transformation is rare in framework solids, where elevated temperatures usually cause the loss of crystallinity and a transformation to a denser phase. The same authors have proposed a mechanism for the transformation, in which bond-breaking and bond-forming occurs in a concerted fashion without the formation of an intermediate. To investigate this process, a sample was prepared by

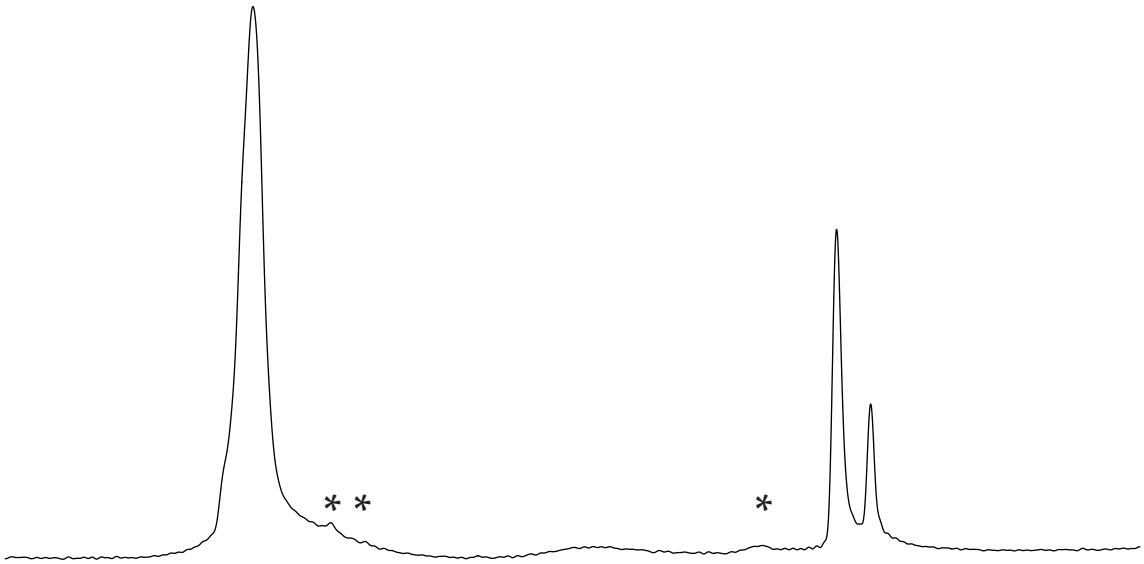

Figure 7.1. An ^{27}Al (130.2 MHz) MAS spectrum of a mixture of AlMePO-α and AlMePO-β, where the phase transformation between the two polymorphs was interrupted. The displayed spectral width equals 15 kHz (cut down from 25 kHz). The following experimental conditions were used: 128 transients (consisting of 512 points) were averaged, the relaxation interval was 500 ms, a radiofrequency pulse of duration 2.0 μs was used, and the spinning speed was 6.7 kHz. The positions of spinning sidebands are labelled by *. The small hump at the centre corresponds to an amorphous impurity.

Vinton Carter (of St. Andrew's University) where the phase transformation was interrupted (by allowing the sample to cool slowly back to room temperature) before the conversion to the α polymorph was complete. In this and the following section, ^{27}Al MQMAS spectra of this material are presented, which are compared, at the end of Section 7.4, with those obtained for the pure α and β forms.

Figure 7.1 presents an ^{27}Al MAS spectrum of the phase-transformation interrupted α, β mixture. While two octahedral sites are clearly observed (at lower frequency), the presence of residual second-order quadrupolar broadening prevents any of the tetrahedral sites being resolved; only a shoulder at high frequency hints at the presence of more than one site. The ratio of the α and β polymorphs can be determined from the relative integrals of the two octahedral peaks, *i.e.*, in this case, the ratio β:α equals approximately 2 (the chemical shift of the α form is more negative).

Figure 7.2 (overleaf) presents triple-quantum ^{27}Al MQMAS spectra of the phase-transformation interrupted α, β mixture recorded on the MSL 500 spectrometer using, (a) and (b), the *z*-filtered simple amplitude-modulated experiment in Fig. 5.11 and, (c) and (d), the phase-modulated split-t_1 experiment in Fig. 6.10b. It should be noted that the displayed F_1 spectral width is 12/31 times smaller in (c) and (d), which, as discussed in Section 6.1, is the reduction which would result from shearing the spectra in (a) and (b). (Although the sheared spectra are not presented, it was found, in this case, that such a shearing transformation caused significant distortion to the two-dimensional lineshapes.) The tetrahedral and octahedral regions are so far separated in frequency that they are plotted separately in (a) and (c), and (b) and (d), respectively. Examining the spectra corresponding to the tetrahedral sites, it can be seen that the triple-quantum MQMAS technique has enabled the resolution of two tetrahedral sites.

The spectrum in Fig. 7.2b of the two octahedral sites illustrates a further important feature of the MQMAS experiment, namely that the gradient of an observed ridge does not always equal the MQMAS ratio [42]. For spin I = 5/2, the (triple-quantum) MQMAS ratio equals 19/12, and a dashed line with this gradient is labelled A (for anisotropic). It is clearly seen that the gradients of the two observed ridges are not equal to 19/12. This is unsurprising since the quadrupolar coupling constants for these octahedral sites are very small [62], and hence there is little inhomogeneous quadrupolar broadening. Instead, the ridges are observed to lie along a line with a gradient of 3, which corresponds to a distribution of isotropic chemical shifts (labelled CS).

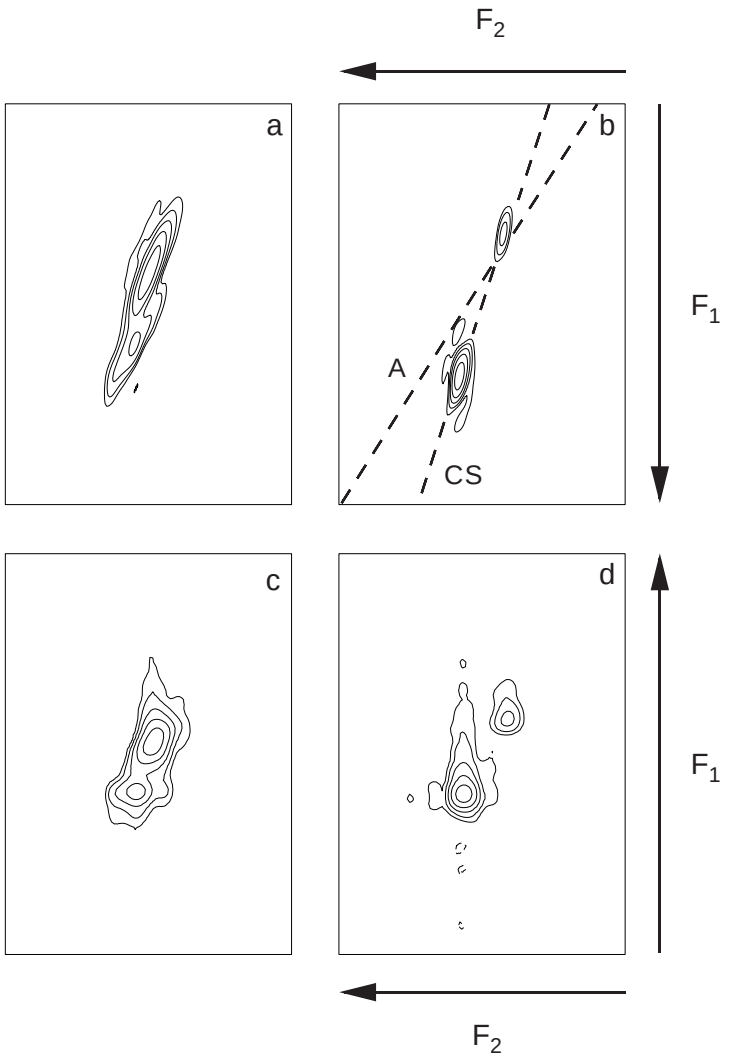

Figure 7.2. Contour plots taken from ^{27}Al (130.2 MHz) MQMAS spectra of a mixture of AlMePO-α and AlMePO-β, where the phase transformation between the two polymorphs was interrupted. The tetrahedral and octahedral regions are shown separately in (a) and (c), and (b) and (d), respectively. Spectra were obtained with, (a) and (b), the *z*-filtered simple amplitude-modulated experiment of Fig. 5.11 and, (c) and (d), the phase-modulated split-t_1 experiment of Fig. 6.10b. In all spectra, the displayed F_2 spectral width equals 4.2 kHz (cut down from 31.3 kHz). The displayed F_1 spectral widths equal 3 and 1.6 kHz (cut down from 50 and 19.4 kHz) for the amplitude-modulated and phase-modulated experiments, respectively. In both experiments, 192 transients (consisting of 512 points) were averaged for each of 256 increments of t_1, the relaxation interval was 500 ms, the spinning speed was 6.7 kHz, and the duration of the triple-quantum excitation pulse was 5.0 μs. For the *z*-filtered simple amplitude-modulated experiment, the duration of the p = ±3 to p = 0 pulse was 2.0 μs, while that of the p = +3 to p = +1 pulse in the phase-modulated split-t_1 experiment was 1.6 μs. The spin-echo interval, τ, was 4.1 ms in the phase-modulated experiment. For pulses acting on the central transition, the nutation frequency, $\omega_1/2\pi$, was reduced to 7 kHz, with the p = 0 to p = –1 and central transition inversion pulses having durations 18 and 36 μs, respectively. Sign discrimination was restored in the amplitude-modulated experiment using the TPPI method of incrementing the phase of the first pulse by 30° for each increment of t_1. In (b), dotted lines indicate the direction of the anisotropic (A) and isotropic chemical shift (CS) axes, with gradients 19/12 and 3, respectively.

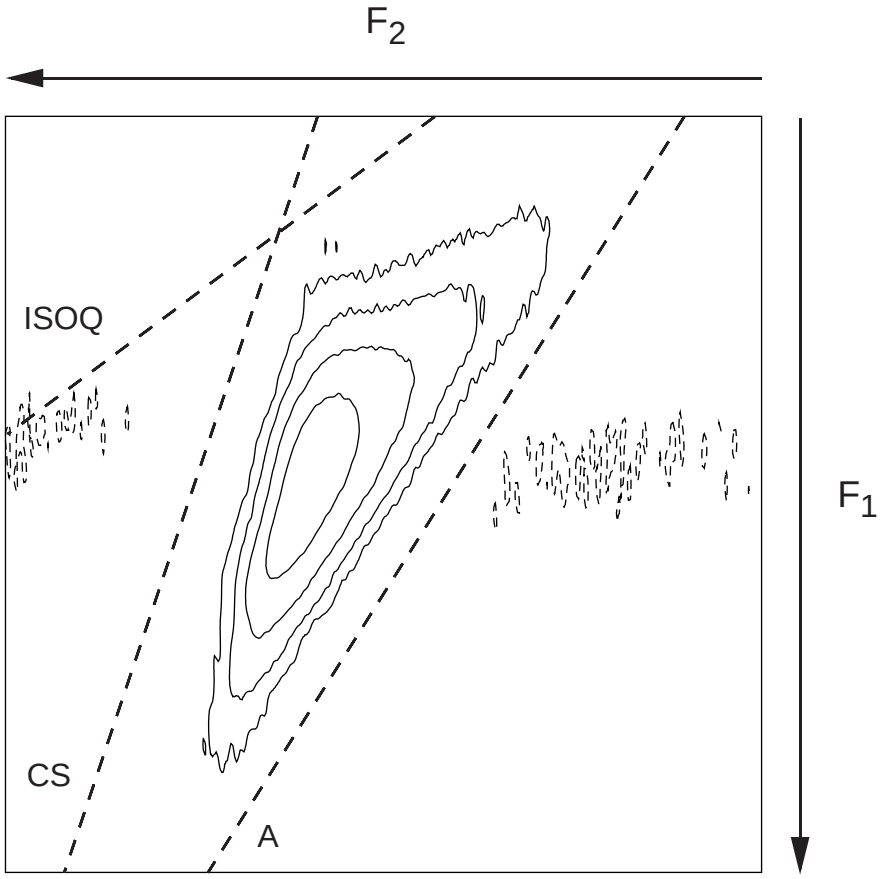

Figure 7.3. Contour plot, showing the octahedral site centre band, taken from the ^{27}Al MQMAS spectrum of γ-alumina, previously presented in Fig. 5.10b. The displayed F_1 and F_2 spectral widths equal 10 kHz. Dotted lines indicate the direction of the anisotropic (A), the isotropic chemical shift (CS), and the isotropic second-order quadrupolar shift (ISOQ) axes, with gradients 19/12, 3, and 3/4, respectively. The bottom contour corresponds to 8% of the maximum height.

In MQMAS spectra of disordered materials, *e.g.*, glasses, more complicated lineshapes can be observed [53], since it is further possible to have a distribution of isotropic second-order quadrupolar shifts, the gradient of which, in the notation of Table 3.1, equals $A_s^I / A_{1/2}^I$, *i.e.*, –3 and 3/4 for spin I = 3/2 and I = 5/2 (triple-quantum), respectively. An example of an MQMAS spectrum displaying such a complicated distribution has already been presented, namely the spectrum of γ-alumina in Fig. 5.10b. To illustrate this, the region of the spectrum corresponding to the octahedral site centreband is presented again in Fig. 7.3, with dashed lines indicating the three gradients of interest. This ability of the MQMAS experiment to identify such distributions of both isotropic chemical shifts and isotropic second-

order quadrupolar shifts provides further useful information with regards to the understanding of the structure of disordered materials.

For the split-t_1 experiment, where the anisotropic gradient equals zero, it can be shown that a distribution of isotropic chemical shifts would give rise to, for a spin I = 5/2 triple-quantum experiment, a ridge with a gradient equal to –17/31. This distribution is, however, less apparent in Fig. 7.2d since, for the octahedral region, it was necessary to apply a symmetric weighting function in t_2 to remove sinc "wiggles" in the final spectrum due to the necessary truncation of the whole echo (a longer spin-echo interval, τ, resulted in an unacceptable sensitivity reduction). This requirement to apply a weighting function means that the whole-echo experiment is not well-suited to studying the octahedral region; however, it is the tetrahedral region which is of interest in this study, and no such problems were observed there.

7.4 Quintuple-Quantum MQMAS NMR of AlMePOs

For spin I = 5/2 nuclei, in addition to the triple-quantum MQMAS experiment, it is further possible to perform a quintuple-quantum MQMAS experiment. Although, as discussed in Section 4.2.2, quintuple-quantum excitation and reconversion is less efficient than triple-quantum excitation and reconversion, Amoureux and co-workers have shown that significant enhancement in resolution can be achieved using the quintuple-quantum MQMAS experiment [42, 47, 62]. Such improvements in resolution are due to two factors: firstly, the isotropic chemical shift is 5/3 times bigger; and secondly, and more importantly, the isotropic second-order quadrupolar shift, for spin I = 5/2, is 25/3 times bigger.

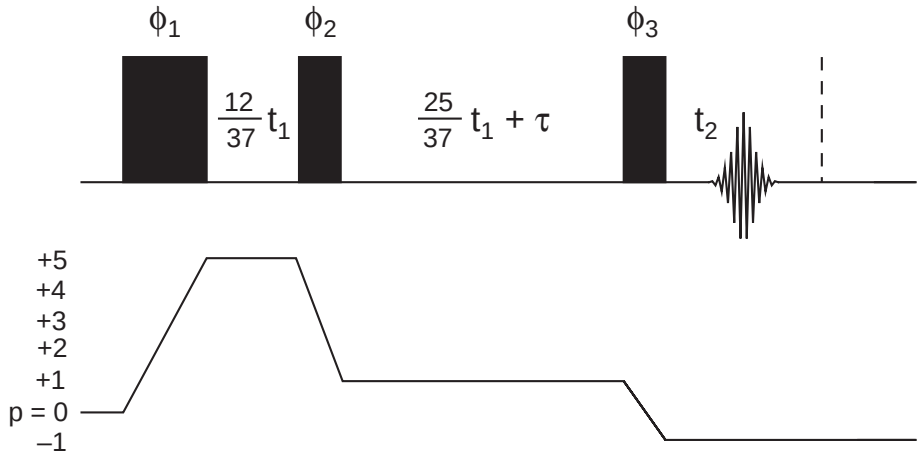

Figure 7.4. Pulse sequence and coherence transfer pathway diagram for the optimum quintuple-quantum phase-modulated split-t_1 experiment for spin I = 5/2 nuclei. The evolution period, t_1, is split between single- and quintuple-quantum evolution according to the MQMAS ratio as indicated. A whole echo always forms at the centre of the acquisition period, t_2, for all values of t_1. A phase cycling scheme for the pulse phases ϕ_1, ϕ_2, and ϕ_3 and for the receiver R_x is given in Table H4 of Appendix H.

The pulse sequence and coherence transfer pathway diagram for the optimum quintuple-quantum phase-modulated split-t_1 MQMAS experiment is presented in Fig. 7.4. It can be seen that the single-quantum and quintuple-quantum evolution periods are partitioned in the ratio of the spin I = 5/2 quintuple-quantum MQMAS ratio, 25/12. Since the MQMAS ratio is positive, the single-quantum evolution period now follows the second pulse.

Figure 7.5 (overleaf) presents ^{27}Al MQMAS spectra of the phase-transformation interrupted α, β mixture obtained on the MSL 400 spectrometer using the triple-quantum and quintuple-quantum phase-modulated split-t_1 experiment of Figs. 6.10b and 7.4, respectively. (It is interesting to note that, since the quadrupolar coupling constants are small, optimum multiple-quantum excitation and reconversion was achieved by reducing the nutation frequency, ω_1, from its maximum value.) The tetrahedral and octahedral regions are again shown separately. In all spectra, the displayed spectral widths in both dimensions equal 3 kHz, and it is very clear that the separation of the individual sites is significantly increased in the quintuple-quantum spectra. In particular, the

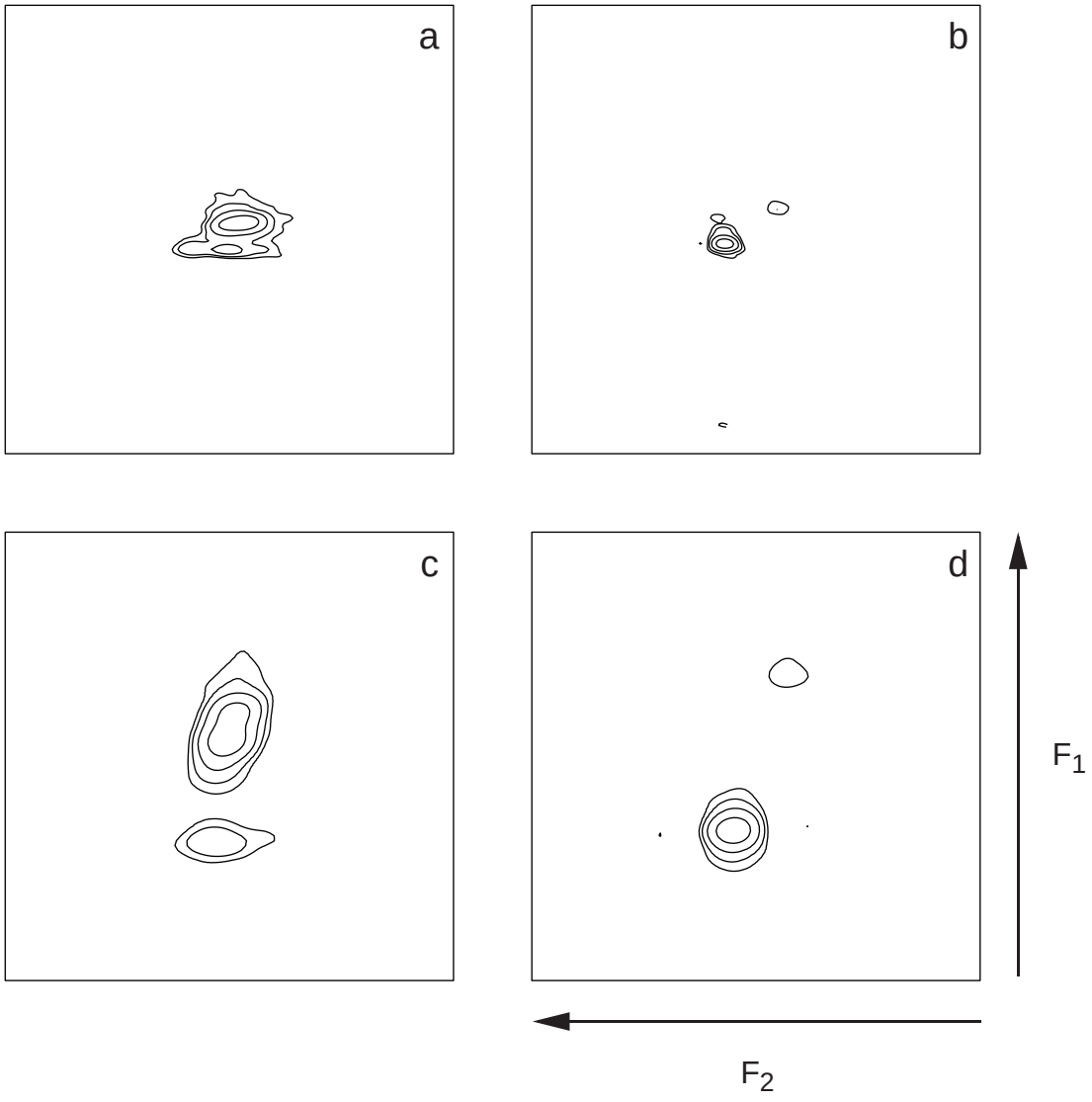

Figure 7.5. Contour plots taken from ^{27}Al (104.3 MHz) MQMAS spectra of a mixture of AlMePO-α and AlMePO-β, where the phase transformation between the two polymorphs was interrupted. The tetrahedral and octahedral regions are shown separately in (a) and (c), and (b) and (d), respectively. Spectra were obtained with, (a) and (b), the triple-quantum and, (c) and (d), the quintuple-quantum phase-modulated split-t_1 experiments of Figs. 6.10b and 7.4, respectively. In all spectra, the displayed F_1 and F_2 spectral widths equal 3 kHz. In both experiments, the full F_2 spectral width was 25 kHz, the relaxation interval was 500 ms, the spinning speed was 7.4 kHz, and the duration of the central transition inversion pulse was 60 μs, with the nutation frequency, $\omega_1/2\pi$, being reduced to 4 kHz. For the triple- and quintuple-quantum experiments, respectively, the multiple-excitation pulses were of duration 4.0 and 5.5 μs, the p = +3 to p = +1 and p = +5 to p = +1 reconversion pulses were of duration 1.0 and 1.75 μs, the spin-echo interval, τ, was 5.3 and 2.7 ms, 96 and 160 transients (consisting of 512 and 256 points) were averaged for each of 192 increments of t_1, and the full F_1 spectral width equalled 19.4 and 30.8 kHz The bottom contour in each spectrum corresponds to 8% of the maximum height.

apparent two tetrahedral sites in (a) are clearly separated in (c), where the upper peak can be seen to consist of two peaks very close together. A further interesting feature is the fact that the homogeneous linewidths in F_1 are larger in Figs. 7.5c and 7.5d (quintuple-quantum) than in Figs. 7.5a and 7.5b (triple-quantum). Further research is required to determine which factors cause this difference.

^{27}Al MQMAS spectra of the tetrahedral region for samples of pure AlMePO-α and pure AlMePO-β (again prepared by Vinton Carter) are presented in Figs. 7.6a and 7.6b (overleaf), respectively. As expected, while three distinct sites are clearly observed for the β-polymorph, only one site is observed for the α-polymorph. (The differentiation of the three tetrahedral sites in Fig. 7.6b is in agreement with spectra published by Rocha *et al.* [62] who carried out triple-quantum and quintuple-quantum simple amplitude-modulated experiments on AlMePO-β.)

The MAS spectrum of the phase-transformation interrupted mixture in Fig. 7.1 indicated that the α and β polymorphs were present in the ratio 1:2, and, therefore, it is instructive to add together the spectra due to the pure forms in this ratio; the resulting spectrum is presented in Fig. 7.6c. Comparing this spectrum with that for the phase-transformation interrupted mixture, which is repeated in Fig. 7.6d, it is apparent that the separation of the two tetrahedral peaks at higher F_1 is greater in Fig. 7.6c than in Fig. 7.6d. This is more clearly seen in Fig. 7.7 (on page 141) which presents the F_1 (isotropic) projections of the spectra in Fig. 7.6. Furthermore, an MQMAS spectrum (not shown) obtained for a physical mixture of the pure α and β polymorphs in the same ratio showed a similar clear separation of the two tetrahedral peaks at higher F_1 as that observed in Fig. 7.7c.

The question that then arises is, what insight do the observed MQMAS spectra offer with regards to the understanding of the phase transformation? There is no evidence in the spectrum of the phase-transformation interrupted

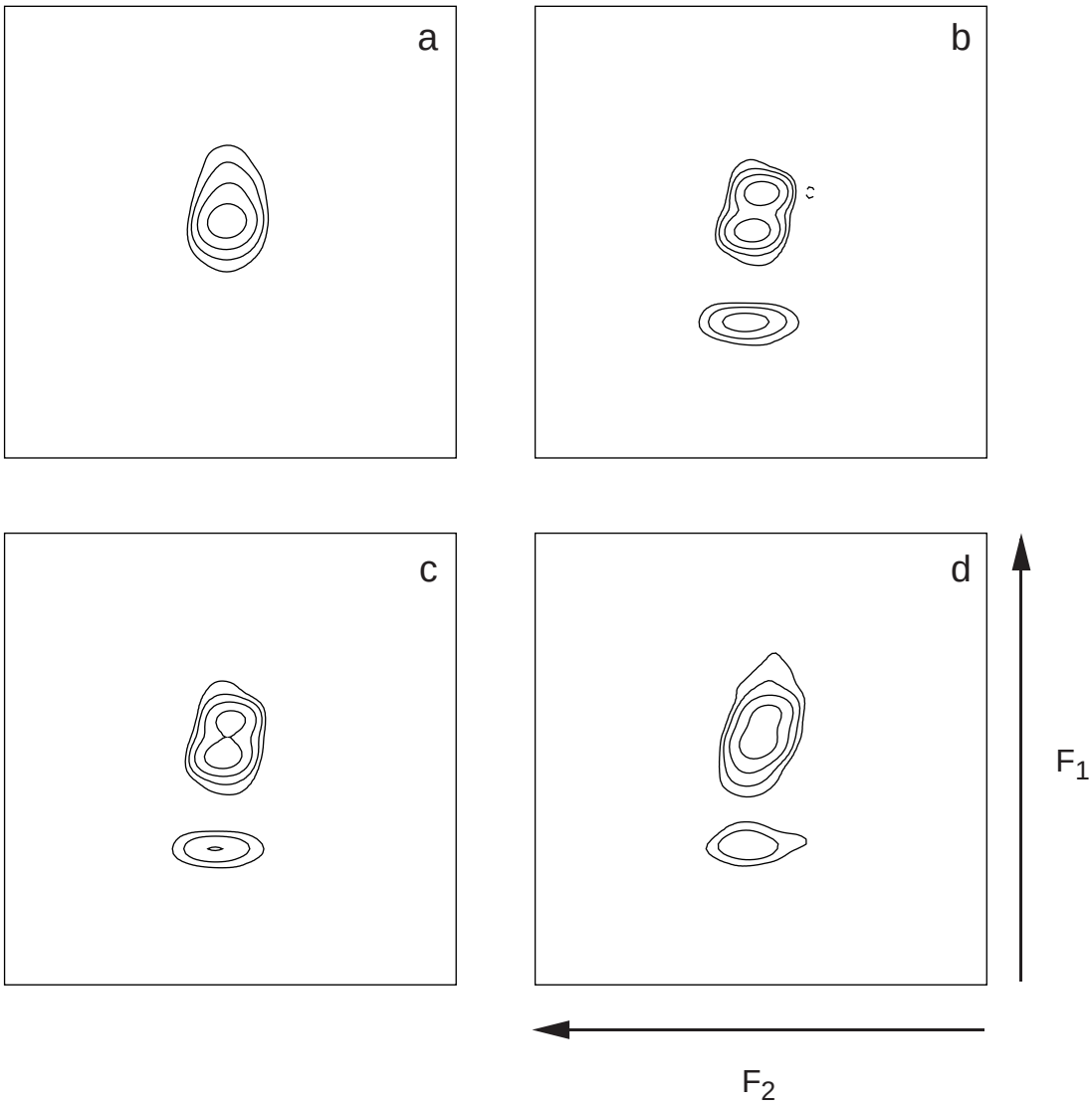

Figure 7.6. (a), (b) Contour plots corresponding to the tetrahedral region taken from ^{27}Al (104.3 MHz) MQMAS spectra of (a) pure AlMePO-α and (b) pure AlMePO-β, obtained with the quintuple-quantum phase-modulated split-t_1 experiment of Fig. 7.4. The spectrum in (a) was recorded in collaboration with Sharon Ashbrook. In all spectra, the displayed F_1 and F_2 spectral widths equal 3 kHz (cut down from 25 and 30.8 kHz, respectively). In both experiments, the relaxation interval was 500 ms, the spin-echo interval, τ, was 2.7 ms, and the p = +5 to p = +1 reconversion pulse was of duration 1.75 μs. In (a) and (b), respectively, 320 and 160 transients (consisting of 256 points) were averaged for each of 192 increments of t_1, the spinning speed was 9.0 and 7.4 kHz, the quintuple-excitation pulse was of duration 6.5 and 5.5 μs, and the duration of the central transition inversion pulse was 50 and 60 μs, with the nutation frequency, $\omega_1/2\pi$, being reduced to 5 and 4 kHz. The spectrum in (c) results from the combination of the spectra in (a) and (b) in the ratio 1:2. For comparison, (d) is a repeat of the spectrum in Fig. 7.5c for the mixture of AlMePO-α and AlMePO-β, where the phase transformation between the two polymorphs was interrupted. The bottom contour in each spectrum corresponds to 8% of the maximum height.

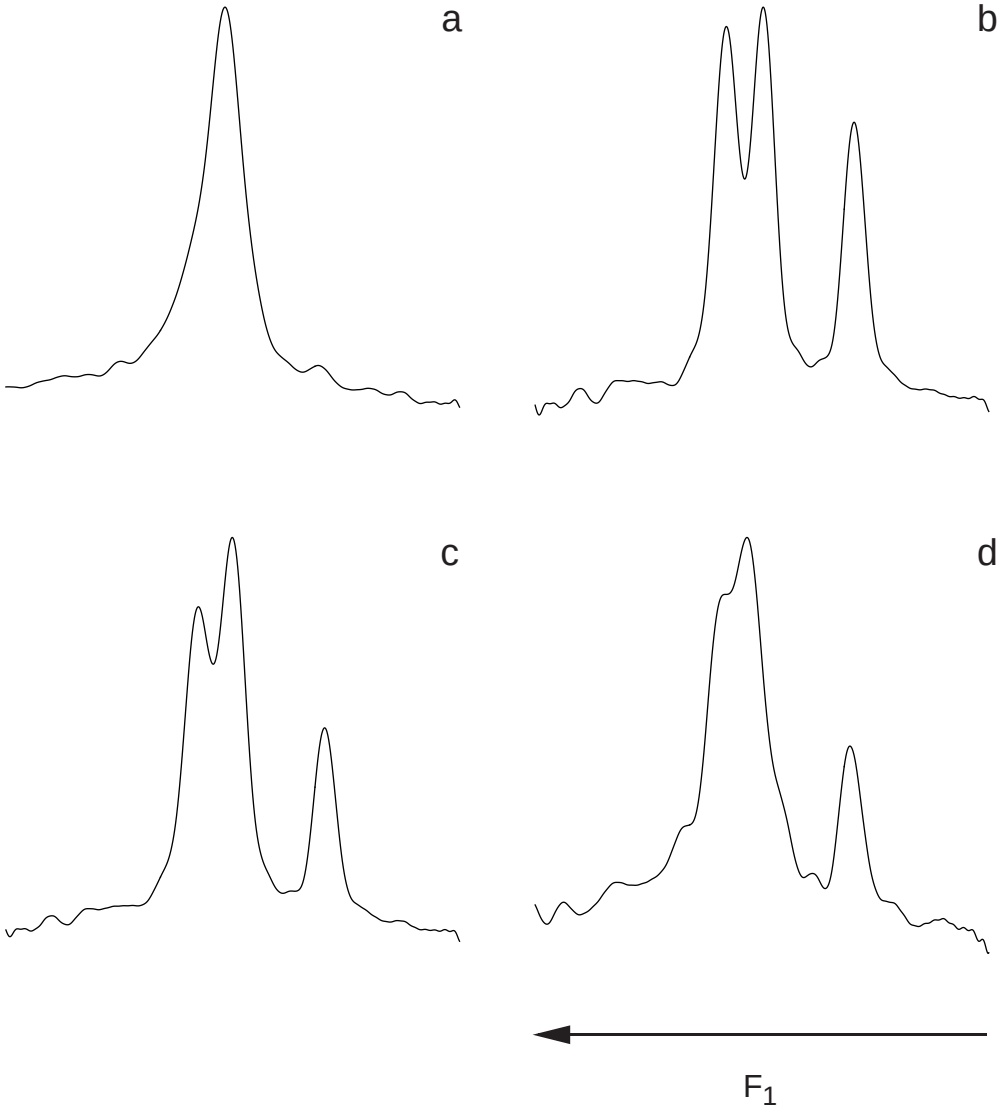

Figure 7.7. F_1 projections for the corresponding spectra presented in Fig. 7.6.

mixture of peaks not observed for the pure α and β polymorphs. This, therefore, supports the proposition that the phase transformation occurs in a topotactic fashion without the formation of a stable intermediate. The origin of the observed blurring of the tetrahedral resonances is not fully understood, but is probably a consequence of the bond-breaking and bond-forming process at the reaction boundary. It is hoped that investigation of further samples, where the phase transformation is interrupted at a different stage will provide additional evidence and information.

7.5 Extraction of the Isotropic Shifts

An interesting feature of the MQMAS technique is that the relative position of two ridges in an MQMAS spectrum varies according to the magnetic field strength, B_0, of the spectrometer. For example, compare the MQMAS spectra in Figs. 5.8d and 6.9a, which were obtained for a sample of $RbNO_3$ at Larmor frequencies of 98.2 and 130.9 MHz, respectively; it is seen that the relative separation of the three ridges is different, with the resolution being, surprisingly, better at the lower field. This phenomenon arises from the dependence of the F_1 and F_2 frequency of a ridge on the combination of the isotropic chemical shift and the isotropic second-order quadrupolar shift, which are, respectively, directly and inversely proportional to ω_0.

This dependence further explains the change in the appearance, with increasing ω_0, of the MAS spectra of $RbNO_3$, presented in Fig. 3.6. Indeed, before the advent of the MQMAS technique, the only way of extracting the two isotropic shifts was to record spectra at more than one field strength. However, the different single- and multiple-quantum evolution of the isotropic chemical shift and the isotropic second-order quadrupolar shift means that the two separate shifts can be determined from a single MQMAS spectrum [43]. The purpose of this section is then to show how the two shifts can be determined, using as an example the three resolved tetrahedral sites in the spectrum of AlMePO-β presented in Fig. 7.6b.

It is first necessary to determine the dependence of the F_1 and F_2 frequencies on the two isotropic shifts, for the spin I = 5/2 quintuple-quantum phase-modulated split-t_1 experiment in Fig. 7.4. This can be calculated by considering evolution under solely, first, the isotropic chemical shift, here represented by Ω^{cs}:

$$s(t_1, t_2) = \exp\{ -i (2\pi) \Omega^{cs} [(5 \times \frac{12}{37}) + \frac{25}{37}] t_1 \} \exp\{ +i (2\pi) \Omega^{cs} t_2 \}$$

$$= \exp\{ \frac{-i (2\pi) \Omega^{cs} 85 t_1}{37} \} \exp\{ +i (2\pi) \Omega^{cs} t_2 \} , \quad (7.1)$$

and second, the isotropic second-order quadrupolar shift:

$$s(t_1, t_2) = \exp\{ -i (2\pi) \Omega_Q^{iso} [(\frac{20}{3} \times \frac{12}{37}) - (\frac{16}{15} \times \frac{25}{37})] t_1 \} \exp\{ -i \frac{16 (2\pi) \Omega_Q^{iso}}{15} t_2 \}$$

$$= \exp\{ -i \frac{160 (2\pi) \Omega_Q^{iso}}{111} t_1 \} \exp\{ -i \frac{16 (2\pi) \Omega_Q^{iso}}{15} t_2 \} , \quad (7.2)$$

where

$$\Omega_Q^{iso} = \frac{(\omega_Q^{PAS})^2}{(2\pi) \omega_0} Q^0(\eta) . \quad (7.3)$$

The F_1 and F_2 frequencies in hertz, υ_1 and υ_2, are then given by

$$\upsilon_1 = -\frac{85}{37} \Omega^{cs} - \frac{160}{111} \Omega_Q^{iso} \quad (7.4a)$$

$$\upsilon_2 = \Omega^{cs} - \frac{16}{15} \Omega_Q^{iso} . \quad (7.4b)$$

It should be noted that Eq. (7.4) is equally valid for isotropic shifts and F_1 and F_2 frequencies in units of ppm. Analogous expressions for the dependence of υ_1 and υ_2 on Ω^{cs} and Ω_Q^{iso} are given in Appendix G for all the spin I = 3/2 and I = 5/2 MQMAS experiments presented in this thesis.

Rearranging Eqs. (7.4a) and (7.4b), it can easily be shown that

$$\Omega_Q^{iso} = -\frac{37}{144} \{ \upsilon_1 + \frac{85}{37} \upsilon_2 \} \quad (7.5a)$$

$$\Omega^{cs} = -\frac{37}{135} \{ \upsilon_1 - \frac{50}{37} \upsilon_2 \} . \quad (7.5b)$$

TABLE 7.2 Calculation of the Isotropic Shifts

υ_1/ kHz	υ_1/ ppm	υ_2/ kHz	υ_2/ ppm	Ω^{cs}/ ppm	Ω_Q^{iso} / ppm	SOQE/ MHz
–15.9	–107.1	0.5	41.6	44.8	3.0	2.4
–15.3	–101.3	0.4	41.1	43.0	1.8	1.8
–15.0	–98.6	0.3	40.1	41.9	1.6	1.8

Therefore, all that is required to calculate the two isotropic shifts, is the determination of the observed frequencies υ_1 and υ_2 in ppm units. The υ_2 values in kHz for the three sites in Fig. 7.6b are given in Table 7.2. In this case, since the second-order quadrupolar broadening is small, determining the observed isotropic shift in υ_2 is straight-forward. In other cases, it is necessary to refer to Fig. 3.4 to determine which feature of the second-order quadrupolar-broadened lineshape corresponds to the isotropic shift. To determine the frequency corresponding to zero ppm, it was necessary to perform a separate experiment in which a few drops of 1M aluminium nitrate, $Al(NO_3)_3$, were placed inside an identical 4 mm rotor inside the same probe. Using the observed zero ppm frequency of –3.86 kHz, the υ_2 values in ppm are given in Table 7.2.

It is slightly more complicated to determine the observed υ_1 values in ppm, since the scaling of the resonance offset must be taken into account. The centre of the spectrum, of which Fig. 7.6b is a part, corresponds to a frequency of –4.11 kHz, and, therefore, an aluminium site at zero ppm has a resonance offset of + 250 Hz. Thus, using Eq. (7.4a), the frequency in F_1 corresponding to zero ppm equals $\{ -4.1 + (-85/37) \times 250) \} = -4.7$ kHz. The observed υ_1 values for the three sites in Hz and ppm are given in Table 7.2. The isotropic chemical and second-order quadrupolar shifts

are then easily calculated using Eqs. (7.5a) and (7.5b), and their values are again shown in Table 7.2. A comparison to Ref. [62] reveals that the results presented in Table 7.2 are in close agreement with those obtained by Rocha *et al*.

From the isotropic second-order quadrupolar shift alone, the quadrupolar parameters C_Q and η cannot be determined separately. Instead, it is found (starting with Eq. (7.3)) that a field-independent quantity referred to as the "second-order quadrupolar effect parameter" (SOQE) is given in hertz as

$$C_Q \left(1 + \frac{\eta^2}{3} \right)^{1/2} = \frac{4\, I\, (2I - 1)\, \upsilon_0 \sqrt{\Omega_Q^{iso}}}{3 \infty 10^3} , \qquad (7.6)$$

where υ_0 is the Larmor frequency in hertz, and Ω_Q^{iso} is in units of ppm. (The numerical factor I(2I – 1) equals 3 and 10 for spin I = 3/2 and I = 5/2, respectively.) The SOQE values for the three sites in AlMePO-β are given in Table 7.2. To obtain the separate parameters C_Q and η, it is necessary to perform a fitting procedure on the individual lineshapes. For example, such a fitting procedure (performed by Sharon Ashbrook) for the site with the largest SOQE revealed the following values for the quadrupolar parameters: C_Q = 2.2 MHz and η = 0.8. These results give a SOQE in perfect agreement with the value given in Table 7.2.

7.6 Oxygen-17 MQMAS NMR

The only oxygen nuclide accessible to NMR is ^{17}O (spin I = 5/2). However, its very low natural abundance (0.037%) means that an acceptable sensitivity can only be achieved for enriched samples. In spite of the considerable effort and expense required to achieve such enrichment, the presence of oxygen in an enormous range of compounds and materials has encouraged the development of ^{17}O NMR. In the 1980s, Oldfield and co-workers presented MAS and VAS spectra of a variety of solid samples [136-138], including simple oxides, minerals, zeolites, and transition-metal carbonyls. Although individual oxygen sites are usually not fully

resolved in such spectra as a consequence of second-order quadrupolar broadening, the large spread of ^{17}O chemical shifts (approximately 600 ppm) often allows individual lineshapes to be extracted by a fitting process. In the early 1990s, Pines and co-workers showed that much higher resolution can be achieved using DAS and DOR [139, 140], such that the validity of the earlier assignment of ^{17}O sites in enriched minerals could be confirmed. Very recently, Dirken *et al.* [73] have shown that two oxygen sites in an aluminosilicate glass, which are unresolved by MAS, are clearly resolved in an ^{17}O MQMAS spectrum.

In this section, an ^{17}O MQMAS spectrum of synthesised forsterite is presented. Forsterite (Mg_2SiO_4) is closely related to a form of the mineral olivine with the composition $Mg_{1.8}Fe_{0.2}SiO_4$ which is the principal component of the earth's mantle (the region between the core and the crust). Mantle olivine is estimated to contain 1% water by weight, and there is much interest in how this water may be stored [141-143]. Although infra-red spectroscopy and ^{1}H and ^{29}Si NMR have provided useful information [144-146], a full knowledge of the mechanism and site of water incorporation remains elusive. To date, it has not been possible to directly probe the oxygen atoms themselves, and, in this context, ^{17}O MQMAS NMR offers considerable potential.

A sample of water-free ^{17}O-enriched pure forsterite was prepared by Andrew Berry (formerly at the Department of Earth Sciences, Oxford University, currently at the Research School of Earth Sciences, Australian National University, Canberra) in the following way. Starting with 35% enriched $H_2{}^{17}O$, $Mg^{17}O$ and $Si^{17}O_2$ were first synthesised. To prepare $Mg^{17}O$, $H_2{}^{17}O$ was added dropwise to Mg_3N_2 in CCl_4, under argon, and the mixture was stirred for several hours. The vigorous reaction was moderated by the solvent, CCl_4, which was removed by evaporation. The resulting powder was heated under argon at 500°C for 12 hours to give $Mg^{17}O$:

$$Mg_3N_2 + 6\ H_2{}^{17}O \ \text{---->}\ 3\ Mg(^{17}OH)_2 + 2\ NH_3 \qquad (7.7a)$$

$$Mg(^{17}OH)_2 \ \text{---->}\ Mg^{17}O + H_2{}^{17}O\ . \qquad (7.7b)$$

$Si^{17}O_2$ was prepared in the following way [139]. $H_2{}^{17}O$ was added dropwise to $SiCl_4$ and refluxed under argon for 4 hours. Excess $SiCl_4$ was removed by evaporation. Silica was obtained by heating the resulting white solid under argon at 1100°C for 12 hours:

$$SiCl_4 + 2\ H_2{}^{17}O \ \text{---->}\ Si^{17}O_2 + 4\ HCl\ . \qquad (7.8)$$

Forsterite was then synthesised by mixing together, pressing into a pellet, and heating under argon at 1500°C for 12 hours a stoichiometric amount of $Mg^{17}O$ and $Si^{17}O_2$:

$$2\ Mg^{17}O + \ Si^{17}O_2 \ \text{---->}\ Mg_2Si^{17}O_4\ . \qquad (7.9)$$

An ^{17}O MQMAS spectrum of $Mg_2Si^{17}O_4$, recorded using the triple-quantum phase-modulated split-t_1 experiment of Fig. 6.10b, is presented in Fig. 7.8 (overleaf). This spectrum was obtained in collaboration with Sharon Ashbrook. The presence of three ridges corresponding to the three crystallographically-distinct oxygen sites is clearly seen, and the resolution is much better than that achieved by DAS or DOR at the same field strength [139]. For comparison, Fig. 7.9 (on page 149) presents the MAS spectrum together with the isotropic MQMAS projection. (It should be noted that a larger spectral width is shown than that presented in Fig. 7.8.)

It has hence been established that a high-resolution ^{17}O MQMAS spectrum of forsterite can be obtained in a reasonable length of time (the total acquisition time was 7 hours.) Future work will involve an investigation of hydrated

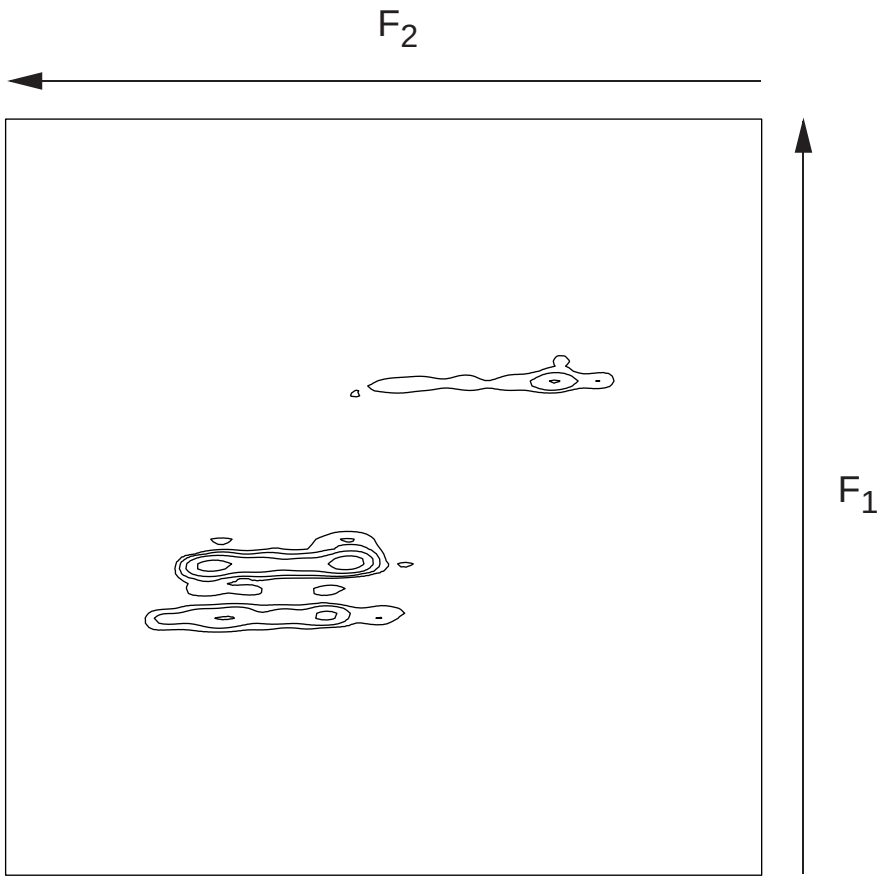

Figure 7.8. A contour plot taken from an ^{17}O (54.3 MHz) MQMAS spectrum of ^{17}O-enriched forsterite recorded using the triple-quantum phase-modulated split-t_1 experiment in Fig. 6.10b. The displayed spectral widths are 1.45 and 3.75 kHz (cut down from 9.7 and 25 kHz) in F_1 and F_2, respectively. The following experimental conditions were used: 192 transients (consisting of 512 points each) were averaged for each of 256 increments of t_1, the relaxation interval was 500 ms, and the spinning speed was 5.4 kHz. The durations of the triple-quantum excitation and the p = +3 to p = +1 conversion pulses were 9.0 and 1.5 μs, respectively. The duration of the central transition inversion pulse was 48 μs, with the nutation frequency, $\omega_1/2\pi$, being reduced to 5 kHz. The spin-echo interval, τ, was 5.3 ms.

forsterite. In particular, it is hoped that information about water incorporation can be obtained using CP MQMAS. Although cross polarisation to a quadrupolar nucleus [147-149] is less straightforward than in the more familiar abundant spin I = 1/2 (*e.g.* ^{1}H) to "dilute" spin I = 1/2 (*e.g.* ^{13}C or ^{29}Si) case, both ^{1}H-^{17}O CP MAS [138] and, more recently, ^{19}F-^{23}Al and ^{1}H-^{23}Al CP MQMAS [67, 69] have been successfully demonstrated. In the latter work, the addition of a cross-polarisation step resulted in an MQMAS spectrum in which only peaks corresponding to Al atoms directly bonded to ^{19}F or ^{1}H were observed. It is hoped that similar "spectral editing" in an

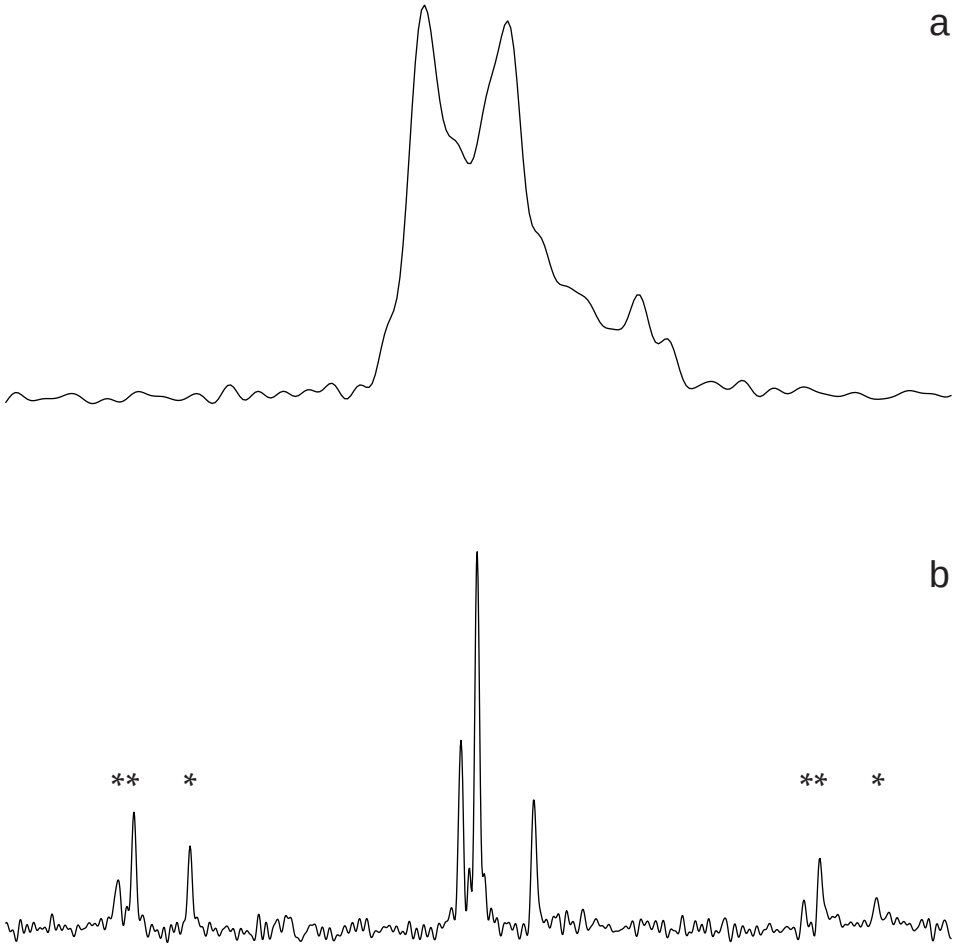

Figure 7.9. ^{17}O (54.3 MHz) (a) MAS and (b) isotropic MQMAS spectra of ^{17}O-enriched forsterite. In both cases, the displayed spectral width equals 7.5 kHz. In (a), the following experimental conditions were used: 16 transients (consisting of 1024 points) were averaged, the full spectral width was 50 kHz, the relaxation interval was 500 ms, and a radiofrequency pulse of duration 1.2 μs was used. Experimental parameters for (b) are given in Fig. 7.8. Spinning sidebands are indicated by *.

^{17}O MQMAS spectrum of hydrated forsterite will determine which oxygen sites are hydrated.

Appendix A

Density Operator Theory

A.1 The Expectation Value of an Observable

Using the expansion of $\psi(t)$ in a complete set of orthonormal basis functions described by Eq. (2.1), the expectation value of an observable, corresponding to the operator A, is given in Eq. (2.2) as

$$< A > = \sum_{s,\, r} c_s(t)\, c_r(t)^* \langle r|A|s\rangle \,. \tag{A.1}$$

If an ensemble average is considered, Eq. (A.1) becomes (by substituting in the expression in Eq. (2.3) for the definition of the density operator)

$$< A > = \sum_{s,\, r} \langle s|\sigma(t)|r\rangle \langle r|A|s\rangle \,. \tag{A.2}$$

The completeness theorem [150] states that

$$\sum_{n} |n\rangle \langle n| = 1 \,, \tag{A.3}$$

and therefore Eq. (A.2) simplifies to

$$< A > = \sum_{s} \langle s|\sigma(t)\, A|s\rangle \,. \tag{A.4}$$

The right-hand side of Eq. (A.4) simply corresponds, as stated in Eq. (2.4), to the trace of the product of the matrix representation of the operator and the density matrix, *i.e.*,

$$< A > \; = \; \mathrm{Tr}\{ A \, \sigma(t) \} \; = \; \mathrm{Tr}\{ \sigma(t) \, A \} \, . \tag{A.5}$$

A.2 The Liouville-von Neumann Equation

The time-dependent Schrödinger equation, again using the expansion of $\psi(t)$ in a complete set of orthonormal basis functions described by Eq. (2.1), is of the form

$$\sum_k \frac{dc_k(t)}{dt} \; |k\rangle \; = \; -i \, H(t) \sum_k c_k(t) \; |k\rangle \, . \tag{A.6}$$

Premultiplying by $\langle s|$, Eq. (A.6) becomes

$$\frac{dc_s(t)}{dt} \; = \; -i \; \sum_k \langle s|H(t)|k\rangle \, c_k(t) \, . \tag{A.7}$$

Similarly,

$$\frac{dc_r(t)^*}{dt} \; = \; i \; \sum_k c_k(t)^* \, \langle k|H(t)|r\rangle \, . \tag{A.8}$$

From the definition of the density operator in Eq. (2.3),

$$\frac{d\sigma_{sr}(t)}{dt} \; = \; c_s(t) \, \frac{dc_r(t)^*}{dt} \; + \frac{dc_s(t)}{dt} \; c_r(t)^* \, . \tag{A.9}$$

(Although it is not explicitly stated, an ensemble average is assumed in Eq. (A.9).) Using Eqs. (A.7) and (A.8), Eq. (A.9) becomes

$$\frac{d\sigma_{sr}(t)}{dt} = i \sum_k c_s(t)\, c_k(t)^* \langle k|H(t)|r\rangle - i \sum_k \langle s|H(t)|k\rangle\, c_k(t)\, c_r(t)^* . \qquad (A.10)$$

Again using the definition of the density operator in Eq. (2.3),

$$\frac{d\sigma_{sr}(t)}{dt} = i \sum_k \langle s|\sigma(t)|k\rangle \langle k|H(t)|r\rangle - i \sum_k \langle s|H(t)|k\rangle \langle k|\sigma(t)|r\rangle$$

$$= i \langle s|\sigma(t)\, H(t)|r\rangle - i \langle s|H(t)\, \sigma(t)|r\rangle$$

$$= i \langle s|(\, \sigma(t)\, H(t) - H(t)\, \sigma(t)\,)\, |r\rangle , \qquad (A.11)$$

where the completeness theorem of Eq. (A.3) has again been used. Thus, the Liouville-von Neumann equation,

$$\frac{d\sigma(t)}{dt} = -i\, [\, H(t), \sigma(t)\,] , \qquad (A.12)$$

is revealed.

Appendix B

Matrix Representations of the Spin Angular Momentum Operators

B.1 Spin I = 1/2

$$I_x = \frac{1}{2}\begin{pmatrix} 0 & 1 \\ 1 & 0 \end{pmatrix} \qquad I_y = \frac{i}{2}\begin{pmatrix} 0 & -1 \\ 1 & 0 \end{pmatrix} \qquad I_z = \frac{1}{2}\begin{pmatrix} 1 & 0 \\ 0 & -1 \end{pmatrix}$$

B.2 Spin I = 3/2

$$I_x = \frac{1}{2}\begin{pmatrix} 0 & \sqrt{3} & 0 & 0 \\ \sqrt{3} & 0 & 2 & 0 \\ 0 & 2 & 0 & \sqrt{3} \\ 0 & 0 & \sqrt{3} & 0 \end{pmatrix} \qquad I_y = \frac{i}{2}\begin{pmatrix} 0 & -\sqrt{3} & 0 & 0 \\ \sqrt{3} & 0 & -2 & 0 \\ 0 & 2 & 0 & -\sqrt{3} \\ 0 & 0 & \sqrt{3} & 0 \end{pmatrix}$$

$$I_z = \frac{1}{2}\begin{pmatrix} 3 & 0 & 0 & 0 \\ 0 & 1 & 0 & 0 \\ 0 & 0 & -1 & 0 \\ 0 & 0 & 0 & -3 \end{pmatrix}$$

B.3 Spin I = 5/2

$$I_x = \frac{1}{2}\begin{pmatrix} 0 & \sqrt{5} & 0 & 0 & 0 & 0 \\ \sqrt{5} & 0 & \sqrt{8} & 0 & 0 & 0 \\ 0 & \sqrt{8} & 0 & 3 & 0 & 0 \\ 0 & 0 & 3 & 0 & \sqrt{8} & 0 \\ 0 & 0 & 0 & \sqrt{8} & 0 & \sqrt{5} \\ 0 & 0 & 0 & 0 & \sqrt{5} & 0 \end{pmatrix}$$

$$I_y = \frac{i}{2}\begin{pmatrix} 0 & -\sqrt{5} & 0 & 0 & 0 & 0 \\ \sqrt{5} & 0 & -\sqrt{8} & 0 & 0 & 0 \\ 0 & \sqrt{8} & 0 & -3 & 0 & 0 \\ 0 & 0 & 3 & 0 & -\sqrt{8} & 0 \\ 0 & 0 & 0 & \sqrt{8} & 0 & -\sqrt{5} \\ 0 & 0 & 0 & 0 & \sqrt{5} & 0 \end{pmatrix}$$

$$I_z = \frac{1}{2}\begin{pmatrix} 5 & 0 & 0 & 0 & 0 & 0 \\ 0 & 3 & 0 & 0 & 0 & 0 \\ 0 & 0 & 1 & 0 & 0 & 0 \\ 0 & 0 & 0 & -1 & 0 & 0 \\ 0 & 0 & 0 & 0 & -3 & 0 \\ 0 & 0 & 0 & 0 & 0 & -5 \end{pmatrix}$$

Appendix C

Larmor Frequencies

The table below gives the Larmor frequencies on the AC 300 (7.05 T), MSL 400 (9.40 T), and MSL 500 (11.75T) spectrometers for the nuclei observed in this thesis (and also ^{1}H for comparison). Brackets indicate that spectra are not presented for a particular nucleus at a particular field strength.

Nucleus	Larmor frequency/MHz		
	7.05 T	9.40 T	11.75 T
^{1}H	(300.0)	(400.0)	(500.0)
^{17}O	(40.7)	54.2	(67.8)
^{23}Na	(79.4)	105.8	(132.3)
^{27}Al	(78.2)	104.3	130.3
^{87}Rb	98.2	130.9	163.6

Appendix D

Matrix Representations of the Spherical Tensor Operators

This appendix presents the matrix representations of the spin I = 3/2 tensor operators relevant to the calculation in Section 3.1. The matrix elements are normalised according to the convention of Müller *et al.* [151], which also presents the matrix representations of all spin I = 1/2, I = 1, and I = 3/2 tensor operators. (The matrix representations of the spin I = 5/2 tensor operators can be found in Ref. [152].)

$$T_{2,0} = \frac{1}{2}\begin{pmatrix} 1 & 0 & 0 & 0 \\ 0 & -1 & 0 & 0 \\ 0 & 0 & -1 & 0 \\ 0 & 0 & 0 & 1 \end{pmatrix}$$

$$T_{2,+1} = \frac{1}{\sqrt{2}}\begin{pmatrix} 0 & -1 & 0 & 0 \\ 0 & 0 & 0 & 0 \\ 0 & 0 & 0 & 1 \\ 0 & 0 & 0 & 0 \end{pmatrix} \qquad T_{2,-1} = \frac{1}{\sqrt{2}}\begin{pmatrix} 0 & 0 & 0 & 0 \\ 1 & 0 & 0 & 0 \\ 0 & 0 & 0 & 0 \\ 0 & 0 & -1 & 0 \end{pmatrix}$$

$$T_{2,+2} = \frac{1}{\sqrt{2}}\begin{pmatrix} 0 & 0 & 1 & 0 \\ 0 & 0 & 0 & 1 \\ 0 & 0 & 0 & 0 \\ 0 & 0 & 0 & 0 \end{pmatrix} \qquad T_{2,-2} = \frac{1}{\sqrt{2}}\begin{pmatrix} 0 & 0 & 0 & 0 \\ 0 & 0 & 0 & 0 \\ 1 & 0 & 0 & 0 \\ 0 & 1 & 0 & 0 \end{pmatrix}$$

Appendix E

Reduced Rotation Matrix Elements

This appendix lists the reduced rotation matrix elements relevant to the calculations in Chapter 3. A comprehensive listing is given in Refs. [95, 153].

***l* = 2**

$$d^2_{0,0}(\beta) = (1/2)\,(3\cos^2\beta - 1)$$

$$d^2_{0,-1}(\beta) = d^2_{1,0}(\beta) = -d^2_{0,1}(\beta) = -d^2_{-1,0}(\beta) = -\sqrt{(3/2)}\,\sin\beta\,\cos\beta$$

$$d^2_{0,2}(\beta) = d^2_{2,0}(\beta) = d^2_{0,-2}(\beta) = d^2_{-2,0}(\beta) = \sqrt{(3/8)}\,\sin^2\beta$$

***l* = 4**

$$d^4_{0,0}(\beta) = (1/8)\,(35\cos^4\beta - 30\cos^2\beta + 3)$$

$$d^4_{0,2}(\beta) = d^4_{0,-2}(\beta) = -(\sqrt{10}/64)\,(7\cos^4\beta - 4\cos^2\beta - 3)$$

$$d^4_{0,4}(\beta) = d^4_{0,-4}(\beta) = (\sqrt{70}/128)\,(\cos^4\beta - 4\cos^2\beta + 3)$$

Appendix F

Shearing – An Analytical Study

An inhomogeneously-broadened lineshape is the sum of a very large number of homogeneous lineshapes with a distribution of resonance frequencies Ω [87]. Analytically, this summation corresponds to evaluating the convolution integral of the two-dimensional lineshape and a function $P(\omega)$ describing the inhomogeneous distribution of frequencies. The form of $P(\omega)$ used here is the very simplest one – a constant amplitude function between limits $-\Omega_L$ and $+\Omega_L$ and zero everywhere else:

$$P(\omega) = 1 \text{ for } -\Omega_L \leq \omega \leq +\Omega_L \quad ; \quad P(\omega) = 0 \text{ elsewhere.} \tag{F.1}$$

Consider first the case where the inhomogeneous distribution lies along the $\omega_1 = \omega_2$ axis. Using the expression for an absorptive Lorentzian lineshape given in Eq. (2.14a), the resulting two-dimensional lineshape is given by

$$L_2^{DIAG}(\omega_1, \omega_2) = \int_{-\Omega_L}^{+\Omega_L} \frac{1}{(R^2 + (\omega_1 - \Omega)^2)\,(R^2 + (\omega_2 - \Omega)^2)}\, d\Omega$$

$$= (A + B)/C\,, \tag{F.2}$$

where

$$A = (\omega_1 - \omega_2)\left(\tan^{-1}\left(\frac{\Omega_L + \omega_1}{R}\right) + \tan^{-1}\left(\frac{\Omega_L - \omega_1}{R}\right) + \tan^{-1}\left(\frac{\Omega_L + \omega_2}{R}\right) + \tan^{-1}\left(\frac{\Omega_L - \omega_2}{R}\right)\right)$$

$$B = R \ln\left(\frac{(R^2 + (\Omega_L + \omega_1)^2)\,(R^2 + (\Omega_L - \omega_2)^2)}{(R^2 + (\Omega_L - \omega_1)^2)\,(R^2 + (\Omega_L + \omega_2)^2)}\right)$$

$$C = R\,(\omega_1 - \omega_2)\,(4R^2 + (\omega_1 - \omega_2)^2)\,. \qquad \text{(F.3)}$$

Performing a shearing transformation on the expression in Eq. (F.2) corresponds to making the change of variable:

$$\omega_1' = \frac{\omega_1 - \omega_2}{2}\,. \qquad \text{(F.4)}$$

In addition, it is necessary to include a factor of two corresponding to the different normalisation factor associated with the convolution. The resulting sheared lineshape then becomes

$$L_2^{SHEAR}(\omega_1', \omega_2) = (A' + B')/C'\,, \qquad \text{(F.5)}$$

where

$$A' = 2\omega_1'\left(\tan^{-1}\left(\frac{\Omega_L + \omega_1^*}{R}\right) + \tan^{-1}\left(\frac{\Omega_L - \omega_1^*}{R}\right) + \tan^{-1}\left(\frac{\Omega_L + \omega_2}{R}\right) + \tan^{-1}\left(\frac{\Omega_L - \omega_2}{R}\right)\right)$$

$$B' = R \ln\left(\frac{(R^2 + (\Omega_L + \omega_1^*)^2)\,(R^2 + (\Omega_L - \omega_2)^2)}{(R^2 + (\Omega_L - \omega_1^*)^2)\,(R^2 + (\Omega_L + \omega_2)^2)}\right)$$

$$C' = 4\,R\,\omega_1'\,(R^2 + \omega_1'^2)\,, \qquad \text{(F.6)}$$

with ω_1^* equal to $2\omega_1' + \omega_2$.

It is then necessary to derive the analogous expression for the case where the inhomogeneous distribution lies along the $\omega_1 = 0$ axis (*i.e.*, the inhomogeneous broadening has been removed in ω_1); the resulting two-dimensional lineshape is then given by

$$L_2^{PAR}(\omega_1, \omega_2) = \int_{-\Omega_L}^{+\Omega_L} \frac{1}{(R^2 + \omega_1^2)\,(R^2 + (\omega_2 - \Omega)^2)}\, d\Omega$$

$$= \frac{1}{R\,(R^2 + \omega_1^2)} \left(\tan^{-1}\left(\frac{\Omega_L + \omega_2}{R}\right) + \tan^{-1}\left(\frac{\Omega_L - \omega_2}{R}\right)\right) . \qquad \text{(F.7)}$$

Inspection of Eqs. (F.6) and (F.7) reveals that the mathematical forms of the two lineshapes are not the same, and therefore shearing has distorted the lineshape. However, in the limit where $\Omega_L >> R, \omega_1, \omega_2$, *i.e.*, when the inhomogeneous broadening is much larger than the homogeneous broadening, the two lineshapes are equivalent:

$$L_2^{PAR}(\omega_1, \omega_2) = \frac{\pi}{R\,(R^2 + \omega_1^2)} \qquad \text{(F.8a)}$$

$$L_2^{SHEAR}(\omega_1', \omega_2) = \frac{\pi}{R\,(R^2 + (\omega_1')^2)} \; . \qquad \text{(F.8b)}$$

Appendix G

Determination of the Isotropic Shifts

Equations (7.4a) and (7.4b) described the dependence of the resonance frequencies in the F_1 and F_2 dimensions, υ_1 and υ_2, on the isotropic chemical and second-order quadrupolar shifts, Ω^{cs} and Ω_Q^{iso}, for the quintuple-quantum phase-modulated split-t_1 experiment in Fig. 7.4. This appendix then gives expressions for all the spin I = 3/2 and I = 5/2 MQMAS experiments presented in this thesis:

G.1 Simple Amplitude-Modulated (unsheared spectrum)

Identical expressions are obtained for the *z*-filtered simple amplitude-modulated experiment, the amplitude-modulated whole-echo experiment, and phase-modulated whole-echo experiments with p = –3 evolution during t_1. For phase-modulated whole-echo experiments with p = +3 evolution during t_1, the sign of the υ_1 frequency is reversed. The observed υ_1 frequencies after shearing are the same as those given in Section G.2 for the amplitude-modulated split-t_1 experiments.

G.1.1 Spin I = 3/2

$$\upsilon_1 = 3\,\Omega^{cs} + \frac{6}{5}\,\Omega_Q^{iso} \qquad \text{(G.1a)}$$

$$\upsilon_2 = \Omega^{cs} - \frac{2}{5}\,\Omega_Q^{iso} \; . \qquad \text{(G.1b)}$$

G.1.2 Spin I = 5/2 Triple-Quantum

$$\upsilon_1 = 3\,\Omega^{cs} - \frac{4}{5}\,\Omega_Q^{iso} \tag{G.2a}$$

$$\upsilon_2 = \Omega^{cs} - \frac{16}{15}\,\Omega_Q^{iso} \quad . \tag{G.2b}$$

G.1.3 Spin I = 5/2 Quintuple-Quantum

$$\upsilon_1 = 5\,\Omega^{cs} + \frac{20}{3}\,\Omega_Q^{iso} \tag{G.3a}$$

$$\upsilon_2 = \Omega^{cs} - \frac{16}{15}\,\Omega_Q^{iso} \quad . \tag{G.3b}$$

G.2 Split-t_1 Experiments

The expressions given here are for the phase-modulated split-t_1 experiments with p = +3 evolution during t_1. For amplitude-modulated experiments, the sign of the υ_1 frequency is simply reversed.

G.2.1 Spin I = 3/2

$$\upsilon_1 = -\frac{17}{8}\,\Omega^{cs} - \frac{1}{2}\,\Omega_Q^{iso} \tag{G.4a}$$

$$\upsilon_2 = \Omega^{cs} - \frac{2}{5}\,\Omega_Q^{iso} \quad . \tag{G.4b}$$

G.2.2 Spin I = 5/2 Triple-Quantum

$$\upsilon_1 = -\frac{17}{31}\,\Omega^{cs} - \frac{32}{93}\,\Omega_Q^{iso} \tag{G.5a}$$

$$\upsilon_2 = \Omega^{cs} - \frac{16}{15}\,\Omega_Q^{iso} \quad . \tag{G.5b}$$

G.2.3 Spin I = 5/2 Quintuple-Quantum

$$\upsilon_1 = -\frac{85}{37}\,\Omega^{cs} - \frac{160}{111}\,\Omega_Q^{iso} \qquad \text{(G.6a)}$$

$$\upsilon_2 = \Omega^{cs} - \frac{16}{15}\,\Omega_Q^{iso} \quad . \qquad \text{(G.6b)}$$

Appendix H

Phase Cycling

This appendix lists phase cycles for all the MQMAS experiments described in this thesis. The design of a phase cycle to select a desired coherence transfer pathway (or pathways) is simplified by the following two rules [86]:

(i) If the phase of a pulse or group of pulses is shifted by ϕ, then a coherence undergoing a change in coherence order of $\Delta p = p' - p$ experiences a phase shift of $-\phi\Delta p$, as detected by the receiver.

(ii) If a phase cycle uses steps of $360°/N$, then, along with the desired pathway Δp, pathways $\Delta p \pm nN$, where $n = 1, 2, 3, ...$, will also be selected. All other pathways will be suppressed.

TABLE H1

Examples of phase cycles for experiments in Figs. 5.1a and 5.11

Simple Echo Experiment (Spin I = 3/2) (Fig. 5.1a)

ϕ_1 : 0° 30° 60° 90° 120° 150° 180° 210° 240° 270° 300° 330°
ϕ_2 : 0°
R_x : 0° 90° 180° 270°

Simple Antiecho Experiment (Spin I = 3/2) (Fig. 5.1a)

ϕ_1 : 0° 30° 60° 90° 120° 150° 180° 210° 240° 270° 300° 330°
ϕ_2 : 0°
R_x : 0° 270° 180° 90°

Simple Amplitude-Modulated Experiment (Fig. 5.1a)

ϕ_1 : 0° 60° 120° 180° 240° 300° 90° 150° 210° 270° 330° 30°
180° 240° 300° 0° 60° 120° 270° 330° 30° 90° 150° 210°
ϕ_2 : 6 (90°) 6 (180°) 6 (270°) 6 (0°)
R_x : 3 (0° 180°) 3 (90° 270°) 3 (180° 0°) 3 (270° 90°)

Simple Amplitude-Modulated Experiment with z-filter (Fig. 5.11)

ϕ_1 : 0° 60° 120° 180° 240° 300°
ϕ_2 : 0°
ϕ_3 : 6 (0°) 6 (90°) 6 (180°) 6 (270°)
R_x : 3 (0° 180°) 3 (90° 270°) 3 (180° 0°) 3 (270° 90°)

TABLE H2

Examples of phase cycles for experiments in Fig. 5.1b

Shifted-Echo Experiment (Spin I = 3/2)

ϕ_1 : 0° 30° 60° 90° 120° 150° 180° 210° 240° 270° 300° 330°

ϕ_2 : 0°

ϕ_3 : 12 (0°) 12 (45°) 12 (90°) 12 (135°)
12 (180°) 12 (225°) 12 (270°) 12 (315°)

R_x : 3 (0° 90° 180° 270°) 3 (90° 180° 270° 0°)
3 (180° 270° 0° 90°) 3 (270° 0° 90° 180°)

Shifted-Antiecho Experiment (Spin I = 3/2)

ϕ_1 : 0° 30° 60° 90° 120° 150° 180° 210° 240° 270° 300° 330°

ϕ_2 : 0°

ϕ_3 : 12 (0°) 12 (45°) 12 (90°) 12 (135°)
12 (180°) 12 (225°) 12 (270°) 12 (315°)

R_x : 3 (0° 270° 180° 90°) 3 (90° 0° 270° 180°)
3 (180° 90° 0° 270°) 3 (270° 180° 90° 0°)

Amplitude-Modulated Whole-Echo Experiment

ϕ_1 : 0° 60° 120° 180° 240° 300°

ϕ_2 : 0°

ϕ_3 : 6 (90°) 6 (135°) 6 (180°) 6 (225°)
6 (270°) 6 (315°) 6 (0°) 6 (45°)

R_x : 3 (0° 180°) 3 (90° 270°) 3 (180° 0°) 3 (270° 90°)

TABLE H3

Examples of phase cycles for experiments in Figs. 6.3 and 6.10a

---

Amplitude-Modulated Split-t_1 Experiment with z filter (Spin I = 3/2) (Fig. 6.3a)

ϕ_1 : 0° 60° 120° 180° 240° 300°
ϕ_2 : 24 (0°) 24 (90°) 24 (180°) 24 (270°)
ϕ_3 : 0°
ϕ_4 : 6 (0°) 6 (90°) 6 (180°) 6 (270°)
R_x : 3 (0° 180°) 3 (90° 270°) 3 (180° 0°) 3 (270° 90°)
3 (180° 0°) 3 (270° 90°) 3 (0° 180°) 3 (90° 270°)

Amplitude-Modulated Split-t_1 Experiment (Spin I = 3/2) (Fig. 6.3b)

ϕ_1 : 4 (0° 60° 120° 180° 240° 300°) 4 (90° 150° 210° 270° 330° 30°)
4 (180° 240° 300° 0° 60° 120°) 4 (270° 330° 30° 90° 150° 210°)
ϕ_2 : 6 (0°) 6 (90°) 6 (180°) 6 (270°) 6 (90°) 6 (180°) 6 (270°) 6 (0°)
6 (180°) 6 (270°) 6 (0°) 6 (90°) 6 (270°) 6 (0°) 6 (90°) 6 (180°)
ϕ_3 : 24 (90°) 24 (180°) 24 (270°) 24 (0°)
R_x : 3 (0° 180°) 3 (180° 0°) 3 (0° 180°) 3 (180° 0°)
3 (90° 270°) 3 (270° 90°) 3 (90° 270°) 3 (270° 90°)
3 (180° 0°) 3 (0° 180°) 3 (180° 0°) 3 (0° 180°)
3 (270° 90°) 3 (90° 270°) 3 (270° 90°) 3 (90° 270°)

Amplitude-Modulated Split-t_1 Experiment (Spin I = 5/2) (Fig. 6.10a)

ϕ_1 : 0° 60° 120° 180° 240° 300°
ϕ_2 : 24 (0°) 24 (45°) 24 (90°) 24 (135°)
24 (180°) 24 (225°) 24 (270°) 24 (315°)
ϕ_3 : 0°
ϕ_4 : 6 (0°) 6 (90°) 6 (180°) 6 (270°)
R_x : 3 (0° 180°) 3 (90° 270°) 3 (180° 0°) 3 (270° 90°)
3 (180° 0°) 3 (270° 90°) 3 (0° 180°) 3 (90° 270°)

TABLE H4

Examples of phase cycles for quintuple-quantum experiments

Simple Amplitude-Modulated Experiment with z-filter

ϕ_1 : 0° 36° 72° 108° 144° 180° 216° 252° 288° 324°
ϕ_2 : 0°
ϕ_3 : 10 (0°) 10 (90°) 10 (180°) 10 (270°)
R_x : 5 (0° 180°) 5 (90° 270°) 5 (180° 0°) 5 (270° 90°)

Phase-Modulated Split-t_1 Experiment (Fig. 7.4)

ϕ_1 : 0° 18° 36° 54° 72° 90° 108° 126° 144° 162°
180° 198° 216° 234° 252° 270° 288° 306° 324° 342°
ϕ_2 : 0°
ϕ_3 : 20(0°) 20 (45°) 20 (90°) 20 (135°)
20 (180°) 20 (225°) 20 (270°) 20 (315°)
R_x : 5 (0° 270° 180° 90°) 5 (90° 0° 270° 180°)
5 (180° 90° 0° 270°) 5 (270° 180° 90° 0°)

Appendix I

Further Effects of Sample Rotation

The removal of second-rank anisotropic broadening by MAS is an integral part of the MQMAS experiment, and the effect of MAS on one-dimensional spectra was discussed at length in Chapter 3. The purpose of this Appendix is to discuss two further effects of MAS.

I.1 Spinning Sidebands in F_1

An obvious feature of many of the MQMAS spectra presented in this thesis (*e.g.,* Figs. 5.10, 6.2, 6.6, 6.8, 6.11, 6.12, and 7.9b) is the extensive spinning sideband manifold in F_1. In particular, it is found that the F_1 spinning sidebands extend significantly further than those in F_2. Marinelli and Frydman [78] have recently presented an explanation for this phenomenon. They have shown that the observed patterns can be explained solely in terms of a first-order approximation for the quadrupolar contribution to the energy levels. In this case, there is no evolution of the central transition during either t_1 or t_2. Instead, spinning sidebands arise as a consequence of the dependence of the excitation of multiple-quantum coherence and its subsequent reconversion to single-quantum coherence on the instantaneous orientation of a crystallite with respect to the B_0 magnetic field.

The origin of extensive spinning sidebands in F_1 can be understood in the following way. Unless the duration of a t_1 evolution period is an integral number of rotor periods, each crystallite is at a different orientation, described by the angle ($\xi - \omega_r t$) in Eq. (3.21), at the start and end of the evolution period. This difference in

orientation gives rise to different values of ω_Q, which govern the efficiency of excitation and reconversion of multiple-quantum coherence. Moreover, this difference in ω_Q (which is a function of the spinning speed) is modulated as t_1 is incremented, hence explaining the existence of spinning sidebands in F_1. The dependence of this mechanism on first-order rather than second-order quadrupolar terms in the Hamiltonian (as shown in Chapter 3, the latter determine the appearance of the spinning sideband manifold in F_2) explains the greater preponderance of spinning sidebands in F_1. It is interesting to note that a similar mechanism has been proposed by Spiess and co-workers [119] to explain the observed F_1 spinning sidebands in double-quantum filtered MAS spectra of dipolar-coupled abundant spin I = 1/2 nuclei.

For the experiments presented in Chapter 5, where only triple-quantum evolution occurs during t_1, spinning sidebands are predicted to appear at integer multiples of the spinning speed. However, in some spectra (*e.g.*, Figs. 5.10, 6.2, 6.6, and 6.11), additional anomalous peaks are observed. As an example, Fig. I.1 presents the F_1 projection for the octahedral site in γ-alumina (taken from Fig. 5.10b). In addition to the genuine spinning sidebands (indicated by *) at the spinning speed,

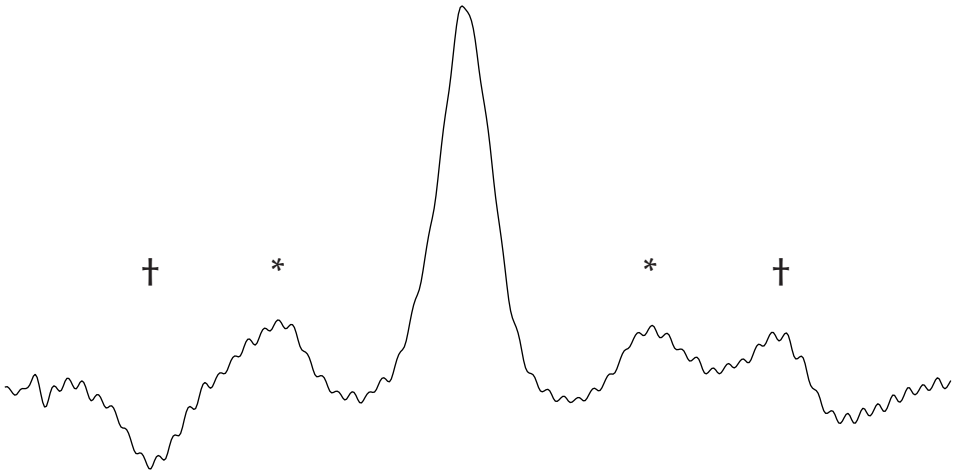

Figure I.1. The F_1 projection of the part of the spectrum in Fig. 5.10b corresponding to the octahedral site in γ-alumina. The displayed spectral width equals 50 kHz. The positions of genuine spinning sidebands, at the spinning speed (8.9 kHz), are labelled by *. TPPI artefacts are labelled by †.

8.9 kHz, two peaks are observed either side of the centreband at 16.5 kHz (indicated by †). Further work showed that the position of these anomalous peaks in this and other spectra was independent of the spinning speed. These peaks have only been observed for amplitude-modulated experiments recorded using TPPI, and are believed to arise as a consequence of a systematic error in the way the spectrometer implements the TPPI phase shift.

For split-t_1 experiments where the single-quantum part of the t_1 evolution period is separated from the acquisition period by a pulse or group of pulses, two sets of F_1 spinning sidebands corresponding to single- and multiple-quantum evolution are expected to arise. This is indeed observed in Figs. 6.2c, 6.6c, 6.8, and 6.11c. (Care must be taken in the interpretation of Fig. 6.2c, since the position of the first pair of single-quantum spinning sidebands corresponds to the position of the TPPI artefacts in Fig. 6.2b.) For the optimum spin I = 5/2 phase-modulated triple-quantum split-t_1 experiment, the single-quantum part of the t_1 evolution period follows the final pulse, and hence only triple-quantum spinning sidebands are observed in F_1 (see Figs. 6.12 and 7.9b).

I.2 Rotor-Synchronised Spin Echoes

For whole-echo experiments, care must be taken to ensure that the spin-echo interval, τ, is an integral number of rotor periods [43, 53]. (The length of the reduced-power central transition inversion pulse must also be taken into account.) Otherwise, a reduction in sensitivity is observed. This can be seen in Fig. I.2 (overleaf), which presents plots of the observed signal as a function of the spin-echo interval τ for the simple spin-echo (Fig. 2.3a) and the triple-quantum spin I = 3/2 shifted-antiecho (solid pathway in Fig. 3.1b) experiments. Maximum sensitivity is observed for τ equals 330 μs (one rotor period) in Figs. I.2a and I.2b, and τ equals 4950 μs (15 rotor periods) in Fig. I.2c.

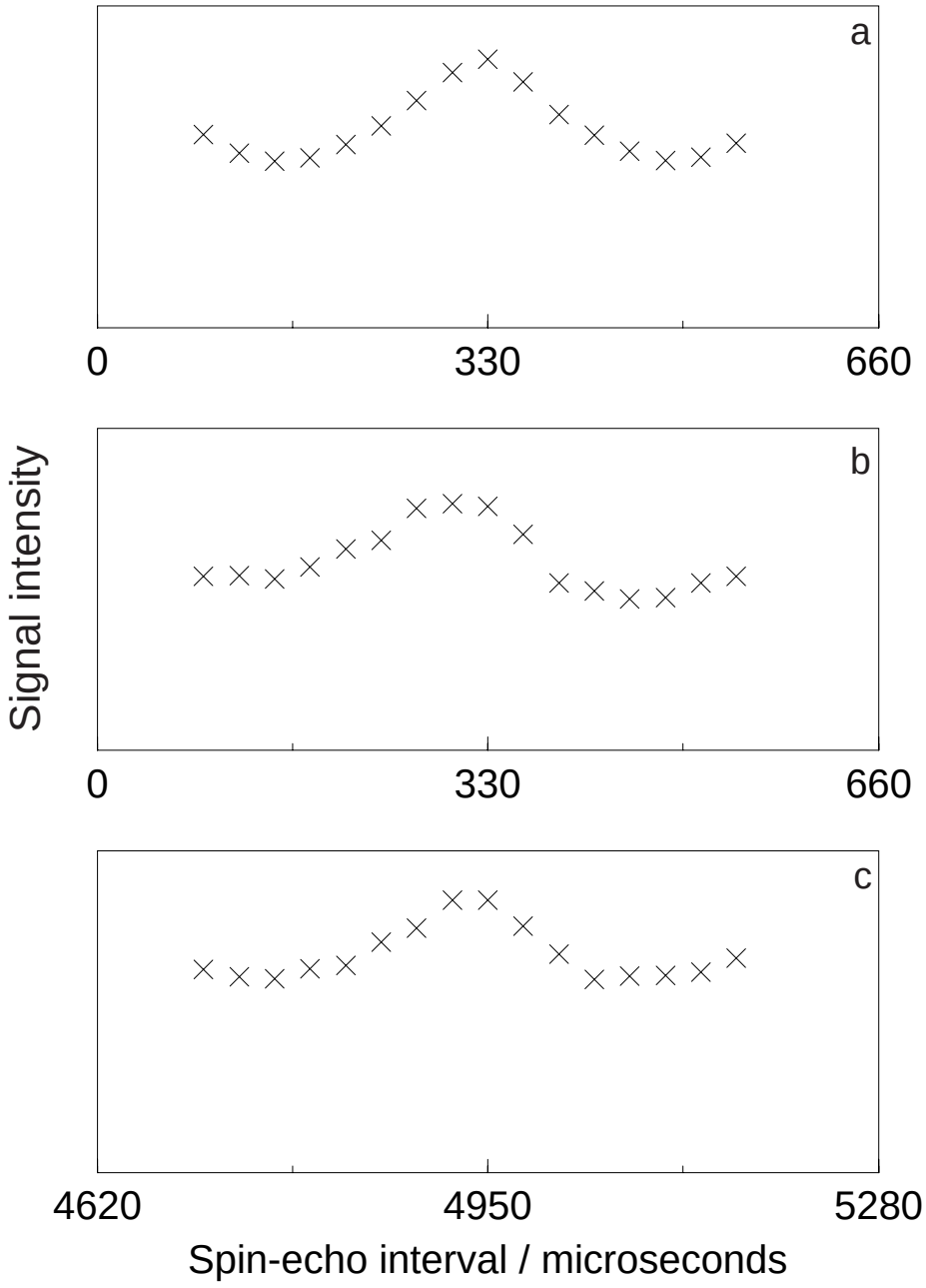

Figure I.2. Experimental ^{87}Rb (130.2 MHz) results for $RbNO_3$ showing how the frequency-domain signal intensity varies as a function of the spin-echo interval, τ, for (a) the simple spin-echo experiment in Fig. 2.3a, and (b) and (c) the triple-quantum spin I = 3/2 shifted-antiecho (solid pathway in Fig. 3.1b) experiments. In all plots, the vertical scale is linear, with the origin corresponding to zero. In all experiments, the spinning speed was 3.032 kHz, corresponding to a rotor period of 330 μs. The following experimental conditions were used: the spectral width was 50 kHz in (a) and (b) and 29.4 kHz in (c), 32 in (a) and 96 in (b) and (c) transients (consisting of 512 points) were averaged, the relaxation interval was 100 ms. In (a), the first pulse was of duration 1.2 μs, while the triple-quantum excitation and p = +3 to p = +1 conversion pulses in (b) and (c) were of duration 7 and 1.2 μs, respectively. In each case, the central transition inversion pulse was of duration 40 μs, with the radiofrequency field strength, $\omega_1/2\pi$, being reduced to 6 kHz.

REFERENCES

1. F. Bloch, W. W. Hansen, and M. Packard, *Phys. Rev*. **69**, 127 (1946).

2. E. M. Purcell, H. C. Torrey, and R. V. Pound, *Phys. Rev*. **69**, 37 (1946).

3. E. R. Andrew, A. Bradbury, and R. G. Eades, *Nature* **182**, 1659 (1958).

4. E. R. Andrew, A. Bradbury, and R. G. Eades, *Nature* **183**, 1802 (1959).

5. I. J. Lowe, *Phys. Rev. Lett.* **2**, 285 (1959).

6. M. Lee and W. I. Goldburg, *Phys. Rev.* **140**, A1261 (1965).

7. J. S. Waugh, L. M. Huber, and U. Haeberlen, *Phys. Rev. Lett.* **20**, 180 (1968).

8. U. Haeberlen and J. S. Waugh, *Phys. Rev.* **175**, 453 (1968).

9. P. Mansfield, M. J. Orchard, D. C. Stalker, and K. H. B. Richards, *Phys. Rev.* **B7**, 90 (1973).

10. W.-K. Rhim, D. D. Elleman, and R. W. Vaughan, *J. Chem. Phys.* **58**, 1772 (1973).

11. W.-K. Rhim, D. D. Elleman, and R. W. Vaughan, *J. Chem. Phys.* **59**, 3740 (1973).

12. D. P. Burum and W.-K. Rhim, *J. Chem. Phys.* **71**, 944 (1979).

13. D. P. Burum, M. Linder, and R. R. Ernst, *J. Magn. Reson.* **44**, 173 (1981).

14. A. Pines, M. G. Gibby, and J. S. Waugh, *J. Chem. Phys.* **56**, 1776 (1971).

15. A. Pines, M. G. Gibby, and J. S. Waugh, *J. Chem. Phys.* **59**, 569 (1973).

16. S. R. Hartmann and E. L. Hahn, *Phys. Rev.* **128**, 2042 (1962).

17. J. Schaefer, E. O. Stejskal, and R. Buchdahl, *Macromolecules* **8**, 291 (1975).

18. J. Schaefer and E. O. Stejskal, *J. Am. Chem. Soc.* **98**, 1031 (1976).

19. J. Schaefer, E. O. Stejskal, and R. Buchdahl, *Macromolecules* **10**, 385 (1977).

20. E. O. Stejskal, J. Schaefer, and J. S. Waugh, *J. Magn. Reson.* **28**, 105 (1977).

21. M. Mehring, A. Pines, W.-K. Rhim, and J. S. Waugh, *J. Chem. Phys.* **54**, 3239 (1971).

22. F. Bloch, *Phys. Rev.* **111**, 841 (1958).

23. W. L. Earl and D. L. VanderHart, *J. Magn. Reson.* **48**, 35 (1982).

24. B. C. Gerstein, R. G. Pemberton, R. C. Wilson, and L.M Ryan, *J. Chem. Phys.* **66**, 361 (1977).

25. G. E. Maciel, C. E. Bronnimann, and B. L. Hawkins, *Adv. Magn. Reson.* **14**, 125 (1990).

26. S. Hafner and H. W. Spiess, *Solid State Nucl. Magn. Reson.* **8**, 17 (1997).

27. E. Kundla, A. Samoson, and E. Lippmaa, *Chem. Phys. Lett.* **83**, 229 (1981).

28. E. Oldfield, S. Schramm, M. D. Meadows, K. A. Smith, R. A. Kinsey, and J. Ackerman, *J. Am. Chem. Soc.* **104**, 919 (1982).

29. S. Ganapathy, S. Schramm, and E. Oldfield, *J. Chem. Phys.* **77**, 4360 (1982).

30. F. Lefebvre, J. P. Amoureux, C. Fernandez, and E. G. Derouane, *J. Chem. Phys.* **86**, 6070 (1987).

31. A. Samoson, E. Lippmaa, and A. Pines, *Mol. Phys.* **65**, 1013 (1988).

32. A. Llor and J. Virlet, *Chem. Phys. Lett.* **152**, 248 (1988).

33. B. F. Chmelka, K. T. Mueller, A. Pines, J. Stebbins, Y. Wu, and J. W. Zwanziger, *Nature* **339**, 42 (1989).

34. A. Samoson, E. Lippmaa, and A. Pines, *J. Magn. Reson.* **84**, 410 (1989).

35. K. T. Mueller, B. Q. Sun, G. C. Chingas, J. W. Zwanziger, T. Terao, and A. Pines, *J. Magn. Reson.* **86**, 470 (1990).

36. K. T. Mueller, E. W. Wooten, and A. Pines, *J. Magn. Reson.* **92**, 620 (1991).

37. I. J. Farnan, P. J. Grandinetti, J. H. Baltisberger, J. Stebbins, U. Werner, M. A. Eastman, and A. Pines, *Nature* **358**, 31 (1992).

38. P. J. Grandinetti, J. H. Baltisberger, A. Llor, Y. K. Lee, U. Werner, M. A. Eastman, and A. Pines, *J. Magn. Reson. A* **103**, 72 (1993).

39. J. H. Baltisberger, S. L. Gann, P. J. Grandinetti, and A. Pines, *Mol. Phys.* **81**, 1109 (1994).

40. L. Frydman and J. S. Harwood, *J. Am. Chem. Soc.* **117**, 5367 (1995).

41. C. Fernandez and J. P. Amoureux, *Solid State Nucl. Magn. Reson.* **5**, 315 (1996).

42. C. Fernandez and J. P. Amoureux, *Chem. Phys. Lett.* **242**, 449 (1995).

43. D. Massiot, B. Touzo, D. Trumeau, J. P. Coutures, J. Virlet, P. Florian, and P. J. Grandinetti, *Solid State Nucl. Magn. Reson.* **6**, 73 (1996).

44. A. Medek, J. S. Harwood, and L. Frydman, *J. Am. Chem. Soc.* **117**, 12779 (1995).

45. G. Wu, D. Rovnyak, B. Sun, and R. G. Griffin, *Chem. Phys. Lett.* **249**, 210 (1996).

46. C. Jäger, K. Herzog, B. Thomas, M. Feike, and G. Kunath-Fandrei, *Solid State Nucl. Magn. Reson.* **5**, 51 (1995).

47. C. Fernandez, J. P. Amoureux, L. Delmotte, and H. Kessler, *Microporous Materials* **6**, 125 (1996).

48. R. E. Youngman, U. Werner-Zwanziger, and J. W. Zwanziger, *Z. Naturforschung* **51a**, 321 (1996).

49. S. P. Brown, S. J. Heyes, and S. Wimperis, *J. Magn. Reson. A* **119**, 280 (1996).

50. J. V. Hanna, M. E. Smith, and H. J. Whitfield, *J. Am. Chem. Soc.* **118**, 5772 (1996).

51. J. P. Amoureux, C. Fernandez, and L. Frydman, *Chem. Phys. Lett.* **259**, 347 (1996).

52. C. Fernandez, J. P. Amoureux, J. M. Chezeau, L. Delmotte, and H. Kessler, *Microporous Materials* **6**, 331 (1996).

53. J. H. Baltisberger, Z. Wu, J. F. Stebbins, S. H. Wang, and A. Pines, *J. Am. Chem. Soc.* **118**, 7209 (1996).

54. A. Samoson, *J. Magn. Reson. A* **121**, 209 (1996).

55. G. Wu, D. Rovnyak, and R. G. Griffin, *J. Am. Chem. Soc.* **118**, 9326 (1996).

56. J. Rocha, A. P. Esculas, C. Fernandez, and J. P. Amoureux, *J. Phys. Chem.* **100**, 17889 (1996).

57. D. Massiot, R. Conanec, W. Feldmann, R. Marchand, and Y. Laurent, *Inorg. Chem.* **35**, 4957 (1996).

58. D. Massiot, *J. Magn. Reson. A* **122**, 240 (1996).

59. H. Kraus, R. Prins, and A. P. M. Kentgens,
J. Phys. Chem. **100**, 16336 (1996).

60. C. Jäger, P. Hartmann, G. Kunath-Fandrei, O. Hirsch, P. Rehak, J. Vogel, M. Feike, H. W. Spiess, K. Herzog, and B. Thomas,
Ber. Bunsenges. Phys. Chem. **100**, 1560 (1996).

61. J. P. Amoureux, C. Fernandez, and S. Steuernagel,
J. Magn. Reson. A **123**, 116 (1996).

62. J. Rocha, Z. Lin, C. Fernandez, and J. P. Amoureux,
Chem. Commun. **22**, 2513 (1996).

63. P. Sarv, C. Fernandez, J. P. Amoureux, and K. Keskinen,
J. Phys. Chem. **100**, 19223 (1996).

64. S. H. Wang, Z. Xu, J. H. Baltisberger, L. M. Bull, J. F. Stebbins, and A. Pines,
Solid State Nucl. Magn. Reson. **8**, 1 (1997).

65. M. J. Duer and C. Stourton, *J. Magn. Reson.* **124**, 189 (1997).

66. S. J. Hwang, C. Fernandez, J. P. Amoureux, J. Cho, S. W. Martin, and M. Pruski, *Solid State Nucl. Magn. Reson.* **8**, 109 (1997).

67. M. Pruski, D. P. Lang, C. Fernandez, and J. P. Amoureux,
Solid State Nucl. Magn. Reson. **7**, 327 (1997).

68. G. Wu, S. Kroeker, R. E. Wasylishen, and R. G. Griffin,
J. Magn. Reson. **124**, 237 (1997).

69. C. Fernandez, L. Delevoye, J. P. Amoureux, D. P. Lang, and M. Pruski,
J. Am. Chem. Soc. **119**, 6858 (1997).

70. M. Hanaya and R. K. Harris, *Solid State Nucl. Magn. Reson.* **8**, 147 (1997).

71. S. H. Wang, S. M. De Paul, and L. M. Bull, *J. Magn. Reson*. 125, 364 (1997).

72. S. P. Brown and S. Wimperis, *J. Magn. Reson.* **124**, 279 (1997).

73. P. J. Dirken, S. C. Kohn, M. E. Smith, and E. R. H. van Eck,
Chem. Phys. Lett. **266**, 568 (1997).

74. S. Ding and C. McDowell, *Chem. Phys. Lett.* **270**, 1 (1997).

75. B. Ollivier, R. Retoux, P. Lacorre, D. Massiot, and G. Ferey,
J. Mater. Chem. **7**, 1049 (1997).

76. L. Delevoye, S. Liu, M. Welch, C. Fernandez, J. P. Amoureux, and J. Klinowski, *J. Chem. Soc. Faraday Trans.* **93**, 2591 (1997).

77. S. P. Brown and S. Wimperis, *J. Magn. Reson.* **128**, 42 (1997).

78. L. Marinelli and L. Frydman, *Chem. Phys. Lett.* **275**, 188 (1997).

79. P. J. Hore, "Nuclear Magnetic Resonance", Oxford University Press, Oxford, 1995.

80. A. E. Derome, "Modern NMR Techniques for Chemistry Research", Pergamon Press, Oxford, 1987.

81. R. Kemp-Harper, S. P. Brown, C. E. Hughes, P. Styles, and S. Wimperis, *Prog. NMR Spectrosc.* **30**, 157 (1997).

82. C. P. Slichter, "Principles of Magnetic Resonance", 3rd Edn., p. 157-165, Springer-Verlag, Berlin, 1990.

83. R. R. Ernst, G. Bodenhausen, and A. Wokaun, "Principles of Nuclear Magnetic Resonance in One and Two Dimensions", Chap. 6, Clarendon Press, Oxford, 1987.

84. A. G. Redfield and S. D. Kunz, *J. Magn. Reson.* **19**, 250 (1975).

85. G. Bodenhausen, R. Freeman, G. A. Morris, R. Niedermeyer, and D. L. Turner, *J. Magn. Reson.* **25**, 559 (1977).

86. G. Bodenhausen, H. Kogler, and R. R. Ernst, *J. Magn. Reson.* **58**, 370 (1984).

87. S. P. Brown and S. Wimperis, *Chem. Phys. Lett.* **237**, 509 (1995).

88. D. J. States, R. A. Haberkorn, and D. J. Ruben, *J. Magn. Reson.* **48**, 286 (1982).

89. D. Marion and K. Wüthrich, *Biochem. Biophys. Res. Commun.* **113**, 967 (1983).

90. F. D. Doty, *in* "Encyclopedia of Nuclear Magnetic Resonance" (D. M. Grant and R. K. Harris, Eds.), Vol. 7, p. 4475, Wiley, Chichester, 1996.

91. C. P. Slichter, "Principles of Magnetic Resonance", 2nd Edn., p. 486-497, Springer-Verlag, Berlin, 1990.

92. J. P. Amoureux, *Solid State Nucl. Magn. Reson.* **2**, 83 (1993).

93. S. Ashbrook, Part II Thesis, Oxford University, 1997.

94. R. N. Zare, "Angular Momentum", Chap. 5, Wiley, Chichester, 1988.

95. R. N. Zare, "Angular Momentum", Chap. 3, Wiley, Chichester, 1988.

96. P. W. Atkins, "Molecular Quantum Mechanics", 2nd Edn., Chap. 8, Oxford University Press, Oxford, 1983.

97. R. N. Zare, "Angular Momentum", Chap. 2, Wiley, Chichester, 1988.

98. M. M. Maricq and J. S. Waugh, *J. Chem. Phys.* **70**, 3300 (1979).

99. J. Herzfeld and A. E. Berger, *J. Chem. Phys.* **73**, 6021 (1980).

100. M. H. Levitt, *J. Magn. Reson.* **82**, 427 (1989).

101. S. Vega and A. Pines, *J. Chem. Phys.* **66**, 5624 (1977).

102. A. Wokaun and R. R. Ernst, *J. Chem. Phys.* **67**, 1752 (1977).

103. S. Vega, *J. Chem. Phys.* **68**, 5518 (1978).

104. G. Bodenhausen, *Prog. NMR Spectrosc.* **14**, 137 (1981).

105. D. P. Weitekamp, *Adv. Magn. Reson.* **11**, 111 (1983).

106. T. J. Norwood, *Prog. NMR Spectrosc.* **24**, 295 (1992).

107. U. Piantini, O. W. Sørensen, and R. R. Ernst, *J. Am. Chem. Soc.* **104**, 6800 (1982).

108. A. J. Shaka and R. Freeman, *J. Magn. Reson.* **51**, 169 (1983).

109. G. M. Clore and A. M. Gronenborn, *Prog. NMR Spectrosc.* **23**, 43 (1991).

110. A. Bax, R. Freeman, and T. A. Frenkiel, *J. Am. Chem. Soc.* **103**, 2102 (1981).

111. M. H. Levitt and R. R. Ernst, *J. Chem. Phys.* **83**, 3297 (1985).

112. D. M. Doddrell, D. T. Pegg, and M. R. Bendall, *J. Magn. Reson.* **48**, 323 (1982).

113. G. Jaccard, S. Wimperis, and G. Bodenhausen, *J. Chem. Phys.* **85**, 6282 (1986).

114. T. J. Norwood and L. D. Hall, *in* "Encyclopedia of Nuclear Magnetic Resonance" (D. M. Grant and R. K. Harris, Eds.), Vol. 5, p. 3138, Wiley, Chichester, 1996.

115. Y.-S. Yen and A. Pines, *J. Chem. Phys.* **78**, 3579 (1983).

116. J. Baum, M. Munowitz, A. N. Garroway, and A. Pines, *J. Chem. Phys.* **83**, 2015 (1985).

117. R. Tycko and S. O. Smith, *J. Chem. Phys.* **98**, 932 (1993).

118. W. Sommer, J. Gottwald, D. E. Demco, and H. W. Spiess, *J. Magn. Reson. A* **113**, 131 (1995).

119. J. Gottwald, D. E. Demco, R. Graf, and H. W. Spiess, *Chem. Phys. Lett.* **243**, 314 (1995).

120. A. Pines, D. J. Ruben, S. Vega, and M. Mehring, *Phys. Rev. Lett.* **36**, 110 (1976).

121. S. Vega, T. W. Shattuck, and A. Pines, *Phys. Rev. Lett.* **37**, 43 (1976).

122. S. Vega and Y. Naor, *J. Chem. Phys.* **75**, 75 (1981).

123. W. P. Aue, E. Bartholdi, and R. R. Ernst, *J. Chem. Phys.* **64**, 2229 (1976).

124. P. T. Callaghan, "Principles of Nuclear Magnetic Resonance Microscopy", Chap. 2, Clarendon Press, Oxford, 1987.

125. R. M. Bracewell, "The Fourier Transform and its Applications", Chap. 6, McGraw-Hill, New York, 1987.

126 R. R. Ernst, G. Bodenhausen, and A. Wokaun, "Principles of Nuclear Magnetic Resonance in One and Two Dimensions", Chap. 8, Clarendon Press, Oxford, 1987.

127. O. W. Sørensen, M. Rance, and R. R. Ernst, *J. Magn. Reson.* **56**, 527 (1984).

128. H. Eckert, *Prog. NMR Spectrosc.* **24**, 159 (1992).

129. H. Eckert, *in* "Encyclopedia of Nuclear Magnetic Resonance" (D. M. Grant and R. K. Harris, Eds.), Vol. 2, p. 756, Wiley, Chichester, 1996.

130. K. Maeda, Y. Kiyozumi, and F. Mizukami, *Angew. Chem. Int. Ed. Engl.* **33**, 22 (1994).

131. K. Maeda, J. Akimoto, Y. Kiyozumi, and F. Mizukami, *J. Chem. Soc. Chem. Commun.* 1033 (1995).

132. K. Maeda, J. Akimoto, Y. Kiyozumi, and F. Mizukami, *Angew. Chem. Int. Ed. Engl.* **34**, 1199 (1995).

133. V. J. Carter, P. A. Wright, J. D. Gale, R. E. Morris, E. Sastre, and J. Perez-Pariente, *J. Mater. Chem.* **7**, 2287 (1997).

134. J. Klinowski, *in* "Encyclopedia of Nuclear Magnetic Resonance" (D. M. Grant and R. K. Harris, Eds.), Vol. 5, p. 3104, Wiley, Chichester, 1996.

135. I. W. C. E. Arends, R. A. Sheldon, M. Wallau, and U. Schuchardt, *Angew. Chem. Int. Ed. Engl.* **36**, 1145 (1997).

136. S. Schramm, R. J. Kirkpatrick, and E. Oldfield, *J. Am. Chem. Soc.* **105**, 2483 (1983).

137. S. Schramm and E. Oldfield, *J. Am. Chem. Soc.* **106**, 2502 (1984).

138. T. H. Walter, G. L. Turner, and E. Oldfield, *J. Magn. Reson.* **76**, 106 (1988).

139. K. T. Mueller, Y. Wu, B. F. Chmelka, J. Stebbins, and A. Pines, *J. Am. Chem. Soc.* **113**, 32 (1991).

140. K. T. Mueller, J. H. Baltisberger, E. W. Wooten, and A. Pines, *J. Phys. Chem.* **96**, 7001 (1992).

141. D. R. Bell and G. R. Rossman, *Science* **255**, 1391 (1992).

142. B. J. Wood, *Science* **268**, 74 (1995).

143. B. J. Wood, A. Pawley, and D. R. Frost, *Phil. Trans. R. Soc. Lond.* **A 354**, 1495 (1996).

144. E. Libowitzky and A. Beran, *Phys. Chem. Min.* **22**, 387 (1995).

145. S. C. Kohn, *Am. Min.* **81**, 1523 (1996).

146. B. L. Phillips, P. C. Burnley, K. Worminghaus, and A. Navrotsky, *Phys. Chem. Min.* **24**, 179 (1997).

147. A. J. Vega, *J. Magn. Reson.* **96**, 50 (1992).

148. A. J. Vega, *Solid State Nucl. Magn. Reson.* **1**, 17 (1992).

149. W. Sun, J. T. Stephen, L. D. Potter, and Y. Wu, *J. Magn. Reson. A* **116**, 181 (1995).

150. P. W. Atkins, "Molecular Quantum Mechanics", 2nd Edn., p.98, Oxford University Press, Oxford, 1983.

151. N. Müller, G. Bodenhausen, and R. R. Ernst, *J. Magn. Reson.* **75**, 297 (1987).

152. C.-W. Chung and S. Wimperis, *Mol. Phys.* **76**, 47 (1992).

153. H. A. Buckmaster, *Can. J. Phys.* **42**, 386 (1964).